Plasmonic Interactions in the Quantum Tunnelling Regime

Kevin John Savage
Jesus College
University of Cambridge

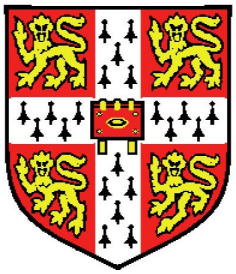

A thesis submitted for the degree of
Doctor of Philosophy
September 2012

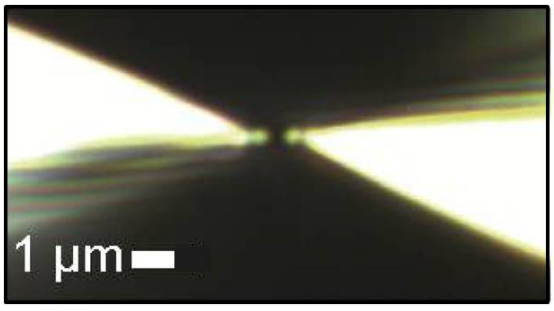

Declaration

The work presented in this thesis was carried out at the Nanophotonics Group in the Cavendish Laboratory, University of Cambridge between October 2007 and September 2011. This dissertation is the result of my own work and includes nothing which is the outcome of work done in collaboration except where specifically indicated in the text. It has not been submitted in whole or in part for any degree at this or any other university, and is less than sixty thousand words long.

Kevin. J. Savage

The picture on the title page is a dark-field image of two axially aligned, gold coated, atomic force microscopy tips. Each tip apex is functionalised with a spherical ball (effective nanoparticle) supporting a localised surface plasmon polariton resonance in the visible spectrum, thus giving them their green appearance. The image is over-exposed to accentuate the scattered light from the nanoparticle on each tip apex.

To my parents John and Sonia, and my brothers Mark and Gareth.

Acknowledgements

I would like to thank my supervisor Professor Jeremy Baumberg for giving me the opportunity to be a founding student member of the Cambridge node of the Nanophotonics Centre. His creativity, inclusive philosophy, 'patience with the student', hard-work, and general zest for exploring the unknown, have been inspirational and much appreciated. Our regular discussions gave me a deeper understanding of scientific research and every aspect covered in this thesis. I am confident that without Jeremy's support, enthusiasm, understanding and foresight the research could well have been cut-short leading to a significantly different conclusion.

Throughout my studies I have thoroughly enjoyed the fact that modern experimental research is impractical without the close interaction of many people. I am therefore indebted to many more people that I can mention individually. So to everyone as a whole, I would like to say that I am extremely grateful for your guidance, facilitation, patience, friendship and (usually) constructive criticism during my time at the Cavendish lab.

The advice, help, insight, knowledge and fun I gained from working with Dr. Bruno Soares was invaluable throughout the first two years of my studentship, and we had many enjoyable times both inside and outside the lab. In my final year I had the pleasure of working closely with Dr. Matthew Hawkeye whose scientific method, extensive knowledge, ability in the lab (and on the football pitch), positive attitude and patience taught and helped me a great deal in a short time. Both Bruno and Matt were great companions around the lab and helped advance the project enormously. Here I would also like to thank Richard Hardy, who was the group's technician for the majority of my studies. His prompt, high-quality work, presence in the office, and advice on the 'finer things in life' were all greatly appreciated.

I would like to say a huge thank you to all the past and present post-docs, students, associates and visitors of the Cambridge Nanophotonics group I had the pleasure to work with, especially: Prof. F. J. García de Abajo (BEMAX!), Dr. Max Bock, Dr. Gabriel Christmann, Peter Christofolini, Dr. Stavros Christopoulos, Dr. Robin Cole, Dr. Chris Coulson, Dr. Richard Denk, Petros Farah (computer issues!), Dr. Alex Finnemore, Dr. Nick Gibbons, Cornelius Grossmann, Dr. Stefan Guldin, Andrew Haines, Lars Herrmann, Dr. Fu Min Huang, James

Hugall (JDAP, amongst many other things!), Andreas Kontogeorgos, Dr. Niraj Lal, Ben Michaelis, Dr. David Snoswell, Christian Steuwe, Jason Sussman, Richard Taylor and Dr. Silvia Vignolini. Additionally, the more recent members of the group, Lindsey Ibbotson, Matt Millyard, Wendy Niu, Alan Sanders and Qibin Zhao, who all arrived near the end of my studies, were friendly companions during my final months in the lab. I can honestly say every single person in the group provided me with assistance, advice, friendship and some damn good times during my studies. I will fondly remember (and in some cases try to forget) our office banter, late nights in the lab, Fountain sessions, frequent excursions, winter schools, early morning cycles home, and all the ups, downs, and everything in between.

The continuous support and encouragement from all my friends outside the lab in Cambridge kept me buoyant through the tough and frustrating times, and I would very much like to acknowledge Dr. James Birrell, Dr. Ruaidhri Farrell, Bethan Shaffery, Dr. Ben Tolley and Debbie Toms. I especially thank Chris Coulson, who not only was a fellow Nanophotonics group member and contributed immensely to my studies both hands-on in the lab and through countless hours of wide-ranging discussion and debate, but also willingly suffered through my ever-presence as one of his housemates. His eclectic music selections provided a sometimes surreal soundtrack to many an evening lab session where the topics of conversation were often far 'outside the box'.

I would like to extend my whole-hearted gratitude to all the Cavendish mechanical and electronic workshop staff who assisted me with the construction of the experimental rig and various trinkets, with special thanks going to Nigel Palfrey. Additionally I would like to thank all the secretarial and IT staff who kept the project running smoothly behind the scenes, especially Angela Campbell and Colin Edwards. Here I would also like to acknowledge the funding from the EPSRC that made this project possible, and provided me with such a great opportunity to add my own research contribution.

Outside Cambridge, I would like to thank all my friends from Southampton and Wokingham, particularly Lucy Collins, David and Paul Dodds, Nick Neish, Dr. Dean Read, Alex Wilson and Karl Wojna, who have been ever-ready to provide ample retreats from the world of physics.

Finally, I thank my family for their unwaivering support and encouragement in every aspect of my life, and it is to them to which this thesis is dedicated.

Abstract

Driven by exciting new research and applications, top-down and bottom-up fabrication techniques are producing ever more intricate, reproducible, plasmonic nanoarchitectures with gaps and junctions approaching the single nanometre and atomic scales. Such atomic-sized features promote the intersection of physics, chemistry and biology in plasmonics. Consequently, understanding light-matter interactions in such closely spaced, electromagnetically coupled, metallic nanosystems is of vital importance to a tremendous variety of current and future nanophotonic technologies. This thesis describes the first dynamically controlled, optically broadband, experimental investigations of light-driven plasmonic coupling between two metal nanostructures with sub-nanometre separation.

A new experimental apparatus and nanosystem alignment technique was developed to enable the required sub-nanometre inter-nanoparticle geometry to be created and probed. Two conducting atomic force microscopy tips with nanoparticle functionalised apices are brought into nanoscale 'tip-to-tip' axial alignment with dynamically-controlled spacing and ultra-wide optical access. Resonant electrical parametric mixing, created by oscillating the electromechanically coupled tips, is utilised to extract an electronic signal due to nanoscale changes in inter-tip position. Experimental results match theory confirming the viability of the technique. By functionalising the tip apices, this unique multi-functional observation platform allows the plasmonic response of nanoparticle dimers with sub-nanometre separations to be characterised.

By simultaneously capturing both the electrical and optical properties of tip-mounted gold nanoparticles with controllable sub-nanometre separation, the first evidence for the quantum regime of optically driven tunnelling plasmonics is revealed in unprecedented detail. It is demonstrated that quantum mechanical effects are critically important at approximately the 0.3 nm scale where spatially non-local tunnelling plasmonics controls the optical response. All observed phenomena are in good agreement with a recently developed quantum-corrected model of plasmonic systems. The findings imply that tunnelling establishes a quantum limit for plasmonic field enhancement and confinement. Additionally, the work suggests the highly enhanced local density of photonic states in nanoscale cavities could enable coherent plasmon-exciton coupling. This thesis prompts new experimental and theoretical investigations into quantum-domain plasmonic systems, and impacts the future of nanoplasmonic device engineering, nanoscale photochemistry and plasmon-mediated electron tunnelling.

List of Publications

K. J. Savage, M. M. Hawkeye, R. Esteban, A. G. Borisov, J. Aizpurua and J. J. Baumberg, "Revealing the quantum regime in tunnelling plasmonics," *Nature*, vol. 491, no. 7425, pp. 574-577, 2012.

K. J. Savage, M. M. Hawkeye, B. F. Soares and J. J. Baumberg, "From microns to kissing contact: Dynamic positioning of two nano-systems," *Applied Physics Letters*, vol. 99, p. 053110, 2011.

Contents

List of Figures

Chapter 1

Introduction

Initial investigations into the interaction of light with metals were first carried out in the early 1900's and over the following century the field has been rediscovered under several different guises. Around three decades after the introductory classical plasma model treatments of metallic media, the advent of quantum mechanics had transformed the description of all materials in the solid state. Consequently the immediate potential of Semi-Conductor (SC) devices as switches was realised and, as illustrated by Fig. (1.1), the advances in solid state physics rapidly overtook the stagnating scope of light-metal interactions. The experimental study of light-metal coupling was eventually resumed in the 1960's under the brand of 'metal optics' and substantial progress was made confirming recently developed theories. Over the next four decades investigations into metal optics provided the basis for what is now known as plasmonics, analogous to how solid state physics research formed the basis for modern electronics. Driven forward primarily by chemical sensing applications, e.g. Surface Enhanced Raman Scattering (SERS), this latest re-incarnation of the field of light-metal interactions emerged strongly towards the end of the 1990's, and over the last 15 years has undergone rapid growth and diversification. This explosion in research output can be attributed to several factors, perhaps the most prominent being our ever increasing capability to specifically tailor and characterise complex nanosystems [1–3]. Such control, in tandem with continuously improving theoretical modelling, now enables the creation of novel nanosystems specifically designed to reveal and exploit new aspects of the plasmonically determined optical response.

However, it is not just progression in technical capacity powering the active expansion of plasmonics research and application output. To explore the

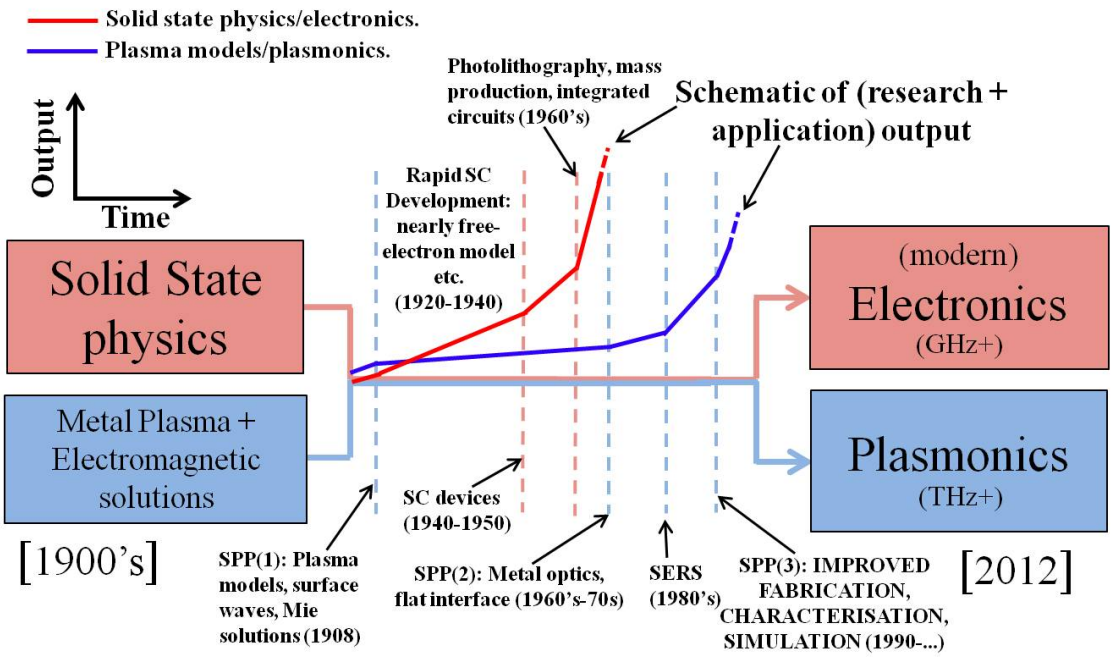

Figure 1.1: A schematic timeline showing the evolution, and combined research and commercial output, relating to the fields of electronics and plasmonics. Note the vertical axis is scaled to accentuate differences in output up to around the 1970's. Plasmonics currently lags electronics by around 30-40 years.

full breadth of plasmonic investigation demands collaboration over a range of disciplines including physics, chemistry, and increasingly biology. Nanoscale plasmonics thus provides impetus for the coalescence of historically separate fields into new multi-disciplinary frameworks. The possibilities for scientific exploration in this cross-over regime are innumerable, exciting, and offer direct routes to new discoveries and *original applications*. It is not surprising then that plasmonic interactions in nanosystems already have a wide-ranging and rapidly expanding list of research level applications, for example, in metamaterials [4], solar cells [5], biosystems [6], Surface Enhanced Raman Spectroscopy (SERS) [7], photonic circuits [8] and cancer research [9].

The intersection of the natural sciences in plasmonics requires that the energy and information carried by light be transferred into, and extracted from, truly nano- and molecular scale volumes. In general, the principles behind the sub-wavelength propagation, localisation and manipulation of electromagnetic waves dictate the blueprint of almost all plasmonic architectures and devices. The necessary deep sub-wavelength control of light is now beginning to

be made possible by plasmonic design and nanoscale construction, and therefore it is highly likely that plasmonic research will lead to an expansive range of potentially revolutionary 'real-world' applications, for example in energy production [10], medicine [11], computing [12] and optics [13].

To this end, top-down and bottom-up nanofabrication techniques continue to produce ever smaller, more intricate, nanosystems driving towards the molecular and atomic size regimes. It is therefore imperative that plasmonic interactions on the 2 nm$\rightarrow$'0' nm 'quantum length' scale are investigated and understood. Almost every present and future utilisation of plasmonic systems could benefit from an improved understanding of this critical regime, with specific examples including, molecular-opto electronics, single-emitter SERS, optical frequency domain metamaterials, high-efficiency solar cells, active plasmonics, extreme non-linear interactions, and quantum optics and computation.

The description of the majority of plasmonic phenomena can be initialised by considering the specific type of surface excitations known as Surface Plasmons (SPs) and Surface Plasmon Polaritons (SPPs), where SPPs describe a mixed state of propagating light and metallic matter [14]. When SPPs are confined locally on an extended system, or on an isolated nanosystem, they are commonly referred to as Localised Surface Plasmons Polaritons (LSPPs). Understanding LSPP and SPP properties and interactions in innovative nanosystems is therefore key to advancing the field and hence creating new, or extending existing applications.

As LSPPs are often highly radiative in nature a copious amount of information on the plasmonic response of a nanosystem is found from using broadband, far-field, optical elastic scattering spectroscopy as a non-destructive probe. Therefore the aim of the work described in this thesis becomes clear: the first broadband optical scattering measurements revealing the plasmonic response of a single nanosystem where the effects due to physical features on the quantum length scale are expected to be prevalent.

The type of nanosystem engineered to expose this intriguing quantum regime was a NanoParticle (NP) pair, commonly referred to as a NP (homo-) dimer in analogy to a molecular dimer. In this case each individual NP is created on the vertex of a commercially available Atomic Force Microscopy (AFM) tip by functionalisation of the apex. Two such AFM tips were then maneuvered into axial tip-to-tip alignment and the inter-NP (apex) separation dynamically controlled from microns to less than 1 nm. The NP dimer system created was exam-

ined by simultaneous measurement of the optical scattering and electronic conduction characteristics. Investigation of the non-classical plasmonic response, introduced by the sub-nanometre gaps created, was the primary goal of the present work.

1.1 Thesis Layout

The thesis is organised into six chronologically ordered chapters. The first three chapters describe the motivation for the work, the current physical understanding of the phenomena, and the experimental framework developed. This foundation shows how the work and results described in the last three chapters are relevant, viable and ultimately a useful contribution to the field of plasmonics.

Firstly, Chapter (2) provides a brief theoretical overview of the concepts in electrodynamics and solid state theory relevant to plasmonics in general. More specific attention is devoted to SPPs on semi-infinite, planar, metal-dielectric interfaces, and LSPPs on isolated NPs and electromagnetically coupled NP dimers. Recent developments in experiments and theory describing LSPPs in nanosystems with features on the order of the quantum length scale are highlighted and discussed in the context of the work undertaken. By combining the well established theoretical basis for plasmonic nanosystems in the classical regime, and current experimental and theoretical state-of-the-art work by the wider community, some open questions are posed. Finally, with these background components in place, a summary of current understanding and research intentions is presented.

A new system was developed to create NP dimers with sub-nanometre separation as current methods cannot provide the required combination of low-background ultra-wide optical access, electronic measurement capability, dynamic position control, and appropriate NP size and shape characteristics. The experimental rig built to create and interrogate the required NP dimer systems, formed by the functionalised apices of two AFM tips, is described in Chapter (3). Here the mechanical, electronic and optical design characteristics of the developed rig are described in detail to provide the basis for all subsequent experimental work. An overview of the versatile observation platform produced concludes the chapter.

The creation of the required NP dimer systems demanded the experimental and theoretical validation of a new, general, nanosystem pair alignment method. The technique developed is described in Chapter (4) and is based on the resonant electromechanical actuation of the coupled, dual AFM cantilever, tip and apex NP composite system. Changes in AFM cantilever (and therefore tip) oscillation amplitude, i.e. changes in inter-tip position, are measured electronically as one of the AFM tips is scanned in an alignment grid. This enables the NP functionalised apices of the AFM tips to be aligned on the nanoscale thus creating an effective NP dimer with controllable inter-NP separation. First, an analytical toy model is outlined to provide physical insight into the complex non-linear coupled system, followed by a more rigorous numerically implemented model. The experimental results are compared against the developed simulation, and conclusions drawn on the effectiveness of the technique.

In Chapter (5) the preceding work is amalgamated to create NP dimers with sub-nanometre inter-NP separation. The plasmon mediated optical response and inter-NP electronic conduction are measured simultaneously in the deep sub-nanometre regime. The experimental results reveal optically driven quantum tunnelling plasmonic coupling phenomena for the first time and are compared against recently developed theory. A simple charge transfer time-scale model is presented to provide an improved physical understanding of the plasmonic response in the sub-nanometre regime and conclusions are drawn. The measurements also show features possibly attributable to coherent plasmon-exciton coupling in the inter-NP nanocavity, that would provide the first evidence of 'plexcitonic' quasiparticles in such NP dimer systems. A basic classical argument is presented to support the strong-coupling hypothesis.

Finally, Chapter (6) presents a summary of all the work carried out in this thesis. Based on the motivations, theoretical background, results and analysis, several possible future investigations are recommended.

Chapter 2

Theoretical Background

2.1 Introduction

The foundations of what is now known as the field of plasmonics were laid by Drude in 1900. Inspired by Maxwell's work on electromagnetism Drude developed a theory to describe the collective response of conduction electrons in a material to incident electromagnetic radiation [15]. The Drude model assumes that a material contains immobile positive ions surrounded by a free-electron plasma in which the electrons can be considered to be classical and non-interacting with each other. These assumptions imply that the response of electrons in a material can be modelled by only considering the force exerted on them by a perturbing electromagnetic field and the damping force present due to their electromagnetic interactions with scatterers, e.g. impurities and phonons. Although a relatively simple classical kinetic gas model, it provides very good explanations of the electrical conductivity and optical response of metals, as characterised by frequency dependent, complex dielectric and conductivity functions, $\widetilde{\varepsilon}_m(\omega)$ and $\widetilde{\sigma}_m(\omega)$ respectively. The Drude model also predicts the existence of collective longitudinal oscillations in the bulk, and surface, of the free-electron plasma. In the following years a quantum mechanical treatment of the problem defined a Bulk Plasmon (BP) and SP as quasi-particles describing quanta of these oscillations [16, 17].

In 1902, soon after Drude's work predicted BPs, Wood unknowingly discovered the first evidence of SPPs while investigating the light reflected from diffraction gratings [18]. He observed anomalous behaviour in the intensity of the reflected light as a function of wavelength. At the time these results

could not be explained and they became known as Wood's anomalies. Near the beginning of 1908, in seemingly unrelated theoretical work, Mie published the electromagnetic solutions to Maxwell's equations for the optical response of spherical particles [19]. Concurrently Zenneck found solutions describing electromagnetic waves guided along a planar conductor-dielectric interface [20]. It would not be until almost 70 years later that Drude's simple model, Wood's anomalies, and Mie's and Zenneck's solutions could all be interpreted under a unified theory of electromagnetic surface waves hybridised with spatial oscillations of the surface electron plasma.

Rayleigh provided a partial explanation for Wood's anomalies in 1907 [21], but it was not until important theoretical contributions from Fano in 1941 [22] and Bohm [16], Pines [17] and Ritchie [23] in the 1950's, that a theoretical framework was in place to describe collective electron behaviour and the possibility of light strongly coupling to metallic surfaces. These theories explained the experimentally measured electron energy loss on transmission through thin metallic films, most notably conducted by Powell and Swan [24]. The electron transmission experiments spurred on the first theoretical work by Stern and Ferrell describing the SP [25]. In the late 1960's light was first deliberately coupled onto metallic surfaces, most prominently by Ritchie [26], Kretschmann and Reather [27][1], and Otto [29]. The description of this phenomena was achieved through a general theory describing the coupling of collective surface electron oscillations to electromagnetic surface waves, and a new class of quasi-particle describing this phenomena was introduced as a SPP by Cunningham in 1974 [30]. Only now could the final aspects of the anomalous reflectance behaviour observed by Woods be fully understood as a result of SPP excitation. The (Sommerfeld-)Zenneck electromagnetic surface waves are naturally recovered in the low-frequency limit of the SPP dispersion, while the renewed interest in SPs also led to the re-interpretation of Mie's electromagnetic solutions for spherical geometries. The solutions for metallic particles could now be described intuitively in terms of localised SP modes [31], or more generally as SPPs confined to a particle, referred to as LSPP modes.

Over the last three decades, SPPs and LSPPs excited on metallic systems with dimensions and features designed and controlled on the nanoscale, have

[1]It should be noted that in 1959 Turbader [28] had already used the so called 'Kretschmann' experimental configuration for reflectance measurements on aluminium films. The characteristic reflection dips recorded were due to light coupling to the metallic surface.

been extensively studied due to their huge range of plasmonic responses and associated applications. The present work is concerned with the study of the electromagnetic interactions between LSPPs confined on individual metallic NP systems as they are brought into conductive contact. This chapter will therefore first present a brief theoretical background on the electromagnetic response of metals under the Drude model framework. From this starting point a basic theoretical treatment of SPs and SPPs in simple planar systems is presented followed by an introduction to LSPPs and coupled LSPP interactions in NP systems. The open questions that the current work has aimed to address are then presented within the context of the theoretical background.

2.2 Optical Frequency Response of Metals

A full description of how classical optical frequency electromagnetic waves interact with different media is of vital importance to understand and predict plasmonic behaviour. This can be achieved by finding solutions to the macroscopic Maxwell's equations which fit the boundary conditions and distributions of charge and current appropriate to the system in question. The fundamental macroscopic material parameters through which these solutions are expressed are the main topic of this section.

2.2.1 Electromagnetic Waves in Media

The macroscopic Maxwell's equations describing electromagnetic waves with wavevector $\tilde{\mathbf{q}}$ and angular frequency ω within an isotropic linear medium take the form[2]

$$\nabla \cdot \mathbf{D} = \rho_{ext} \tag{2.1}$$

$$\nabla \cdot \mathbf{B} = 0 \tag{2.2}$$

$$\nabla \times \mathbf{E} = -\frac{\partial \mathbf{B}}{\partial t} \tag{2.3}$$

[2]S.I units are used throughout this work. For clarity, in certain cases the tilde annotation $\tilde{}$ is used to emphasise a complex quantity. The 'wide-hat' annotation $\hat{}$ denotes a quantity that has undergone a Fourier transform.

$$\nabla \times \mathbf{H} - \frac{\partial \mathbf{D}}{\partial t} = \mathbf{J_{ext}} \tag{2.4}$$

where the displacement field $\mathbf{D}$ and electric field $\mathbf{E}$ are linked via the constitutive relation $\mathbf{D} = \varepsilon_0 \widetilde{\varepsilon}_r \mathbf{E}$ and the magnetic flux density field $\mathbf{B}$ and magnetic field $\mathbf{H}$ are linked via the constitutive relation $\mathbf{B} = \mu_0 \widetilde{\mu}_r \mathbf{H}$. Here ε_0 and μ_0 are the permittivity and permeability of free-space respectively and $\widetilde{\varepsilon}_r$ and $\widetilde{\mu}_r$ are the relative dielectric constant (relative permittivity) and relative permeability respectively. In general $\widetilde{\varepsilon}_r$ and $\widetilde{\mu}_r$ are tensors, however as the medium is assumed to be isotropic these quantities reduce to complex scalars. Finally ρ_{ext} is the external charge density and $\mathbf{J_{ext}}$ is the external current density. The physics of the 'free' and 'bound' internal charges and currents are described by the dynamics of a *total* internal polarisation ($\mathbf{P}$) of the system via $\mathbf{D} = \varepsilon_0 \mathbf{E} + \mathbf{P}$ and the magnetisation ($\mathbf{M}$) of the system via $\mathbf{H} = \frac{1}{\mu_0}\mathbf{B} + \mathbf{M}$. Re-arranging Eqns. (2.3) and (2.4) to eliminate $\mathbf{H}$ leads to a wave equation in terms of $\mathbf{E}$ and $\mathbf{J_{ext}}$

$$-\nabla\left(\nabla \cdot \mathbf{E}\right) + \nabla^2 \mathbf{E} = \varepsilon_0 \widetilde{\varepsilon}_r \mu_0 \widetilde{\mu}_r \frac{\partial^2 \mathbf{E}}{\partial t^2} + \mu_0 \widetilde{\mu}_r \frac{\partial \mathbf{J_{ext}}}{\partial t} \tag{2.5}$$

Taking the Fourier transform ($\nabla \rightarrow i\widetilde{\mathbf{q}}$, $\frac{\partial}{\partial t} \rightarrow -i\omega$) of Eqn. (2.5) and assuming the medium to be non-magnetic ($\widetilde{\mu}_r = 1$) gives

$$\widetilde{\mathbf{q}}\left(\widetilde{\mathbf{q}} \cdot \widehat{\mathbf{E}}\right) - \widetilde{q}^2 \widehat{\mathbf{E}} = -\widetilde{\varepsilon}_r k_0^2 \widehat{\mathbf{E}} - i\omega\mu_0 \widehat{\mathbf{J}}_{\mathbf{ext}} \tag{2.6}$$

where $k_0 = (\omega/c)$ is the free-space wavenumber with c equal to the speed of light *in vacuo*. For transverse (electromagnetic) solutions $\widetilde{\mathbf{q}} \cdot \widehat{\mathbf{E}} = 0$ [3] and assuming there are no sources of external stimuli present, i.e. $\widehat{\rho}_{ext} = 0$ and $\widehat{\mathbf{J}}_{\mathbf{ext}} = 0$, Eqn. (2.6) reduces to

$$\widetilde{q} = \sqrt{\widetilde{\varepsilon}_r^T} k_0 \qquad \Rightarrow \qquad \sqrt{\widetilde{\varepsilon}_r^T} = \frac{\widetilde{q}}{k_0} \tag{2.7}$$

where $\widetilde{\varepsilon}_r^T$ is the relative permittivity for transverse excitations. For longitudinal (electrostatic) solutions $\widetilde{\mathbf{q}} \cdot \widehat{\mathbf{E}} = \widetilde{q}\widehat{E}$ and assuming no external stimuli Eqn. (2.6)

[3] It should be stressed that this equation, and similar equations throughout this work, do not have their usual geometrical meaning because $\widetilde{\mathbf{q}}$ is a complex quantity. In other words, transverse (longitudinal) excitations in an absorbing medium are not required to have $\widehat{\mathbf{E}}$ entirely perpendicular (parallel) to $\Re[\widetilde{\mathbf{q}}]$.

reduces to

$$\widetilde{\varepsilon}_r^L = 0 \tag{2.8}$$

where $\widetilde{\varepsilon}_r^L$ is the relative permittivity for longitudinal excitations. In general the approximation $\widetilde{\varepsilon}_r^T = \widetilde{\varepsilon}_r^L = \widetilde{\varepsilon}_r$ is valid, however for large $\widetilde{\mathbf{q}}$ the difference in dielectric response has to be taken into account.

Considering the relationship between $\mathbf{D}$ and the internal current density $\widetilde{\mathbf{J}}_{\mathbf{int}}(= \frac{\partial \mathbf{P}}{\partial t} = \widetilde{\sigma}\mathbf{E})$ yields the fundamental link between $\widetilde{\varepsilon}_r$ and the conductivity $\widetilde{\sigma}$ [32]

$$\widetilde{\varepsilon}_r = 1 + \frac{i\widetilde{\sigma}}{\varepsilon_0 \omega} \tag{2.9}$$

Substituting Eqn. (2.9) into Eqn. (2.7) gives

$$\widetilde{q} = k_0 \left(1 + \frac{i\widetilde{\sigma}}{\varepsilon_0 \omega}\right)^{\frac{1}{2}} \tag{2.10}$$

The relative dielectric constant and conductivity are in general complex, i.e. $\widetilde{\varepsilon}_r = \varepsilon_1 + i\varepsilon_2$ and $\widetilde{\sigma} = \sigma_1 + i\sigma_2$. These macroscopic material parameters relate the bulk material electromagnetic response to the averaged response of the constituent atoms and electrons. The complex refractive index of the medium can be defined as $\widetilde{n} = n + i\kappa = \sqrt{\widetilde{\varepsilon}_r}$ where n is the real refractive index and κ is the extinction coefficient[4]. The complex relative dielectric constant and refractive index can be linked by equating their real and imaginary parts

$$\varepsilon_1 = n^2 - \kappa^2 \tag{2.11}$$

$$\varepsilon_2 = 2n\kappa \tag{2.12}$$

From Eqns. (2.11) and (2.12) the expressions for n and κ for media without gain characteristics are

[4]Strictly $\widetilde{n} = \pm\sqrt{\widetilde{\varepsilon}_r \widetilde{\mu}_r}$. As the complex refractive index is a derived concept (does not appear in Maxwell's equations) either sign can be taken. All materials considered in this work are so called 'epsilon negative' materials (over the frequency range of interest) and the positive root is taken. However for certain metamaterials, e.g. double negative materials (not found in nature), the negative root should be taken [33]. Note causality is maintained in both cases [34].

$$n = \sqrt{\frac{\sqrt{\varepsilon_1^2 + \varepsilon_2^2} + \varepsilon_1}{2}} \qquad \text{and} \qquad \kappa = \sqrt{\frac{\sqrt{\varepsilon_1^2 + \varepsilon_2^2} - \varepsilon_1}{2}} \tag{2.13}$$

For a monochromatic electromagnetic plane wave travelling in the x-direction through a medium it is postulated that the electric field varies as

$$\mathbf{E} = \mathbf{E_0} e^{i(\widetilde{q}x - \omega t)} \tag{2.14}$$

where $\mathbf{E_0}$ is the electric field amplitude with the vectorial character describing the polarisation (linear polarisation in this case). Substituting the complex wavenumber $\widetilde{q} = k_0\sqrt{\widetilde{\varepsilon}_r} = k_0\widetilde{n}$ into Eqn. (2.14) gives

$$\mathbf{E} = \mathbf{E_0} \exp\left(-k_0\kappa x\right) \exp\left(i\omega\left(\frac{n}{c}x - t\right)\right) \tag{2.15}$$

This shows how the real and imaginary components of the complex refractive index (and hence complex relative dielectric constant) of the medium affect the propagation of an incident electromagnetic wave. The argument of the left hand exponential is real and describes the attenuation of the wave as it propagates through the medium. The argument of the right hand exponential is imaginary and hence describes the oscillatory part of the wave. If $|\varepsilon_1| \gg |\varepsilon_2|$ the real part of the refractive index n is mainly determined by ε_1 and therefore ε_1 describes the change in phase velocity ($v_p = \frac{\omega}{k_0 n}$) of the propagating wave due to polarisation of the medium. The group velocity $v_g = \frac{\partial\omega}{\partial\Re[\widetilde{q}]}$ determines the velocity of energy propagation through the medium.

2.2.2 The Drude Model

Through $\widetilde{\varepsilon}_r$ the macroscopic Maxwell's equations provide the framework to describe how electromagnetic waves interact with different media. A brief discussion on how the Drude model describes $\widetilde{\varepsilon}_r$ for metallic media is now presented to provide a physical understanding of the origin of this most important parameter.

Until now $\widetilde{\varepsilon}_r$ has been referred to as the complex relative dielectric *constant* of the medium. However the dielectric and conductive response of a homoge-

neous[5] medium are functions of the frequency (temporal non-locality) of the incident electromagnetic wave and the wavevector $\widetilde{\mathbf{q}}$ (spatial non-locality) it acquires inside the medium due to the scattering with electrons. In certain metallic media the approximate frequency dependence of $\widetilde{\varepsilon}_m(\widetilde{\mathbf{q}},\omega)$ and $\widetilde{\sigma}_m(\widetilde{\mathbf{q}},\omega)$ is well described by the Drude model[6]. The $\widetilde{\mathbf{q}}$ dependence of the dielectric and conductive response can be described by a more rigorous quantum mechanical hydrodynamic-Drude model where the electrons can now feel the forces due to variations in pressure of the electron gas, created mainly due to the Pauli exclusion principle.

In most situations the wavevector contribution to $\widetilde{\varepsilon}_m(\widetilde{\mathbf{q}},\omega)$ and $\widetilde{\sigma}_m(\widetilde{\mathbf{q}},\omega)$ can be neglected, as the $\widetilde{\mathbf{q}}$ dependent terms are small in the optical regime. It is important to note that this simplification is not always valid, and it has to be taken into account that not only light, but also electrons in the metal, transport energy. For example, when light interacts with a NP dimer with inter-NP separation d, evanescent wavevector components $\widetilde{\mathbf{k}}_{\mathbf{E}}$ are created with magnitude $\left|\widetilde{k}_E\right| = 2\pi/d$. These can in turn impart a significant momentum $\hbar\widetilde{\mathbf{q}}$ to the electrons in the vicinity of the nanogap between the NP dimer. For metals, if $d \lessapprox 5$ nm then $\widetilde{\mathbf{q}}$ is no longer negligible and can modify the material response considerably [35].

In this large $\widetilde{\mathbf{q}}$ regime, the response of an electron at position $\mathbf{r_e}$ now also depends on the electron excitations at nearby positions $\mathbf{r'_e}$. The homogeneity approximation greatly simplifies the description of the system by allowing the dependence on electron position to enter $\widetilde{\varepsilon}_m$ and $\widetilde{\sigma}_m$ via $\widetilde{\varepsilon}_m\left(\mathbf{r_e}-\mathbf{r'_e}, t-t'\right)$ and $\widetilde{\sigma}_m\left(\mathbf{r_e}-\mathbf{r'_e}, t-t'\right)$ respectively. Thus the *spatial and temporal non-locality* enter $\widetilde{\varepsilon}_m$ and $\widetilde{\sigma}_m$ via $\widetilde{\varepsilon}_m(\widetilde{\mathbf{q}},\omega)$ and $\widetilde{\sigma}_m(\widetilde{\mathbf{q}},\omega)$ respectively in the Fourier domain [14]. The spatially non-local short-range interactions are contained within a volume defined by the penetration depth of the induced-surface-charge $\delta_e \approx 0.5$ nm, and the dimensions of the nanogap. Here δ_e is defined by the $1/e$ decay length of the induced longitudinal charge density oscillations (BPs), i.e. $\delta_e \sim 1/\Im\left[\widetilde{\mathbf{q}}_\mathbf{0}\right]$, where $\widetilde{\mathbf{q}}_\mathbf{0}$ is defined via the longitudinal dielectric function of the metal under the required condition $\widetilde{\varepsilon}_m^L(\widetilde{\mathbf{q}}_\mathbf{0},\omega) = 0$ (Eqn. (2.8)). This effect contributes to the overall non-local screening response of the nanosystem. It is important to stress

[5]Homogeneous in the sense that all relevant length scales are substantially larger than the lattice spacing of the metal, e.g. approximately 0.4 nm for Au.

[6]Throughout this thesis subscripts 'm' and 'd' denote metallic and dielectric media respectively.

that in the large $\left|\widetilde{k}_E\right|$ domain, BPs (and SPs) can be excited not only by particle impact, but also by light. Finally, it should also be noted that the homogeneity approximation is perhaps on the edge of validity in this regime. This can be overcome by the extremely computationally expensive, *ab initio*, full quantum mechanical methods described in Sec. (2.3.3).

Similarly, such spatial non-locality also has to be taken into account when considering individual metal NPs of dimensions less than $\approx$ 10 nm, substantially less than the mean free path length of the excited electrons around the Fermi-level[7]. Under the high symmetry case of a single spherical NP the spatial non-locality is typically taken into account phenomenologically by increasing the damping rate associated with the conduction electrons in the material [38]. The increase in damping is attributed to the rate of electron collisions with the NP surface for the electrons moving close to the Fermi-level, and is therefore intuitively understood as a surface scattering phenomena. Recent work has shown that the physical nature of this effect is more generally described by considering the role of the large $\widetilde{\mathbf{q}}$ components created [35]. The large $\widetilde{\mathbf{q}}$ components describe how the induced-surface-charges (screening charges) now penetrate inside the NP by a non-negligible amount ($\approx$ 0.5 nm) compared to the NP dimensions via BP excitation. This is in contrast to the spatially local description where the induced-surface-charges follow a surface-delta-function. The excitation of dispersive BPs into the NP's interior, and the associated pressure variations (due to Pauli-exclusion effect) in the electron gas, describe a component of the spatially non-local response of the dielectric function.

In the Drude model the electron-electron interaction and lattice potential specifics are not taken into account. Instead the assumption is made that some aspects of the metal's band structure are incorporated into the effective optical mass m_e^* of each electron. It is also assumed that the perturbing field $\mathbf{E}$ is a self-consistent field that includes the mean value of the field produced by the electrons themselves (mean-field approximation). It should be noted that the Drude model was extended by Sommerfeld in 1933 to include quantum mechanical Fermi-Dirac statistics, thus forming the well known free-electron (Drude-Sommerfeld) model. This model showed that only the electrons near the

[7] In the single NP case, spatial non-locality is often referred to as the 'finite-size effect', 'surface scattering effect' or 'interface damping effect'. This should not be confused with quantum confinement effects, and additional electron-density 'spill-out' mediated non-local screening, that are only non-negligible in NPs of less than approximately 4 nm diameter [36,37].

Fermi-level contribute as the Pauli-exclusion principle does not allow electrons occupying lower levels to change their electronic state. However the following results are the same regardless of which model is used.

Under the long-wavelength (spatially local response) approximation the wavelength of all exciting light components is much greater than the metal's unit cell dimensions. This simplification ensures that the forces due to the variations in the pressure of the electron gas are negligible. Thus spatially non-local quantum mechanical models need not be used and the dielectric function of the metal $\widetilde{\varepsilon}_m^T(\widetilde{\mathbf{q}},\omega) = \widetilde{\varepsilon}_m^L(\widetilde{\mathbf{q}},\omega) = \widetilde{\varepsilon}_m(\omega)$. Following from these assumptions, the equation of motion for a conduction electron in an isotropic free-electron plasma can be written as

$$m_e^* \ddot{\mathbf{r}}_\mathbf{e} + m_e^* \gamma \dot{\mathbf{r}}_\mathbf{e} = -e\mathbf{E}(\mathbf{r}_\mathbf{e}, t) \tag{2.16}$$

where γ is the phenomenological electron collision frequency and e is the charge of an electron. Moreover, assuming a macroscopic spatially uniform perturbing field $\mathbf{E}(\mathbf{r_e}, t) \rightarrow \mathbf{E}(t)$, with a harmonic time dependence, and a linear response, gives

$$\mathbf{E}(t) = \mathbf{E_0} e^{-i\omega t} \tag{2.17}$$

$$\widetilde{\mathbf{r}}_\mathbf{e}(t) = \widetilde{\mathbf{r}}_\mathbf{0} e^{-i\omega t} \tag{2.18}$$

where $\widetilde{\mathbf{r}}_\mathbf{0}$ is the complex amplitude of the electron oscillation. Substituting (2.17) and (2.18) into (2.16) and solving for $\widetilde{\mathbf{r}}_\mathbf{0}$ allows the macroscopic polarisation of the metal to be determined. This leads to an expression that describes the frequency dependence of $\widetilde{\varepsilon}_m(\omega)$ via $\mathbf{D} = \varepsilon_0 \mathbf{E} + \mathbf{P}$

$$\widetilde{\varepsilon}_m(\omega) = 1 - \frac{\omega_p^2}{\omega^2 + i\gamma\omega} \tag{2.19}$$

where ω_p is the bulk plasma frequency defined as $\omega_p^2 = \frac{n_e e^2}{\varepsilon_0 m_e^*}$ with n_e being the conduction electron density of the metal. The real and imaginary components of $\widetilde{\varepsilon}_m(\omega)$ are given by

$$\Re\left[\widetilde{\varepsilon}_m(\omega)\right] = \varepsilon_1(\omega) = 1 - \frac{\omega_p^2\tau^2}{1+\omega^2\tau^2} \tag{2.20}$$

$$\Im\left[\widetilde{\varepsilon}_m(\omega)\right] = \varepsilon_2(\omega) = \frac{\omega_p^2\tau}{\omega(1+\omega^2\tau^2)} \tag{2.21}$$

where $\tau = 1/\gamma$ is the phenomenological electron relaxation time. Using the same arguments as above an expression for $\widetilde{\sigma}_m(\omega)$ can also be obtained via $\mathbf{J_{int}} = \frac{\partial \mathbf{P}}{\partial t} = \widetilde{\sigma}_m \mathbf{E}$

$$\widetilde{\sigma}_m(\omega) = \frac{\omega_p^2\varepsilon_0\tau}{1-i\omega\tau} = \frac{\sigma_0}{1-i\omega\tau} \tag{2.22}$$

where $\sigma_0 = \omega_p^2\varepsilon_0\tau$ is the zero-frequency conductivity. Note that by comparing Eqns. (2.19) and (2.22) the general result of Eqn. (2.9) is recovered as expected.

A first extension to this model can be made by including the contribution of the bound electrons to the polarisability of the metal. For example, in the noble metals, the filled d-band close to the Fermi surface creates a highly polarised environment. This so called 'quasi-free' electron Drude model yields a dielectric function of the form

$$\widetilde{\varepsilon}_m(\omega) = \varepsilon_{bk} - \frac{\omega_p^2}{\omega^2 + i\gamma\omega} \tag{2.23}$$

where ε_{bk} is the background contribution to the dielectric function found as $\omega \to \infty$ [14]. The form of the real and imaginary components of $\widetilde{\varepsilon}_m(\omega)$ are shown in Fig. (2.1).

In the small damping limit $\omega_p\tau \gg 1$, and thus Eqns. (2.20) and (2.21) show $\widetilde{\varepsilon}_m\left(\omega_p\right) \approx 0$. For a longitudinal oscillation $\widetilde{\mathbf{q}} \cdot \widehat{\mathbf{E}} = \widetilde{q}\widehat{E}$, therefore if there are no external sources of current present Eqn. (2.6) demands $\widetilde{\varepsilon}_m\left(\omega\right) = 0$. These results imply that at frequency ω_p transverse electromagnetic modes cannot be supported in the metal, hence ω_p defines the natural frequency of a collective purely longitudinal oscillation in the metal's free-electron plasma. These plasma waves cannot therefore couple to purely transverse electromagnetic waves[8] and can generally only be excited by direct particle impact, for example from external in-

[8] In the $\widetilde{\mathbf{q}} = 0$ (long-wavelength or spatially local) limit Gauss's law shows that a purely transverse electromagnetic wave in a bulk medium cannot create charge density fluctuations (longitudinal oscillations) in a free-electron plasma.

cident electrons. In a quantum mechanical treatment it is shown that the quanta of collective longitudinal charge oscillations are quasi-particles known as BPs. Spatial non-locality also introduces modifications to the BP dispersion due to an entire series of collective longitudinal oscillations at higher frequencies with finite $\widetilde{\mathbf{q}}$ dependence. To 0^{th} order (only considering a spatially local response) BPs oscillate with associated discrete plasma frequency ω_p. As discussed previously, this approximation is usually considered to be valid as higher-order terms in the series only become non-negligible for incident wavenumber $k \gtrapprox 10^9$ m^{-1}, i.e. far outside the typical free-space and evanescent optical regimes.

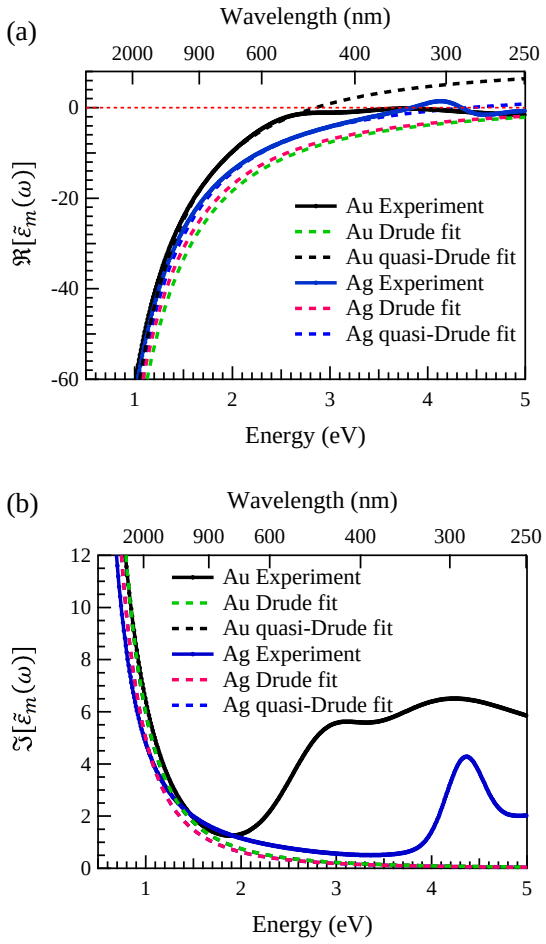

Figure 2.1: (a) Graph comparing the experimental values of $\Re\left[\widetilde{\varepsilon}_m(\omega)\right]$ for gold and silver (see, e.g. Palik Handbook [39]) against Drude model fits, and quasi-Drude model fits to the region below 2 eV. (b) Same as in (a) but for $\Im\left[\widetilde{\varepsilon}_m(\omega)\right]$. Physical model fitting parameters for gold are $\omega_p = 1.34 \times 10^{16}$ rad s^{-1}, $\tau = 8.5 \times 10^{-15}$ s, $\varepsilon_{bk} = 9.5$ and for silver $\omega_p = 1.29 \times 10^{16}$ rad s^{-1}, $\tau = 9.5 \times 10^{-15}$ s, $\varepsilon_{bk} = 2.7$ [40]. Note the poor agreement at visible and shorter wavelengths due to interband transitions.

The Drude model is reasonable at modelling certain metals, e.g. the alkali and noble groups, especially at low incident photon energies ($\lessapprox$ 1.5 eV). The alkali metals have closed shells of valence electrons that are effectively inert and conduction bands that are at considerably higher energies. Therefore the approximately spherical Fermi surface is far from the edges of the first Brillouin zone and hence the lattice (periodic potential) only very weakly perturbs (scatters) the electrons. For the noble metals the situation is complicated because the contribution from the electrons occupying the valence d-bands cannot be neglected. However the effect is found to be moderate and hence the alkali and noble metals are often referred to as 'nearly-free-electron' metals where absorption of light is assumed to be proceed primarily by intraband transitions. It is interesting to note, at lower energies, the agreement between the experimentally measured $\Re\left[\widetilde{\varepsilon}_m\left(\omega\right)\right]$ and the Drude model fit is significantly worse than that between the associated $\Im\left[\widetilde{\varepsilon}_m\left(\omega\right)\right]$ and Drude model fit. This is because the resonant interband transitions affect $\Re\left[\widetilde{\varepsilon}_m\left(\omega\right)\right]$ over a much broader frequency range due to the Lorentzian lineshape of the resonant transitions.

As shown in Fig. (2.1), the quasi-Drude Model predicts the optical response of gold and silver with good experimental agreement at low energies[9]. However, at around approximately 1.5 eV optically induced interband transitions from the occupied states at the top of the d-bands to the empty states around the Fermi-level begin to occur. Hence, although the quasi-Drude model is effective for describing the more delocalised ('nearly-free') sp-band electron contributions, it does not superimpose the resonant behaviour of the induced interband transitions. These resonant phenomena can be modelled under the Drude-Lorentz formalism where interband transitions are described classically by including extra oscillators of type I, with mass m_I^*, density of charge n_I, collision frequency γ_I and resonance frequency ω_{0I}, to Eqn. (2.16). This leads to a theoretical approach that involves solving systems of Lorentz oscillators [41] and yields a dielectric function of the form

$$\widetilde{\varepsilon}_m(\omega) = \varepsilon_{bk} + \frac{\omega_p^2}{\omega^2 + i\gamma\omega} + \sum_I \frac{n_I e^2}{\varepsilon_0 m_I^*(\omega_{0I}^2 - \omega^2 - i\omega\gamma_I)} \tag{2.24}$$

[9]Here ε_{bk} takes into account not only the background polarisation, but also some of the effects of interband transitions. This approach is therefore questionable. Ideally the full approach described by Eqn. (2.24) should be appropriately fitted to the experimentally measured values of $\widetilde{\varepsilon}_m(\omega)$.

The additional terms are used to represent interband transitions, but can also be used to describe 'bound' electrons (dielectric insulators), impurity atoms and phonons in the metal. This model can therefore also be used to phenomenologically describe dielectric functions for insulators and semi-conductors. Despite these theoretical advances, accurately modelling such complex systems is still an immense challenge and hence all the subsequent work in this thesis uses dielectric values found from experiment. For the metals investigated in this work the values for the real and imaginary parts of $\widetilde{\varepsilon}_m(\omega)$ are compiled from appropriate sources, e.g. the Palik *Handbook of Optical Constants of Solids II* [39], and are plotted for Au and Ag in Fig. (2.1). It therefore should be noted that even though spatial non-locality is not characterised by the experimentally found $\widetilde{\varepsilon}_m(\omega)$, the dielectric data used in all theoretical calculations throughout this work still inherently includes some quantum mechanical (transition) effects.

2.3 Plasmonic Excitations

The most basic systems that can sustain both SPs and SPPs are those that can be considered as a semi-infinite flat isotropic single interface. Modern experiments and applications have now moved beyond investigation of this simple system, however this fundamental example still provides excellent insight into what these phenomena actually are, their properties, and requirements for excitation. A theoretical treatment for a simple SP and SPP system will be described first, followed by brief overviews of LSPP excitations on NPs and coupled LSPP interactions between NP pairs.

2.3.1 Surface Plasmons and Surface Plasmon Polaritons

A BP is defined in a semi-infinite three-dimensional (3D) isotropic metal. At an effectively two-dimensional (2D) metal-dielectric interface a natural collective longitudinal oscillation of the metal's surface electrons can be excited, known as a SP. Due to their purely longitudinal nature, in the spatially local regime, SPs (like BPs) are *non-propagating* ($v_g = 0$) excitations and can generally only be excited by particle impact. It is important to note that BPs and SPs are associated with *electrostatic* rather than electromagnetic fields. This can be seen directly by considering the irrotational nature of a purely longitudinal oscillation

$$i\widetilde{\mathbf{q}} \times \widehat{\mathbf{E}}(\omega) = 0 \quad \Rightarrow \quad \nabla \times \mathbf{E}(t) = 0 \tag{2.25}$$

Recalling that $\nabla \times \nabla\Phi = 0$ it immediately follows that the electric field of a purely longitudinal oscillation can be expressed as the gradient of an electrostatic potential, $\mathbf{E} = -\nabla\Phi$. Combining this result with Gauss's law (Eqn. (2.1)) yields Poisson's equation. Furthermore, assuming the medium to be charge neutral ($\rho_{int} = 0$) and $\rho_{ext} = 0$, the problem is reduced to solving Laplace's equation to determine the associated SP resonances. Solving for the SP resonances in the electrostatic limit is often referred to as finding the non-retarded SP behaviour of the system as the interactions between different parts of the metal surface is considered to be instantaneous ($c = \infty$).

The coupling of an incident *electromagnetic* wave to the interface can be theoretically treated by modelling the resulting SPP as an interface bound electromagnetic wave[10]. Assuming that the incident electromagnetic wave has no E_y-component the simplest system geometry can be modelled as shown in Fig. (2.2). Using Maxwell Eqn. (2.4), under the assumptions of harmonic time dependence and no external sources of charge and current density, one can find explicit expressions relating the different field components of the Transverse Magnetic (TM) or p-polarised modes (E_x, E_z and H_y are non-zero) for the system defined in Fig. (2.2)

$$E_x = -i\frac{1}{\omega\varepsilon_0\widetilde{\varepsilon}_r}\frac{\partial H_y}{\partial z} \tag{2.26}$$

$$E_z = i\frac{1}{\omega\varepsilon_0\widetilde{\varepsilon}_r}\frac{\partial H_y}{\partial x} \tag{2.27}$$

Transverse Electric (TE) or s-polarised modes will not be considered in this case as they have no longitudinal (E_x) and normal (E_z) **E**-field components. In this system purely TE waves cannot be bound to the interface[11] and cannot excite the required longitudinal oscillations in the surface free-electron plasma. Therefore SPPs are only associated with light that has both normal and longitudinal **E**-field components with respect to the interface.

[10] In almost all cases the SPPs excited can be thought of as proxies for the incident light and thus carry the same information.

[11] For the system considered boundary conditions demand that the amplitude of the E and H components of a TE-polarised wave equal zero at the interface, thus confirming this statement.

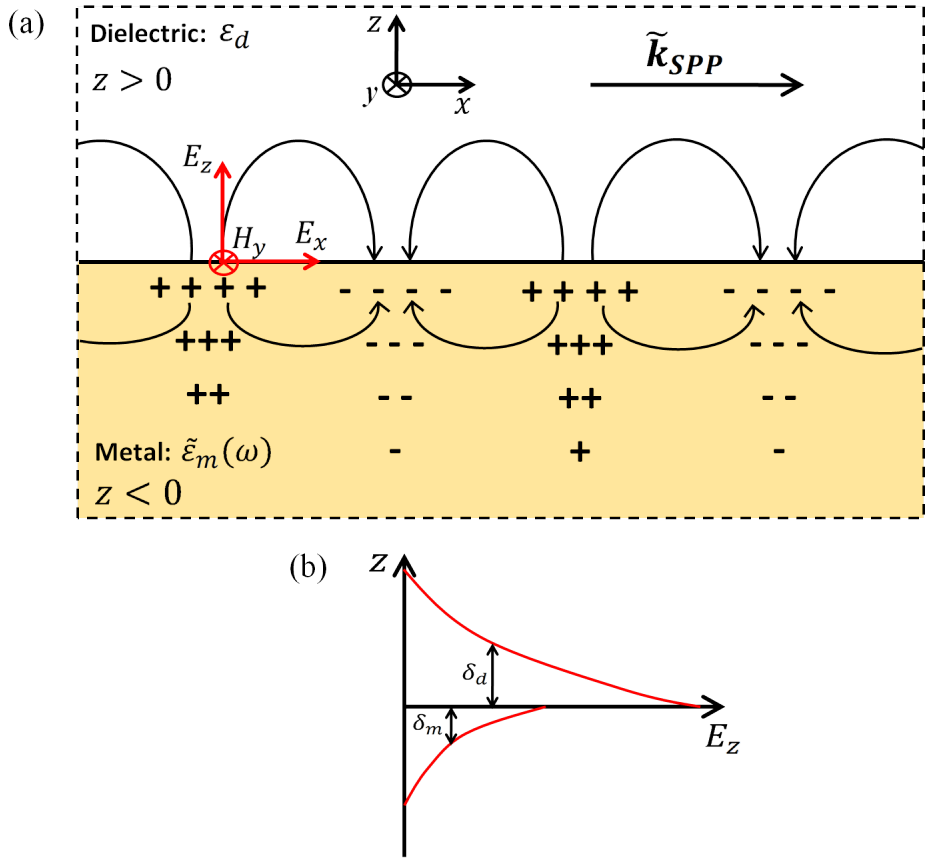

Figure 2.2: (a) Schematic of the metal-dielectric interface showing the surface bound electromagnetic wave, coupled to longitudinal oscillations of the surface charge, propagating in the x-direction. (b) Magnitude of the electric field decays away exponentially on both sides of the interface thus reflecting the excitations bound nature. The E_z-field penetration depths into the respective media are δ_m and δ_d.

Under the additional assumptions that both the metallic and dielectric mediums are non-magnetic and macroscopically homogeneous (negligible variation of dielectric function over distances on the order of a wavelength), Eqn. (2.5) reduces to the Helmholtz wave equation. Considering transverse electromagnetic waves propagating along the interface with harmonic time dependence hence allows the governing wave equation for TM modes to be determined

$$\frac{\partial^2 H_y}{\partial z^2} + \left(k_0^2 \tilde{\varepsilon}_r - \tilde{k}_{spp}^2\right) H_y = 0 \tag{2.28}$$

where $\tilde{k}_{spp}$ is the x-component of wavevector. Seeking a propagating wave so-

lution bound to the surface, i.e. with evanescent decay in the perpendicular z-direction, on each side of the metal-dielectric interface, requires

$$\text{For } z > 0: \qquad H_y = A_d \, e^{i(\widetilde{k}_{spp}x + \widetilde{k}_{zd}z)} \tag{2.29}$$

$$\text{For } z < 0: \qquad H_y = A_m \, e^{i(\widetilde{k}_{spp}x - \widetilde{k}_{zm}z)} \tag{2.30}$$

with $\Im[\widetilde{k}_{zm}] \wedge \Im[\widetilde{k}_{zd}] > 0$. Here A_m and A_d are the field amplitude coefficients in the metal and dielectric respectively and $\widetilde{k}_{zm}$ and $\widetilde{k}_{zd}$ are the z-components of the wavevector associated with the SPP excitation in the metal and dielectric respectively. Substituting these solutions into Eqns. (2.26) and (2.27) and solving the appropriate boundary conditions to ensure the continuity of H_y and E_x at the interface gives the results

$$A_m = A_d \qquad \text{and} \qquad \frac{\widetilde{k}_{zd}}{\widetilde{k}_{zm}} = -\frac{\varepsilon_d}{\widetilde{\varepsilon}_m} \tag{2.31}$$

where ε_d is the dielectric function of the dielectric medium. Note as the components of $\widetilde{k}_{zm} \wedge \widetilde{k}_{zm} \wedge \varepsilon_d > 0$ for a surface bound electromagnetic wave, it is apparent $\Re[\widetilde{\varepsilon}_m] < 0$. As described in Section (2.2.2) the Drude model shows that in the non-transparent regime ($\omega < \omega_p$) negative permittivity is a result of collective oscillations in the free-electron plasma. In other words, if an electromagnetic wave (see Fig. (2.2)) is *confined* and propagating along the interface it *must* be coupled to collective longitudinal oscillations in the free-electron plasma, otherwise the electromagnetic field boundary conditions and the Drude model would not be simultaneously satisfied.

Finally, implementing conservation of momentum on each side of the interface, i.e. satisfying Eqn. (2.28), yields the complex SPP dispersion relation under the spatially local response approximation

$$\widetilde{k}_{spp} = k_0 \left(\frac{\widetilde{\varepsilon}_m \varepsilon_d}{\widetilde{\varepsilon}_m + \varepsilon_d} \right)^{1/2} \tag{2.32}$$

Several properties of SPPs can be obtained from this equation by decomposing it into its real and imaginary components and considering momentum conservation on each side of the interface. From this analysis the SPP propagation

length L_{spp} and penetration depths δ_m and δ_d into the metallic and dielectric mediums respectively can all be determined. In the negligible damping limit $\Re\left[\varepsilon_m(\omega)\right] \gg \Im\left[\varepsilon_m(\omega)\right]$ and maintaining that $\Im[\widetilde{k}_{zm}] \wedge \Im[\widetilde{k}_{zd}] > 0$ it is found that

$$L_{spp} \approx \frac{1}{k_0}\left(\frac{\Re\left[\widetilde{\varepsilon}_m\right]\varepsilon_d}{\Re\left[\widetilde{\varepsilon}_m\right]+\varepsilon_d}\right)^{-3/2}\frac{\left(\Re\left[\widetilde{\varepsilon}_m\right]\right)^2}{\Im\left[\widetilde{\varepsilon}_m\right]} \tag{2.33}$$

$$\widetilde{k}_{zm} \approx k_0\left(\frac{\left(\Re\left[\widetilde{\varepsilon}_m\right]\right)^2}{\Re\left[\widetilde{\varepsilon}_m\right]+\varepsilon_d}\right)^{1/2} \quad \text{with} \quad \delta_m = \frac{1}{\left|\Im\left[\widetilde{k}_{zm}\right]\right|} \tag{2.34}$$

$$\widetilde{k}_{zd} \approx k_0\left(\frac{\left(\varepsilon_d\right)^2}{\Re\left[\widetilde{\varepsilon}_m\right]+\varepsilon_d}\right)^{1/2} \quad \text{with} \quad \delta_d = \frac{1}{\left|\Im\left[\widetilde{k}_{zd}\right]\right|} \tag{2.35}$$

As Eqns. (2.31), (2.34) and (2.35) show it is required that $\Re\left[\widetilde{\varepsilon}_m\right]\varepsilon_d \wedge \left(\Re\left[\widetilde{\varepsilon}_m\right]+\varepsilon_d\right) < 0$ to yield a surface bound solution. Therefore, in general, SPPs only exist at interfaces where $\Re\left[\widetilde{\varepsilon}_m\right]$ is negative and greater in magnitude than ε_d. The process of SPP attenuation in this system is described by the decay of electron-hole pairs, created by SPP induced interband and intraband transitions of electrons. The attenuation therefore proceeds via free-electron damping processes, e.g. scattering with phonons and lattice ions [42].

Due to their longitudinal (electrostatic) nature BP and SP decay can generally be described by Landau damping. The electrons associated with BPs and SPs have phase velocities almost equal to that of the longitudinal plasma wave ($v_p = \omega_p/k_0 n$). As a consequence these electrons experience an essentially static electric field which can be either positive or negative depending on the relative phase between the electron motion and the plasma wave. After averaging over all possible phases, an individual electron therefore has an equal chance of being accelerated or decelerated by the wave. However, due to the Maxwellian distribution of electron velocities, there are more electrons with velocities slightly less than that of the plasma wave. Therefore, on average, more electrons are being accelerated than decelerated by the wave. This results in a net transfer of energy from the plasma wave to individual electrons in the metal, i.e. the plasma wave is damped [14].

Ideal Surface Plasmon Polaritons

The behaviour of $\widetilde{k}_{spp}$ at the interface between a Drude metal with negligible damping (and local response) and air is shown in Fig. (2.3). A SP has only a discrete frequency of resonant excitation (assuming no linewidth of the resonance) in this system. However it is evident that an incident electromagnetic wave coupling to the surface and exciting longitudinal oscillations in the 2D free-electron plasma allows resonant excitation of SPPs at a continuum of frequencies. A SPP is a *propagating* surface bound electromagnetic wave coupled to longitudinal oscillations in the metal's surface charge density[12]. The full electrodynamic solution for the SPP dispersion presented here includes the effects from retardation, i.e. the finite speed of light is taken into account. This is therefore often referred to as a solution derived in the retarded limit.

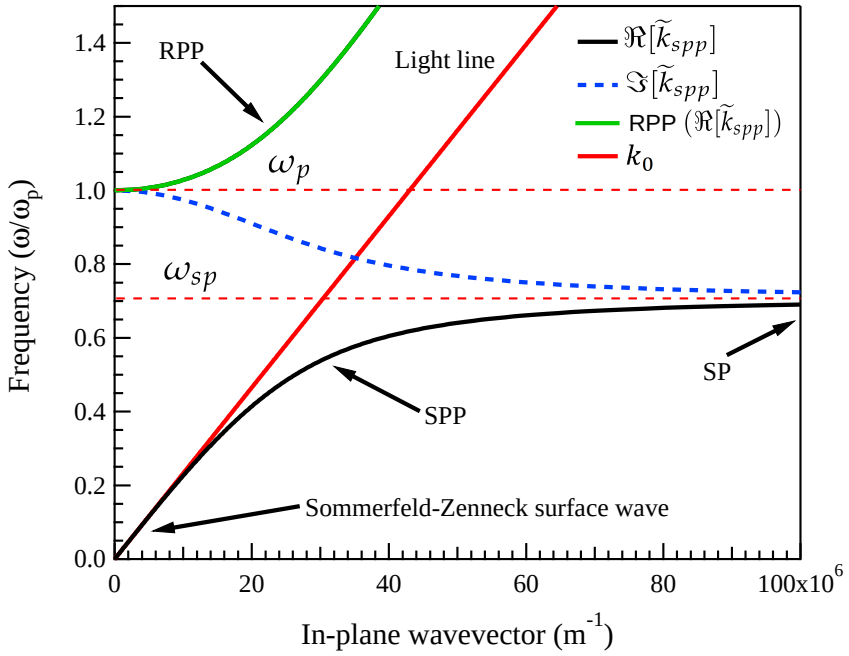

Figure 2.3: Graph showing the behaviour of $\widetilde{k}_{spp}$ for a Drude metal (with negligible damping) compared with that of the light line k_0. The dashed horizontal lines show the positions of the BP and SP resonances. Note that the in-plane wavevector component $k_{||} = \Re[\widetilde{k}_{spp}] = k_0 n_d \sin\theta_i$ where n_d is the refractive index of the dielectric medium and θ_i is the angle of an incident electromagnetic wave.

[12]The electric field in the dielectric medium that is associated with a SPP is mostly transverse in nature, i.e. $E_z \gg E_x$ and is purely transverse (electromagnetic wave in a homogeneous medium) as $\Re[\widetilde{k}_{spp}] \to 0$. As $\Re[\widetilde{k}_{spp}] \to \infty$ (electrostatic limit) it can be shown that $E_z = E_x$.

The frequency of collective longitudinal oscillation induced in the free-electron plasma depends on $\Re[\widetilde{k}_{spp}]$ with the asymptotic value being the natural resonance frequency of a SP. The electric field associated with a BP and SP is electrostatic and hence the characteristic SP resonance frequency of the metal can be obtained via a straight-forward solution of Laplace's equation for the single interface geometry shown in Fig. (2.2). This yields the relation between ω_p and the surface plasmon frequency ω_{sp} which is found to be $\omega_{sp} = \omega_p/\left(\sqrt{1+\varepsilon_d}\right)$, and thus $\omega_{sp} = \omega_p/\sqrt{2}$ in air. For $\omega < \omega_{sp}$ the SP becomes polaritonic in nature (a SPP) and the dispersion strongly deviates from the dashed horizontal line (Fig. (2.3)) predicted by the electrostatic treatment. In real metals, damping processes, interband transitions and spatially non-local effects contribute to corrections to this result and re-definitions of ω_p and ω_{sp} are required [43, 44].

At low-frequencies the light barely interacts with the surface electrons and hence is not usually referred to as a SPP but rather a grazing incidence Sommerfeld-Zenneck wave. Between ω_{sp} and ω_p there is only a purely imaginary $\widetilde{k}_{spp}$ and hence no SPP propagation. In the transparent regime above ω_p, electrons in the metal can no longer respond rapidly enough to screen the incoming electromagnetic wave. Therefore radiation into the metal occurs and the (bulk) Radiative Plasmon Polariton (RPP) dispersion is observed. The form of the RPP dispersion is given by substituting $\widetilde{\varepsilon}_m(\omega)$ given by Eqn. (2.19) into the transverse dispersion relation Eqn. (2.7). For negligible damping this yields

$$\widetilde{q} = \left(\frac{\omega^2 - \omega_p^2}{c^2}\right)^{1/2} \quad \Rightarrow \quad \frac{\omega}{\omega_p} = \left(1 + \frac{c^2\widetilde{q}^2}{\omega_p^2}\right)^{1/2} \tag{2.36}$$

The transition into the transparent regime is clearly shown by Eqn. (2.36) as when $\omega > \omega_p$ the complex wavenumber $\widetilde{q}$ of the transverse excitation has $\Im\left[\widetilde{q}\right] = 0$. In the spatially non-local regime longitudinal excitations in the bulk and on the surface, i.e. BPs and SPs, feel the forces due to pressure variations in the electron gas and hence show dispersive character described by the longitudinal dielectric function under the condition $\widetilde{\varepsilon}_m^L(\widetilde{\mathbf{q}}_\mathbf{0}, \omega) = 0$ [32]. This allows BPs and SPs to be excited at a continuum of frequencies (at $\Re[\widetilde{k}_{spp}] \gtrapprox 10^9$ m^{-1}) rather than the discrete frequencies labelled in Fig. (2.3). These excitations thus become *propagating* ($v_g \neq 0$), however they maintain their electrostatic nature.

As can be seen from Fig. (2.3) $\Re[\widetilde{k}_{spp}]$ is always to the right of the k_0 line because as the coupling between the light and electrons on the metallic surface increases the light has to 'drag' the electrons along the surface to a greater extent. Therefore free-space electromagnetic waves cannot directly couple to the flat semi-infinite interface and some intermediate step is required to overcome the momentum mismatch. Several techniques [45] to do this are; prism coupling, direct emission into SPP via light-emitting diode, scattering from a defect on a surface and scattering from a periodically corrugated metal surface, traditionally a diffraction grating. All of these techniques can be used to impart momentum to the light (increase of the in-plane wavevector component) so that it can couple (or de-couple) to SPP modes. It can now be understood how some of the aforementioned Wood's anomalies, that could not be fully explained by Rayleigh, arose in Wood's experiments. The diffraction grating used in the experiment imparted additional momentum to the incident light thus allowing resonant coupling into SPPs with dispersion similar to that shown in Fig. (2.3). Therefore resonant SPP excitation produced relatively high absorption at certain frequencies. These SPP resonances manifested themselves as the drops in reflectivity that Woods measured at specific wavelengths.

Real Surface Plasmon Polaritons

When considering the experimentally obtained values of $\widetilde{\varepsilon}_m(\omega)$ the SPP dispersion is modified dramatically as shown in Fig. (2.4). It is apparent that SPPs in real metals approach a maximum *finite* wavenumber at ω_{sp}. This is because when damping (real metal) is introduced, *purely* longitudinal BPs and SPs can no longer exist. For example in the case of a BP the condition for longitudinal oscillation, $\widetilde{\varepsilon}_m(\omega_p) = 0$, can no longer be satisfied. For real metals one can modify the definitions of ω_p and ω_{sp} accordingly. This limitation puts a lower bound on both the SPP wavelength and the amount of SPP confinement perpendicular to the dielectric side of the interface, e.g. for gold $\lambda_{spp} = 2\pi/\Re[\widetilde{k}_{spp}] \approx 470$ nm, $\delta_m \approx 37$ nm (skin-depth) and $\delta_d \approx 170$ nm at ω_{sp}. The expected current density $\widetilde{\mathbf{J}}_{\mathbf{int}}$ induced by the electric field propagates parallel to the surface and is significant up to a depth $\sim \mathcal{O}(\delta_m)$. Therefore for NPs with dimensions $\sim \mathcal{O}(2\delta_m)$ induced current density is expected to be significant throughout the entire NP volume.

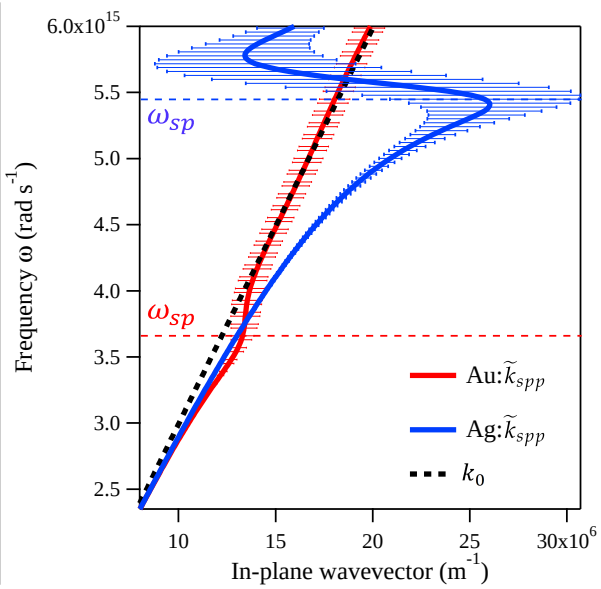

Figure 2.4: Graph showing the behaviour of $\widetilde{k}_{spp}$ for gold and silver compared with the light line k_0. The horizontal dashed lines show the positions of the SP resonances. The shaded regions (horizontal lines with width equal to $|\Im[\widetilde{k}_{spp}]|$) describe the FWHM of the SPP resonance in k-space.

The quasi-bound part of the SPP dispersion relation between ω_{sp} and ω_p is also allowed when considering real metals. In this regime $\Re[\widetilde{k}_{zm}]$ and $\Re[\widetilde{k}_{zd}]$ are non-negligible and hence the excitation begins to propagate away from the surface. A definition of ω_p can be introduced by considering when $\Im[\widetilde{k}_{spp}]$ crosses the light-line as now SPPs take on a more radiative nature, as shown in Fig. (2.3). However in the frequency range $\omega > \omega_p$ field penetration into the metal (δ_m and δ_d) does not increase significantly as interband absorption processes dominate the metals response.

2.3.2 Localised Surface Plasmon Polaritons

In this thesis nearly-touching and touching NP functionalised AFM tips are the plasmonic structures of interest and hence an understanding of the LSPP modes that can be excited on these nanostructures is essential. The LSPP mediated response of these nanosystems can be understood by separating the response into two regimes. The LSPP response of an isolated NP and the LSPP response of a strongly electromagnetically coupled identical NP-NP homo-dimer, referred to as a NP dimer for brevity. A brief overview of LSPPs on isolated spherical NPs is first presented.

After initial investigations by Faraday [46] in the 1800's, and Mie's seminal work in 1908, it was not until the late 1970's that metallic NPs were once again heavily studied. The realisation of the role of LSPPs on metallic NPs in SERS drove the re-interpretation of absorption and scattering by NPs under the plasmonics framework [31, 47]. Over the past 30 years the quest to create ever more complex plasmonic nanosystems for surface-enhanced spectroscopies [48], single molecule detection [49], metamaterials [4] and optical circuitry and components [50] has seen the field expand exponentially. Now new synthesis techniques have produced NP morphologies such as spheres [51], cubes [52], cups [53], rings [54], rods [55] and recently even 'nanodecahedra' [56] and 'nanostars' [57]. Another interesting class of NP type are 'nanoshells' [58]. A nanoshell consists of a dielectric core surrounded by a thin (thickness < 30 nm) metallic shell that hence creates a dielectric-metal-dielectric interface. Nanoshells therefore exhibit a substantially different plasmonic response to that created by the single metal-dielectric interface of a homogeneous NP. For simplicity only homogeneous isotropic spherical NPs are addressed here in further detail, however the ideas presented here are applicable to the understanding of almost all plasmonic nanosystems.

As depicted in Fig. (2.5), unlike the semi-infinite planar interface system discussed in section (2.3.1) the curved surfaces of NPs provide confinement of all participating electrons to a nanoscale volume via the boundary conditions on **E**, **D**, **B** and **H** at the position $r = a$ where a is the radius of the NP.

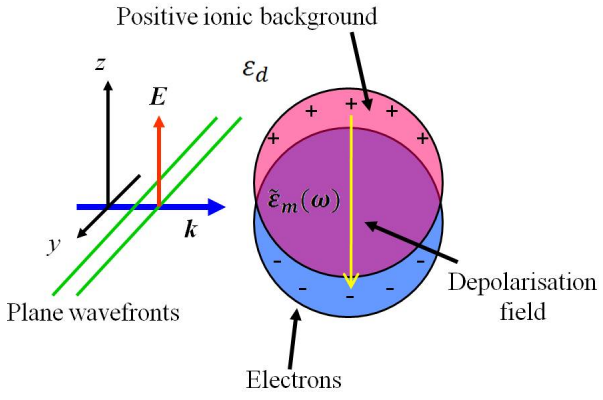

Figure 2.5: Schematic representation showing the $\ell = 1$ dipole distribution of participating electrons in a spherical NP (outline not shown) under infinite plane-wave excitation. The depolarisation field (**yellow**) creates an effective restoring force and thus resonant electron oscillations can occur in analogy to a driven damped harmonic oscillator.

The electrons all move in response to an incident electromagnetic plane wave and the electric-field oscillations thus create a time-varying build-up of polarisation charges on the surface of the NP. The depolarisation field created acts as an effective restoring force hence allowing resonant electron oscillations at specific excitation frequencies. More fundamentally, the boundary conditions constrain the electron plasma, and naturally, resonance conditions result.

In Fig. (2.6a) the phase of the electromagnetic wave is approximately constant over the volume of the NP as $a \ll \lambda_0/n_d = \lambda$, where λ_0 and λ are the wavelength of the incident light in free-space and a dielectric medium respectively.

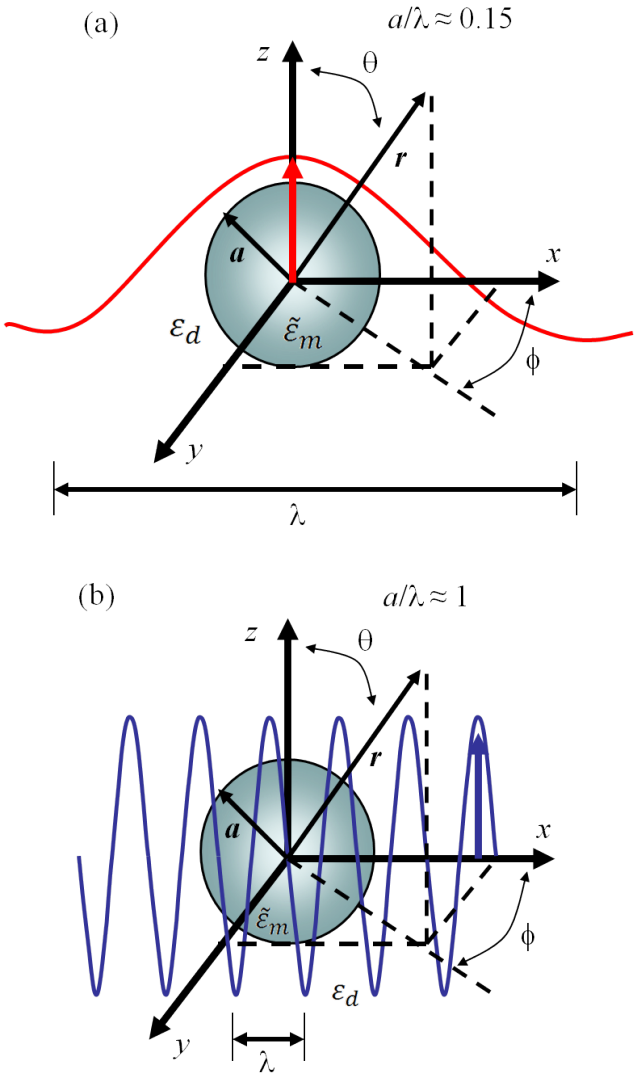

Figure 2.6: Schematic representations of LSPP excitation in the (a) quasi-static (ideally $a \ll \lambda$) and (b) Mie ($a \sim \lambda$) regimes.

The resulting Localised Surface Plasmon (LSP) resonance frequencies can be calculated via Laplace's equation under the electrostatic field approximation, i.e. in the non-retarded limit. Extending this to the quasi-static approximation yields the associated absorption and scattering cross-sections by allowing for a time-varying field but neglecting the non-uniform phase (retardation) over the NP volume.

These simplifications cannot be made for the situation shown in Fig. (2.6b) where $a \sim \lambda$. The phase of incident electromagnetic field is not constant over the NP's volume and the LSPP response has to be obtained including retardation of the fields via a full electrodynamic solution to Maxwell's equations. In broad terms LSPPs can be thought of as propagating SPPs confined to a NPs geometry that hence interfere to form a standing wave (localised) SPP at specific frequencies. A rigorous description of LSPPs on spherical geometries was achieved by Mie in 1908 [19]. Mie showed that the different electromagnetic eigenmodes of spherical particles are dipolar or multipolar in character and that their excitation magnitude can be determined by expanding the internal and scattered fields into a set of normal modes described by vector spherical harmonic functions. The Mie solutions can therefore model the LSPP response of any diameter particle (metallic or dielectric) in the classical regime. However, if $a \gg \lambda$ the laws of geometric optics may be more appropriate to describe a NP's response to light.

Strictly speaking a LSP cannot be excited by propagating light illumination because like a SP a truly LSP is a purely longitudinal excitation and must be associated with an electrostatic field. A LSP can be thought of as the asymptotic limit of an LSPP as $c \to \infty$ (non-retarded limit). Equivalently, as SPPs propagate into more confined regions of a nanosystem they can be adiabatically transformed toward the LSP limit, i.e. the electric field associated with the SPP becomes increasingly electrostatic in character ($\mathbf{B} \to 0$) [59]. In this thesis SPPs localised on a nanosystem with critical dimensions much less than L_{spp} are referred to as LSPPs. A more detailed discussion on the nature of BPs, SPs, LSPs and the polaritonic character of SPPs can be found in [44,60] and the references therein.

Quasi-static solutions

A good intuition into the LSPP response of NPs can be gained from the quasi-static approximations of the multipolar LSPs driven by a general electrostatic field of infinite extent. This is achieved by expressing Laplace's equation in a spherical polar basis and looking for solutions of the form [14]

$$\Phi_{\ell,m}(r,\theta,\phi) = \sum_{\ell=0}^{\infty}\sum_{m=-\ell}^{\ell}\left[A_\ell^m r^\ell + B_\ell^m r^{-(\ell+1)}\right] P_\ell^m(\cos\theta)e^{im\phi} \tag{2.37}$$

where $\ell = 1,2,3...$ is the orbital angular momentum number, e.g. $\ell = 1$ for a dipole, $m = -\ell...0...\ell$ (in integer steps) is the azimuthal number, e.g. $m = 0$ for azimuthally symmetric fields, and $P_\ell^m(\cos\theta)$ are the associated Legendre Polynomials of order (ℓ, m). The coefficients A_ℓ^m and B_ℓ^m are determined both inside and outside the sphere by ensuring continuity of the tangential **E**-field and normal **D**-field components at $r = a$ and enforcing physical boundary conditions as $r \to (0,\infty)$. As expected the electrostatic field and charge distributions determined closely resemble atomic orbitals.

Using Eqn. (2.37) the resonance frequencies ω_{np}^ℓ and polarisabilities α^ℓ of a spherical NP under the quasi-static approximation are[13] [61]

$$\omega_{np}^\ell = \omega_p\left(\frac{\ell}{\varepsilon_d(\ell+1)+\ell}\right)^{1/2} \tag{2.38a}$$

$$\alpha^\ell = 4\pi\varepsilon_d a^{(2\ell+1)}\frac{\ell(\widetilde{\varepsilon}_m - \varepsilon_d)}{\ell\widetilde{\varepsilon}_m + (\ell+1)\varepsilon_d} \tag{2.38b}$$

The m dependence vanishes due to the symmetry implied by the spatially infinite electrostatic excitation of the spherical NP. As ℓ increases the polarisability decreases and hence higher-order modes are generally not evident for small NPs with $a \lessapprox 40$ nm. Typically the quasi-static formalism is only used in the regime where $a \lessapprox \lambda/10$. In this case, assuming an infinite *uniform* driving electrostatic field ($\ell = 1$ and $m = 0$), only the dipole mode can be excited. For non-spherical NPs with sharp asperities higher-order modes can still be excited due to the non-uniform electrostatic field created. When $\ell \to \infty$ the SP resonance condi-

[13] It is stressed here that the ℓ in ω_{np}^ℓ and α^ℓ is used as an annotation while in the RHS of Eqns. (2.38) all instances of ℓ denote a numerical value.

tion is recovered as expected because the surface electron oscillations become of short enough wavelength that they effectively feel a quasi-planar interface. The resonant nature of α^{ℓ} implies that the surface charge density must be resonant in character and hence on resonance a strongly enhanced electric near-field will be present in certain regions just above the NP's surface.

There are generally a large number of different LSP and LSPP modes that can be excited on nanosystems due to their complex curved surfaces. The curved geometry also allows LSPP resonances to be excited by direct light illumination, i.e. none of the momentum matching techniques mentioned in Section (2.3.1) are required. This can be explained by considering that the wavenumber k of the exciting light can be enlarged by wavevector components determined by the spatial Fourier transform of the NP geometry [62]. These relatively large magnitude wavevector components are contained within the evanescent near-field in the immediate vicinity of the NP. The LSPP 'dispersion' [14] relation can be determined by comparing the LSPP resonance frequency against the tangential wavenumber $\Re[\widetilde{k}_{lspp}]$ given by

$$\Re[\widetilde{k}_{lspp}] = \frac{2\pi}{\lambda_{lspp}} = \frac{2\pi}{(2\pi a/\ell)} = \frac{\ell}{a} \tag{2.39}$$

where λ_{lspp} is the wavelength of the LSPP given by the circumference of the NP divided by the orbital angular momentum number ℓ. Note that there are 2ℓ density nodes in the longitudinal electron standing wave around any given circumference. In general the LSPP dispersion lies much closer to the light-line than the dispersion of a well confined SPP (see Fig. (2.3)) [63]. Thus the additional momenta required to excite LSPPs on closed curved geometries is reduced considerably from that required to excite SPPs on semi-infinite planar geometries. Another consequence of the curved nanosystems is that the boundary conditions associated with the curved interfaces allow both TM and TE modes to couple to LSPP excitations.

The far-field scattering and absorption cross-sections C^{qs}_{sca} and C^{qs}_{abs} respectively, are calculated under the quasi-static approximation by allowing the non-retarded solutions for the multipole moments determined from Eqn. (2.38b) to

[14] Non-interacting LSPPs are non-dispersive excitations. Here 'dispersion' refers to a plot showing the evolution of the discrete LSPP resonance energies against the associated discrete wavevector magnitudes.

oscillate in time. The radiation of the oscillating multipole creates scattering of the incident field. For small spherical NPs $a \ll \lambda$ hence the dipole mode ($\ell = 1$) dominates the response. In this regime C_{sca}^{qs} and C_{abs}^{qs} are given by [64]

$$C_{sca}^{qs} = \frac{3}{2\pi} V_{np}^2 \left(\frac{\omega}{c}\right)^4 \varepsilon_d^2 \left|\frac{\widetilde{\varepsilon}_m - \varepsilon_d}{\widetilde{\varepsilon}_m + 2\varepsilon_d}\right|^2 \tag{2.40a}$$

$$C_{abs}^{qs} = 3V_{np} \left(\frac{\omega}{c}\right) \varepsilon_d^{\frac{1}{2}} \Im\left[\frac{\widetilde{\varepsilon}_m - \varepsilon_d}{\widetilde{\varepsilon}_m + 2\varepsilon_d}\right] \tag{2.40b}$$

where $V_{np} = (4/3)\pi a^3$ is the volume of the NP. The extinction cross-section C_{ext}^{qs} is given by

$$C_{ext}^{qs} = C_{sca}^{qs} + C_{abs}^{qs} \tag{2.41}$$

It is important to note that for NPs with $a \lessapprox \lambda/5$, C_{ext}^{qs} is approximately proportional to V_{np} and hence the coupling strength of light to an isolated nanosystem, or for example NPs in suspension, will be greatly reduced compared to that for semi-infinite structures. The scattering response in the $\ell = 1$ dipole limit is sometimes referred to as Rayleigh scattering, as in 1871 Lord Rayleigh first treated the scattering of light from molecules in the sky under these approximations. The results demonstrated by Eqns. (2.38) and (2.40) imply that the major factors influencing the LSP and therefore LSPP resonances are:

- The NP size (and shape, as shown by a more comprehensive treatment of ellipsoidal NPs [65]).
- The dielectric function of the metal.
- The dielectric function of the dielectric environment.

Although inferred, it should be noted that two other critical factors influencing the LSP and LSPP resonance response are the NP shape and type. Deviations from spherical symmetry necessitate an asymmetric polarisability and hence α^ℓ becomes a tensor rather than a scalar quantity. In general the LSP and LSPP resonance wavelengths for light polarised parallel to the long-axis of a nanorod tend to red-shift with increasing nanorod aspect ratio. The type of NP, e.g. whether the NP is a homogeneous sphere or a non-homogeneous spherical

core-shell structure, can also strongly affect the plasmonic resonance properties, depending on the exact properties of the inhomogeneity [66]. The influence of NP shape and type will be discussed in greater detail in Chapter (5).

For small or slowly varying $\Im\left[\widetilde{\varepsilon}_m(\omega)\right]$ around the dipole resonance, the resonance condition of Eqn. (2.38b) simplifies to $\Re\left[\widetilde{\varepsilon}_m(\omega)\right] = -2\varepsilon_d$. This is known as the Frölich resonance condition and the associated mode of induced oscillating charge density is the dipole LSP with frequency (in air, $\varepsilon_d = 1$) $\omega_{np}^1 = \omega_p/\sqrt{3}$ as given by Eqn. (2.38a). As Eqns. (2.40a) and (2.40b) show, it is also important to note for $a \lessapprox 20$ nm absorption processes dominate while for $a \gtrapprox 30$ nm scattering begins to dominate the LSP (and LSPP) mediated optical response of the NP.

In this work all the NPs investigated have $a > 30$ nm hence they will have a relatively large plasmonically (resonantly) enhanced scattering cross-section. Due to this, Dark-Field (DF) measurements, where only the scattered light is collected, will be used to directly observe the LSPP response of the NP systems. The DF optical measurement techniques employed are described in detail in Chapter (3).

Mie solutions

In this work the tip apex NPs are of too large diameter ($a \approx 150$ nm $\sim \lambda/5$) to be accurately modelled using the quasi-static approximation and hence the exact Mie solutions are more appropriate to yield further insight into LSPPs supported on such NPs. The Mie solutions are obtained by first re-expressing Maxwell's wave equation in polar coordinates via use of Debye potentials. By considering a single uniform incident infinite plane-wave, boundary conditions are imposed to ensure continuity of the fields at $r = a$ and hence solutions for the Debye potentials are found in terms of spherical harmonics [62]. The electric and magnetic field solutions are therefore reconstructed in terms of vector spherical harmonics. The far-field response is described by the scattering coefficients $\widetilde{a}_\ell$ and $\widetilde{b}_\ell$ that are given by

$$\widetilde{a}_\ell = \frac{\eta^2\psi_\ell(\eta\alpha)\psi'_\ell(\alpha) - \psi_\ell(\alpha)\psi'_\ell(\eta\alpha)}{\eta^2\psi_\ell(\eta\alpha)\xi'_\ell(\alpha) - \xi_\ell(\alpha)\psi'_\ell(\eta\alpha)} \tag{2.42a}$$

$$\widetilde{b}_\ell = \frac{\psi_\ell(\eta\alpha)\psi'_\ell(\alpha) - \psi_\ell(\alpha)\psi'_\ell(\eta\alpha)}{\psi_\ell(\eta\alpha)\xi'_\ell(\alpha) - \xi_\ell(\alpha)\psi'_\ell(\eta\alpha)} \tag{2.42b}$$

where $\eta = (\widetilde{n}_m/n_d)$, the size parameter $\alpha = 2\pi a n_d/\lambda_0$ and the Riccati-Bessel functions $\psi_\ell(z) = zj_\ell(z)$ and $\xi_\ell(z) = z\widetilde{h}^{(1)}_\ell(z)$ with j_ℓ and $\widetilde{h}^{(1)}_\ell$ denoting spherical Bessel and Hankel functions respectively. Here the prime $'$ denotes the derivative of the function with respect to the argument. There is no m dependence in Eqns. (2.42) as for uniform infinite single plane-wave excitation the boundary conditions at $r = a$ require $m = 1$ for all ℓ. By considering the Poynting vector of the total electromagnetic field surrounding the NP the far-field scattering and extinction cross-sections are given by [67]

$$C_{sca} = \frac{2\pi}{k^2}\sum_{\ell=1}^{\infty}(2\ell+1)\left(|\widetilde{a}_\ell|^2 + |\widetilde{b}_\ell|^2\right) \tag{2.43}$$

$$C_{ext} = \frac{2\pi}{k^2}\sum_{\ell=1}^{\infty}(2\ell+1)\Re\left[\widetilde{a}_\ell + \widetilde{b}_\ell\right] \tag{2.44}$$

where $k = 2\pi n_d/\lambda_0$ is the wavenumber of the incident light in the surrounding dielectric medium. The absorption cross-section C_{abs} can be obtained via Eqn. (2.41). The Mie solutions show significant modifications to the quasi-static results are required for NPs with $a \gtrapprox 20$ nm. The three most prevalent corrections are

- For noble metals, an additional overall red-shift of the dipole and higher-order modes with increasing NP diameter due to retardation of the exciting and depolarisation fields.
- Retardation creates a non-uniform field over the volume of a NP and hence higher-order (e.g. quadrupole) LSPP modes can be excited by the incident light even for spherically symmetric NPs. This effect becomes significant when $a \gtrapprox 100$ nm.
- A new decay channel: radiation damping due to direct radiative decay of LSPPs into photons. For increasing NP diameter the radiative damping overwhelms the decrease in absorption and hence the LSPP resonances broaden significantly.

Radiation damping increases the homogeneous LSPP mode energy linewidth Γ^{ℓ}_{LSPP} (as shown in Fig. (2.7)) and thus reduces the LSPP mode lifetime (dephasing time) τ^{ℓ}_{LSPP} according to

$$\tau^{\ell}_{LSPP} = \frac{2\hbar}{\Gamma^{\ell}_{LSPP}} \tag{2.45}$$

The strength of the LSPP mode can hence be expressed in terms of a mode quality factor Q^{ℓ}_{LSPP} via $Q^{\ell}_{LSPP} = E^{\ell}_{LSPP}/\Gamma^{\ell}_{LSPP}$, where E^{ℓ}_{LSPP} is the resonant energy associated with the LSPP mode. The Mie solutions thus give the dependence of τ^{ℓ}_{LSPP} on particle diameter and dielectric surroundings and yields values between $2-10$ fs for NPs between $150-20$ nm diameter[15] in air, for $\ell = 1$. For NPs of $\lessapprox 10$ nm diameter spatially non-local effects, primarily non-local screening due to finite penetration of induced-surface-charge into the NP interior, act to broaden the LSPP modes significantly. Therefore the LSPP mode lifetimes are substantially reduced compared to those calculated assuming spatially local response only.

Finally, it is important to note that both the traditional quasi-static and Mie solutions assume a single infinite incident plane-wave. In experiment this condition is never met. For example, under the DF illumination conditions used in this work, both the incident and scattered light are defined over certain angular ranges given by the Numerical Aperture (NA) of the various optical components. This can modify the measured optical response considerably [68] and hence must be acknowledged when comparisons are made between experiment and theory. It has also been reported that the measured optical response can be significantly altered when LSPPs are excited with non-homogeneous illumination, e.g. a focussed Gaussian beam [69].

2.3.3 Numerical Methods Overview

Since Mie's solution for spherical systems in 1908, analytical electromagnetic solutions have been found for other regular geometries and for inhomogeneous incident illumination, e.g. Generalised Lorenz-Mie Theory (GLMT). Such solutions can be used to calculate the LSPP resonances of nanosystems such as

[15] For NPs with $a < 50$ nm Γ^{ℓ}_{LSPP} *must* be extracted from C_{ext} as non-radiative decay becomes comparable, and eventually dominates, radiative decay as NP size decreases.

multi-layered spheres, ellipsoids, infinitely long circular cylinders, infinitely long elliptical cylinders and spheres with an eccentrically located spherical inclusion, all under different illumination conditions [70]. At the present time determination of the polarisability of NPs with more complicated geometries usually requires numerical methods, such as the Boundary Element (BEM) [71], Discrete Dipole Approximation (DDA) [72] and Finite Difference Time Domain (FDTD) methods [73]. However it is important to note that substantial progress has been made on analytical solutions for more complicated nanosystems, most notably spherical and cylindrical NP dimers [74,75]. Recent analytical theoretical treatments have also begun to take into account non-local screening due to the finite penetration of induced-surface-charge for just-touching NP dimer systems via a non-local hydrodynamic dielectric function [76].

In the present work, a Boundary Element Method for AXially (BEMAX) symmetric nanosystems [77] is used for all classical theoretical calculations. The simulation is based on a rigorous result derived from vector diffraction theory, that is, the electromagnetic field inside each homogeneous region of a composite structure is unambiguously determined by the fields and their derivatives at the boundary of that region, or equivalently, by the distribution of charges and currents on that boundary. The method begins by expressing the electromagnetic field scattered by a nanosystem in terms of equivalent boundary charges and currents. Imposing the boundary conditions for the continuity of the parallel components of the electric and magnetic fields in the presence of an external incident electromagnetic wave, leads to a system of surface-integral equations. This system is solved self-consistently by discretisation of the integrals using N representative points distributed on the boundaries, thus transforming the integrals into a set of linear equations that are solved using standard numerical techniques. Demanding axial symmetry of the nanosystem allows analytical evaluation of the azimuthal surface-integrals hence only the contours of the nanosystem need to be parameterised rather than the entire nanosystem surface. This effectively reduces the nanosystem from 2D to 1D and the number of discrete points typically required to reach convergence from $N \sim \mathcal{O}(10^4)$ to $N \sim \mathcal{O}(10^2)$. The only assumptions made are that the media are described by spatially local, frequency dependent dielectric functions $\widetilde{\varepsilon}_r(\omega)$ that terminate abruptly at the material boundaries.

A comparison of the scattering cross-sections calculated using the quasi-

static, Mie and BEMAX formalisms is shown in Fig. (2.7). The BEMAX simulations were run on the University of Cambridge high performance computing cluster by submitting an appropriate input file. The general procedure for running a BEMAX simulation is as follows

1. Setup the experimental dielectric function data input for all materials used in the simulation and set the maximum azimuthal number m used in the proceeding calculation.

2. Set the type (e.g. single plane-wave or Gaussian beam), direction, polarisation and wavelength range of the incident electromagnetic radiation.

3. Define the material and geometry of each nanosystem using input dielectric functions, appropriate lines and arcs, and number of discretisation points. Check geometry output.

4. Define the scanning parameters, e.g. the grid size and density for near-field calculations, and angular range of collection for optical cross-section calculations.

5. Set the calculations to be performed, e.g. scattering cross-section or induced surface charge density.

6. Submit input file containing all the above information. Run the simulation.

7. Run the simulation again to check original output for convergence in number of discretisation points and m.

8. Transfer the output data to a lab computer and plot using appropriate data handling software, in this case IGOR Pro (Wavemetrics).

As can be seen in Fig. (2.7), the agreement between the scattering cross-sections determined via the electromagnetic Mie solutions and the BEMAX simulation is excellent. The red-shift and broadening of the LSPP resonance due to retardation effects (Mie and BEMAX solutions) is clearly evident. Here the BEMAX simulations were used to explore the expected response of spherical NP dimers over a range of NP separations as well as axially symmetric tip systems. The simulations also provided valuable insight into LSPP excitations and the range of LSPP response that could be expected for different nanosystem geometries.

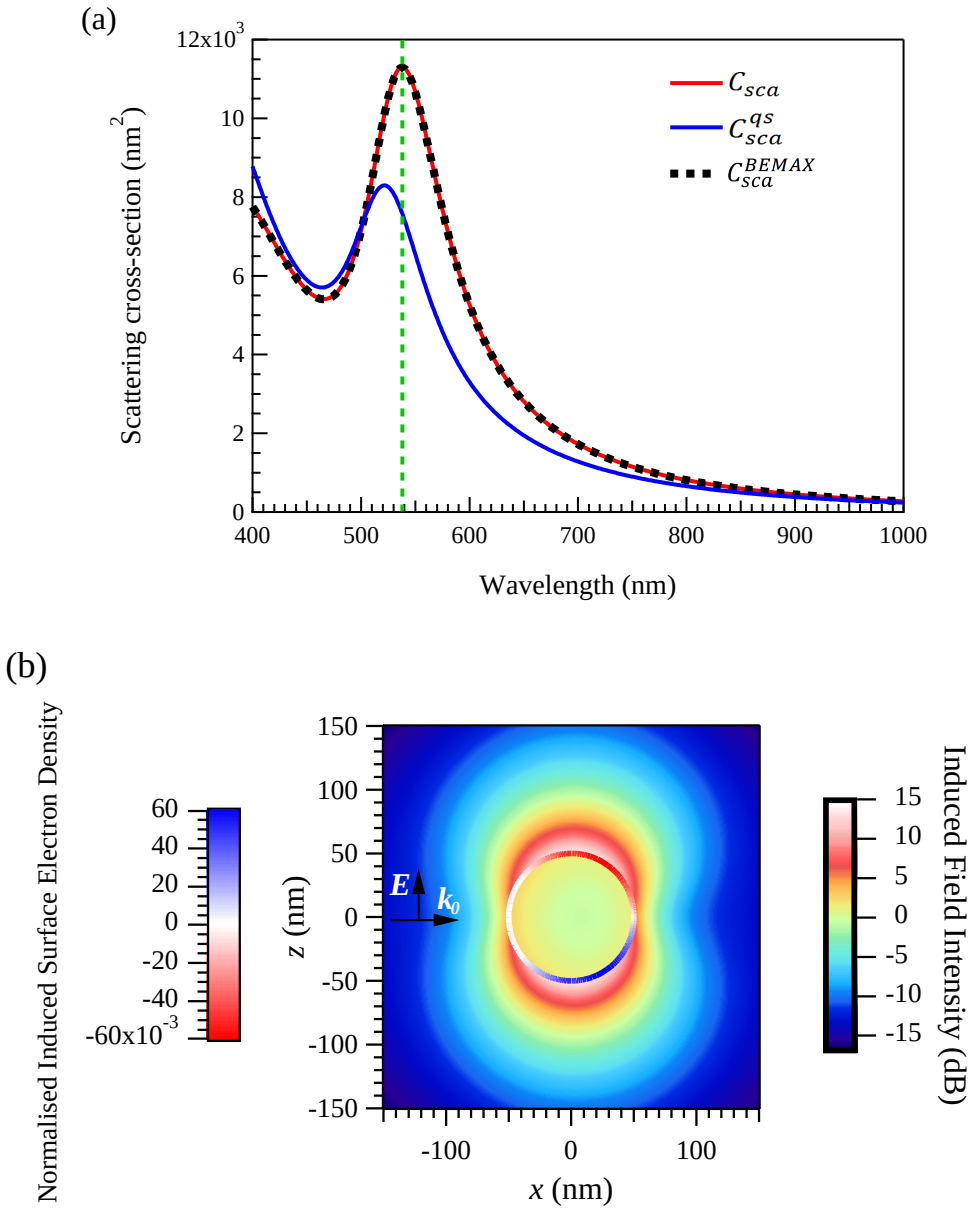

Figure 2.7: (a) Comparison of scattering cross-sections for a 100 nm diameter Au NP (in air) calculated using the quasi-static (C_{sca}^{qs}), Mie (C_{sca}) and BEMAX (C_{sca}^{BEMAX}) formalisms. (b) Electric near-field intensity and representative induced surface charge density distributions for 100 nm Au NP (in air) excited by an incident infinite plane-wave (see Fig. (2.5)) on the dipole LSPP resonance ($\lambda_0 = 538$ nm) calculated using BEMAX.

Initial BEMAX simulations showed that the field enhancement in the vicinity of the NP on each tip apex can arise from resonant excitation of LSPPs on the coupled tip-apex NP system, and the 'lightning rod' effect [78]. Resonant LSPP excitation on the coupled tip-apex NP system depends on the NP mate-

rial, size, shape, type and the coupling of the NP to the bulk of the supporting tip structure. The lightning rod effect is non-resonant and depends only on the geometry of the metallic system, in this case mainly on the radius of the tip apex NPs. The physical origin of the lightning rod effect is metallic screening (due to electromagnetic boundary conditions) producing a crowding of field lines at sharp features, as shown in Fig. (2.8). If the metallic tip was infinitely sharp the electric near-field magnitude would become singular at the tip apex as an infinite surface-charge density would be required to screen the incident electromagnetic fields [67]. Due to the relatively large radius of curvature of the apex NPs (and quantum mechanics!) there is not any unphysical singular behaviour, however the approximately equipotential surface of each NP still produces a large potential gradient in a nanoscale volume. Therefore the lightning rod effect contributes a non-negligible near-field intensity enhancement concentrated between the tip apex NPs.

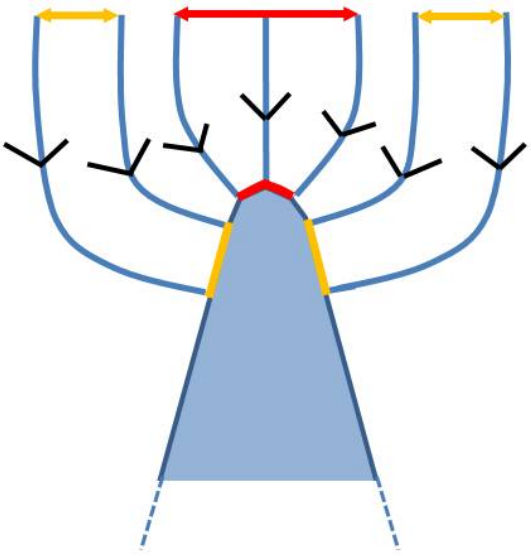

Figure 2.8: Schematic of lightning rod effect in a metallic tip system. The length of the red line on the tip apex surface is significantly shorter than that in free-space, thus demonstrating field line crowding (enhanced electric near-field). On the flat tip edges no field line crowding occurs (orange lines of equal length).

The focus of the present work was primarily to investigate NP dimers (formed by two tip apex NPs) with separation $d \ll 5$ nm, hence, as discussed in Sec. (2.2.2), spatially non-local screening effects at the NanoGap or nano-Junction (NGJ) created, modify the nanosystem dielectric response significantly. This therefore limits the validity of the BEMAX simulations. Additionally, at

sub-nanometre separations, the non-local quantum effect of spill-out electron density enables optical frequency tunnelling currents across the nanogap. Both of these quantum phenomena are expected to strongly affect the LSPP response of nanosystems with sub-nanometre NGJ's.

At present new numerical simulations are being developed to take into account the spatial non-locality of the dielectric function via non-phenomenological parameter-free calculations [79, 80]. This enables some effects of spatial non-locality in complex nanosystems to be investigated, e.g. a NP dimer with $d \lessapprox 5$ nm, and hence quantum mechanical effects to be further taken into account. However to consider the full range of non-local effects, including quantum electron density spill-out, tunnelling and confinement, *ab initio* calculations such as Time-Dependent Density Functional Theory (TDDFT) are required. Unfortunately, even under the approximations made in TDDFT (local-density approximation, linear response (for frequency-space TDDFT)), such calculations are still extremely time consuming and generally require the use of supercomputers [81] or further strong approximations (jellium model (no interband transitions)). As of yet, such calculations cannot be practically used to model nanosystems $\gtrapprox 3$ nm in dimension and thus are not suitable for the modelling of the vast majority of plasmonic architectures. However, the results found can be used to deduce a semi-quantitative picture of the expected non-local LSPP response of larger nanosystems [37, 82], and are described further in Chapter (5). Such *ab initio* numerical methods would also be required to model the more realistic atomic-scale geometries expected for the NGJ created upon break-of-contact, or contact between two NPs. It is well known from Scanning Tunnelling Microscopy (STM) that the exact atomic structure of the NGJ created modifies quantum tunnelling and confinement effects significantly [83].

Currently numerical methods are also generally required to study quantum confinement effects in plasmonic systems. The number of participating conduction electrons in NPs of less than approximately 4 nm diameter is small enough for quantum confinement effects to become non-negligible. If the absolute number of participating conductions is small, i.e. $N_e = n_e V_{np} \lessapprox 500$ where V_{np} is the NP volume, the energy imparted to each electron in the system by an incident photon $\Delta E_e \approx \hbar\omega / N_e$, and the spacings of the electron energy levels, are both comparable to the thermal excitation energy $E_T = k_B T$, where k_B is the Boltzmann constant and T is absolute temperature. In this regime the quantised

nature of the electron energy levels can no longer be discarded and generally comprehensive atomistic theoretical simulations or novel analytical approaches are required [36,84].

Even though the NPs considered in this work are relatively large, resulting in negligible spacing between electron energy levels, effects due to quantum confinement could still be accessible if quantum emitters, e.g. appropriate quantum dots or molecules, are present in the inter-NP NGJ's created. In this case the interband (or inter-orbital) resonances of the quantum emitters interact with the broad plasmonic modes highly-localised in the NGJ (see Sec. (2.3.4)). This results in the hybridisation of the quantum emitters resonant transitions and the LSPP resonances. The properties, e.g. excitation rate, and radiative and non-radiative decay rates, of quantum emitters present in NGJ's are hence significantly modified, even in the weak-coupling regime [85]. If appropriate quantum emitters are present in suitable nanoscale NGJ's strong exciton-photon coupling is expected to promote Fano interference and vacuum Rabi-splitting phenomena that can be measured in the broadband, optical, far-field scattering response. These effects are currently of interest due to the potential applications in quantum information devices [86,87]. In the current work, the focus is maintained on non-local screening and tunnelling phenomena as the exact molecular content of the NGJ's created is not investigated in detail.

2.3.4 Coupled Localised Surface Plasmon Polaritons

The electromagnetic coupling of LSPPs in NP dimer nanosystems with different inter-NP separation d have been extensively studied both experimentally [88] and theoretically [89] in the $d > 1$ nm domain. Due to the inherent reduction in nanosystem symmetry, compared to that of a single nanosphere, analytical solutions for the coupled LSPP modes of non-overlapping NP dimers have primarily only been determined under the electrostatic approximation for spherical geometries [90], most notably using the plasmon hybridisation method [74]. New analytical transformation optics techniques have begun to include some retardation effects (radiation damping) [91] and to consider overlapping cylindrical NP dimers [75] thus extending the validity of such analytical treatments. While the analytical theories provide a good intuitive understanding of LSPP modes present in NP dimers, numerical methods have to be used for precise calcu-

lation of the LSPP response. Strong LSPP coupling between NPs with $d \lessapprox a$ creates LSPP mode shifting, mixing and splitting with concomitant near-field enhancement and localisation. These aspects are highly desirable for many applications, including high-sensitivity chemical and biological sensors [92], optical frequency switching and measurement [93], quantum optics [94], highly non-linear optics [95] and solar cells [10].

While the LSPP coupling between spherical NPs ($a \gtrapprox 5$ nm) with $d \gtrapprox 5$ nm is well understood under a classical framework, controlled experimental measurement of the LSPP response in the combined spatially non-local screening and electron tunnelling regime ($d \lessapprox 1$ nm) has as of yet been intractable. Recent theoretical work has led the way in beginning to investigate this important and interesting regime by retarded hydrodynamic model based simulations [80] and TDDFT simulations [82,96]. In the following, a brief overview of classically coupled LSPP behaviour in a prototypical NP dimer system used to approximate the NP dimer system under investigation is presented. This provides a foundation for further detail on LSPPs in the non-local screening and quantum regime given in Chapter (5).

The present work is concerned with the LSPP interactions between two NP functionalised AFM tips with apex (NP) separation ranging from $d \sim \mathcal{O}(\mu\text{m-Å})$ proceeding into $d \sim \mathcal{O}(\text{nm})$ overlapping negative separation. Therefore understanding LSPP interactions between an AFM tip and a NP, and between NP pairs is essential. The simplest model to describe both these nanosystems, in the classical regime, is an identical spherical NP dimer in two different regimes of separation

1. LSPP coupling between AFM tip apex NPs: represented as two identical spherical NPs with d ranging from 500 nm to full conductive contact at $d = 0$ nm (see Sec. (3.3.2) for the definition of 'full conductive contact at $d = 0$ nm') and into small overlap $d \sim -1$ nm.

2. LSPP coupling between bulk AFM tip and NP apex: represented as two overlapping (e.g. $d = -10$ nm) identical spherical NPs where one NP represents the bulk AFM tip. Note this is a working hypothesis to help formulate an initial basis of understanding and is not necessarily a good approximation of the system. A more rigorous treatment of the coupling between a NP apex and bulk AFM tip body is presented in Chapter (5).

Schematics of these two regimes are shown in Fig. (2.9). It should be noted that more realistic asymmetric NP (hetero-)dimers where the individual NPs differ in size, shape or composition are also of great interest [97]. Such asymmetric NP dimer systems can amplify certain physical effects, e.g. plasmonic Fano resonances and visible LSPP mode splitting, not prevalent in the identical (homo-)dimer systems assumed throughout this section.

The LSPP mediated optical response of the NP dimer geometries described in (1) and (2) can be determined using BEMAX in the classical limit. Here the specifics of the methods used will not be discussed, but an overview of LSPP behaviour in these two different regimes will be presented.

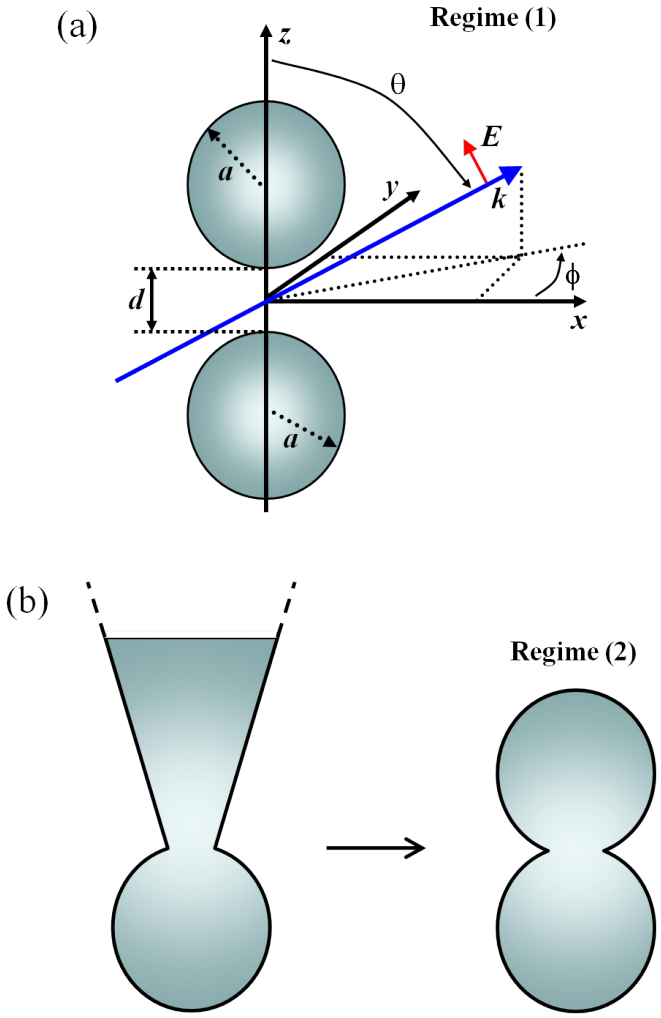

Figure 2.9: Non-contact and overlapping NP dimer configurations used to represent tip nanosystem. (a) NP dimer described in regime (1). (b) NP dimer described in regime (2). The coordinate system implemented in BEMAX is labelled in (a) with a plane-wave of arbitrary incident direction marked.

Non-contact regime

As $d \sim a$ the electromagnetic near-field interactions become significant and the NPs become capacitively coupled. Assuming $a \ll \lambda$, and a uniform exciting field, coupled LSPPs on a NP dimer can be described as a system of two interacting, oscillating electric dipoles (quasi-static limit). Depending on the orientation of the NP dimer and the polarisation of the incident light one can distinguish between two limiting cases of polarisation, either parallel or perpendicular to the NP dimer axis. The two possible configurations are shown in Fig. (2.10).

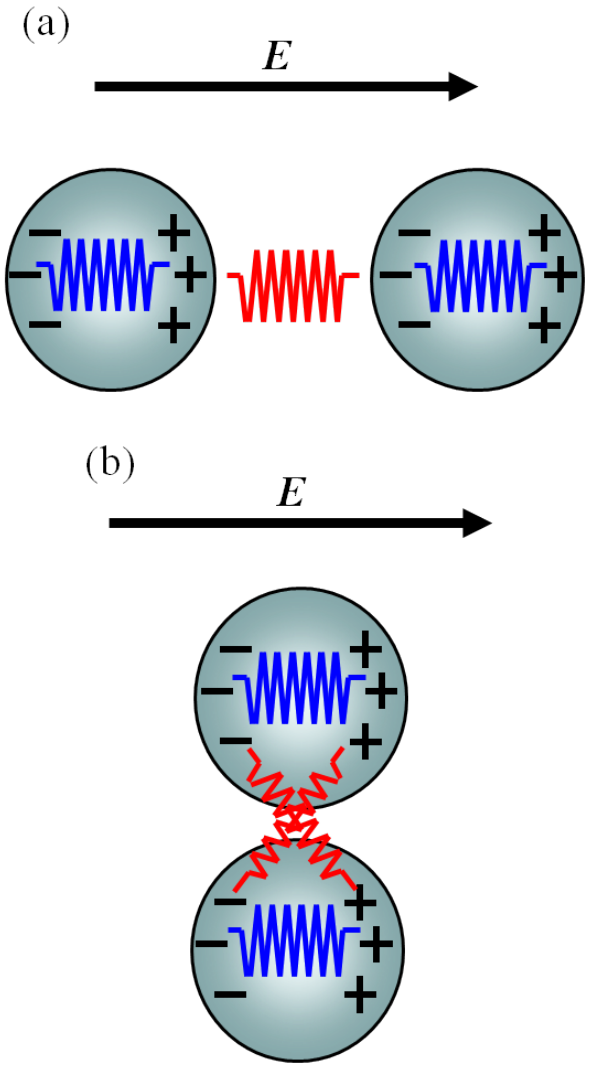

Figure 2.10: NP dimer LSPP coupling configurations. (a) and (b), two limiting configurations of the NP dimer with respect to the polarisation of the exciting field ((a)= parallel, (b)=perpendicular).

The Coulombic coupling between the individual NPs creates a system analogous to a coupled harmonic oscillator. The Coulombic restoring force acting on the oscillating electrons inside each particle is either decreased (Fig. (2.10a)) or increased (Fig. (2.10b)) due to the induced charge distribution of its neighbouring particle. Therefore the LSPP resonances will either shift to lower frequencies (red-shift) or higher frequencies (blue-shift) respectively. This insight allows an intuitive understanding of how LSPPs on the individual tip apex NPs will interact with each other. In short, as the inter-tip distance decreases it is expected that the LSPP resonances of the system will either red-shift or blue-shift depending on whether the incident exciting light is polarised parallel or perpendicular to the dimer axis. It is important to note that light polarised parallel to the dimer axis creates a far greater LSPP coupling strength relative to the case of perpendicular polarisation. This is due to the hugely increased electric near-field magnitude created in the vicinity of each particle under these conditions. As parallel polarisation is required to create a strong plasmonic response, primarily only this orientation of light with respect to the NP dimer axis will be considered further.

The locally induced electric near-field intensity, and representative induced surface charge density distribution, on an Au NP dimer excited at the hybridised dipole resonance for incident light polarised parallel to the dimer axis ($d = 1$ nm, $\theta = 90^\circ$ and $\phi = 0^\circ$) are shown in Fig. (2.11a). The term 'hybridised' is used as the LSPP modes of the individual NPs mix and hybridise in analogy with the theoretical treatment of the quantum states of diatomic molecules in terms of interacting molecular orbitals. Under the plasmon hybridisation formalism, as d is reduced, the dipolar ($\ell = 1$) LSPP modes of the two NPs interact with each other (and higher-order modes when $d \lesssim 10$ nm) to form bonding (bright) and anti-bonding (dark) hybridised dipolar LSPP modes [74]. Only the bright dipolar bonding mode has a non-zero dipole moment and hence a significant light scattering cross-section, as shown in Fig. (2.11b). It is important to note the hybridised bonding and anti-bonding modes are only labelled as 'dipolar' excitations as the primary interactions are between the $\ell = 1$ LSPP modes of the individual NPs. However, as $d \to 0$ the hybridised dipolar bonding mode contains interactions with higher-order modes therefore the shift in mode wavelength does not only have a $1/d^3$ dependence as higher powers of $1/d$ also contribute for small d.

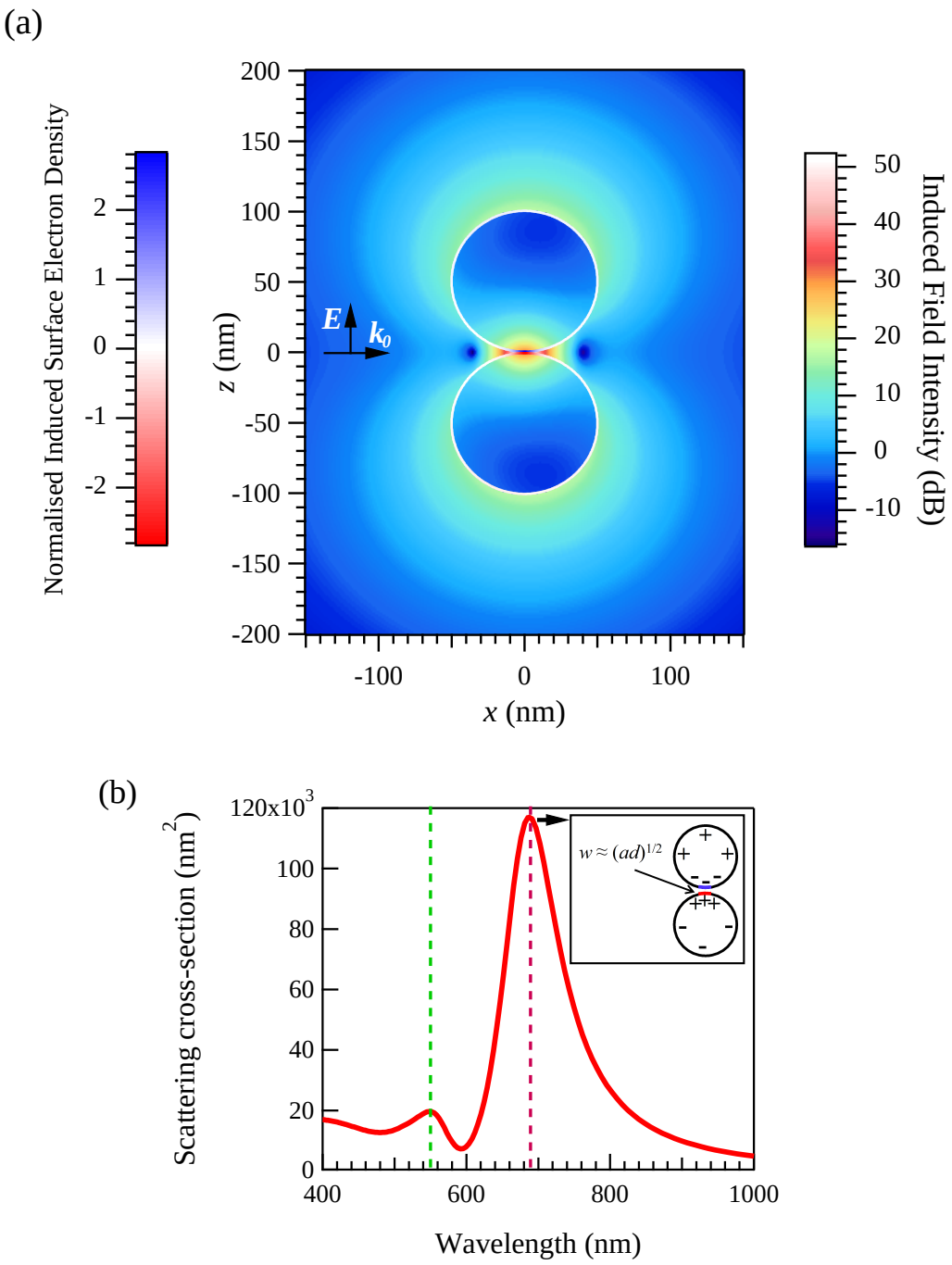

Figure 2.11: Near-field intensity map and associated scattering cross-section for an Au NP dimer (in air) with $d = 1$ nm and incident light polarised parallel to the dimer axis. (a) Near-field intensity map and representation of the induced surface charge density at the hybridised dipolar LSPP resonance $\lambda_0 = 685$ nm. (b) Associated scattering cross-section C_{sca}^{BEMAX} showing the hybridised dipolar mode (maroon dotted line). Inset shows schematic of associated surface charge distribution. Note the higher-order hybridised ('quadrupole') mode at $\lambda_0 = 550$ nm (**green** dotted line) created by the admixture of different ℓ-modes.

Here the NPs remain separated (in the classical sense) hence the large resonant charge build-up at the nanogap must be compensated by the charge distribution around the remainder of the individual NPs surfaces in order to maintain charge neutrality. The lateral width of the charge pile-up along the NP surface is on the order of $w \approx \sqrt{ad}$ for the hybridised dipole mode [89]. As Fig. (2.11a) shows, extreme field intensity enhancements are predicted in the volume of the nanogap, approximately 5×10^3 greater than the maximum found in the single NP case. In reality the hybridised LSPP modes will be slightly blue-shifted and broadened due to the spatially non-local screening effects of induced-surface-charge penetration and electron density spill-out around the vicinity of the nanogap. The electric near-field intensity enhancement at the nanogap will also be reduced by a factor ranging from $\times 2 \rightarrow \times 10$ because of the spatially non-local screening increasing the damping and effective d due to BP excitation.

Following the intuitive description given in Fig. (2.10a), as d decreases to 1 nm the hybridised dipolar bonding LSPP mode is strongly red-shifted from that of the dipole LSPP resonance of a single NP, i.e. 538 nm to 685 nm. At $d \sim 10$ nm the $\ell = 1$ LSPP dipole mode of each NP starts to interact significantly with higher-order LSPP modes of the other NP, therefore hybridised higher-order LSPP modes (e.g. labelled hybridised quadrapole mode for strong interaction between $\ell = 1$ and $\ell = 2$ modes) also begin to be strongly excited (dipole-active) as shown in Fig (2.11b). These higher-order modes are less dipolar in nature than the hybridised dipolar bonding LSPP mode and hence their excitation involves yet higher powers of $1/d$. All of these modes are associated with extremely large charge pile-up at the nanogap and hence are highly sensitive to the geometry and dielectric response of the nanogap itself. As $d \rightarrow 0$ the classical BEMAX simulation predicts that the red-shift of the hybridised LSPP modes becomes singular, as demonstrated in Fig. (2.13). This non-physical singular behaviour is evident because spatially non-local dielectric functions, and non-local electron spill-out density and tunnelling effects, are not considered in the BEMAX model.

Contact regime

In the classical regime conductive contact occurs when at least one atom forms a conductive bridge between the NP dimer. In this case intraparticle charge neutrality is no longer required and new LSPP modes are enabled. The polarisability of the new combined structure created, primarily determines the LSPP response for a given incident electromagnetic wave, i.e. the ability of the surface charges to redistribute over the whole surface of the combined structure. The conductive nanojunction is not equivalent to a zero-frequency conductor as the NP dimer system is being driven at optical frequencies. In the optical frequency regime the approximation $\widetilde{\sigma}_m(\omega) \approx \sigma_0$ is no longer valid. The flow of charge across the nanojunction is therefore considered as a displacement current, given by $\widetilde{\mathbf{I}}_\mathbf{d} = A\frac{\partial \mathbf{P}}{\partial t}$, rather than a conduction current $I_c = \sigma_0 AE$ (where A is the effective cross-sectional area of the nanojunction) that is found in typical electronic circuits operating at frequencies up to $f \sim \mathcal{O}(\text{GHz})$. The notion of the conductivity of the nanojunction is hence understood as the magnitude of the effective dipole (or higher-order) moment of the combined NP dimer structure that the nanojunction enables, i.e. the magnitude of the effective electric susceptibility $|\chi_e|$ of the nanosystem as a whole. This 'plasmonic' conduction hence depends on the orientation of the nanosystem with respect to the driving electric field and thus it can be substantially different to the traditional electronic conduction.

As the dimer NPs begin to overlap a new long-wavelength true (non-hybridised) dipole mode is formed, as shown in Fig. (2.12b), where each constituent NP has a net charge that oscillates in dipolar fashion over an optical cycle. The locally induced electric near-field intensity, and representative induced surface charge density distribution, on the Au NP dimer excited at the true dipole resonance for incident light polarised parallel to the dimer axis ($d = -2$ nm, $\theta = 90°$ and $\phi = 0°$) are shown in Fig. (2.12a). This LSPP reponse can be understood under the plasmon hybridisation formalism by considering the hybridisation of the unphysical monopolar ($\ell = 0$) LSPP modes[16] of the individual NPs. Upon contact the unphysical monopolar modes hybridise to create a physical true dipole mode involving the entire structure.

[16]Monopolar LSPP modes are unphysical for isolated NPs as charge neutrality within each NP would not be maintained.

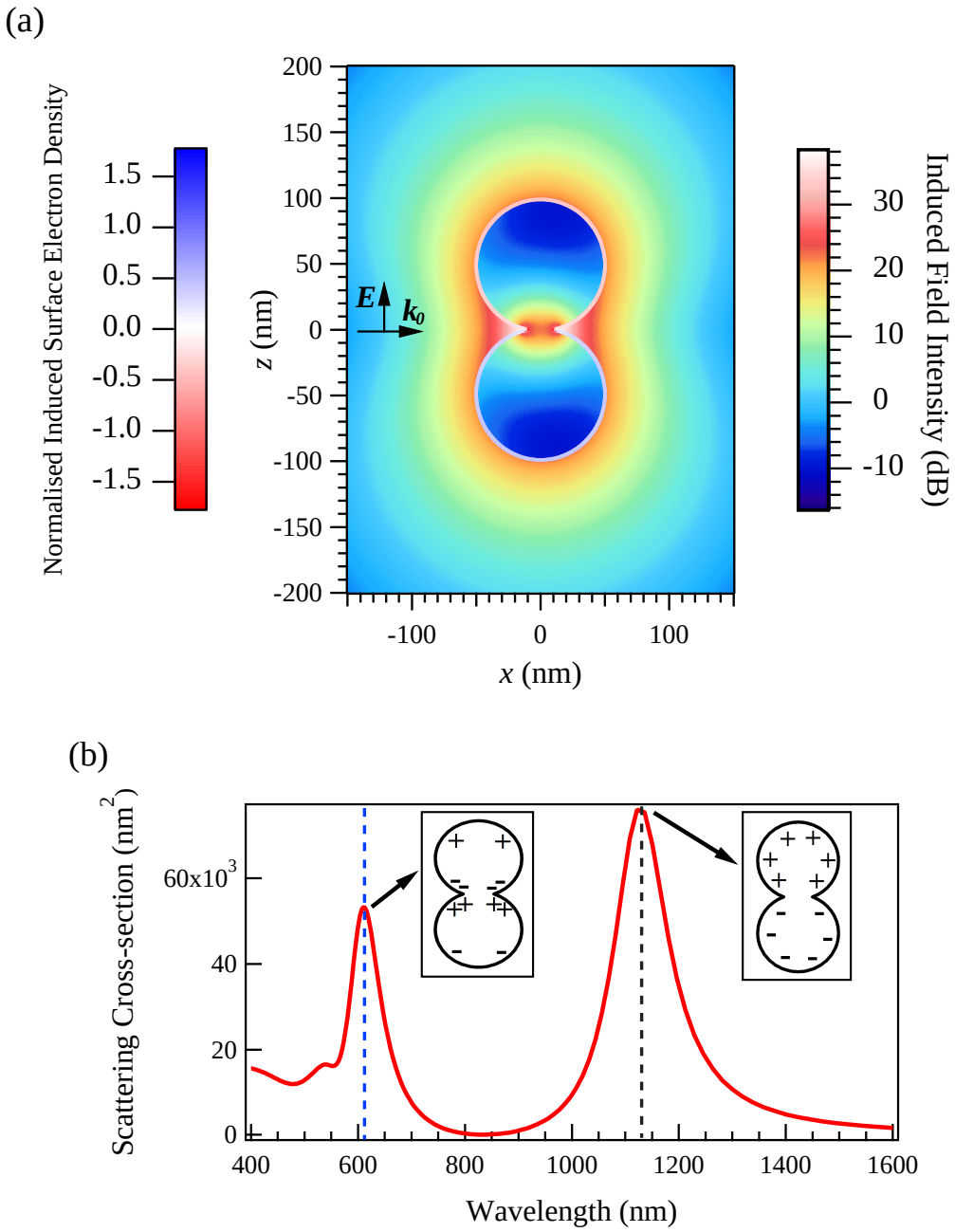

Figure 2.12: Near-field intensity map and associated scattering cross-section for an overlapping Au NP dimer (in air) with $d = -2$ nm and incident light polarised parallel to the dimer axis. (a) Near-field intensity map and representation of the induced surface charge density at the true dipolar LSPP resonance $\lambda_0 = 1128$ nm. (b) Associated scattering cross-section C_{sca}^{BEMAX} showing the true dipolar mode (**black** dotted line). Note the strongly hybridised dipolar mode at $\lambda_0 = 611$ nm (blue dotted line) created by the admixture of the $\ell = 1$ modes and higher-order ℓ-modes. Insets show schematics of associated surface charge distributions.

A comprehensive analysis of the LSPP modes through the conductive contact regime was performed using BEMAX [89] and the LSPP mode evolution is shown in Fig. (2.13). Immediately at contact there is a discontinuous 'jump' in the NP dimer system polarisability, and hence also the LSPP modes, and the true dipole mode appears (labelled C-D). From this singularity, as the NP overlap increases, all LSPP modes begin to blue-shift.

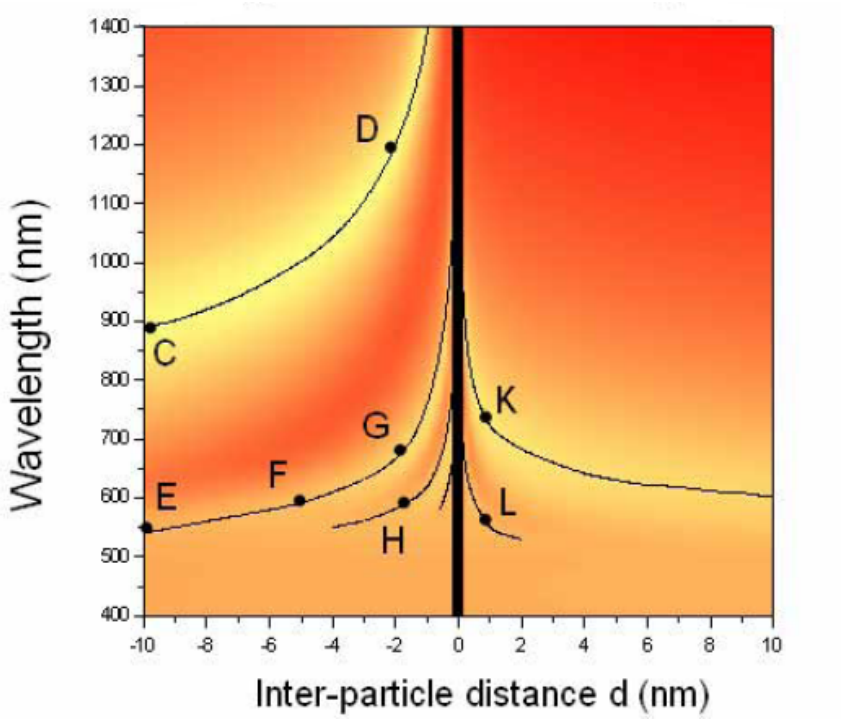

Figure 2.13: Evolution of LSPP dimer modes as NP ($a = 60$ nm) separation d is reduced through the non-touching to overlapping transition (from [89]). Note the unphysical asymptotic and discontinuous behaviour of the LSPP modes as $d \to 0$.

For small overlaps ($d/a \approx -0.05$) there is still considerable charge build-up within the nanojunction (anti-wedge) region, as shown in Fig (2.12a). Therefore higher-frequency modes created by the admixture of dipolar and multipolar LSPPs are present even after conductive contact (labelled E-G and H). The transition from a separated to plasmonically connected dimer has been studied in more detail under a classical framework by considering a NP dimer linked by bridges of different conductivity and conductance [98]. This has allowed theoretical estimates of the threshold electrical properties of the nanojunction required for the onset of the true dipolar charge transfer mode and the blue-

shifting of higher-order modes. It is through this -0.5 nm $\lessapprox d \lessapprox 2$ nm transition where the most extreme LSPP mediated field-enhancements (localisation), LSPP environmental sensitivity and LSPP mode shifts, mixing and splitting occur. As described previously, at these separations d is comparable to the scale of the electronic wavefunction (at the Fermi energy) and hence spatially non-local screening effects and quantum transport phenomena are expected to play a vital role in determining the nature of all the LSPP modes throughout this regime.

For large NP dimer overlap, as depicted in Fig. (2.9b), the true dipolar LSPP mode begins to de-localise charge from the nanojunction volume as the NP dimer begins to take on the character of a single elongated NP. The higher-order multipolar LSPP modes also become increasingly de-localised from the nanojunction and weaken in oscillator strength rapidly as the NP overlap increases. The true dipolar mode is significantly red-shifted compared to the hybridised dipolar mode present before contact. As overlap increases the post-contact LSPP modes settle into the positions expected for a nanorod geometry (effectively a spherical NP with an anisotropic polarisability). As discussed in detail in Chapter (5), understanding the complex combined NP-tip dimer system is challenging due to the extended nature of the tips, however the overall tip-NP dimer structure is modelled effectively.

2.4 Open Questions

As introduced throughout this chapter, the LSPP interactions between two identical spherical NPs ($a \gtrapprox 5$ nm) that form a dimer with inter-NP separation $d \gtrapprox 5$ nm are well understood when considering infinite uniform planar illumination. The rapid development of existing and novel fabrication techniques is enabling a new class of truly engineered nanosystems to be created [88, 99]. Dimensions and features of these nanosystems are beginning to be created on the single nanometre or even sub-nanometre scales. The limit for achievable nanogap d is currently set by several existing methods under various stages of development that are beginning to create nanogap electrodes with $d \lessapprox 1$ nm [99]. However, as of yet, none of these techniques can produce relatively large ($a > 20$ nm), individual NP dimer systems with the controlled variable separation -0.5 nm $\lessapprox d \lessapprox 2$ nm required for investigations of LSPP response in the spatially non-local screening and quantum transport regime. The existing methods and

their relevant limitations are described in detail in Sec. (3.1).

As detailed in Sec. (2.3.4) a huge number of applications are entirely dependent on the properties of the nanogaps created in nanosystems with a strong plasmonic response, i.e. NP dimers with $a > 20$ nm and $d < 20$ nm. Not only does understanding the LSPP response of nanogaps with $d \lessapprox 2$ nm strongly affect all existing applications but also nanogaps with $d \lessapprox 1$ nm are expected to yield new exciting applications including single-molecule plasmon-assisted transport, photoelectrochemistry on the sub-zeptolitre scale, optical rectification, electrical excitation of plasmons and improved methods for molecular spectroscopy and sensing. As fabrication techniques improve, and become more controllable, an understanding of the electromagnetic coupling between LSPP modes in the -0.5 nm $\lessapprox d \lessapprox 2$ nm regime is thus essential.

Experimental techniques for creating such relatively large NP dimer systems with dynamic separation control for -0.5 nm $\lessapprox d \lessapprox 3$ nm, whilst also allowing simultaneous optical and electronic characterisation of dimer LSPP response, are extremely challenging to realise. The challenges involved are mainly due to all the inherent difficulties of precise truly nanoscale positioning, manipulation and stability, coupled with the requirement for simultaneous high-quality optical and electronic measurement.

Current numerical and analytical theoretical work has yet to take into account the quantum nature of the transition from non-touching to atomically linked NP dimers with $a \gtrapprox 2$ nm. This is mainly due to the problems involved in modelling relatively large scale nanosystems on the atomic level because the fully quantum mechanical methods required, e.g. TDDFT, scale in computational complexity as N_e^3.

From this foundation it is clear three vital questions must be addressed as the field of plasmonics moves into the molecular and atomic-scale regimes. Firstly, from an experimental basis: what experimental rig and associated methods can be developed to create the necessary NP dimer systems ($a > 20$ nm, -0.5 nm $\lessapprox d \lessapprox 2$ nm) whilst allowing for effective simultaneous optical and electronic characterisation? The advances made in addressing this question are described in detail in Chapters (3) and (4).

Secondly, the development of such an apparatus now enables some of the most critical outstanding questions concerning the LSPP response in NP dimer systems to be experimentally addressed for the first time: how do the LSPP

modes of a NP dimer ($a > 100$ nm) shift, split and mix in the non-local screening and quantum transport regime ($d \lessapprox 1$ nm)? The progress made in addressing these important questions is described in detail in Chapter (5).

Finally the experimental work will for the first time enable comparison with new theoretical models, currently under development. This enables investigation into what non-local screening and quantum transport effects are of vital importance to include in theoretical models for a given d, i.e. are the new models sufficient to allow an understanding of plasmonic phenomena in the complex quantum-scale regime?

2.5 Summary

Following the open questions that arise from the theoretical background, the primary goal of the present work is directed at experimental measurement of the quantum transport mediated LSPP response of NP dimers with $a > 100$ nm and $d < 1$ nm. This enables the experimental resolution of the long-standing problem of the classically predicted singular nature of the contact transition [89] described in Sec. (2.3.4). Simultaneously, preliminary experimental investigations into how non-local screening, described in Sec. (2.2.2), affects the LSPP response are also carried out in a controlled manner. Additionally, recently predicted plasmon-exciton coupling phenomena, introduced in Sec. (2.3.3), may also be measurable in such NP dimer systems, and hence possible evidence is scrutinised. As all experimental data are taken for individual NP dimers over the full inter-NP separation range of interest, trends in LSPP response in the non-local quantum transport and screening regime, are for the first time fully comparable with classical, and emerging quantum corrected theoretical simulations.

Chapter 3

Experimental Rig

3.1 Introduction

A substantial component of the present work was concerned with the conceptual and physical creation of a novel, multi-purpose observation platform to enable study into the open questions described in Sec. (2.4) and beyond. This required an apparatus that could provide an optically accessible, suitably aligned metallic NP dimer with dynamically controllable separation from over 500 nm down to the ångström level. It was essential that the rig allowed high-quality, high-speed, nanolocalised optical DF measurements, and electronic measurements, to be taken simultaneously at all NP dimer separations.

Schematics of several techniques currently used to create NP dimers and metallic NGJs are shown in Fig. (3.1). At present, methods for NP dimer creation include directed self-assembly [100–102], top-down electron-beam lithography (EBL) [103] and discrete-step nanomechanical manipulation [104]. Very recent self-assembly methods [105] and top-down electron-beam lithography [106] methods enable spectroscopy on NP dimers of fixed separations down to $d \approx 0.5$ nm. However, none of these techniques provide dynamic control of dimer alignment and separation, limiting their capability for optical investigations of NP dimer interactions at the quantum scale. For example, the self-assembled NP dimer shown in Fig. (3.1a) has a minimum separation limited by the molecular layer used for the self-assembly process. These techniques also lack the capability for simultaneous measurement of individual NP dimer optical and electronic response, as making conductive contact to the dimer's constituent NPs is challenging.

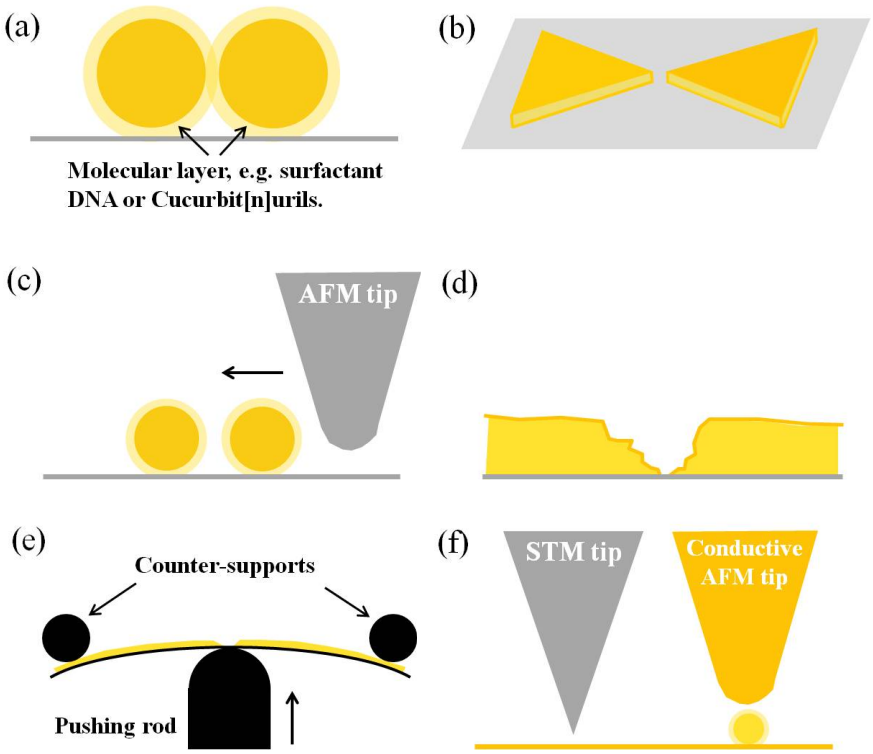

Figure 3.1: Schematics of techniques for NP dimer and nanocavity creation. (a) Directed self-assembly via molecular layer. (b) Top-down EBL or angle-evaporation using EBL manufactured mask. (c) Discrete-step nanomechanical manipulation. (d) Electromigration. (e) Mechanically controllable break-junction. (f) Break-junction nanocavity and NP dimer formed by STM tip and conductive AFM tip respectively.

In the field of molecular electronics, conductive contact to molecular junctions for simultaneous dynamic optical and electronic measurement has been achieved using electromigration [107] and Mechanically Controllable Break-Junction (MCBJ) methods [108] (Figs. (3.1d)-(3.1f)). The use of electromigration and MCBJ techniques provides the stability required to create long-lived molecular scale junctions. However the techniques lack the dynamic range of alignment, separation, NP geometry, and control of contact required to investigate the full range of plasmonic response. The effective NP dimer created between a NP and a conductive AFM tip, e.g. in a Tip-Enhanced Raman Spectroscopy (TERS) setup [109], is shown schematically in Fig. (3.1f). Such a system meets the general requirements, but suffers from an overwhelmingly large scattering background and poor optical access, therefore preventing measurement of the broadband optical (plasmonic) scattering response directly.

As described in the previous chapters the technique was conceived by envisaging the 3D nanoscale alignment of two conducting AFM probes, with NP functionalised apices, in an optically accessible, co-axial 'tip-to-tip' configuration. As the inter-tip separation is reduced the NP functionalised AFM tip apices effectively create a NP dimer geometry. A NP can be created on the apex of each probe by a wide variety of AFM industry standard methods including, metallic coating [110], Electron-Beam Deposition (EBD) [111], mechanically-directed or chemically-based NP attachment [112], and focused ion beam milling [113]. Creating an effective NP dimer by axially aligning the NP functionalised apices of conducting AFM tips has several advantages over the existing techniques, as it allows for,

- Simultaneous optical and electronic measurement in order to characterise the plasmonic response.
- Dynamic, NP dimer nanoscale alignment and separation control from $d > 500$ nm down to the ångström level via an all electronic feedback mechanism.
- Excellent optical access due to the accessible tip-to-tip geometry thus enabling DF spectroscopy techniques under the required light polarisation conditions.
- A greatly reduced background optical scattering signal compared to that from NP dimers created by structured substrates and NP dimers formed in TERS configurations [114].
- A stationary or alternating electric potential to be placed across an individual NP dimer and the associated current flow to be measured.
- Potential freedom in selection of NP dimer type and functionalisation.

It should also be noted that by utilising existing AFM tip technology, the cost and complexity of the rig and associated methods were greatly reduced, whilst the repeatability and reproducibility of the methods realised were increased. It is also stressed here that almost all the apparatus was controlled remotely using IGOR Pro to send Virtual Instrument Software Architecture (VISA) commands via GPIB to the experimental equipment. User friendly software was

also created using IGOR Pro to automatically log data and run experimental procedures thus increasing the efficiency of rig development and experimental investigations. The rig development and setup can be separated into three categories; mechanical, electronic and optical design. In this chapter each of these categories is discussed in detail to provide the necessary background information on the experimental setup.

3.2 Mechanical Design

The experimental setup required a mechanical system capable of the nanoscale alignment of two AFM tips in a tip-to-tip configuration whilst also providing the necessary framework to allow full access for a multi-purpose optical microscope with laser illumination DF nano-spectroscopy capabilities. The mechanical construction of the overall rig can therefore be split into two components, the AFM tip alignment unit and the optical microscope unit. In this section a concise description of the overall mechanical rig construction is presented.

3.2.1 AFM Tip Alignment Unit

The AFM tip alignment unit was constructed from two lockable manually controlled micron resolution stages (Newport DS25), one computer controlled three-axis nanometre resolution piezoelectric stage (PI733.3CD), and various specially designed support structures. Critically, using this combination of positioning stages allowed the inter-tip position to be moved over a range from *millimetres down to nanometres* with nanometre resolution in x, y and z. The tips used for development were 17 μm long, standard platinum or gold coated, contact mode AFM tips ($\approx$ 0.2 Nm^{-1} spring constant), that were formed with a conducting 450 μm long cantilever to an industry standard sized chip holder. The alignment unit was carefully designed to allow,

- Industry standard AFM chips of dimension 3.4 mm $\times$1.6 mm $\times$0.3 mm to be easily attached and removed from the setup.
- Electrical connections to be made to each AFM chip while electrically isolating the vast majority of the overall rig.

- Dark-field microscope objectives of up to 100× magnification (NA 0.9) to be brought within their short working distance (1 mm) to image the tips and obtain DF optical measurements.
- Creation of tip-to-tip geometry with maximum stability whilst retaining the ability to control the inter-tip position in 3D on the nanoscale.
- Ultra-wide optical access to the tip apices to enable a wide range of optical measurements to be performed effectively, under suitable incident light polarisation conditions, e.g. DF scattering and transmission measurements with light linearly polarised parallel and perpendicular to the tip axes.
- Extensions to be added, such as stray electromagnetic field and air current shielding, and additional electronics.

As discussed in Sec. (2.3.4), for a NP dimer to yield a strong plasmonic response the incident light needs to be polarised parallel to the dimer axis. The system geometry shown in Fig. (3.2) is required so that incident light, linearly polarised parallel to the tip axes (dimer axis), can be directed onto the tip apices (NP dimer).

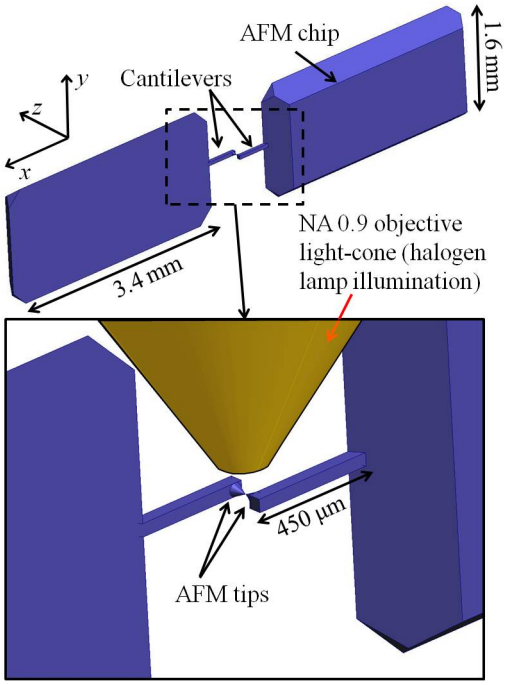

Figure 3.2: Scaled drawing (apart from the tips and cantilever thickness, enlarged for clarity) of the co-axial tip-to-tip geometry in relation to the light-cone produced by a NA 0.9 microscope objective under halogen lamp illumination.

Using this setup, complicated polarisation transformation techniques [115] used in conventional tip-enhanced spectroscopies [114], are not required to create a polarisation state parallel to the dimer axis. This allows the generation of strong LSPP coupling across the NP dimer when $d \lessapprox a$.

A Computer Aided Design (CAD) drawing of the tip alignment unit constructed to meet the necessary requirements is shown in Fig. (3.3). The AFM chips (and therefore tips) are held securely in place by a phosphor bronze 'chip clip' pressing against the underside of the AFM chip thus clamping it into a precisely machined alignment groove, as shown in the inset in Fig. (3.3). The compressive force on each chip is supplied by tightening two brass screws threaded between the chip clip and the control rod. The control rods and chip clips were carefully designed to allow DF objectives (with greater diameter than standard objectives) to be brought from above to within 1 mm of the tips. The only factor limiting the objective approach is the width of the AFM chip itself, as shown in Fig. (3.2). The manual y-axis stage on the left-hand side of Fig. (3.3) is secured

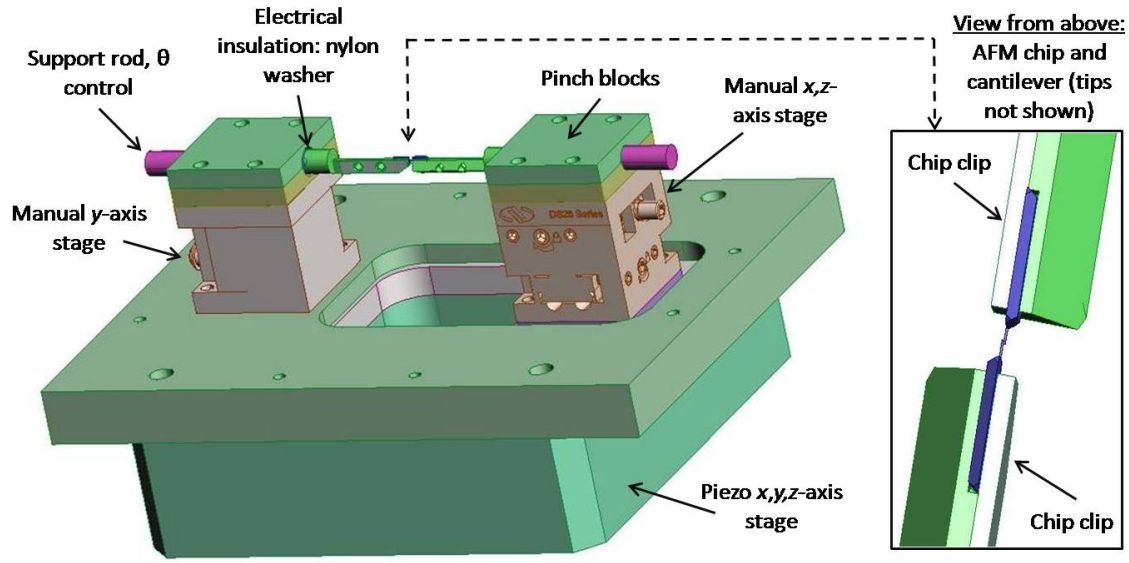

Figure 3.3: CAD drawing of the AFM tip alignment unit. The AFM chips are firmly secured by the chip clips. The opposing ends of the control rods were carefully designed to enable maximum optical access. A top-down view of the AFM chips and cantilevers is shown in the inset.

to the main base plate (green) which in turn is secured to the fixed piezoelectric stage chassis. The manual combined x and z-axis stage on the right-hand side is connected through to the piezoelectric driven base plate (purple) that

is firmly secured to the 3D piezoelectric actuator. Thus only one of the tips is mounted on the piezoelectric actuator which provides the nanomechanical facility for inter-tip alignment on the nanoscale.

A photo of the completed mechanical unit is shown in Fig. (3.4). Apart from the standard 25 nm thickness gold or platinum coated tips, several other types of AFM probe were used during the system development. Most importantly, for the simultaneous optical and electronic measurements, nano-indentation AFM probes with a 'neck and ball' apex geometry and an overall 50 nm thick gold coating were typically used, as they created the desired spherical dimer geometry at the apices. These functionalised 'dimer tips' were produced by Nanotools GmbH by performing EBD on standard AFM probes and subsequently evaporating on the required coating layer[1].

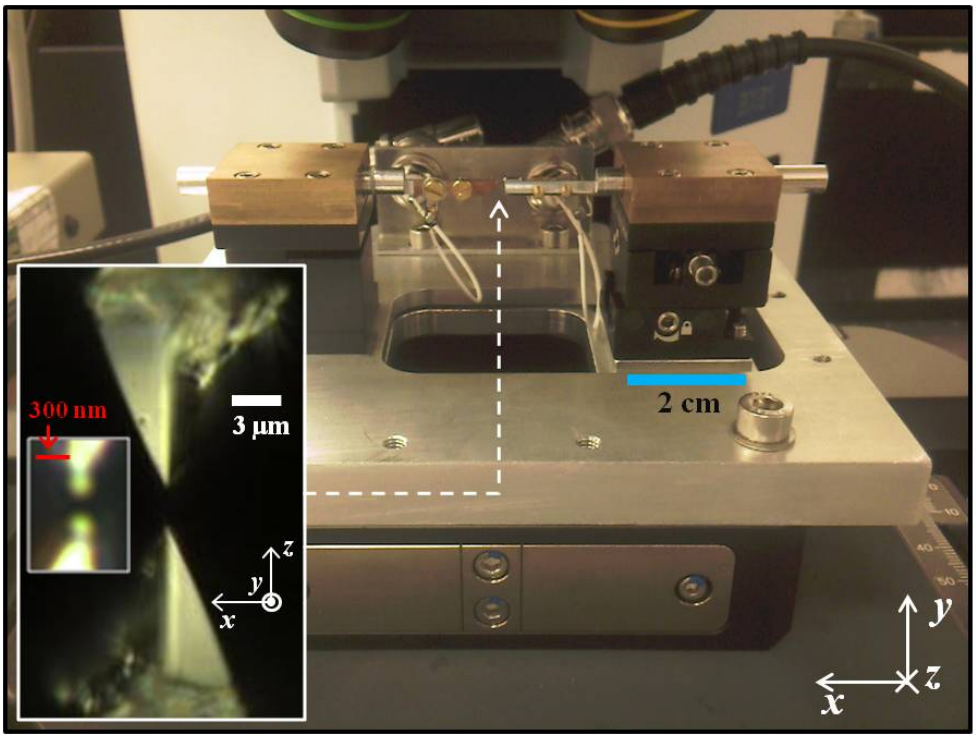

Figure 3.4: Photo of the completed tip alignment unit mounted on the translation stage of an Olympus BX51 optical microscope. The inset and sub-inset (note change of axes) show DF images taken from above of typical AFM tips used, at maximum (2×100×) magnification.

[1]Au NP functionalised AFM tips were also produced in-house by attaching an AFM tip to a nano-manipulator and picking up individual NPs under a SEM (using a small electrostatic force). However time-constraints ruled this process out as a viable functionalisation method.

Typical DF images of standard platinum coated tips, and functionalised dimer tips, in the tip-to-tip configuration used are shown in the inset and sub-inset respectively in Fig. (3.4). The specifics of the tip geometries and cantilever specifications used are described in more detail in Chapters (4) and (5).

The electrical connection to each tip was made by a solder tag secured to each control rod via one of the chip clip fixing screws. The current signal was transfered by highly flexible, low capacitance, mini-coaxial (white) cable to standard coaxial connectors shown in the background of Fig. (3.4). The tips themselves were electrically isolated from the rest of the alignment unit by 5 mm thick nylon washers placed just before the control rods contact the pinch blocks. The two sides of a control rod were connected by a nylon stud screw to maintain electrical isolation. The pinch blocks hold each control rod securely in position at a chosen angle between the tip axes, and are constructed from brass to avoid possible cold welding to the aluminium alloy control rods.

3.2.2 Optical Microscope Unit

The initial testing and development of the tip alignment unit was carried out under an Olympus BX51 microscope. As the work progressed it became apparent that a custom built microscope setup would be needed to meet the following stringent requirements,

- A high level of stability and resistance to external vibration sources, e.g. vibrations originating from the laboratory floor, optical bench surface and equipment racks.
- A reasonable level of isolation from air currents, electromagnetic fields and heat sources.
- Computer controlled 3D translation of the tip alignment unit under the illumination with >2 cm travel range and <50 nm resolution in x, y and z.
- Facility for a high quality, high magnification, lamp-sourced, Bright-Field (BF) reflection imaging and DF scattering imaging setup.
- Facility for an ultra-low background laser (supercontinuum) sourced confocal DF nano-spectroscopy setup that can be used *simultaneously* with the

halogen lamp sourced imaging system.

- All free-space coupling of light sources between microscope and measurement equipment, i.e. no optical fibers.

A photo of the overall apparatus including the microscope unit is shown in Fig. (3.5). The whole unit was implemented in a horizontal geometry to allow shorter, stiffer, more stable supports.

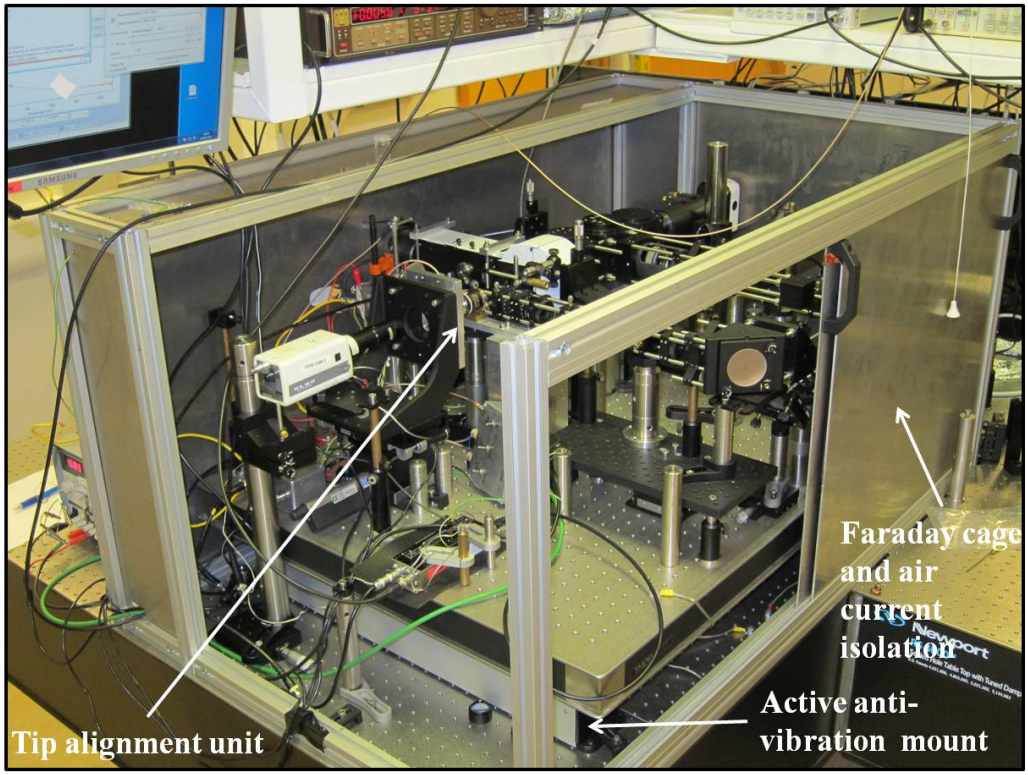

Figure 3.5: Photo of the overall experimental rig including the microscope unit. The optical microscope unit is built entirely upon an optical breadboard mounted across two active anti-vibration platforms, all contained within a Faraday cage.

All critical posts and customised support structures were built for high strength and stability. Additionally, where possible, the support structures had internal passive damping. As shown in Fig. (3.5) the whole microscope setup was mounted on an optical breadboard connected to two active anti-vibration platforms (Halcyonics Vario) to provide vibration damping from 1-300 Hz and additional passive damping at higher frequencies.

The combination of active and passive damping mechanisms implemented throughout the entire rig and optical bench were designed to complement each

other in order to reduce unwanted vibrational resonances of the support structures. The setup provided a high level of vibration isolation from 1 Hz well into the kHz regime. The anti-vibration platform was isolated (no direct physical contact) from the surrounding Faraday cage and air current shielding. All cables connected to components on the anti-vibration platform were double strain relieved to avoid transmission of external mechanical vibrations onto the platform and hence to the AFM tips or sample under investigation.

Due to the horizontal setup, the microscope objectives and the tip alignment unit had to be mounted in an appropriate fashion as demonstrated clearly in Fig. (3.6).

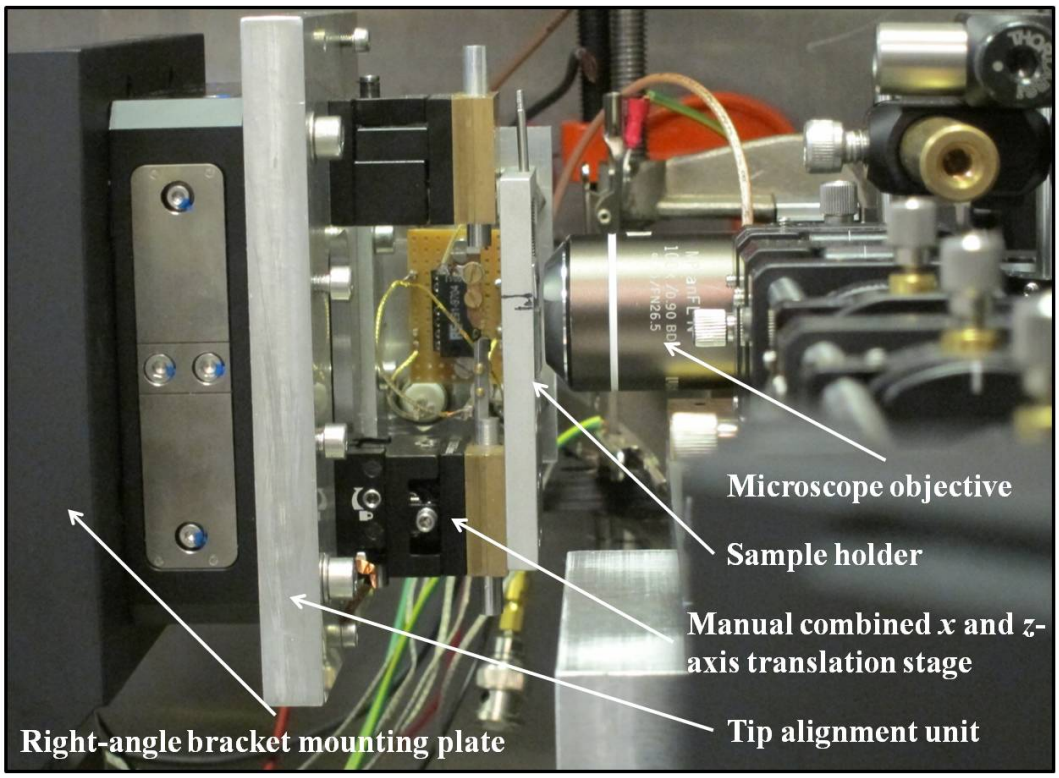

Figure 3.6: Photo of the tip alignment unit mounted 'side on' with sample holder and microscope objective shown. Sample holder is removed when tips are to be studied.

The 3D piezoelectric stage was re-calibrated for the given load under the 'perpendicular' orientation and tuned to provide relatively high stability but slow (≈ 50 Hz) response. The custom built sample holder shown in Fig. (3.6) was mounted on the manual combined x and z-axis translation stage and is thus connected through to the piezoelectric actuator. This allowed standard samples,

e.g. NPs deposited on a microscope slide, to be observed and translated in 3D with nanometre resolution under the custom microscope illumination. When the AFM tips were to be investigated the sample holder was removed and the alignment unit translated along the y-axis towards the objective until the appropriate working distance was obtained.

The typical halogen and laser light paths are marked schematically on the top-down photo of the microscope unit shown in Fig. (3.7). Almost all optical components were held securely within cage systems (Thorlabs) that acted to maintain relative translational and angular alignment. The cage rods and plates also improved the rigidity of the overall apparatus and the resistance to external vibration. The microscope objective itself was mounted on a custom built high-stability (no rotating turret) mount securely fastened to the optical breadboard base.

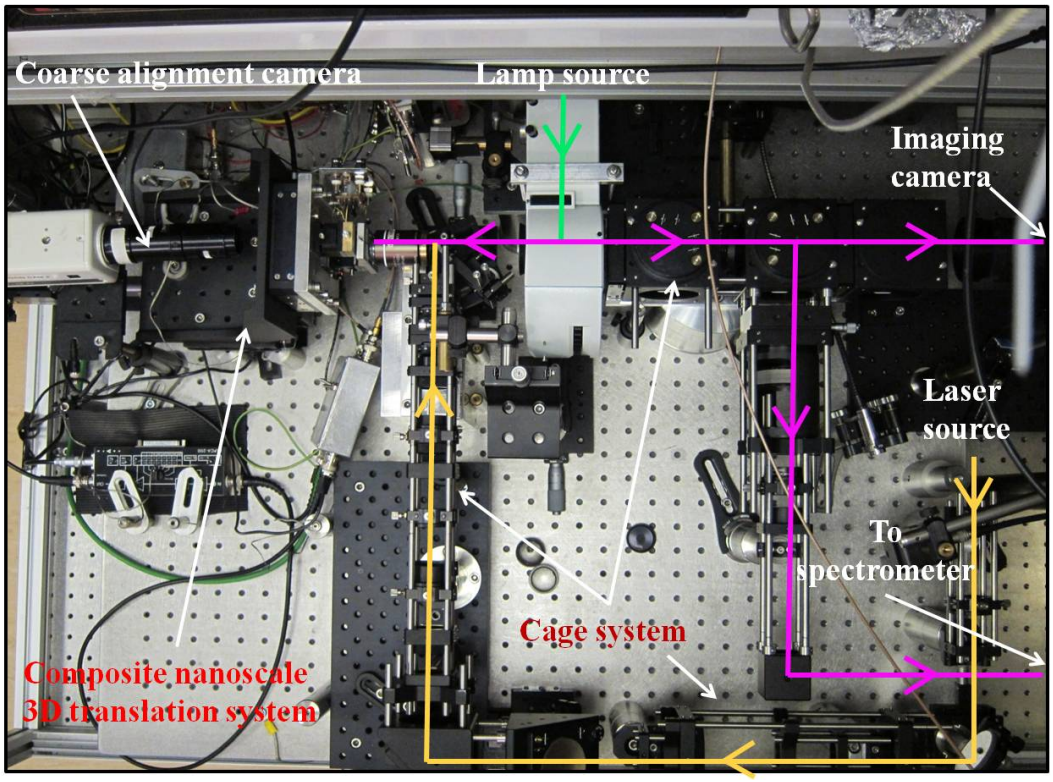

Figure 3.7: Top-down photo of the optical microscope unit with schematic overlay of lamp (**green**), laser (**orange**) and combined (**purple**) light paths.

The halogen lamp (100 W) is not shown in Fig. (3.7) as it protrudes outside the Faraday cage through a specially cut aperture. This keeps the substantial heat (and air convection) source shielded from the tips. Temperature variations

were kept under $\approx \pm 0.1$ K by the laboratory temperature control system thus keeping thermal expansion and contraction of all the mechanical structures to a minimum. The spectrometers were also located outside the shielding and were not physically connected to the anti-vibration platform. This de-coupled the vibrations produced by the spectrometer cooling fans from the alignment and microscope units. The imaging camera and lens tube, labelled in Fig. (3.7), were mounted on a damped support post. The composite 3D translation unit used to position the tip alignment unit (hence the tips) with respect to the microscope objective illumination was formed from three highly stable, low-drift, lockable, steel translation stages (Newport). The motion of both lateral stages was computer controlled via piezoelectric actuators with 30 nm resolution, while the vertical stage motion was computer controlled via a heavy load actuator with 50 nm resolution.

3.3 Electronic Design

The electronic systems were designed and developed to enable the axial tip-to-tip alignment of two AFM tips, i.e. 3D NP dimer alignment, and to perform conductance measurements on the nanojunction created upon (classical) conductive contact of the NP dimer constituents. The electronic setup can thus be separated into two distinct components, the AFM tip alignment electronics and the nanojunction conductance measurement electronics. The electronic setup for both components is described in this section while the detailed reasoning for each setup and the physical principles behind the techniques developed are described in Chapters (4) and (5).

3.3.1 AFM Tip Alignment Electronics

The AFM tip alignment technique, i.e. the 3D dimer alignment mechanism, was based on applying an alternating potential across the conducting AFM tips (Fig. (3.4)) to create an oscillating long-range electrostatic force that drives one of the AFM tips into resonant motion. Alignment feedback was then obtained by measuring the changes in the modulation amplitude of the tip system capacitance (related to tip oscillation amplitude) as the tip mounted on the piezoelectric actuator was scanned in an x, y grid, at a given initial tip apex separation d_0 in the

z-direction. Due to the complexity of the system it was not possible to specify all the necessary electronic equipment from the outset. By practical development, and theoretical modelling of the system, the broad requirement identified to enable an alignment capability from $d_0 \leq 400$ nm was an electronic measurement setup with the ability to measure Alternating Current (AC) amplitudes $I_0^{AC} \approx 0.3 - 1 \pm 0.05$ pA at frequencies $f_{AC} =$ 10-30 kHz. Such measurements correspond to capacitance modulation amplitudes of $C_0^m \approx 1 - 8 \pm 0.1$ aF. Additionally each measurement had to be accurately taken within timescales corresponding to a 100 ms time-constant to allow a typical 20×20 point grid scan to be obtained in a reasonably short time.

A schematic of the AFM tip alignment electronics is shown in Fig. (3.8). The computer controlled signal generator was used to generate an alternating (kHz sine wave) electric potential across the high input impedance of the broadband (0-1 MHz) voltage amplifier. After the amplification stage a current limiting resistor R_{cl} was used to limit the current flow across the nanojunction that would be formed if accidental contact occurred during the tip alignment procedure.

The amplified alternating potential amplitude ($V_0 =$ 1-15 V) creates an oscillating attractive force between the tips that can induce substantial motion of a cantilever-tip assembly when driven on resonance. The motion thus modulates the tip system capacitance, i.e. (approximately) the capacitance between the opposing composite control rod, chip clip, AFM chip, cantilever and tip assemblies, referred to as C in Fig. (3.8). Critically, the modulation of C creates harmonic components of I_{AC} that flow across the capacitor formed by the tip system. These harmonics are related to the cantilever-tip assembly oscillation amplitude and can be measured by lock-in detection. The optimum harmonic component was measured and used for alignment feedback, as described in detail in Chapter (4).

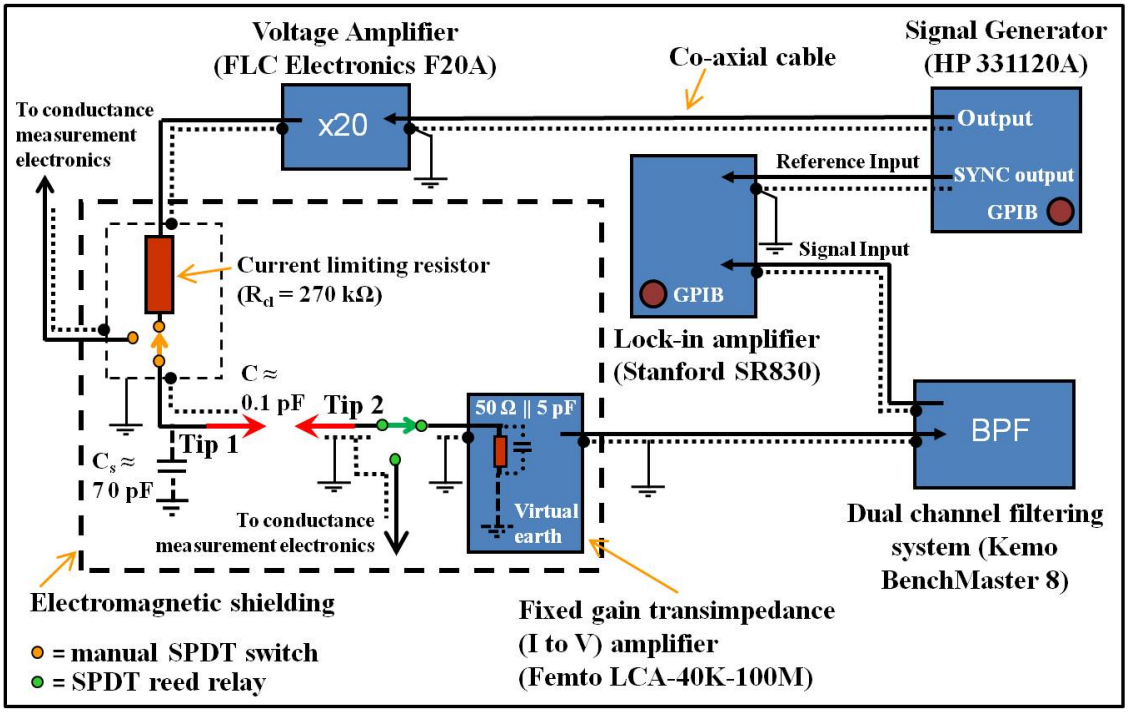

Figure 3.8: Schematic showing the setup of the main electronic measurement equipment used for the axial AFM tip-to-tip alignment technique developed. Note all ground points were connected to a single mains power earth connection point.

In practice a Digital Storage Oscilloscope (DSO) is placed in parallel with C to measure the amplitude and phase of the alternating potential across the AFM tips. This is necessary because the large load impedance $|\widetilde{Z}_c|$ (> 300 MΩ) associated with C is orders of magnitude greater than the impedance $|\widetilde{Z}_s|$ associated with the stray capacitance of the system C_s. Here the required current limiting series resistance $R_{cl} \sim \mathcal{O}(|\widetilde{Z}_s|)$, hence C_s acts to reduce the amplitude of the potential across the AFM tips V_0^T by $\approx 40\%$ compared to V_0[2]. The reduction of V_0^T relative to V_0 has to be taken into account in both experiment and theory.

A manual Single-Pole Double-Throw (SPDT) switch (orange) was used to select the nanojunction conductance measurement voltage source and electronics. In a similar fashion a small, low noise, low vibration SPDT reed relay (green) mounted on the AFM tip alignment unit was used to select (when energised) the appropriate current characterisation equipment for the nanojunction

[2]Connecting the DSO (and the required co-axial cable) in parallel with C also loads the system and reduces the amplitude of the potential across the AFM tips yet further. However it allows accurate measurement of V_0^T and the associated phase.

conductance measurements. The current flow I_{AC} across C is passed through a fixed 10^8 gain, 40 kHz bandwidth transimpedance amplifier with 10 μs rise time. The resulting output voltage signal V_{AC} is then passed through a dual channel filtering system appropriately set to form a Band-Pass Filter (BPF) of ≈ 3 kHz bandwidth around the frequency of interest. The pre-filtering prevents unwanted signals outside the region of interest from overloading the lock-in amplifier.

Finally, the lock-in amplifier, referenced by the signal generator SYNC (TTL) output, is used as an exceptionally narrow BPF filter, and accurate phase detector, to measure V_0^{AC} and the associated phase. The current flow amplitude across C is directly related to V_0^{AC} by $I_0^{AC} = V_0^{AC} \times 10^{-8}$. Tip alignment feedback is obtained using the lock-in amplifier to generate an internal reference signal at the appropriate harmonic frequency of the fundamental, thus enabling measurement of the optimum harmonic component of I_{AC} created by the cantilever-tip oscillation. Each measurement is taken with a 100 ms lock-in time-constant (effectively 0.78 Hz filter bandwidth with 24 dB roll-off) and the data transferred to the experimental control computer via a GPIB interface.

The electronic Signal-to-Noise (SN) ratio was good enough to allow useful alignment measurements to be taken at $d_0 \lessapprox 400$ nm with a 100 ms time-constant. To ensure this measurement capability several improvements were implemented over the course of development of the electronic setup to decrease the amount of induced current noise:

- Reduced capacitive coupling: all electronic equipment and cables in the immediate vicinity of the rig were shielded (aluminium foil) or moved further away from the tips. Additionally all critical components and the overall rig were electromagnetically shielded in Faraday enclosures.

- Reduced microphonic and triboelectric induced noise currents: the shortest possible lengths of double strain relieved, low-noise, low-capacitance co-axial cabling were used, e.g. the cabling between tip 2 and the transimpedance amplifier input was firmly secured and kept to under 30 cm in length.

- Ground loops: care was taken to reduce the effect of ground loops as far as practicable using the available equipment, e.g. all electronic equipment was connected at a single mains power earth connection point.

The short lengths of low-capacitance cabling used ensured that minimal additional loading was introduced and all RC time constants created were kept below ≈ 5 μs, i.e. well below the required 100 ms lock-in time-constant.

Using the electronic equipment shown in Fig. (3.8), optimised for low-level current measurement as described above, a noise level of $\approx \pm 50$ fA at f_{AC} is achieved. This provided a SN ratio that is good enough for alignment to proceed from $d_0 \approx 400$ nm, i.e the initial tip apex separation after diffraction-limited coarse tip-to-tip alignment under the optical microscope unit.

3.3.2 Nanojunction Conductance Electronics

Upon 3D NP dimer alignment d_0 is reduced to zero to form full conductive contact between the NPs, while the Direct Current (DC) conductance of the nanojunction created is continually measured. Stationary voltages $V_{DC} \sim \mathcal{O}(\mu\text{V})$ are applied across the nanojunction whilst simultaneously measuring the associated DC flow $I_{DC} \sim \mathcal{O}(\text{nA-}\mu\text{A})$. The nanojunction DC conductance G_{DC} is calculated via $G_{DC} = I_{DC}/V_{DC}$. Full conductive contact ($d_0 = 0$ nm) is defined by the condition $G_{DC} \geq G_0$ where $G_0 = (2e^2/h)$ is the quantum of conductance (assuming ballistic electron transport through a 1D channel). The required potential was generated by a low-voltage Source Measure Unit (SMU) connected across the NP dimer, as shown in Fig. (3.9).

When DC conductance measurements were required the circuit shown in Fig. (3.9) was selected, as described in Sec. (3.3.1) and shown in Fig. (3.8). The current flow was measured by a low-noise variable gain (10^3-10^{11}) transimpedance amplifier (with a 10 Hz bandwidth low-pass input filter) and the resulting voltage signal measured on a DSO connected to the laboratory computer. The SMU maintained a constant potential across the NP dimer regardless of the contact resistance. The potential was set to compensate for the combined contact potentials (thermoelectric EMF's), and ground potential differences, present in the electronic setup. Temperature gradients were kept to a minimum by the laboratory temperature control system and equipment shielding so that thermoelectric EMF's were small compared to the offset voltage created by the difference in ground potentials. These effects typically produced overall (relatively constant) offset voltages $V_{off} \sim \mathcal{O}(\mu\text{V})$. The compensating offset voltage required ($-V_{off}$) was found by bringing the base of the AFM tips

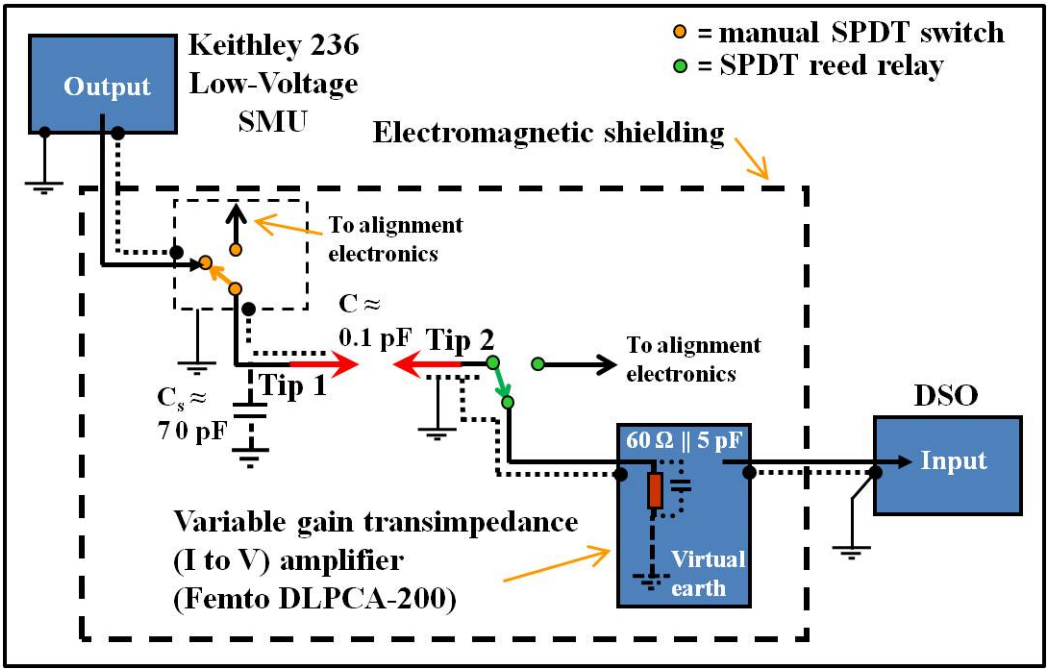

Figure 3.9: Schematic showing the setup of the main electronic measurement equipment used for the tip-to-tip (NP dimer) conductance measurements. Note all ground points were connected to a single mains power earth connection point.

into full conductive contact and using the SMU to adjust the potential across the AFM tips until $I_{DC} = 0$ at an appropriate level of gain. This procedure was carried out before each experimental run thus allowing V_{DC} to be set accurately for the DC conductance measurements. Therefore the quality of DC conductance measurement was mainly determined by the accuracy of the I_{DC} measurement.

3.4 Optical Design

The optical system was designed to enable good quality, high-magnification (BF and DF) imaging of various nanosystems, with the facility for laser-sourced DF nano-spectroscopy measurements to be taken simultaneously. The overall optical setup can therefore be split into two separate components. Firstly, the standard halogen-lamp-sourced microscope imaging setup, and secondly, the confocal DF nano-spectroscopy arrangement utilising supercontinuum laser illumination. The imaging setup was primarily used for nanosystem location and NP dimer (tip-to-tip) microscopic alignment, while the nano-spectroscopy setup

was tailored specifically for dynamic (integration times $\tau_{int} \leq 3$ ms) characterisation of plasmonic nanosystems with small optical interaction cross-sections.

3.4.1 Microscope Unit Imaging Optics

The custom built horizontal microscope unit described in Sec. (3.2.2) was populated with high quality optical components enabling diffraction-limited imaging of all nanosystems investigated. The imaging optics are based on the traditional Köhler illumination optical train, as shown in Fig. (3.10). By placing irises at the appropriate positions within the optical train the range of incident angles (effective NA) illuminating the nanosystem and the area of illumination on the sample (focal) plane can be controlled under BF operation.

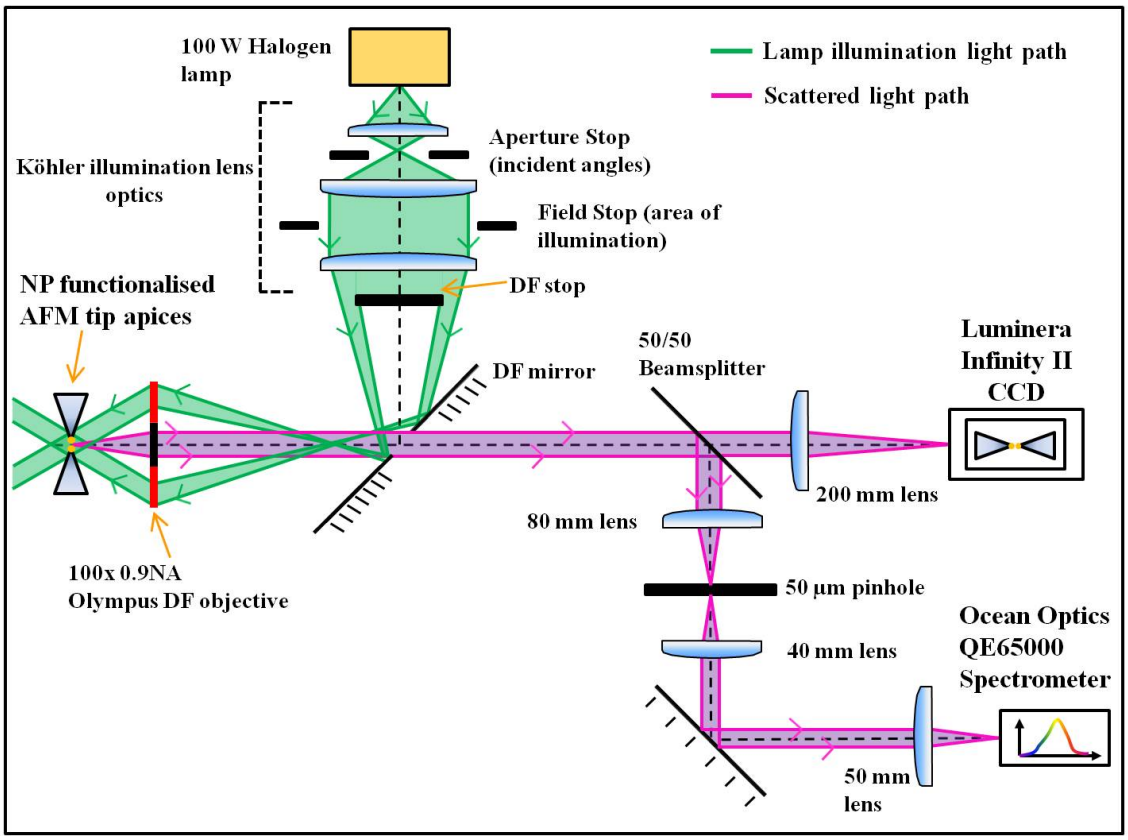

Figure 3.10: Schematic of the halogen lamp imaging optics incorporated into the custom built microscope unit. All optics shown are broadband coated ($\lambda_0 =$ 300 nm-1100 nm) and achromatic over the visible spectrum. The red sections of the objective represent reflective rather than refractive optics.

As all nanosystems investigated in this work are relatively strong scatterers, as described in Sec. (2.3.2), DF microscopy provides a huge increase in contrast over traditional BF methods. Because elastic scattering involves a non-specular change in the propagation direction of the exciting light, the specularly reflected background signal can be removed by implementing a suitable illumination and collection geometry. The technique suppresses the illuminating light using a complementary circular light stop and aperture placed at appropriate positions within the light-path to form a spatial filter, as shown in Fig. (3.10). Light is directed onto the nanosystems only at high-angle by the reflective optics contained within the outer ring of the DF objective. When the nanosystems are situated on a flat, smooth substrate all the specularly reflected light is blocked by the DF mirror and therefore only the light that has been scattered by the nanosystem is measured. This DF optical setup results in isolated nanosystems appearing as a diffraction-limited bright spots on a dark background. By using DF imaging the nanosystems on each AFM tip apex were visually aligned with a high degree of accuracy and repeatability, as the background signal from the specularly reflective AFM tip body is highly suppressed. General samples of nanosystems could also be investigated, as shown in Fig. (3.11). Here Au NPs of different shape with maximal dimension of approximately 100 nm were deposited onto a glass substrate resulting in excellent background suppression and high contrast DF imaging.

Figure 3.11: Dark-field image of Au NPs deposited on a glass substrate. The NPs are of different shapes and maximal dimension of approximately 100 nm. Obtained using the optical setup shown in Fig. (3.10).

All characteristic dimensions of the microscope unit and optics, e.g. lens tube length and tube lens diameter, were designed to avoid the loss of peripheral rays and thus maintain good imaging quality. The scattered light was split equally between the CCD and spectrometer by a broadband coated, wedged BeamSplitter (BS). A 50 μm diameter collection pinhole was used as a spatial filter so only scattered light from the micro-volume of interest is focussed onto the entrance slit of the spectrometer. The micro-volume itself is defined by the objective, pinhole and optical train and can be approximately represented by a cylinder centered on the sample plane with cap area A_C, defined by a radius $R_C = 500$ nm, and length $L_C = 800$ nm. The width of the spectrometer entrance slit (50 μm) and focal length of the relevant focussing optic were chosen to optimise light collection rather than spectral resolution as even higher-order LSPP resonances are generally spectrally broad with wavelength linewidths $\Delta\lambda_{lspp} > 30$ nm. No fibre optic cables were used throughout the setup to avoid additional coupling loss, and interference fringing effects polluting the optical signal.

3.4.2 Supercontinuum Laser Dark-field Spectroscopy Optics

A 100 W halogen lamp can not provide the necessary intensity or confocality required for low-background dynamic dark-field spectroscopy, and hence a broadband laser source is essential. Here a Fianium supercontinuum (450 nm - 1750 nm) laser was incorporated into the microscope unit whilst still allowing for traditional halogen lamp imaging, as shown in Fig. (3.12). The supercontinuum laser light is produced by propagating pulses ($\tau_P \approx 6$ ps, centered at 1064 nm) created by a mode-locked Nd:YAG seed laser through a highly non-linear, single-mode Photonic Crystal Fibre (PCF or holey PCF). The pulse is temporally and spectrally broadened substantially via a cascade of nonlinear processes including self-phase modulation, Raman scattering and four-wave mixing, thus creating the broadband spectrum required for spectroscopy over the entire visible regime [116].

Upon exit from the PCF the unpolarised laser pulse has broadened in time to $\tau_P \approx 700$ ps, has an average spectral power density greater than 2 mW nm^{-1} and an approximately top-hat spectral profile with < 6 dB spectral flatness. A specially designed broadband optic mounted on the end of the PCF is used to collimate the beam ($\phi \sim \mathcal{O}(3$ mm)) over the majority of the output spectrum.

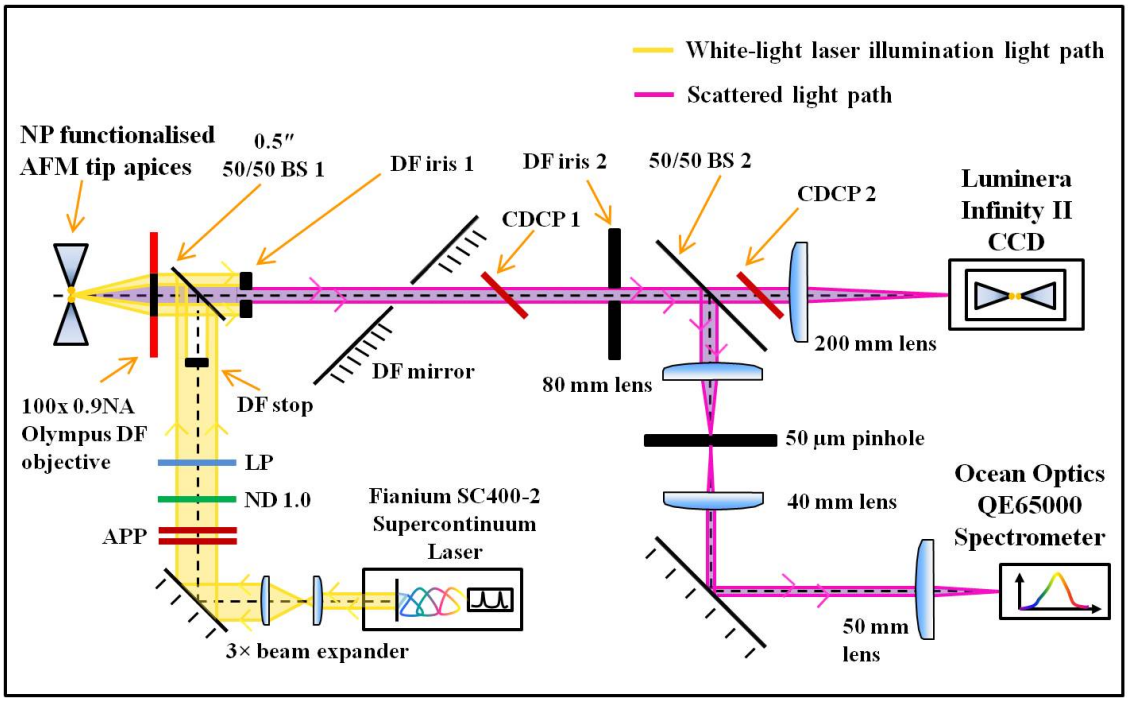

Figure 3.12: Schematic of the supercontinuum laser illumination optics incorporated into the custom built microscope unit. All optics shown are broadband coated (λ_0 = 300 nm-1100 nm) and achromatic over the visible spectrum. The red sections of the objective represent reflective rather than refractive optics. All acronyms are defined in main text.

Thus a highly collimated supercontinuum laser beam with an approximately Gaussian intensity distribution is produced at the Fianium laser output. Due to the effective point-source created by the fibre aperture the resulting collimated 'white-light' laser beam has a high degree of spatial coherence. In contrast, the degree of temporal coherence is low, as the spectral bandwidth is large, and the correlations between the electric fields corresponding to different pulses are weak due to pulse-to-pulse variations in the spectral broadening mechanisms.

The laser beam was aligned onto the optical axis defined by the refracting core (**black**) of the DF objective. To keep additional aberrations, e.g. chromatic and spherical, to a minimum, all elements in the laser light path with optical or diffractive power are precisely aligned in a co-axial manner with the optical axis[3] ($\pm$0.2 mm displacement, $\pm 0.3'$ angular deviation). The laser beam is first expanded (D_L = 10 mm) to completely fill the back aperture of the DF objective

[3]Lateral displacements (1 mm-3 mm) of the laser beam by certain optical components e.g. BS 1 and BS 2 are taken into account.

core ($D_{OC} = 3.24$ mm) and to reduce the power density incident on the optical components to avoid damage. The expansion optics were placed close enough to the objective so the curvature of the laser field (i.e. the laser spot focal position along the optical axis) could be matched to that of the halogen lamp source by a small translation of one of the expansion optics along the optical axis. The collection pinhole is carefully aligned in 3D to be confocal with the focussed laser spot.

The light is further attenuated by a factor of 10 using a reflective Neutral Density (ND 1.0) filter to avoid excessively heating the nanosystem under investigation and prevent damage to the objective coatings. A (Thorlabs LPVIS) nanoparticle Linear film Polariser (LP) was found to introduce considerably less chromatic dispersion than other methods of polarisation (e.g. polarising BS cube and Wollaston prism) and hence was used to linearly polarise the laser light. A custom-built DF stop ($D_S = 2$ mm) with smooth edges was cemented onto a ND 0.1 filter and placed co-axially in the laser beam path to create a symmetric ring of light that enters into the back aperture of the DF objective refractive core, as shown in Fig. (3.13).

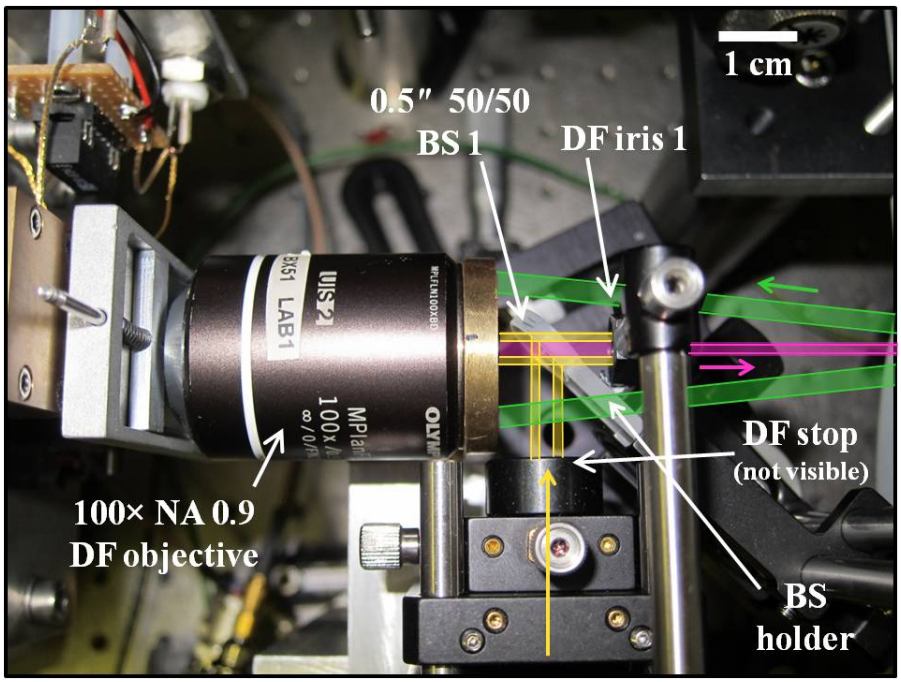

Figure 3.13: Top-down photo of the DF setup for the supercontinuum laser with schematic overlay of halogen lamp (green), laser (yellow) and scattered (purple) light paths.

A custom modified $\phi 0.5''$ BS was cemented in position on a custom-built glass (BK7) holder connected securely to tip-tilt and translation mounts. This transparent BS mount allowed the laser and halogen lamp illumination to be used simultaneously with minimal disruption to the halogen lamp light path.

After all optical elements the total average laser power entering the objective was typically measured to be $P_0 \approx 1$ mW thus yielding an average sample plane intensity $I_0 \sim 10^9$ W m^{-2} and a fluence of $F_{flu} \approx 35$ J m^{-2} per pulse. This relatively large (broadband) intensity can cause considerable sample heating. In the case of an isolated spherical NP the expected maximum initial temperature rise can be found by straightforward energy considerations [117]

$$T = \frac{C_{abs}F_{flu}}{V_{NP}\rho_{Au}c_{Au}} = \frac{C_{abs}F_{flu}}{C_{NP}} \tag{3.1}$$

where $\rho_{Au} = 19.32 \times 10^3$ kg m^{-3} is the mass density of gold, $c_{Au} = 129$ J kg^{-1} K^{-1} is the specific heat capacity of gold and C_{NP} is the heat capacity of the NP. For a gold NP in air with $a = 50$ nm the time required to reach the steady-state regime (approximately 100 ps [118]) is significantly shorter than τ_P and hence Eqn. (3.1) is valid. Appropriately implementing Eqn. (3.1) it is found that $\Delta T \lessapprox 250$ K. This is several hundred degrees less than the NP melting point of $\Delta T \approx 1000$ K [119], and hence minimal sample damage is expected. Furthermore the effective NP on the apex of a NP functionalised gold coated AFM tip is expected to be less susceptible to optical heating as the relatively large AFM tip body acts as an efficient heat-sink. The expected magnitude of optical heating in plasmonically coupled NP dimer systems is described in Chapter (5).

The typical laser illumination and scattered light collection geometries used for investigating a nanosystem are shown in Fig. (3.14a). The maximum collection angle θ_c is defined by the diameter of the DF iris (1) aperture while the range of illumination angles are described by θ_1 and θ_2 and are defined by the diameter of the DF stop and objective NA respectively. The laser light incident on the back aperture of the objective ($\lambda_0 \ll (D_{OC} \wedge D_S)$) is an annular ring with approximately planar wavefronts and a homogeneous intensity distribution due to the beam expansion. Under these conditions an application of scalar diffraction theory can be used to calculate the 'obscured' Airy intensity distribution at the focal (sample) plane of the diffraction-limited system [62].

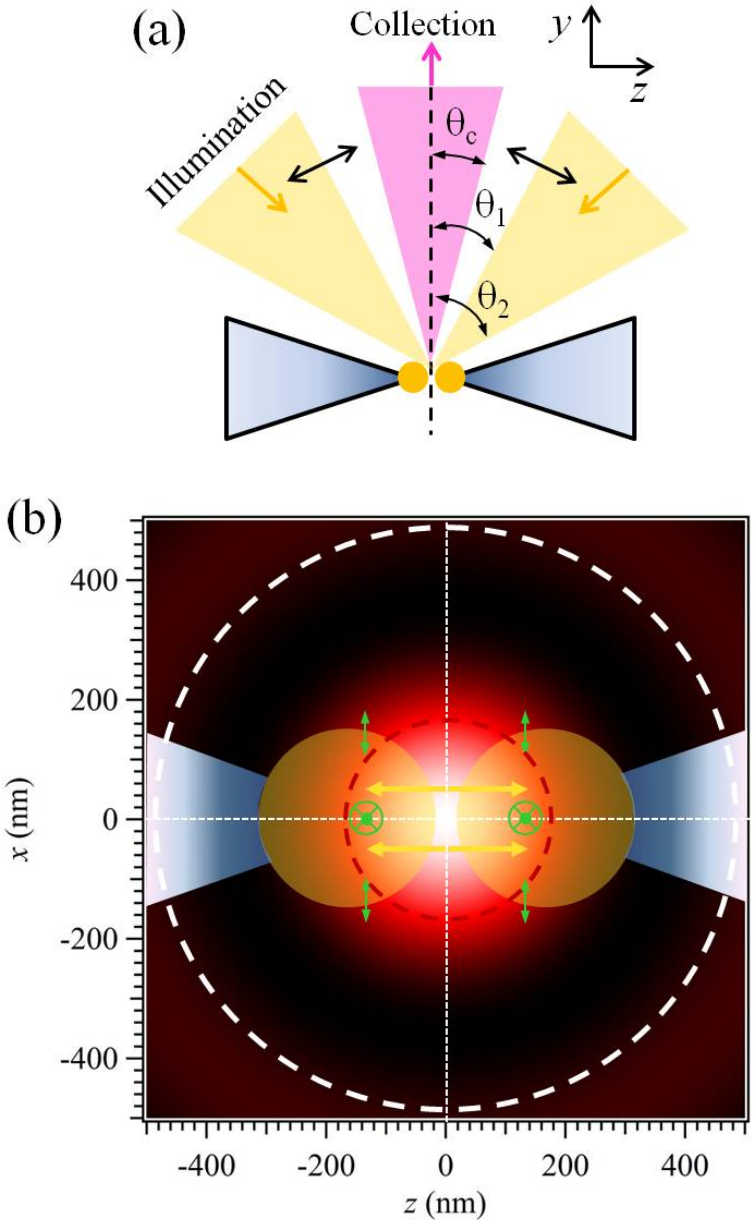

Figure 3.14: Typical laser illumination and scattered light collection geometries, including intensity profile of focussed laser spot. (a) Incident laser illumination angles $\theta_1 = 34°$ and $\theta_2 = 64°$. The maximum collection angle $\theta_c = 20°$. **Black** arrows indicate polarisation of incident light. (b) Top-down view of obscured Airy intensity distribution for $\lambda_0 = 700$ nm with scaled simplified overlay of AFM tips with NP functionalised apices (white for maximum intensity). Schematic of polarisation distribution shown in **yellow** (strong associated intensity) and **green** (weak associated intensity). White dashed ring demarcates collection area A_C defined by objective, pinhole and optical train. **Dark-red** dashed ring demarcates the laser illumination area A_L defined by the FWHM of the fundamental Airy peak.

An intensity plot with a scaled simplified overlay of the AFM tips with NP functionalised apices is shown in Fig. (3.14b) for $\lambda_0 = 700$ nm. The collection micro-volume is set to be confocal with the laser illumination and the collection area circumference is shown by the white dashed line. In this case the incident light is set to have linear polarisation parallel to the AFM tip axes. In practice, due to the high objective NA, a more rigorous vectorial diffraction treatment (c.f. Mie solutions) shows the laser focal spot will have a polarisation distribution coarsely shown by the overlaid **orange** and **green** arrows [120]. However, as the dominant polarisation over the majority of the fundamental disk of the Airy distribution is unchanged compared to the original incident polarisation, the desired optical geometry is achieved with no further modification. Additionally, it should be noted that in reality the focal spot is slightly elongated ($\approx 10\%$) along the direction of the original incident linear polarisation (not shown by the scalar diffraction theory used in Fig. (3.14b)).

Chromatic Dispersion Compensation

An Amici Prism Pair (APP), as shown in Fig. (3.12), is used to compensate for the chromatic dispersion introduced by all optical components present in the laser light path before the light enters the objective. By rotating each prism (circular wedge prism, 30′ wedge angle) individually and monitoring the lateral chromatic separation of the output light focal spot on a CCD, the dispersion already present in the laser light is cancelled out by introducing an opposite dispersion of the same magnitude. A typical example of chromatic dispersion compensation is shown in Fig. (3.15).

A low-level of chromatic dispersion is desirable for investigations of nano-systems smaller than the typical illumination area (denoted A_L for $\lambda_0 = 700$ nm) situated on semi-infinite flat substrates. As can be seen from Figs. (3.15a) and (3.15b) translation of a nanosystem from the white-light chromatic overlap central regions will create artificial spectral shifts[4]. The situation is greatly improved in Fig. (3.15c). Here the spectral variation due to chromatic dispersion is negligible for a large range of non-central nanosystem positions under the illumination.

[4] Artificial spectral shifts still result from nanosystem translation even if the lateral chromatic separation is zero because of the wavelength dependence of the focal spot diameter. However this will only be non-negligible at the extremities of the illumination area and hence is neglected.

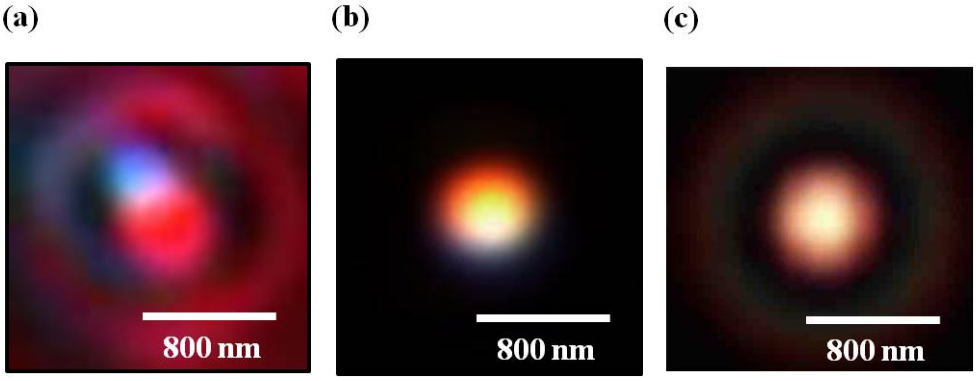

Figure 3.15: Typical example of chromatic dispersion minimisation by high precision optical alignment and Amici prism pair dispersion compensation. Lateral chromatic separation of diffraction-limited supercontinuum laser focal spot on an Au mirror for (a) Coarse optical element alignment (elements with displacement $\gg \pm 0.2$ mm and angular deviation $\gg \pm 0.3'$ from optical axis) and no APP compensation. (b) Optimised optical element alignment and no APP compensation. (c) Optimised optical element alignment and APP compensation.

A minimum of chromatic dispersion is also essential for systematic investigations of complex dynamic nanosystems (smaller than A_L) mounted in *free-space*, approximately at the centroid of the laser illumination, e.g. the NP functionalised apices of the AFM tips. When the measured scattering spectra are normalised against that from a target with an area much greater than A_L, the spectral response of such nanosystems are highly susceptible to experimental artifacts introduced by the lateral chromatic separation of the illumination. In the case depicted in Fig. (3.14b), the area of the overall nanosystem maximal geometric cross-section under the laser illumination is significantly less than A_L and thus a substantial amount of the illumination power propagates away into free-space without interacting with the nanosystem. If the lateral chromatic separation was zero this would cause an approximately spectrally flat reduction in intensity of the measured response. However if the lateral chromatic separation was significant (Fig. 3.15b)) then the reduction in intensity will no longer be spectrally flat. Therefore, purely due to geometrical factors, the lateral chromatic separation produces a significantly different spectral response to that obtained from the normalisation target. This experimental artifact becomes greater with increasing chromatic dispersion and can readily produce anomalous peaks and troughs of $\pm 40\%$ of the normalisation spectrum magni-

tude. The chromatic dispersion compensation techniques, demonstrated by Fig. (3.15c), keep the spectral variation introduced by these experimental artifacts to under $\pm 2\%$.

Finally, additional custom made Chromatic Dispersion Compensation Plates (CDCP's) are introduced as shown in Fig. (3.12) to correct the chromatic dispersion introduced by the wedges of BS 1 and BS 2. The $30'$ BS wedge angle reduces unwanted interference effects and secondary reflections polluting the laser illumination focal spot, however it chromatically disperses the scattered light of interest. Both CDCP 1 and CDCP 2 (circular wedge prisms, $30'$ wedge angle) are appropriately orientated following a similar procedure used for the APP alignment. This ensures the chromatic dispersion of the light is greatly reduced, thus preventing false images and spectra from being recorded.

Minimising the Poisson Spot Background

The high-degree of spatial coherence of the laser illumination has the unwanted side-effect of enabling diffraction around the smooth circular DF stop to become prevalent. The diffracted light substantially diminishes the performance of the dark-field laser setup as demonstrated in Fig. (3.16). In Fig. (3.16a) no laser light is diffracted and hence the smooth glass substrate appears completely dark on the CCD. However, in reality the laser light is strongly diffracted by an angle $-10^{\circ} \leq \theta_D \leq 10^{\circ}$ in the plane defined by the light ray and the optical axis, as shown in Fig. (3.16b). As every point on the circumference on the DF stop can be considered to act as a secondary source of light, all the secondary spherical wavelets constructively interfere on the optical axis thus forming a bright central spot known as a Poisson (or Arago) spot (in the Fresnel regime, approximately 0-2 m after the DF stop) [121]. After a distance of approximately $6D_S$ from the DF stop the Poisson spot has the same intensity as the unperturbed laser light.

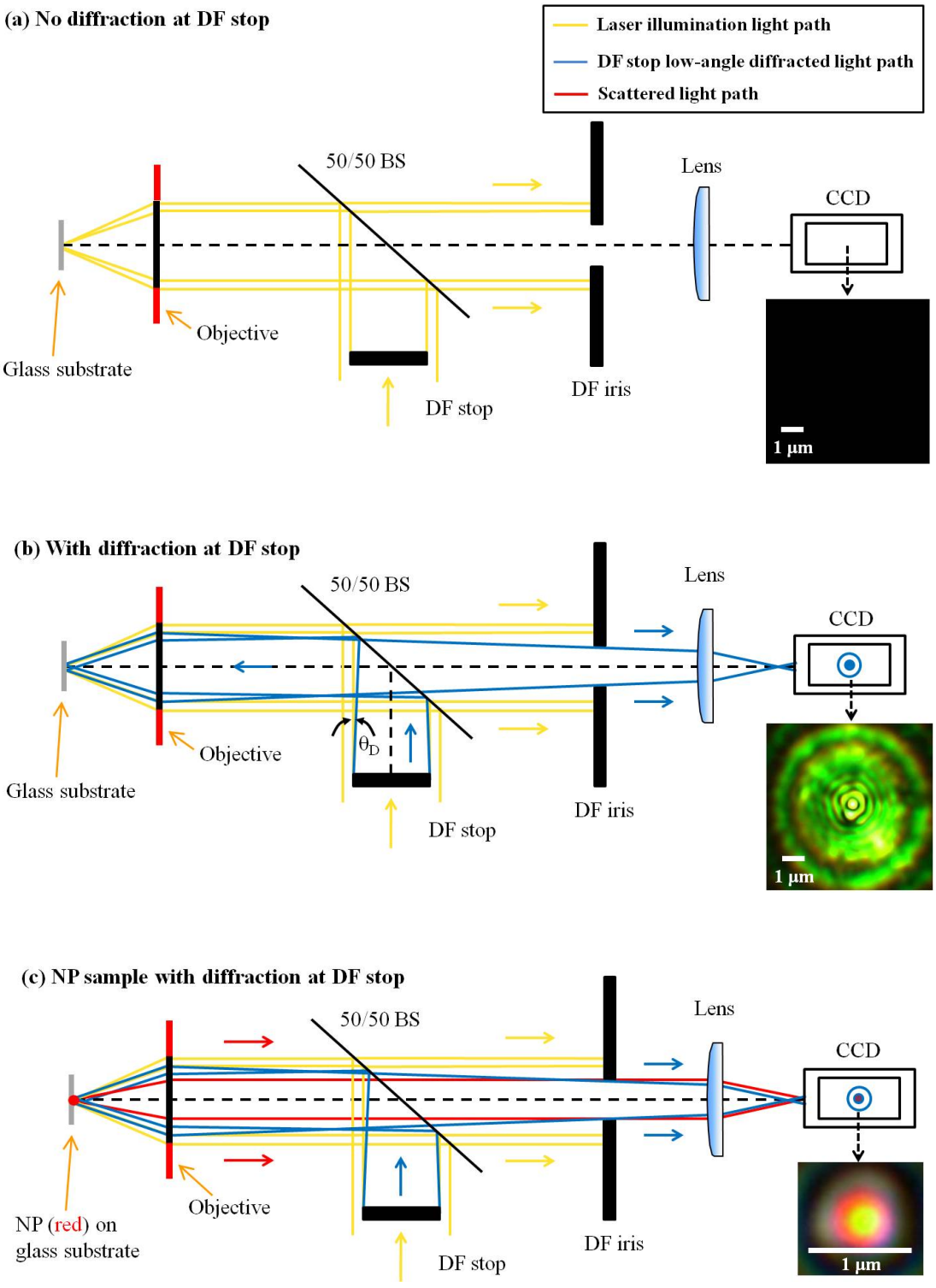

Figure 3.16: Schematic ray diagrams and CCD images showing how laser light diffracted by the DF stop is not filtered out by the normal DF laser setup and hence degrades the DF characterisation capability. (a) No diffraction at DF stop. (b) With diffraction at DF stop. (c) With diffraction at DF stop and NP at the co-axial focal position.

The diffracted light is specularly reflected off the glass substrate and passes through the DF iris. The Poisson spot and subsidiary concentric fringes of illumination formed at the focus of the lens are clearly shown by the CCD image in Fig. (3.16b). The image has been over-exposed to make the subsidiary fringes formed by off-axis constructive interference clearly visible and the supercontinuum laser is not set to full power (full spectral bandwidth) hence the green colour of illumination.

The 'Poisson spot' background can range in power depending on the experimental parameters but is typically over an order of magnitude greater in power than the light scattered by the nanosystem (determined by C_{sca}^{BEMAX}) formed by the dual AFM tips with NP functionalised apices. In the case of a NP with approximately 100 nm maximal dimension the Poisson background swamps the NP scattering signal, as demonstrated in Fig. (3.16c), thus producing poor quality imaging and spectral measurements. For nanosystems situated on homogeneous flat substrates a background subtraction may be appropriate. However, for nanosystems mounted in environments with a complex geometry and composition, e.g. an AFM tip apex NP, performing a suitable background subtraction is often not possible.

Several methods were tested to reduce the Poisson spot background, including high-quality axicon illumination, and using relay optics to form images of the DF stop and DF iris near the objective back focal plane. The optimum solution was found to involve physically moving the DF stop and a DF iris as close as possible to the back aperture of the objective, as shown in Figs. (3.12) and (3.13) and described schematically in Fig. (3.17a). By appropriate placement of DF iris 1 all the parasitic light diffracted at low-angle is now blocked while DF iris 2 blocks all the light diffracted at high-angle. The situation shown in Fig. (3.16a) is thus recovered and high quality supercontinuum laser DF characterisation is enabled, as shown by the CCD image in Fig. (3.17b).

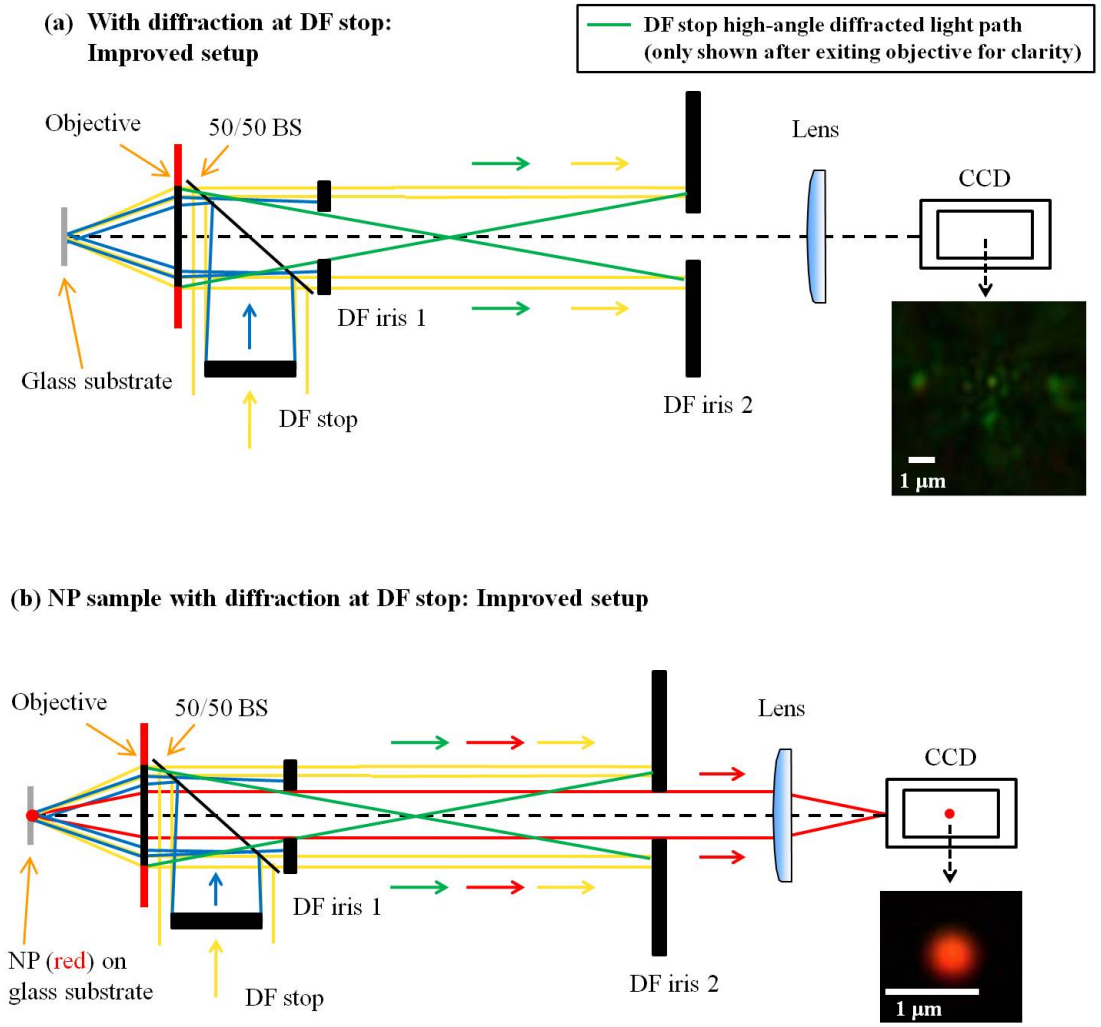

Figure 3.17: Schematic ray diagrams and CCD images showing how laser light diffracted by the DF stop is filtered out by the improved DF laser setup enabling high-quality DF characterisation capabilities. (a) Improved dark-field configuration blocks the majority of the diffracted light. (b) Improved dark-field configuration allows high-quality DF characterisation of all nanosystems. Note the same colour code as that in Fig. (3.16) is used.

Supercontinuum Laser Setup Validation

To ensure the confocal supercontinuum laser DF nano-spectroscopy system was working correctly, Au NPs nominally with $a = 50$ nm were drop-cast onto a plasma cleaned microscope slide and were imaged and spectrally characterised using the laser illumination. The images and scattering spectra obtained for three different NP shapes are shown in Fig. (3.18). The vast majority of the NPs

were almost identical to NP 1, as expected for nominally spherical NPs (BBI International). The spectra and images were taken with $\tau_{int} = 3$ ms and $\tau_{int} = 0.2$ ms respectively. This compares extremely favourably with the integration times of $\tau_{int} > 1$ s and $\tau_{int} \approx 300$ ms (with $\times 10$ gain) for the spectra and image acquisition respectively, required for the halogen lamp illumination.

To compare with analytical theory the presence of a glass substrate can be taken into account in the Mie solutions by using an effective refractive index of the dielectric medium $n_d^e = \upsilon n_d + (1 - \upsilon) n_{glass}$ where $n_{glass} = 1.51$ is the refractive index of the glass substrate and $\upsilon = 0.58$ is an appropriate weighting factor found from [122]. Under this approximation the agreement of the scattering response of NP 1 and that found from the Mie solution is excellent above $\lambda_0 = 500$ nm for a NP with $a = 49$ nm. The discrepancy at short wavelength is commonly found in the literature [123], and in this case can be mainly attributed to the specific dielectric function of Au used, the experimentally defined DF illumination and collection geometries and the remaining influence of the glass substrate not taken into account by the simple model used here.

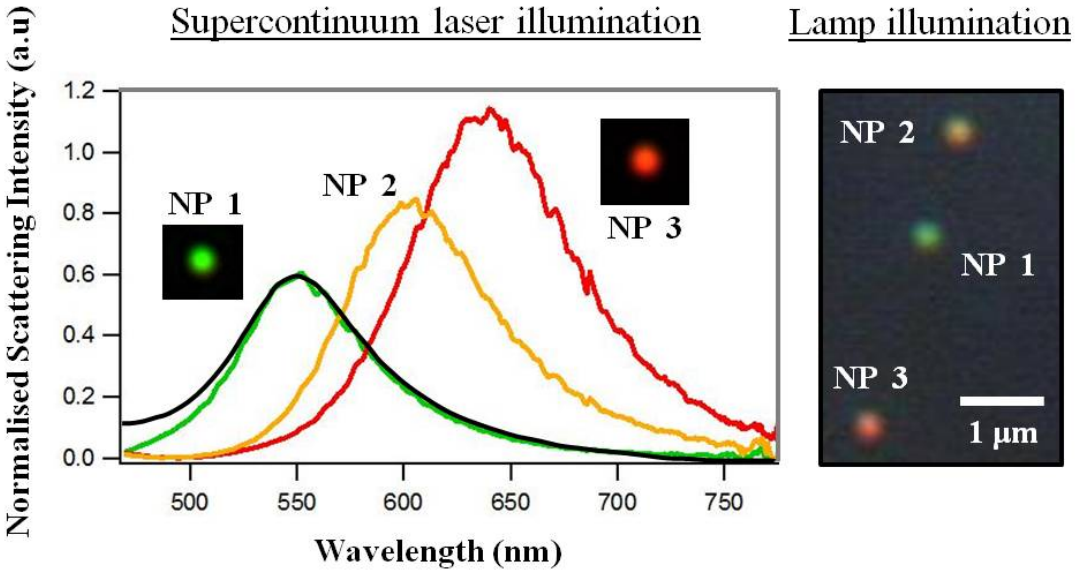

Figure 3.18: Scattering spectra of Au NPs deposited on a glass substrate, with insets showing corresponding NP images. Both spectra and images were taken under supercontinuum laser illumination. RHS image shows corresponding halogen lamp image of NPs. **Black** curve is the theoretical scattering response of a 98 nm Au NP calculated from the Mie solutions.

3.5 Summary

A purpose-built experimental rig, described in Sec. (3.2), was constructed to mechanically enable the creation of a relatively large ($a \approx 150$ nm) NP dimer system with dynamically controllable separation from $d \approx 500$ nm down to full conductive contact ($G_{DC} \geq G_0$). An electronic measurement system, described in Sec. (3.3), was developed and implemented to facilitate the required NP dimer alignment by characterisation of the harmonic current flow across the capacitor formed by the dual, AFM cantilever-tip, composite system. Facility for dimer separation calibration and conductance measurements is provided by the DC conductance measurement electronics. Finally, the optical setup, described in Sec. (3.4), enabled simultaneous DF imaging and optical scattering characterisation, using standard halogen lamp illumination and a supercontinuum laser source respectively. Methods were developed to compensate chromatic dispersion and reduce contamination by diffracted light. The experimental apparatus enables electronic, and far-field optical, characterisation of the LSPP response of NP dimers with sub-nanometre separation.

Chapter 4

Dynamic Positioning of Two Nanosystems

4.1 Introduction

Before the LSPP response of a NP dimer in the quantum regime can be electronically and optically investigated the NP dimer nano-system first needs to be aligned and brought towards sub-nanometre separation in a controlled dynamic manner. The mechanical and electronic setups described in Secs. (3.2) and (3.3) enable a compact approach for creating an *optically accessible* NP dimer with *dynamically* controllable separation from $d_0 \approx 400$ nm to full conductive contact, without the need for top-down processing or the limited optical access of a commercial AFM or STM. As introduced in Chapter (3), the technique is based on the 3D nanoscale alignment of two conducting NP functionalised AFM probes in a 'tip-to-tip' configuration. To achieve a large dynamic range of alignment a novel Electrostatic Force Microscopy (EFM) technique was developed that utilises an alternating potential applied across the conducting AFM tips to create an oscillating *long-range* electrostatic force. By exploiting the nonlinear electrical parametric response of the electromechanically coupled AFM tip system, the NP dimer formed by the two AFM tip apices is aligned with nanometre-scale precision. This chapter describes the theoretical foundations of the technique developed and its experimental verification.

4.2 Theoretical Modelling

The oscillating electromechnically coupled dual cantilever-tip-NP system is shown in Fig. (4.1). First the governing equations of motion for the system are presented. These are then solved under a toy model (strong approximations) to crucially show how parametric mixing creates background-free harmonic signals that are directly related to the magnitude and phase of a tips oscillation. Such harmonic signals hence allow axial tip-tip (NP dimer) alignment to be performed. Following from this, a more rigorous numerically implemented model developed is described in detail. In this model the inter-tip forces and system capacitance is determined to good accuracy, thus allowing effective comparison with experiment.

The coordinate system used for modelling is shown in Fig. (4.1a). The frequency range of interest is around the fundamental flexural mode of the cantilevers and therefore the tip system is modelled as a pair of coupled point-mass harmonic oscillators. The tips are coupled through the superposition of the z-components of the driving electrostatic attractive force F^z_{EL}, and the combined short-range (< 2 nm) Van der Waals and repulsive tip-tip interaction forces F^z_{TT}.

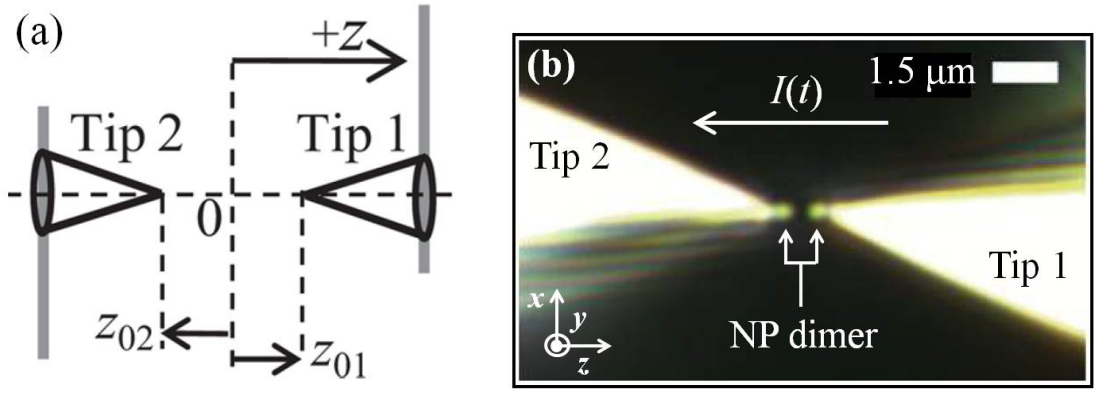

Figure 4.1: Coordinate system used in theoretical analysis of electromechanically coupled dual AFM tip system. (a) Coordinate system used in the analysis. (b) Over-exposed DF image of 50 nm Au coated AFM tips with NP functionalised apices via EBD.

The coupled equations of motion for tips $i = (1,2)$ with apex positions z_i and apex separation $d(t) = z_1(t) - z_2(t)$ are

$$m_i \frac{d^2 z_i}{dt^2} + \beta_i^z \frac{dz_i}{dt} + k_i^z \left(z_i - z_{0i}\right) = \pm \left(F_{EL}^z + F_{TT}^z\right) \tag{4.1}$$

where m_i is the effective mass of the cantilever-tip system, $\beta_i^z = \beta_{0i}^z + \beta_{TT}^z$ is the z-component of the non-linear damping coefficient, $k_i^z = k_{0i}^z + k_{TT}^z$ is the z-component of the cantilever spring constant and z_{0i} is the tip apex position when $F_{EL}^z = F_{TT}^z = 0$. The sign of the RHS force term is positive for tip 1 and negative for tip 2. Tip parameters $m_i = k_{0i}^z/\omega_{0i}^2$ and $\beta_{0i}^z = k_{0i}^z/(\omega_{0i} Q_{0i})$ are derived from the fundamental cantilever spring constant[1] k_{0i}^z and experimentally measured values of the appropriate cantilever resonance frequencies ω_{0i} and Q-factors Q_{0i}. The β_{TT}^z and k_{TT}^z terms are the air 'squeeze' viscous and elastic damping contributions respectively. The fixed parameters of a typical AFM tip are found to be

$$\omega_{0i} = 2\pi(13) \text{ k rad s}^{-1} \tag{4.2a}$$

$$Q_{0i} = 90 \tag{4.2b}$$

$$k_{0i}^z = 0.2 \text{ Nm}^{-1} \tag{4.2c}$$

$$\beta_{0i}^z = 2.7 \times 10^{-8} \text{ kg s}^{-1} \tag{4.2d}$$

$$m_i = 3 \times 10^{-11} \text{ kg} \tag{4.2e}$$

4.2.1 Parametric Mixing: Toy Model

To understand the main principles of the NP dimer alignment technique a basic toy model was developed to elucidate the underlying physical processes. To allow a simple analytical analysis the AFM tip system is approximated as a parallel plate capacitor with no fringe fields. Also, d is assumed to always be in the long-range regime where $F_{TT}^z = \beta_{TT}^z = k_{TT}^z = 0$. In this axially symmetric system the attractive force (at a defined potential V) due to the capacitance is given by

[1] It should be noted the value used for the fundamental cantilever spring constant is calculated theoretically from simple beam theory and hence can be $\leq 5\times$ different from the true value [124].

$$F_{EL}^{z}(V,d) = \frac{\partial U}{\partial d} = \frac{1}{2}\frac{\partial C}{\partial d}V^2(t) = \frac{-\varepsilon_0 A_{ov} V^2(t)}{2d^2} \tag{4.3}$$

where A_{ov} is the area of cantilever overlap and U is the electrostatic potential energy stored in the capacitor. By applying

$$V(t) = V_0 \cos(\omega_S t) \tag{4.4}$$

at a signal frequency $\omega_S \approx \omega_{01}/2$, Eqn. (4.3) shows that F_{EL}^{z} and hence $C(t)$ will primarily oscillate resonantly at $\omega_P = 2\omega_S \approx \omega_{01}$ where ω_P is the pump frequency. Driving at $\omega_{01}/2$ allows only the direct ω_{01} resonance of the tip system to be efficiently excited rather than the mechanical parametric resonance at $2\omega_{01}$. This is critical to avoid driving the tip system response into a parametric instability domain [125]. Assuming $z_{02} = 0$ and tip 2 is stationary, the tip apex separation at zero applied force $d_0 = z_{01} - z_{02} = z_{01}$ and Eqns. (4.1) reduce to a single equation of motion

$$m_1 \frac{d^2 z_1}{dt^2} + \beta_{01}^{z} \frac{dz_1}{dt} + k_{01}^{z}\,(z_1 - d_0) = F_{EL}^{z}(z_1, t) \tag{4.5}$$

Substituting Eqn. (4.3) into Eqn. (4.5) and driving yields

$$m_1 \frac{d^2 z_1}{dt^2} + \beta_{01}^{z} \frac{dz_1}{dt} + k_{01}^{z}\,(z_1 - d_0) = \left(\frac{-\varepsilon_0 A_{ov} V_0^2}{4(d_0 + \Lambda)^2}\right)(1 + \cos(\omega_P t)) \tag{4.6}$$

where $\Lambda = z_1 - d_0$ describes the oscillation of tip 1. Assuming $|\Lambda| \ll d_0$ Eqn. (4.6) can be taken to 1$^{\text{st}}$ order, and to good approximation

$$m_1 \frac{d^2 z_1}{dt^2} + \beta_{01}^{z} \frac{dz_1}{dt} + k_{e1}^{z}\,(z_1 - d_0) \simeq \left(\frac{-\varepsilon_0 A_{ov} V_0^2}{4d_0^2}\right)(1 + \cos(\omega_P t)) \tag{4.7}$$

where k_{e1}^{z} is the z-component of the effective spring constant of tip 1 given by

$$k_{e1}^{z} = k_{01}^{z} - \left(\frac{\varepsilon_0 A_{ov} V_0^2}{2d_0^3}\right)(1 + \cos(\omega_P t)) \tag{4.8}$$

The simplified Eqn. (4.7) can be recast into an ODE that has the same homogeneous form as the Mathieu equation [126]. However, as the mechanical spring constant parameter k_{e1}^{z} oscillates at $\omega_P \approx \omega_{01}$ rather than at $2\omega_{01}$, the oscillation of k_{e1}^{z} does not drive the system into a parametric resonance and thus does not affect the overall system behaviour significantly. Therefore only the time-averaged response of k_{e1}^{z}, i.e. $k_{e1}^{z\prime} = k_{01}^{z} - \varepsilon_0 A_{ov} V_0^2 / 2d_0^3$ is considered. The principle of superposition can now be used to solve the linear differential Eqn. (4.7) thus yielding the steady-state solution for z_1

$$z_1(t) \approx d_0 - \left|z_1^{off}\right| - z_{m1}\cos(\omega_P t + \varphi_1) \tag{4.9}$$

where $\left|z_1^{off}\right|$, z_{m1} and φ_1 are given by

$$\left|z_1^{off}\right| \approx \frac{\varepsilon_0 A_{ov} V_0^2}{4d_0^2 k_{e1}^{z\prime}} \tag{4.10}$$

$$z_{m1} \approx \frac{\varepsilon_0 A_{ov} V_0^2}{4d_0^2\left(\left(k_{e1}^{z\prime} - m_1\omega_P^2\right)^2 + \left(\beta_{01}^{z}\omega_P\right)^2\right)^{1/2}} \tag{4.11}$$

$$\varphi_1 \approx \left(\tan^{-1}\left(\frac{k_{e1}^{z\prime} - m_1\omega_P^2}{\beta_{01}^{z}\omega_P}\right)\right) - \frac{\pi}{2} \tag{4.12}$$

Here $\left|z_1^{off}\right|$ is the magnitude of the additional offset in tip 1 position created because $F_{EL}^{z} \propto V^2$, z_{m1} is the amplitude of tip 1 oscillation and φ_1 is the phase of tip 1 oscillation with respect to the driving potential. The capacitance of the system can hence be obtained as

$$C(t) \approx \frac{\varepsilon_0 A_{ov}}{z_1} + C_{bk} = \frac{\varepsilon_0 A_{ov}}{d_0 - \left|z_1^{off}\right| - z_{m1}\cos(\omega_P t + \varphi_1)} + C_{bk} \tag{4.13}$$

where C_{bk} is the constant background capacitance contribution from the opposing composite control rod, chip clip, AFM chip system. As $\left|z_1^{off}\right|, z_{m1} \ll d_0$ Eqn. (4.13) can be taken to 1st order to good approximation

$$C(t) \approx C_0 \left(1 + \frac{\left|z_1^{off}\right|}{d_0} + \frac{z_{m1}}{d_0}\cos(\omega_P t + \varphi_1)\right) + C_{bk} \tag{4.14}$$

where $C_0 = \varepsilon_0 A_{ov}/d_0$. The 1st order current flow across the oscillating capacitance (mechanical varactor) can now determined[2] by

$$I(t) = \frac{dQ}{dt} = \frac{d(CV)}{dt} = C\frac{dV}{dt} + V\frac{dC}{dt} \tag{4.15}$$

Substituting Eqns. (4.4) and (4.14) into Eqn. (4.15) yields

$$\begin{aligned} I_{AC} = I(t) \approx & -C_0 V_0 \omega_S \left(1 + \frac{\left|z_1^{off}\right|}{d_0} + \frac{C_{bk}}{C_0}\right)\sin(\omega_S t) \\ & - \frac{C_0 V_0 z_{m1}}{2d_0}(\omega_P - \omega_S)\sin((\omega_P - \omega_S)t + \varphi_1) \\ & - \frac{C_0 V_0 z_{m1}}{2d_0}(\omega_P + \omega_S)\sin((\omega_P + \omega_S)t + \varphi_1) \end{aligned} \tag{4.16}$$

Here the difference and sum frequencies are $(\omega_P - \omega_S) = \omega_S$ and $(\omega_P + \omega_S) = 3\omega_S$ respectively. The non-zero complex Fourier coefficients $\widetilde{c}_1$ and $\widetilde{c}_3$ of the current flow, and hence $\widetilde{I}^{\omega_S}$ and $\widetilde{I}^{3\omega_S}$ at ω_S and $3\omega_S$ respectively, are extracted by

$$\widetilde{c}_1 = \frac{\widetilde{I}^{\omega_S}}{2} = \frac{1}{T^{\omega_S}}\int_{\frac{-T^{\omega_S}}{2}}^{\frac{T^{\omega_S}}{2}} I(t)e^{-i\omega_S t}\,dt \tag{4.17a}$$

$$\widetilde{c}_3 = \frac{\widetilde{I}^{3\omega_S}}{2} = \frac{1}{T^{3\omega_S}}\int_{\frac{-T^{3\omega_S}}{2}}^{\frac{T^{3\omega_S}}{2}} I(t)e^{-i3\omega_S t}\,dt \tag{4.17b}$$

[2]The capacitance is treated as a time-dependent linear function of V therefore $Q(t) = C(t)V(t)$, rather than a non-linear function of V, i.e. $Q = \int_0^V C(V)\,dV$. For more detail the interested reader is referred to [127].

where $T^{\omega_S} = 2\pi/\omega_S$ and $T^{3\omega_S} = 2\pi/3\omega_S$. Substituting Eqn. (4.16) into Eqns. (4.17) yields

$$\widetilde{I}^{\omega_S} \approx C_0 V_0 \omega_S \left(1 + \frac{\left| z_1^{off} \right|}{d_0} + \frac{z_{m1}}{2d_0} e^{i\varphi_1} + \frac{C_{bk}}{C_0} \right) e^{i\frac{\pi}{2}} \tag{4.18a}$$

$$\widetilde{I}^{3\omega_S} \approx \frac{3C_0 V_0 \omega_S z_{m1}}{2d_0} e^{i\left(\varphi_1 + \frac{\pi}{2}\right)} \tag{4.18b}$$

The oscillating AFM tip capacitance at ω_P produces electric parametric mixing. This results in power transfer from the fundamental to sum and difference frequency components that are dependent on z_{m1}. The current component at $(\omega_P - \omega_S) = \omega_S$ creates the third term on the RHS of Eqn. (4.18a). The constant $\pi/2$ phase factor in both Eqns. (4.18) is due to the current leading the voltage by 90° after traversing the tip-tip capacitor. Critically, the current component at $(\omega_P + \omega_S) = 3\omega_S$ (Eqn. (4.18b)) provides a background-free signal directly related to the magnitude and phase of the tip oscillation. Now if tip 2 is scanned in the x or y directions, i.e. moved off-axis, F_{EL}^z decreases (z_{m1} decreases) along with C (C_0 decreases) [128]. This therefore allows the AFM tips (NP dimer) to be precisely aligned in 3D by tracking the current magnitude at $3\omega_S$ using lock-in detection.

4.2.2 Numerically Implemented Alignment Simulation

For effective comparison with experiment the coupled non-linear 2nd order ODEs (4.1) are solved numerically in IGOR Pro using a standard fifth-order Runge-Kutta algorithm [129]. The majority of the expressions for the parameters are obtained from analytical theory, and substituted into Eqns. (4.1), thus allowing accurate simulation of the electromechanically coupled AFM tip system.

The position dependent damping and spring constant terms β_{TT}^z and k_{TT}^z were modelled by the air squeeze damping between two parallel plates of area chosen by experimental fit. Here the viscous and elastic damping contributions are determined by solving the Reynolds equation for a compressible gas. The

viscous component β^z_{TT} is created by air being squeezed out of (or pushed into) the space between the AFM tips and is modelled by [130]

$$\beta^z_{TT} \approx \frac{3\mu_a A_F l^2}{4d^3} \tag{4.19}$$

where $\mu_a = 18.4 \times 10^{-6}$ Pa.s is the coefficient of viscosity of air, A_F is the parallel plate area determined by an experimental fit and l is the side length of the parallel plate. The elastic component k^z_{TT} results from the compression of the air between the AFM tips and is modelled by [130]

$$k^z_{TT} \approx \frac{4P_a A_F \sigma_s^2}{15d} \tag{4.20}$$

where $P_a = 100 \times 10^3$ Pa is the ambient air pressure and $\sigma_s \approx 10$ is the squeeze number.

Exact analytical evaluation of F^z_{EL} and the total capacitance (C) for the AFM tip system is not possible due to the complex geometry. However, using the approximations implemented in [131] for an axially symmetric AFM tip, expressions for F^z_{EL} and C are obtained. Here the AFM tips are each separated into three parts; a cantilever, a conical body and a parabolic apex, as depicted in Fig. (4.2). The cantilevers are treated as infinite parallel-plates in order to calculate the capacitance per unit area, and hence the appropriate cantilever contributions to F^z_{EL} and C are included. Both the cone and apex components are decomposed into infinitesimal area elements ($d\mathbf{A}$) that each contribute in the same manner as an infinite dihedral capacitor with identical relative orientation. As both AFM tips are good conductors the field lines are perpendicular to the surface at every point and are well approximated by circular arcs over which the electric potential decays linearly. Therefore the magnitude of the electrostatic field at tip 2 is approximately given by

$$E(x, y, z) \approx \frac{V}{l_{arc}(x, y, z)} \tag{4.21}$$

where l_{arc} is the length of the circular arc connecting two identical points on tip 1 and tip 2 as shown in Fig. (4.2).

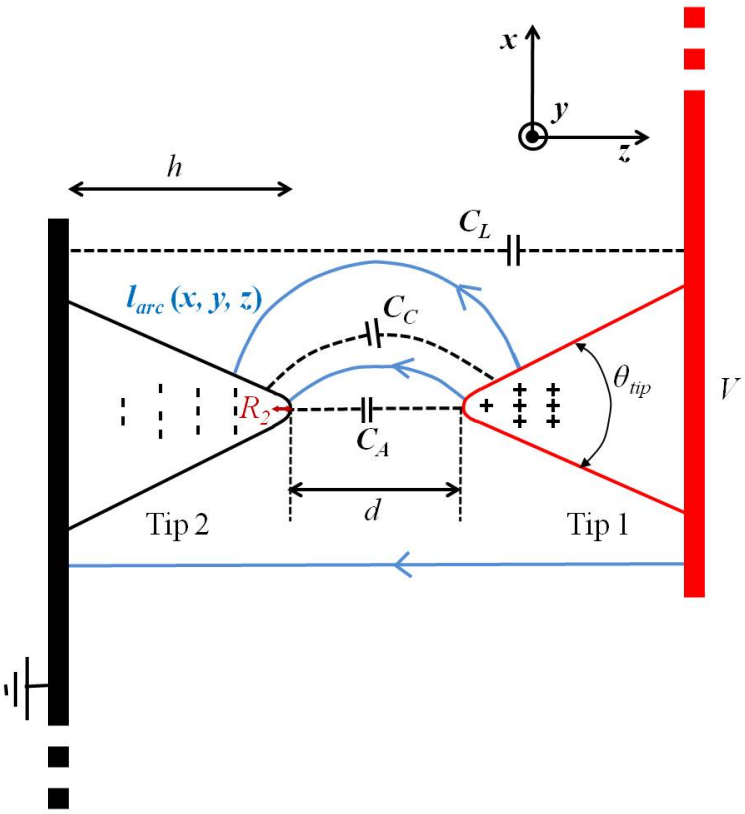

Figure 4.2: Schematic of axially symmetric tip-tip model used for theoretical modelling. Examples of approximate electric field lines l_{arc} are shown in blue. Inter-apex distance d is exaggerated for clarity.

Using Eqn. (4.21) expressions for F_{EL}^z and C are found via [67]

$$\begin{aligned} F_{EL}^z(V,d) &= \frac{\varepsilon_0}{2}\iint_A E^2 d\mathbf{A}\cdot\hat{\mathbf{z}} \\ &\approx \frac{\varepsilon_0 V^2}{2}\iint_A \frac{1}{l_{arc}^2(x,y,z)}\, d\mathbf{A}\cdot\hat{\mathbf{z}} \end{aligned} \tag{4.22}$$

$$C = Q/V \approx \varepsilon_0 \iint_A \frac{1}{l_{arc}(x,y,z)}\,|d\mathbf{A}| \tag{4.23}$$

where $\hat{\mathbf{z}}$ is a unit vector in the z-direction.

This method is found to yield good agreement (less than 5% error) with the exact analytical solution for a simple two sphere system. As l_{arc} is much greater than the dimension of each infintesimal surface element, one could expect treat-

ing each element as a infinite dihedral capacitor of separation l_{arc} to be a poor approximation, as the fringing fields will strongly influence the system. However, as only the global system quantities F^z_{EL} and C are required, it is found that the vast majority of fringing fields cancel out and hence the approximation does not introduce significant errors. The expressions derived are hence only valid if d is not larger than the characteristic physical dimension of the associated AFM tip component, unless additional corrections are implemented. These expressions are functions of cone height ($h_1 = h_2 = h$), apex radius ($R_1 = R_2 = R$), full cone-angle ($\theta_{tip\,1} = \theta_{tip\,2} = \theta_{tip}$) and A_{ov}. The full expressions derived for F^z_{EL} using Eqn. (4.22) are shown below

$$F^z_{EL}(V,d) = F^z_L + F^z_C + F^z_A \tag{4.24}$$

where F^z_L, F^z_C and F^z_A are the contributions of the z-component of force from the AFM cantilevers, AFM tip cones and AFM tip apices respectively. The individual contributions are given by

$$F^z_L \approx -\frac{\varepsilon_0 A_{ov} V^2}{2(2h+d)^2} \tag{4.25a}$$

$$\begin{aligned} F^z_C \approx &-\left(\frac{\varepsilon_0 V^2}{\pi}\right)\sin(\theta_{tip}/2)\times \\ &\left(\ln\left(\frac{d-\delta+2h}{d+\delta}\right) - \sin\left(\theta_{tip}/2\right)\frac{2\left(h-\delta\right)}{d-\delta+2h}\left(\frac{d-\delta}{d+\delta}\right)\right) \end{aligned} \tag{4.25b}$$

$$\begin{aligned} F^z_A \approx &\frac{-\pi\varepsilon_0 V^2 f_z}{4(1+f_A(d/2R)^2)}\left(\frac{R+\frac{d}{4}}{R-d}\right)^2 \times \\ &\left(\left(\frac{R-d}{\frac{d}{2}\left(1+\frac{d}{R}\tan^2(\theta_{tip}/2)\right)}\right) + 2\ln\left(\frac{2d}{d+R+(R-d)\cos\left(\theta_{tip}\right)}\right)\right) \end{aligned} \tag{4.25c}$$

where δ defines the height of the parabolic apex and is given by

$$\delta = \frac{R}{\tan^2(\theta_{tip}/2)} \tag{4.26}$$

and $f_z \approx 0.7$ is a correction factor, calculated separately, that is introduced to take into account that only the z-component of the force is required. Finally, f_A forms part of the empirical correction factor $1/(1 + f_A(d/2R)^2)$ that does not vary the short-range behaviour but gives F_A^z the correct limiting behaviour for $d \gg R$ [131]

$$f_A = \frac{\ln\left(\csc(\theta_{tip}/2)\right)}{(1 - \sin(\theta_{tip}/2))(3 + \sin(\theta_{tip}/2))} \tag{4.27}$$

This correction factor is required as the condition $d < R$ is often not satisfied as coaxial tip-to-tip (NP dimer) alignment is initially carried out in the long-range ($d > 200$ nm) regime. Under this formalism, Eqns. (4.25) are valid for $d \lessapprox 10$ μm and are hence appropriate for all NP dimer separations considered.

In a similar fashion to F_{EL}^z the total capacitance C can be decomposed into four parallel capacitance contributions describing the total system

$$C = C_L + C_C + C_A + C_{bk} \tag{4.28}$$

where C_L is the capacitance associated with the cantilevers, C_C is the capacitance associated with the conical sections of the AFM tips, C_A is the capacitance associated with the AFM tip apices and C_{bk} is the capacitance contribution from the opposing composite control rod, chip clip, AFM chip system. Using Eqn. (4.23) expressions for C_L and C_C are obtained

$$C_L \approx \frac{\varepsilon_0 A_{ov}}{2h + d} + C_F \tag{4.29a}$$

$$C_C \approx \varepsilon_0 \left(\frac{2(h - \delta)}{\cos(\theta_{tip}/2)} + (d - \delta)\tan(\theta_{tip}/2) \ln\left(\frac{d - \delta + 2h}{d + \delta}\right)\right) \tag{4.29b}$$

where C_F is the additional (fringe) capacitance associated with the remaining non-overlapping sections of the cantilevers, calculated using COMSOL. The z-component of force associated with this capacitance is assumed to be negligible ($F_F^z = 0$). The approximate d dependence of C_F is also found numerically by COMSOL simulation. The expression for C_A is calculated from the corrected force expression F_A^z. In general the capacitance of a system is related to the electrostatic force by

$$F(V,x,y,z) = \frac{1}{2}\nabla C(x,y,z)V^2 \tag{4.30}$$

Due to the assumed axial symmetry of the AFM tip apex sub-system Eqn. (4.30) simplifies and an expression for C_A is found from the corrected apex force contribution F_A^z

$$C_A(d) = C_A(\infty) + \int_\infty^d \frac{2F_A^z(V,z)}{V^2}\,dz = \int_\infty^d \frac{2F_A^z(V,z)}{V^2}\,dz \tag{4.31}$$

Analytical evaluation of Eqn. (4.31) is awkward and hence the expression is determined numerically using IGOR for fixed values of R and θ_{tip}. The numerical output is fitted to the functional form described in [132] and a typical expression determined for $R = 70$ nm and $\theta_{tip} = 45°$ is

$$C_A(d) \approx \left(6\times 10^{-19}\right)[\mathrm{F}]\ln\left(1+\frac{10^{-7}[\mathrm{m}]}{d}\right) \tag{4.32}$$

Finally the relatively large constant background capacitance contribution $C_{bk} \approx 0.1$ pF is measured experimentally. The force associated with this capacitance has negligible z-component ($F_{bk}^z \approx 0$) and hence does not induce significant cantilever oscillation.

To approximate F_{EL}^z and C when the AFM tips are moved off-axis, i.e. when scanning a $G_x \times G_y$ μm^2 alignment grid centered on the z-axis at a given d_0, the initial tip separation $d_0^{x,y}$ is used instead of the on-axis AFM tip separation, where

$$d_0^{x,y} \approx \left((d_0+2R)^2 + \left(\frac{g_x}{2}\right)^2 + \left(\frac{g_y}{2}\right)^2\right)^{1/2} - 2R \tag{4.33}$$

where $d_0^{x,y}$ is the distance of closest approach for a given tip 2 position in the alignment grid, and g_x and g_y are the positions of tip 2 in the x and y directions respectively. The range of grid positions for tip 2 are $-G_x/2 \leq g_x \leq G_x/2$ and $-G_y/2 \leq g_y \leq G_y/2$ in x and y respectively. For the majority of the experimental values of $d_0^{x,y}$, the electrostatic driving force $F_{EL}^z \approx F_C$, so the F_C component dominates the tip oscillation response. In all cases $d_0^{x,y}$ is much less than the characteristic dimensions ($\sim \mathcal{O}(10\ \mu\text{m})$) of the conical section. Therefore, it can be assumed that for a typical $G_x = G_y = 1\ \mu$m alignment grid, the maximum geometrically induced reduction in F_{EL}^z and C due to tip 2 being $G = ((G_x/2)^2 + (G_y/2)^2)^{1/2} \approx 0.7\ \mu$m off-axis is relatively small.

The short-range (< 2 nm), non-capacitative Van der Waals and repulsive tip-tip interaction forces F_{TT}^z, are modelled by the Lennard-Jones force between two spherical NPs [133]

$$F_{TT}^z(d) = F_{VdW}^z + H\bar{R}a_0^6/180d^8 \tag{4.34}$$

where $\bar{R} = R_1R_2/(R_1+R_2) = R/2$ for identical AFM tips, H is the material dependent Hamaker constant ($H \approx 25 \times 10^{-20}$ J for gold) and a_0 is the material dependent inter-atomic distance ($a_0 \approx 0.2$ nm for gold). An expression for the z-component of the Van der Waals force F_{VdW}^z between two AFM tips is approximated from [134], where the tip apex geometry is taken into account

$$\begin{aligned} F_{VdW}^z(d) =& \frac{H\bar{R}^2\left(1-\sin(\theta_{tip}/2)\right)\left(\bar{R}\sin(\theta_{tip}/2) - d\sin(\theta_{tip}/2) - \bar{R} - d\right)}{6d^2\left(\bar{R}+d-\bar{R}\sin(\theta_{tip}/2)\right)^2} \\ &- \frac{H\tan(\theta_{tip}/2)\left(d\sin(\theta_{tip}/2) + \bar{R}\sin(\theta_{tip}/2) + \bar{R}\cos(\theta_{tip})\right)}{6\cos(\theta_{tip}/2)\left(\bar{R}+d-\bar{R}\sin(\theta_{tip}/2)\right)^2} \end{aligned} \tag{4.35}$$

Alignment is implemented in the non-contact regime hence contact dynamics, such as adhesion forces and surface deformation are not treated.

For comparison with experiment all relevant expressions are substituted into Eqns. (4.1) and the coupled differential equations are solved numerically for the steady-state behaviour of the system for a given value of $d_0^{x,y}$. It should be noted that the additional modifications to the amplitude and phase of V and V_{AC} due to the stray capacity C_s, and the majority of experimental equipment, were also modelled by appropriate circuit theory within the simulation. The numerical

solution found for the steady-state $d(t)$ is used to calculate values for $C(t)$ and dC/dt that are then substituted into Eqn. (4.15) to give the current flow $I(t)$. The harmonic component at $3\omega_S$ is extracted using a numerical approximation to the lock-in amplifier by

$$\widetilde{I}^{3\omega_S} \approx \frac{2}{\tau_{TC}} \int_0^{\tau_{TC}} I(t) e^{-i3\omega_S t}\, dt \tag{4.36a}$$

$$\widetilde{V}_L^{3\omega_S} \approx \left(\frac{A_{LI} A_T}{\sqrt{2}} \right) \widetilde{I}^{3\omega_S} \tag{4.36b}$$

where $\widetilde{V}_L^{3\omega_S}$ is the $3\omega_S$ voltage signal measured by the lock-in amplifier, $\tau_{TC} = 100$ ms is the time-constant used for all lock-in measurements, A_{LI} is the lock-in amplifier gain, $A_T = 10^8$ VA^{-1} is the transimpedance amplifier gain, and the factor of $1/\sqrt{2}$ converts peak-to-peak to RMS voltage. Using this combined analytical and numerical approach allowed $|\widetilde{I}^{3\omega_S}|$ to be accurately and efficiently calculated with only one free parameter A_F.

4.3 Experimental Apparatus

The entire apparatus is placed on an active anti-vibration platform and contained within a Faraday cage. The tips are initially aligned to within $\pm$400nm in x, y, z under a colinear custom-built microscope with $\times$100, NA$=$0.9 objective. The tips used here are 50 nm Au coated nano-indentation AFM probes with a 'neck and ball' apex geometry. As shown in Fig. (4.3), the AFM tip system is driven by an amplified signal generator and the current flow across the AFM tips is passed through a 10^8 gain transimpedance amplifier (VA). A BPF centered at $3\omega_S$ prevents the current component at ω_S overloading the lock-in. More detail on the experimental rig can be found in Chapter (3).

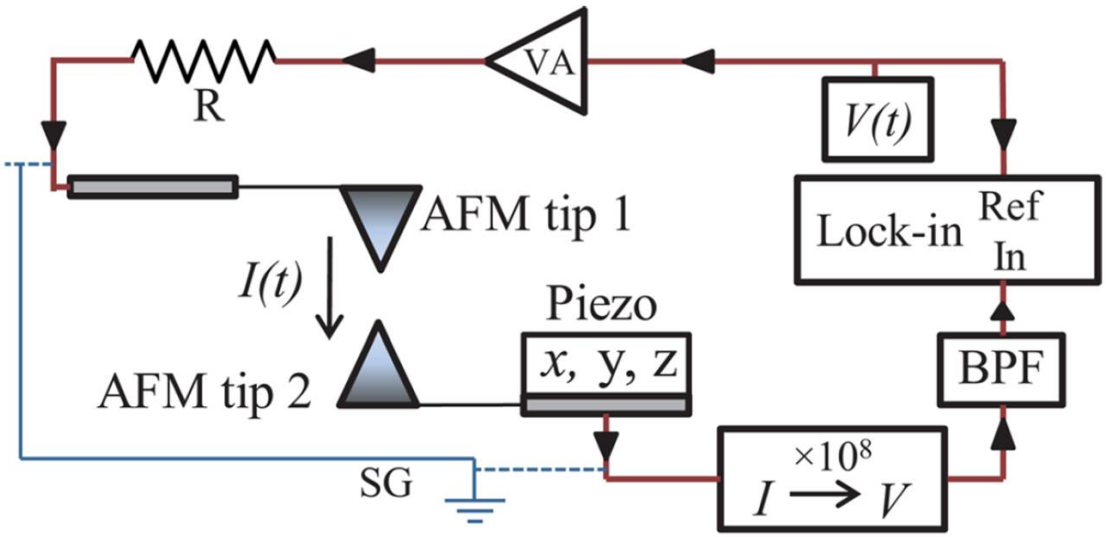

Figure 4.3: Simplified schematic of experimental apparatus with Signal Ground (SG), BPF and VA shown.

The AFM tip system resonance behavior is characterised by performing a frequency sweep whilst measuring $|\widetilde{I}^{3\omega_S}|$. A typical response curve at $d_0^{x,y} = d_0 \approx 340$ nm and $V_0 \approx 10$ V, measured around half the resonance frequency of AFM tip 1 ($f_{01}/2$), is shown in Fig. (4.4). In this case AFM tip 2 is non-resonant and hence is almost stationary. The Fano-like lineshape measured is significantly different to the expected Lorentzian lineshape. This is due to interference between $I^{3\omega_S}$ and the relatively large background signal I_{HD} primarily created by the Harmonic Distortion (HD) present in the output of the electronic amplifiers. The effect of the HD background on the signal can be understood by considering the superposition of the $I^{3\omega_S} = \Re[\widetilde{I}^{3\omega_S}]$ and $I_{HD} = \Re[\widetilde{I}_{HD}]$ waveforms

$$\begin{aligned}\Re\left[\widetilde{I}_C^{3\omega_S}\right] &= I^{3\omega_S} + I_{HD} = |\widetilde{I}^{3\omega_S}|\sin(3\omega_S t + \varphi^{3\omega_S}) + |\widetilde{I}_{HD}|\sin\left(3\omega_S t + \varphi_{HD}\right) \\ &= \left|\widetilde{I}_C^{3\omega_S}\right|\sin\left(3\omega_S t + \psi\right)\end{aligned} \tag{4.37}$$

where $\Re[\widetilde{I}_C^{3\omega_S}] = I_C^{3\omega_S}$ is the corrected $I^{3\omega_S}$ signal, ψ is the phase of the $I_C^{3\omega_S}$ signal, $\varphi^{3\omega_S}$ is the phase of the $I^{3\omega_S}$ signal and φ_{HD} is the phase of the I_{HD} signal. Here all phases are relative to the driving potential.

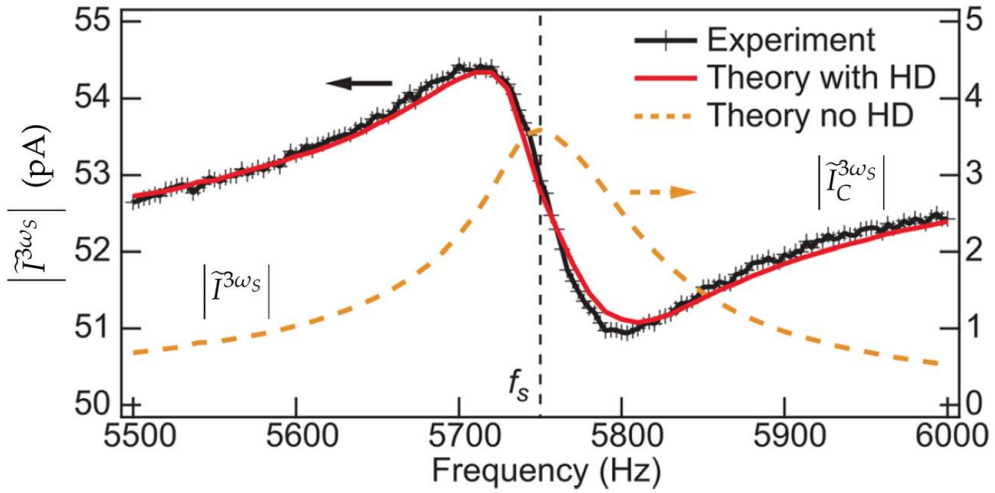

Figure 4.4: Experimentally measured $|\widetilde{I}^{3\omega_S}|$ (solid markers) vs. numerical simulation with the same parameters and harmonic distortion (HD) included (solid line) and absent (dashed line). Here $d_0 \approx 340$ nm and $V_0 \approx 10$ V. The frequency used for alignment scans is f_S.

As $|\widetilde{I}_{HD}| \gg |\widetilde{I}^{3\omega_S}|$ it is found that

$$|\widetilde{I}_C^{3\omega_S}| \approx |\widetilde{I}_{HD}| + |\widetilde{I}^{3\omega_S}| \cos(\Theta) \tag{4.38a}$$

$$\psi = \tan^{-1}\left(\frac{|\widetilde{I}^{3\omega_S}| \sin(\varphi^{3\omega_S}) + |\widetilde{I}_{HD}| \sin(\varphi_{HD})}{|\widetilde{I}^{3\omega_S}| \cos(\varphi^{3\omega_S}) + |\widetilde{I}_{HD}| \cos(\varphi_{HD})}\right) \tag{4.38b}$$

where $\Theta = \left(\varphi^{3\omega_S} - \varphi_{HD}\right)$. As AFM tip 1 is driven through resonance $\Delta(\Theta) = -180^\circ$ hence Eqn. (4.38a) shows that the corrected signal $|\widetilde{I}_C^{3\omega_S}|$ will demonstrate a Fano-like lineshape. Therefore $|\widetilde{I}_C^{3\omega_S}|$ can be directly compared to the experimentally measured $|\widetilde{I}^{3\omega_S}|$. The HD background was characterised using a signal analyser and added to the theoretical model by modifying Eqn. (4.4) to include a $V^{3\omega_S}$ term

$$V(t) = V_0 \cos(\omega_S t) + V_0^{3\omega_S} \cos\left(3\omega_S t + \varphi^{3\omega_S}\right) \tag{4.39}$$

where $V_0^{3\omega_S} \approx 1$ mV is the amplitude of the HD (for $V_0 = 10$ V) and $\varphi^{3\omega_S} \approx -\frac{\pi}{4}$ is the associated HD phase relative to the fundamental. Inclusion of the HD background recovers the correct resonance lineshape and yields the correct

$|\widetilde{I}^{3\omega_S}|$ signal offset, as shown in Fig. (4.4). The resonant frequency of tip 1 is observed and the AFM tips then driven at the frequency that maximises sensitivity, in this case $f_S = f_{01}/2 = 5.75$ kHz.

4.4 Alignment Results

For alignment, AFM tip 2 is scanned over a 1×1 μm^2 grid whilst measuring $|\widetilde{I}^{3\omega_S}|$ at each position. Tip 2 is then moved to the optimal alignment position, the tip apex separation d_0 is reduced, and successive alignment scans are taken.

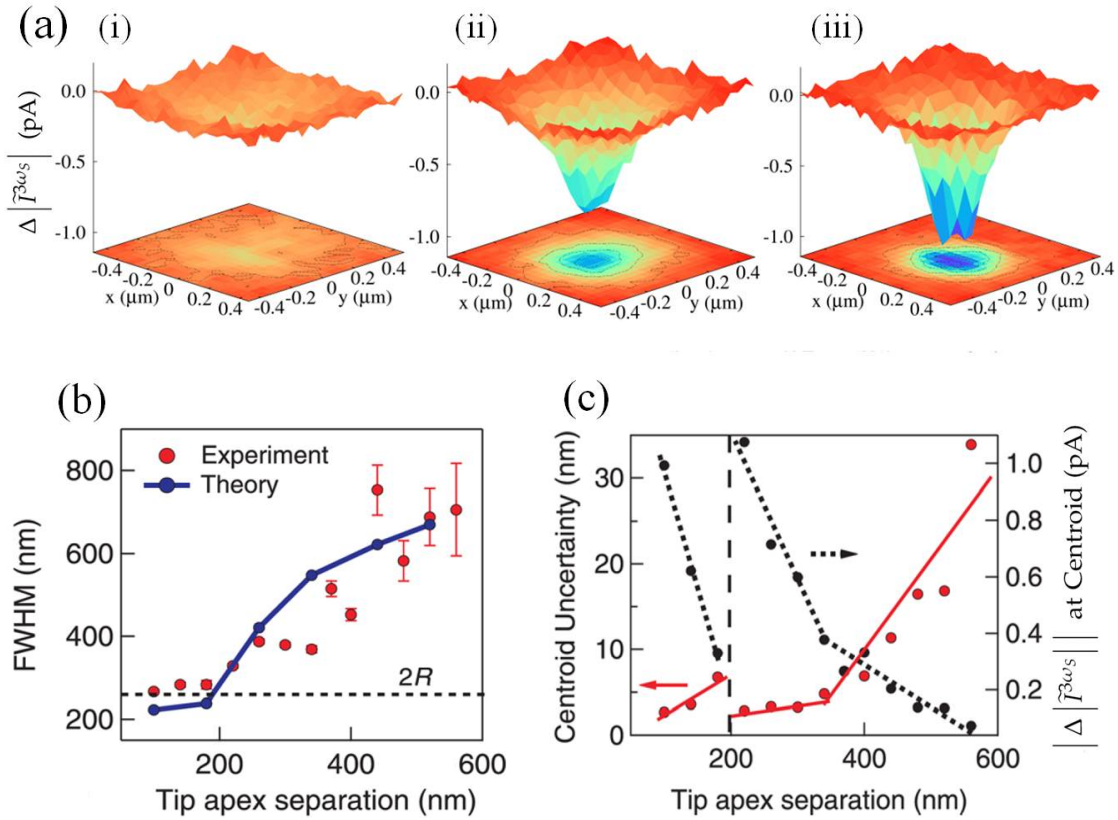

Figure 4.5: Typical alignment scan sequence results for $d_0 = 460$ nm$\rightarrow$ 220 nm with $V_0 \approx 10$ V. Evolution of the FWHM, and uncertainty in position, of the alignment grid minimum are also shown. (a) Change in measured $|\widetilde{I}^{3\omega_S}|$ with respect to HD background vs. position of AFM tip 2 in a 1×1 μm^2 grid for (i) $d_0 \approx 460$ nm, (ii) $d_0 \approx 340$ nm and (iii) $d_0 \approx 220$ nm, all with $V_0 \approx 10$ V. (b) FWHM of $\Delta|\widetilde{I}^{3\omega_S}|$ minimum (from alignment scans) vs. d_0. (c) Uncertainty and magnitude associated with $\Delta|\widetilde{I}^{3\omega_S}|$ centroid (from alignment scans) vs. d_0. Solid and dotted lines guide the eye, dashed vertical line shows where V_0 was reduced to $0.78V_0$ to avoid long-range StoC.

At the same time V_0 is reduced to prevent *long-range* 'Snap to Contact' (StoC) phenomena where ΔF^z_{EL} exceeds the change in cantilever restoring force of either AFM tip 1 or 2. A typical sequence of alignment scans at $d_0 \approx 460$ nm, $d_0 \approx 340$ nm and $d_0 \approx 220$ nm, all with $V_0 \approx 10$ V, are shown in Fig. (4.5a). Here, the change in signal with respect to the HD background ($\Delta|\widetilde{I}^{3\omega_S}| = |\widetilde{I}^{3\omega_S}| - |\widetilde{I}_{HD}|$), is plotted against tip 2 position. The local minimum (rather than maximum) observed is again due to the interference between the $I^{3\omega_S}$ and I_{HD} signals. This can be understood by further examining Eqn. (4.38a)

$$\Delta \left|\widetilde{I}_C^{3\omega_S}\right| = |\widetilde{I}_C^{3\omega_S}| - |\widetilde{I}_{HD}| \approx \left|\widetilde{I}^{3\omega_S}\right| \cos(\Theta) \tag{4.40}$$

where $\Delta|\widetilde{I}_C^{3\omega_S}|$ is the corrected change in signal with respect to the HD background. In all cases AFM tip 1 is always driven slightly above resonance because $f_{01} > f^e_{01}$ where f^e_{01} is the effective resonance frequency due to the electrostatic force and elastic damping. Therefore using Eqn. (4.38a) it can be shown that $\Theta > 90^\circ$ and has a typical value of $\Theta \approx \frac{3\pi}{5}$. Substituting $\Theta \approx \frac{3\pi}{5}$ into Eqn. (4.40) shows that the on-axis $\Delta|\widetilde{I}_C^{3\omega_S}| \approx -\frac{1}{3}|\widetilde{I}^{3\omega_S}| \approx -0.8$ pA (from Fig. (4.4)). This agrees well with the experimentally measured value, shown in Fig. (4.5a(ii)). All parameters plotted in Figs. (4.5), and used for experimental analysis, were extracted from the experimental measurements by fitting an inverted, 2D elliptical Gaussian function to the alignment grid data, assuming zero correlation between each data point.

As the AFM tips approach, the magnitude of the signal minimum increases while the associated FWHM and the uncertainty in centroid location decreases (Figs. (4.5b) and (4.5c)). By thus 'homing-in' on the centroid position to $d_0 < R_i \approx 130$ nm the FWHM tends to $2R$ as expected. The numerical simulation FWHM results are in good agreement with experiment. This is expected as the required corrections in C and F^z_{EL} due to the tips moving off-axis are small. When $d_0 < R$ the uncertainty in centroid position is less than ± 3 nm, i.e. $40\times$ less than R, therefore the NP dimer is axially aligned to a high degree of accuracy. Once in this regime the AC driving potential is set to $V_0 = 0$ and d_0 is further reduced, with nanometre precision, at a rate of 2 nm s^{-1}, using the piezoelectric actuator. An absolute distance scale is obtained by switching to the DC conductance measurement electronics described in Sec. (3.3.2). A small

($V_{DC} \sim \mathcal{O}(50\ \mu\text{V})$) constant potential is applied across the AFM tips and the tip separation d_0 is controllably reduced whilst observing the current rise (I_{DC}) upon (mechanically reversible) atomic-scale kissing contact.

A flow diagram showing the total typical alignment procedure is shown in Fig. (4.6). The frequency sweep and alignment procedures are almost entirely automated using computer code written in IGOR Pro to send VISA commands via GPIB to the experimental equipment[3]. It is found that halting the alignment procedure when setting $V_0 \approx 7$ V yields $|\Delta|\widetilde{I}^{3\omega_S}|| \approx 1$ pA at the grid centroid typically leaves an inter-tip separation of $d \leq 100$ nm.

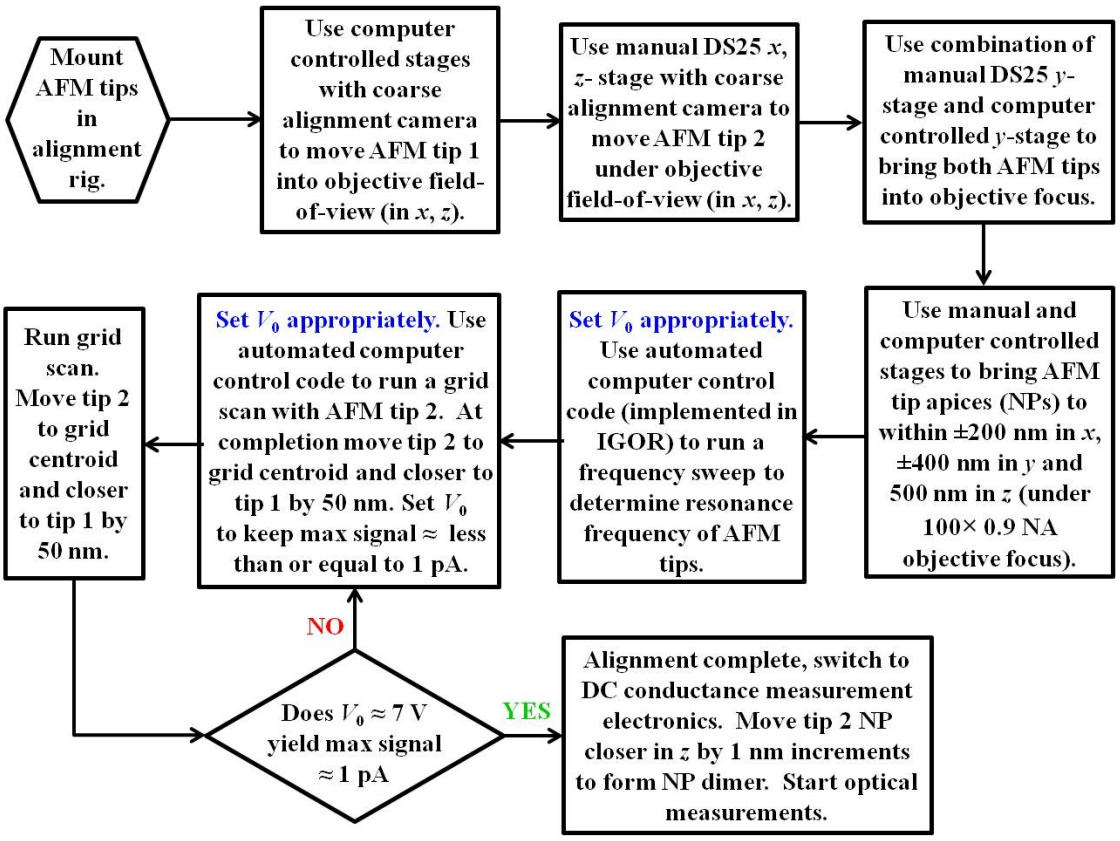

Figure 4.6: Flow diagram of the total AFM tip (NP dimer) alignment procedure. The text in blue labels an action that requires an initial human input.

[3]The AFM tip (NP dimer) alignment software produced, including Graphical User Interface (GUI), can be obtained from the author on request.

4.5 Conclusions

The parametric response of an electromechanically-coupled NP functionalised AFM tip system is utilised as a long-range sensor of 3D AFM tip-tip (NP dimer) alignment. The technique is experimentally and theoretically demonstrated for dynamic separation control of metallic NP dimers on the nanoscale. At all separations the system maintains the facility for simultaneous local optical and electronic measurement. This enables a versatile experimental apparatus to perform time-resolved (ms-μs) dark-field nano-spectroscopy in different plasmonic interaction regimes. By simultaneously measuring the optical response and electrical conductivity at $d_0 < 1$ nm, the non-local effect of quantum transport on the LSPP mediated response of metallic NP dimers is investigated, as described in Chapter (5). It is expected that the techniques developed will also find use in nonlinear and active plasmonics, surface enhanced spectroscopies, THz quantum transport research and studies of strong plasmon-molecular exciton coupling.

Chapter 5

Quantum Tunnelling Plasmonics

5.1 Introduction

The electron correlations supported by quantum tunnelling across the NGJs associated with relatively large ($a > 20$ nm) NP dimer systems require a new description of non-local transport. As introduced by the open questions in Chapter (2), an improved understanding of the effect of non-local quantum transport on plasmonic coupling is crucial for a large variety of applications. Many emerging nanophotonic technologies depend on the careful control of this plasmonic coupling, including optical nanoantennas for high-sensitivity chemical and biological sensors [135], nanoscale control of active devices [136–138], improved photovoltaic devices [10] and nanoscale optical trapping [139]. In general sub-wavelength metallic structures can concentrate light into nanoscale dimensions well below the diffraction limit [140,141] due to reduced field penetration through a dense electron sea. Nanocavities formed inside a NGJ control the coupling of LSPPs, thus allowing cavity-tuning [74, 89, 90] targeted to desirable applications which exploit the enhanced optical fields, e.g. nanoscale optoelectronics and single molecule electronics. However as a NGJ shrinks to atomic length-scales, quantum effects emerge and standard classical approaches to describe the photonics of these systems fail.

As discussed in Sec. (2.2.2), one effect of confining electronic wavefunctions inside small metallic nanostructures is to slightly modify the screening which tunes the plasmons [36]. However tunnelling plasmonics in the Quantum Regime (QR) has more profound effects that cannot be explained through hydrodynamic models that simply account for quantum effects through smear-

ing of the electronic surface-charge [76]. Recent theories show that Quantum Tunnelling (QT) across the cavity strongly modifies the optical response [82,96], but computational limits restrict these quantum simulations to very small systems below a few nanometres. Furthermore, the extreme difficulty in creating and probing sub-nanometre plasmonic cavities has limited experimental investigations of plasmonics in the QR.

Self-assembly and top-down nanofabrication achieves gaps of $d \approx 0.5$ nm between plasmonic NPs, but these fail to reach the QT-regime [105,106], and as described in Sec. (3.1), are not suitable for optically capturing tunnelling plasmonics. Controllable nanocavities with a sub-nanometre dimension are accessed in STM and electro-migrated break-junctions where the combined effects of photo-assisted and photo-induced electron transport can be measured. A significant amount of investigation has been performed into photo-assisted transport by measuring the DC photocurrent produced by the rectification of the non-linear optically driven (optical frequency) QT [142–144]. Photo-induced transport, e.g. tunnelling of hot electrons created by light absorption processes, has been found to enhance DC electron tunnelling in STM [145] and electron transport through metal quantum point contacts [146]. The excitation cross-section and the lifetime of excited electrons in these states ($\sim \mathcal{O}$(fs)) determines the magnitude of this contribution. Finally, inelastic electron tunnelling has been used to electrically excite LSPPs in nanocavities [147] which in turn can excite propagating SPPs [148]. The broadband emission due to the radiative decay of the LSPPs and SPPs is measurable in the far-field and can be used to characterise the nanosystem, e.g. by the visualisation of Fermi's golden rule [149] and the measurement of current shot-noise at optical frequencies [150]. Such investigations to date rely on narrowband illumination conditions and electrically driven LSPP/SPP excitation to show rectification and emission phenomena, but the effect of QT on broadband, optically excited plasmon coupling across sub-nanometre cavities remains unexplored. Here it is shown that *optical* excitation and detection of inter-NP optical-frequency tunnelling is highly successful and informative.

By simultaneously capturing both the electrical and optical properties of a NP dimer, with controllable sub-nanometre separation, the first evidence for the quantum regime of optically controlled tunnelling plasmonics is observed. It is also possible initial experimental evidence for coherent plasmon-exciton coupling in a NP dimer system is obtained for the first time. The experimental

apparatus described in Chapter (3), and the NP dimer alignment technique detailed in Chapter (4), provide the specialised setup required to investigate LSPP interactions in this challenging -0.5 nm $\lessapprox d \lessapprox 2$ nm regime of extreme nonlocality. By simultaneous dynamic measurement of the DC conductance of the NGJ, and the LSPP mediated broadband optical scattering response, the first controlled measurements in this unexplored domain are made possible.

As outlined in Chapter (1), this chapter primarily focuses on the experimental results found due to the culmination of the preceding work presented in this thesis. A theoretical overview and an outline of the Quantum Corrected Model (QCM) of BEMAX are presented first, followed by a brief review of the experimental setup. The remainder of the chapter focusses on experimental results, comparison with theory, analysis and conclusions.

5.2 Theoretical Modelling

For clarity the LSPP modes expected to be present in the AFM tip mounted NP dimer system are first briefly introduced using Sec. (2.3.4) as a theoretical basis, while the specifics of each mode measured are described in detail in Sec. (5.5). Following from this, an introduction to a newly developed theoretical model used to compare against the experimentally obtained data is also presented.

5.2.1 Expected Plasmonic Modes

The LSPP modes for a NP dimer created by the axially aligned pair of NP functionalised AFM tips are modified compared with those of a completely isolated homogeneous NP dimer. The degree of deviation is primarily determined by the apex NPs plasmonic coupling to the overall neck and body of the host AFM tip. The typical geometries of the NP functionalised AFM tips used in the experiments are shown by the Scanning Electron Microscope (SEM) and optical DF images in Fig. (5.1a). The 50 nm Au coated experimental geometry is approximated by a homogeneous Au geometry in the numerical simulations (Fig. (5.1b)) to reduce the number of discrete parameterisation points required. This approximation is valid as the 50 nm Au coating is significantly greater than the skin-depth $\delta_{Au} \sim \mathcal{O}(35\text{ nm})$ (Eqn. (2.34)) thus the LSPP modes are only weakly affected by the underlying dielectric (EBD deposited diamond-like carbon).

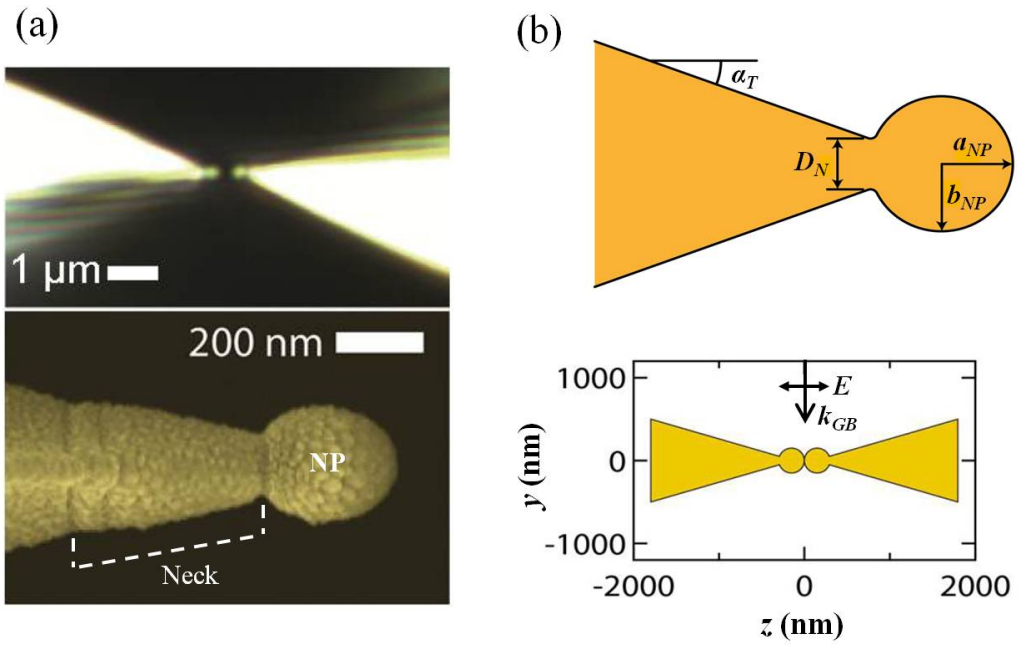

Figure 5.1: Geometry of NP functionalised AFM tips used in experiment (50 nm Au coating) and theoretical simulation (solid Au). (a) Top: typical optical DF image of typical NP functionalised AFM tips. Bottom: typical SEM image (false-colour) of NP functionalised tip apex. (b) Top: typical simplified (axially symmetric) tip apex geometry used for theoretical simulations. Here $\alpha_T \approx 20°$, $D_N \approx 80$ nm, $a_{NP} \approx 160$ nm and $b_{NP} \approx 140$ nm. Bottom: overall truncated AFM tip geometry used for theoretical simulation with direction ($\mathbf{k_{GB}}$) and polarisation of the incident Gaussian beam shown.

Following from the discussion in Sec. (2.3.4), it is clear that the plasmonically coupled apex NP and bulk AFM tip will sustain several resonant LSPP modes of significant scattering cross-section. For example, the particular NP functionalised tip apices shown in Fig. (5.1a) have a LSPP resonance in the green ($\lambda_0 \approx 550$ nm). The exact nature and spectral position of each mode strongly depends on the apex geometry, and the plasmonic coupling of the apex NP to the neck section, labelled in Fig. (5.1a). This plasmonic coupling was intuitively understood by describing a NP dimer with large overlap (negative d) in Sec. (2.3.4). Additionally, tightly localised higher-order LSPP modes will also become significant as the apex NPs are moved into closer proximity[1] (Fig. (2.13)). The LSPP interactions in the nanosystem created can hence possibly be understood as the LSPP interactions present in a relatively large NP dimer system

[1] As these modes are highly-localised they are commonly referred to as LSP modes. However, they can never be truly LSP modes (see Sec. (5.4)) and are hence referred to as LSPP modes.

($a \approx 150$ nm), where the relevant LSPP modes of each NP are red-shifted from those of an isolated NP due to the anisotropic polarisability created by the plasmonic coupling of each NP to the associated extended bulk AFM tip structure. The calculated far-field scattering cross-section for an Au sphere with $a = 150$ nm is shown in Fig. (5.2).

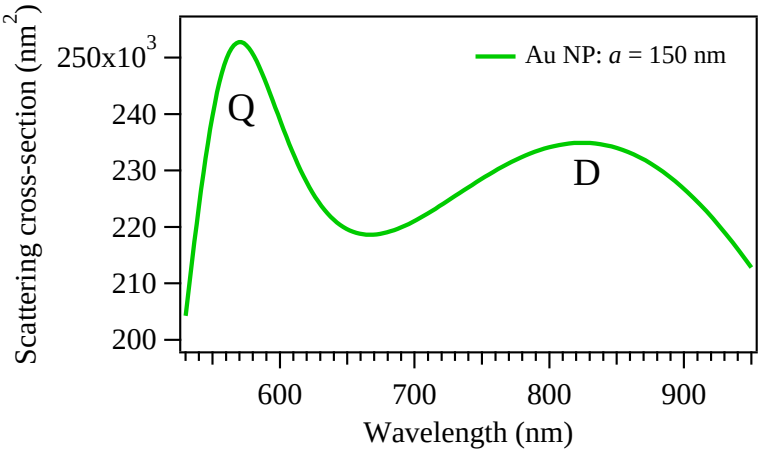

Figure 5.2: Far-field scattering cross-section of a large Au NP ($a = 150$ nm) with incident wavefronts superimposed to approximate a focussed Gaussian beam. The dipole and quadrupole LSPP modes are labelled 'D' and 'Q' respectively. Scattering collected over 4π solid-angle.

The relatively large NP promotes optical excitation of the higher-order quadrupole mode due to the non-uniform field over the volume of the NP created by the combined effects of retardation and the (approximate) focussed Gaussian beam illumination. The relative strength of the quadrupole mode compared to the dipole mode is surprising and is attributed the non-homogeneous incident illumination [69].

The effect of attaching such a NP to the apex of a substantially larger Au tip is demonstrated in Fig. (5.3). The incident laser beam, centred at (y, z)=(0, 0) nm, excites LSPPs highly confined to the apex of both the plain tip (marked by blue dots) and the NP functionalised tip (marked by red dots). Additionally, the illumination launches SPPs that propagate up the tips and reflect from the base [151]. The propagating SPPs thus interfere to form localised quasi-standing-wave resonances (marked by **black** dashed lines). These extended LSPP modes are more apparent in the plain tip geometry due to the reduced loss (higher reflectivity) at the more accommodating apex structure. It should be noted that

while the overall length and cone-angle of the plain and NP functionalised tips are both equal (to aid comparison), the volume of the plain tip is necessarily greater, therefore yielding an increased scattering cross-section. In reality the AFM tips are over an order of magnitude greater in length than those simulated here, and therefore it is expected that such extended standing-wave LSPP modes are negligible in experiment.

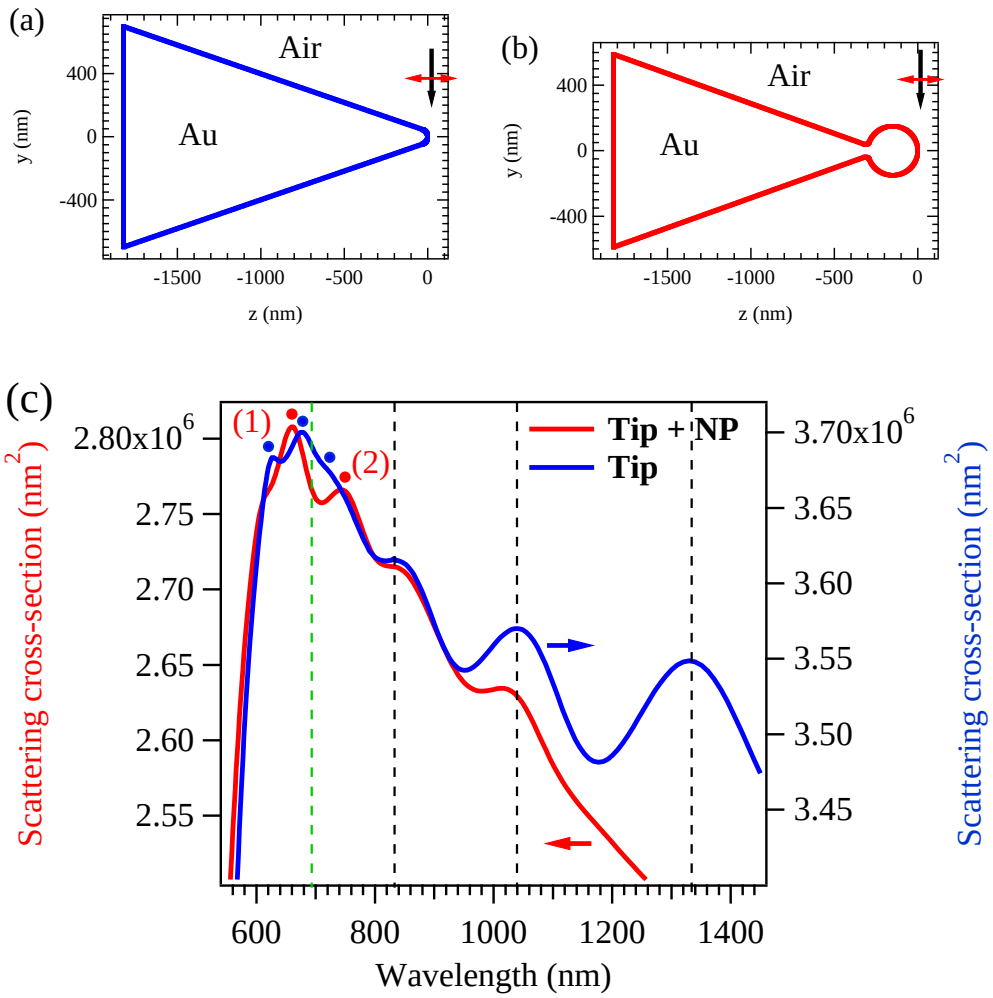

Figure 5.3: Comparison of the far-field scattering cross-section of an Au tip and Au NP functionalised tip, simulated using BEMAX. (a) Geometry of plain Au tip (R = 50 nm), incident wavefronts are superimposed to approximate a focussed Gaussian beam at the tip apex (y, z)=(0, 0) nm. Incident laser beam has $\mathbf{k_{GB}}$ and polarisation perpendicular and parallel to tip axis respectively. (b) Same as in (a) but for NP functionalised tip geometry. (c) Scattering cross-sections associated with the tip (blue) and NP functionalised tip (red) geometries (collected over 4π solid-angle).

The LSPP resonances at $\lambda_0 < 830$ nm are relatively confined to the apex and are hence expected to be present even for an infinitely long tip. It is clear the NP enhances LSPP resonances (1) and (2) relative to the plain tip equivalents. It is interesting to note that LSPP resonance (1) has approximately the same background subtracted cross-section as the quadrupole resonance of the isolated NP (Fig. (5.2)), and it is red-shifted by $\Delta\lambda_0 = 90$ nm. However, more simulations are required to determine the exact nature of this resonance as it could also be associated with a higher-order standing-wave like resonance that has been enhanced by the NP cross-section. For comparison the **green** dashed line marks the position of the theoretically predicted extended standing-wave LSPP resonance. The second enhanced peak, LSPP resonance (2), does not coincide with a standing-wave resonance and is therefore attributed primarily to the apex NP and neck region.

The observed resonances (1) and (2) are associated with a significantly enhanced surface charge density around the apex region compared to the plain tip. Only the resonance(s) that localise significant charge density at the NP apex (rather than, for example, at the neck) will strongly couple (hybridise) to the LSPPs on the the second tip as the NP dimer is formed. Such a LSPP resonance will red-shift on approach, and be further enhanced compared to the LSPP modes more de-localised over the neck and entire tip structure [152]. As $d < a$ it is therefore expected that one LSPP resonance (either (1) or (2)) will dominate the scattering response. At $d \ll a$, increasingly higher-order hybridised LSPP modes will become active, in the same manner as that predicted for a standard NP dimer system (Sec. (2.3.4)). Finally, the rapid decrease in scattering for $\lambda_0 < 600$ nm is attributed to the modified interaction of the incident light with the tip structure as $\omega \to \omega_p$ (ω_p for Au corresponds to $\lambda_0 \approx 520$ nm) where interband transitions begin to dominate the material response.

The LSPP modes between $\lambda = 500$ nm - 1000 nm are experimentally measured and therefore the more localised apex resonances (red dots) shown in Fig. (5.3c) all lie within the experimental measurement window. Furthermore, the extended standing-wave LSPPs are not expected to be present. Upon NP dimer creation (axial tip alignment with $d < a$) such NP apex LSPP modes begin to hybridise and will be strongly modified in the regime of extreme non-locality ($d \sim 1$ nm). The experimentally created NP dimer system hence has strong similarities to the simple NP dimer system described in Sec. (2.3.4). Importantly,

this enables intuitive comparisons with simpler classical NP dimer models to be made. The LSPP modes experimentally measured, and theoretically simulated, are described in detail in Sec. (5.5).

5.2.2 Quantum Corrected Model

The full range of non-local response in NP dimer systems with sub-nanometre separation has only begun to be theoretically treated within the last three years [82, 96]. However, as described in Sec. (2.3.3), such *ab initio* approaches are extremely computationally demanding due to the large number of electrons involved in the optical response. Recent theoretical work on a QCM of BEMAX [153], that is experimentally verified for the first time by the work in this thesis, has made the first step in describing the non-local effect of quantum tunnelling on the LSPP response of large NP dimer systems with $d < 1$ nm and $a > 3$ nm. Using this theoretical model NP dimer systems with $N_e > 10^7$, rather than the typical $N_e \approx 10^3$ limit for TDDFT simulations, can be described in the non-local quantum transport regime. Note, all optical scattering and electric near-field simulations in the remainder of this chapter were performed by R. Esteban and J. Aizpurua and based on the QCM developed [153].

The QCM approximates the non-local quantum tunnelling effect by representing the NGJ between two adjacent NPs as a fictitious conducting medium $\widetilde{\varepsilon}^{QT}(d)$ that mimics electron tunnelling. The calculations employ this fictitious medium to incorporate quantum effects, derived from coherent electron tunnelling and spill-out using Density Functional Theory (DFT), within a classical electromagnetic framework (in this case BEMAX [77]) to treat large plasmonic systems [153]. Under this formalism non-local screening effects within the NGJ (defined by the tunnelling volume) are also taken into account, however this effect could still be significant immediately outside the tunnelling volume (large magnitude $\widetilde{\mathbf{k}}_{\mathbf{E}}$ components are still present) and therefore could be a source of discrepancy. Outside the NGJ the relative permittivity $\varepsilon_{air} \approx 1$ and local dielectric function $\widetilde{\varepsilon}_{Au}$ (taken from experimental data [154]) describe the classical response of the surrounding air and overall Au tip structure respectively.

First, the general approximations are made that the electric field $\mathbf{E}$ in the NGJ is entirely orientated along the dimer axis (z-axis) and is independent of position along the z-axis. Furthermore, under the assumption that the transmis-

sion of electrons at the Fermi energy (Ω_F) through the potential barrier created by the NGJ occurs at a time-scale much shorter than the period of the optical field, the tunnelling current adiabatically follows the field in the NGJ. These assumptions allow the Static Scanning Tunnelling Microscopy (SSTM) model to be used to calculate the inhomogeneous static (DC) tunnelling conductivity of the NGJ, $\sigma_0^{QT}(d(d_0,x,y))$, as a function of on-axis separation d_0 and lateral position in x and y for $d > 3$ Å. Under the SSTM formalism the 1D DC tunnelling conductivity is given by [155]

$$\sigma_0^{QT}(d) = \frac{4\pi m_e^* e^2}{h^3} d \int_0^{\Omega_F} T^{QT}(\Omega, d)\, d\Omega \tag{5.1}$$

where $T^{QT}(\Omega, d)$ is the energy-dependent electron tunnelling probability at each position (d_0, x, y) within the NGJ with separation d. It is also assumed that $eV_{opt} \ll (\Omega_F \wedge \varphi_{WF})$ where $V_{opt} = Ed$ is the optically induced potential across the NGJ and φ_{WF} is the work-function of the NP metal. Full quantum-mechanical treatments (e.g. DFT) can be used to calculate $T^{QT}(\Omega, d)$ as the number of electrons in such simple (assumed flat interfaces as $a \gg d$) systems is relatively small. In this case, for simplicity, a jellium model potential approach rather than a full atomistic simulation was used to determine $T^{QT}(\Omega, d)$ under a DFT framework, for $d > 3$ Å [153]. Under this formalism the many-body nature (local-density approximation) of the problem and long-range image potential interactions are taken into account [156]. For smaller d, the SSTM approach is no longer valid as T^{QT} is not small. Therefore an expression for $\sigma_0^{QT}(d)$ over the full-range of d is estimated by fitting an exponential form to the value at contact ($d \to 0$) together with the SSTM results at large d. In practice the lateral inhomogeneity (x, y dependence) is implemented at the NGJ by considering enough concentric shells in the x-y plane to provide a converged solution.

From this basis the position dependent tunnelling damping parameter $\gamma^{QT}(d)$ is determined via $\sigma_0^{QT}(d) = \sigma^{QT}|_{\omega=0} = \varepsilon_0 \omega_p^2 / \gamma^{QT}(d)$ (c.f. Eqn. (2.22)), and thus the position dependent spatially local dielectric function of the fictitious tunnelling medium is obtained by

$$\widetilde{\varepsilon}^{QT}(d(d_0,x,y),\omega) = \varepsilon_{bk}(d) - \frac{\omega_p^2}{\omega\left(\omega + i\gamma^{QT}(d)\right)} \tag{5.2}$$

where $\varepsilon_{bk}(d)$ is the background screening contribution. In this case $\varepsilon_{bk}(d=0)$ is the screening contribution of the d-orbital electrons to $\widetilde{\varepsilon}_{Au}$. For $d > 0$, $\varepsilon_{bk}(d) \to 0$ exponentially with a characteristic length of 1.5 Å, chosen to be close to the decay of the $5d$-orbital of Au [157]. In this treatment γ^{QT} is considered to be the varying parameter, rather than ω_p, as this is consistent with the resistive, rather than capacitive, nature of the NGJ found from full TDDFT calculations [153]. Both ω_p and $\gamma^{QT}(d=0)$ are set equal to their respective free-electron 'Drude' contribution found from $\widetilde{\varepsilon}_{Au}$. Using Eqn. (5.2) to describe the NGJ within the classical BEMAX framework hence enables the optical response of large-scale nanosystems with a sub-nanometre NGJ to be well approximated [153].

The physical geometries of the NP functionalised AFM tips are modelled as shown in Fig. (5.1b). The plasmonic NGJ is formed by two 150 nm radius spheres connected to ≈ 1.5 μm long cones through rounded 80 nm diameter necks. In this case each cone is terminated with a planar surface at its base. The cones are aligned along the z-axis and both combined NP-cone structures are assumed to be rotationally symmetric.

To model the DF illumination a plane-wave representation of a laser beam propagating in the $-y$-direction (perpendicular to the AFM tip axis) is used, as shown in Fig. (5.1b). The incoming light is described by a plane-wave decomposition of a focussed Gaussian beam (centered at $(x, y, z) = (0, 0, 0)$) under the scalar paraxial approximation[2]. The fields are thus described by a superposition of plane-waves propagating with wavevector $\mathbf{k}$. The electric field $\mathbf{E}$ at a point (x, y, z) can be expressed as

$$\mathbf{E}(x,y,z) \propto \int\int u(k_\rho) e^{-i(k_x x + k_y y + k_z z)} \mathbf{p}(\mathbf{k}) dk_x dk_z \tag{5.3}$$

where $k_\rho = \sqrt{k_x^2 + k_z^2}$, $k_y = \sqrt{k^2 - k_\rho^2}$ and $k_\rho < k$. The function $u(k_\rho)$ is a weighting term that is constant for plane-waves incoming at all angles between $\theta_1 = 34^\circ$ and $\theta_2 = 64^\circ$ with respect to the y-axis, but strongly suppresses other plane-wave contributions to the integral [158]. This is implemented to better describe the experimental DF illumination. Finally, $\mathbf{p}(\mathbf{k})$ defines the polarisation of each plane-wave (TM in the corresponding $\mathbf{k}$-z plane). The total scattering cross-section is obtained by integrating over the full 4π solid-angle.

[2]This is a good approximation to the slightly more 'Airy-like' intensity distribution produced in the experiments.

Overall a number of immediately obvious assumptions are made in the QCM, such as the lack of surface irregularities, the presence of perfect rotational symmetry and the local description of the gold-air interface. For instance, the theoretical simulations used a $D_N = 80$ nm cone-shaped neck to approximate the average of the triangular cross-section of the actual neck shown in the SEM image of Fig. (5.1a). The illumination conditions are mostly described within the theoretical model, even though spatial filtering and the strong focussing (high NA) of the laser illumination in the experimental implementation leads to certain complexities in the field distributions (e.g. polarisation distribution as described in Sec. (3.4.2) and a tighter elliptical focus) that are not taken into account. Due to such complexities the collection conditions are captured in a simplified way within the theoretical model. These combined approximations likely account for some of the differences in the LSPP mode wavelengths and scattering intensities between experiment and theory, and are discussed in more detail in Sec. (5.5.2). The primary effect of changing the illumination and collection conditions in the theory was to alter the signal strength of the different modes. Nevertheless, even after these approximations, the QCM captures the essence of the coherent QT process occurring across the NGJ.

5.3 Experimental Setup

The experimental apparatus is described in detail in Chapter (3). Here a brief review of the setup is presented. The optical setup for the DF scattering measurement is shown in Fig. (5.4a). A custom-built DF microscope designed for use with supercontinuum (450 nm - 1700 nm) laser illumination is used for all scattering measurements. The microscope is designed to provide an ultra-low specular-reflection background and a high degree of mechanical stability, enabling DF spectra to be captured over ms timescales with excellent SN levels. The laser illumination (path shown in red) is expanded by a factor of three with a Keplerian lens pair, then passed through a reflective ND filter (OD = 1.0), an APP to correct chromatic dispersion, and a LP (transmission axis oriented parallel to the tip-tip ($z-$) axis). As the tip apex NPs are centred under the laser illumination the linear polarisation along the NP dimer axis is well maintained even after strong focussing (Fig. (3.14b)). A 2 mm diameter beam stop blocks the central portion of the beam thus creating the DF illumination geom-

etry. The BS 1 directs the laser beam into the objective that focuses the beam to a diffraction-limited, sub-μm spot at the tip apices, as shown schematically in Fig. (5.4b).

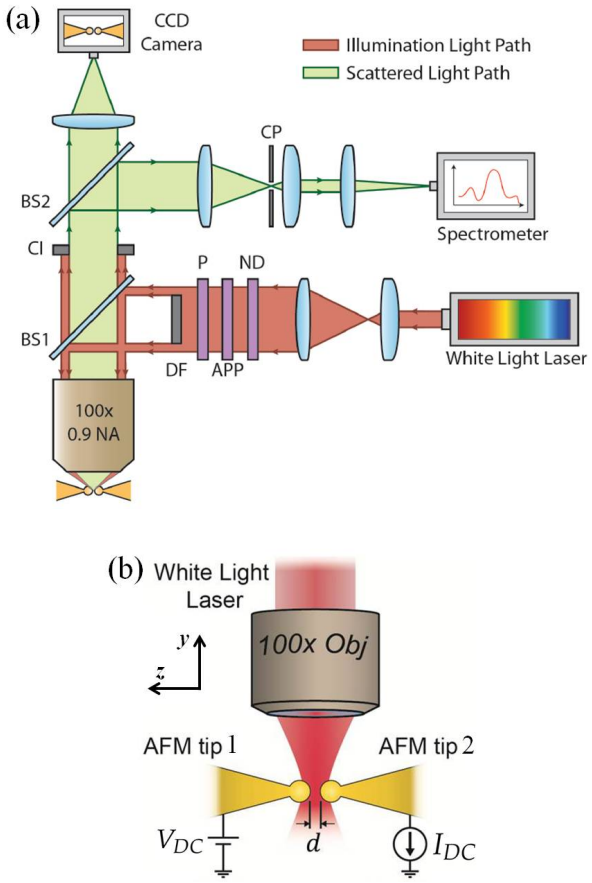

Figure 5.4: Review schematic of experimental setup for measurement of LSPP mediated optical scattering response in the quantum transport regime. (a) Review schematic of optical setup. Here the CP has diameter of 50 μm and the CI has diameter of 1.2 mm. (b) Schematic of illumination of NP functionalised AFM tip apices with static potential applied and DC current flow measured.

Using the laser and a high magnification, high NA objective provides $> 10^4$ times the intensity than that of a typical halogen or xenon lamp setup and illuminates only the volume of interest. Light scattered from the sample (path shown in **green**) is collected with the same objective and a Collection Iris (CI) blocks the high-NA portion of the beam. The scattered light is split by BS 2, with half the light passing to a CCD camera for imaging and the other half focussed onto the spectrometer after spatial filtering with a 50 μm Confocally-aligned Pinhole (CP). Spectrometer integration times of 3 ms were used and

measured spectra were normalised to the reflection from an Au mirror placed at the sample plane.

The Au-coated, ball-type AFM probes were characterised by optical and electron microscopy. Typical cantilever spring constants and (lowest-order) resonance frequencies were $k_{0i}^{z} \approx 0.2$ Nm^{-1} and $f_{0i} \approx 13$ kHz, respectively. Large radius of curvature ($R = a_{NP} \approx b_{NP} \approx 150$ nm) tips are selected to minimise sensitivity to axial tip-tip alignment, to increase the scattering cross-section, and to support higher-order plasmonic cavity modes in the visible spectrum. There is approximately $< 10\%$ variation in the tip apex geometry parameters for all AFM tips used, hence additional LSPP coupling effects prevalent in hetero-dimers are assumed to be small. The AFM tips are mounted on 3-axis piezoelectric (PZ) actuation stages using closed-loop feedback control with capacitive positioning sensors. The tips are then axially aligned with nanoscale accuracy using a recently developed, non-linear EFM technique [159], described in detail in Chapter (4). Briefly, the alignment is performed by placing an AC potential across the AFM tips, and measuring the harmonic frequencies generated by the non-linear electromechanical response of the tip-tip system using lock-in detection. The tips are brought into nanometre-precise 3D alignment by adjusting the tip positions to maximise signal harmonics.

The two Au-NP functionalised AFM tips are hence aligned tip-to-tip in 3D, as shown in Fig. (5.4). The tip apices thus define a NGJ supporting plasmonic resonances created via strong electromagnetic coupling between LSPPs on each tip apex NP [160, 161]. This dual AFM tip configuration provides multiple advantages. First, independent nm-precise movement of both tips is possible with 3-axis piezoelectric stages. Second, conductive AFM probes provide direct electrical connection to the apex NPs enabling simultaneous optical and electrical measurements. Third, the tips are in free space and illuminated from the side in a DF configuration. Finally, as the effective NPs at the tip apices are conductively connected through to bulk AFM tip, cantilever and support structures, these bodies act as thermal sinks thus reducing heating effects on the stability of the NGJ. This arrangement provides for the first time, background-free broadband spectroscopic characterisation of the tip-tip NP dimer (plasmonic nanocavity) throughout the sub-nanometre regime. The inter-tip separation d is initially set to 50 nm and then reduced while recording DF scattering spectra and DC current flow simultaneously.

The inter-NP conductance is measured by applying a DC potential (V_{DC}) across the tips and measuring the resulting current (I_{DC}) with a variable gain (set to 10^6 VA^{-1} in this case) transimpedance amplifier with an integrated 10 Hz low-pass filter. The transimpedance amplifier signal is measured with a DSO and the junction conductance $G_{DC} = I_{DC}/V_{DC}$ is calculated after taking into account series contact resistances in the electronic system. The applied potential V_{DC} has been varied between 50 μV - 500 μV in different experiments to balance the inter-tip forces with an adequate SN. Typically $V_{DC} \sim 50$ μV was used to keep the inter-tip electrostatic force to a minimum.

After alignment the inter-NP separation is initially set to $d \sim 50$ nm and is then reduced in 1 nm decrements with the PZ stage. A DF scattering spectrum and DC current measurement are recorded after each step. Scans progress until Conductive Contact (CC) between the tips is detected, achieved once $G_{DC} > G_0 = 2e^2/h = 7.748 \times 10^{-5}$ S (a single conductance quantum, corresponding to an atomic point contact between the Au surfaces [162]). After CC, the tips are further pressed together with up to an additional 20 nm PZ displacement (corresponding to approximately 2 nN of additional compressive force) to establish firm, yet reversible, mechanical contact. As noted in Chapter (4) all forces calculated using k^z_{0i} can have up to a factor of 5 uncertainty in their value and hence all force measurements quoted throughout this chapter are taken as approximate (or even guideline) values.

As is commonly seen in conductive AFM and STM experiments a *short-range* StoC event is observed when attractive forces between the tips overwhelm the restoring force of the AFM cantilevers [163]. More specifically the condition for StoC is when the force gradient is greater than the effective spring constant of either cantilever

$$\frac{\partial \left(F^z_{EL} + F^z_{TT}\right)}{\partial d} > k^z_{ei} \tag{5.4}$$

As the applied potential in all experiments satisfies $V_{DC} < 0.5$ mV the theoretical simulation described in Sec. (4.2.2) shows that the electrostatic force (F^z_{EL}) is over 10^5 times less than the Van der Waals force at 7 nm $> d >$ 1 nm. Therefore, over the relevant range of d, the attractive Van der Waals component of F^z_{TT} primarily determines when Eqn. (5.4) is satisfied and at what separation StoC occurs. The theoretical model shows StoC typically occurs at $d \approx 5$ nm. Additionally, because the experiments are performed in ambient conditions, the Van

der Waals force causes the water layers (and possibly hydrocarbons) adsorbed on each Au tip-NP surface to become unstable and liable to StoC. This could slightly increase the StoC separation predicted, as the meniscus formed creates a large capillary force that snaps the NP functionalised tips closer together [164]. This situation is shown schematically in Fig. (5.5). It is noted here that as the applied potential is typically $V_{DC} \sim \mathcal{O}(\mu\text{V})$, electrostatic field induced meniscus bridging phenomena [165] are not expected to be present and the Van der Waals force is therefore the predominant factor controlling meniscus formation.

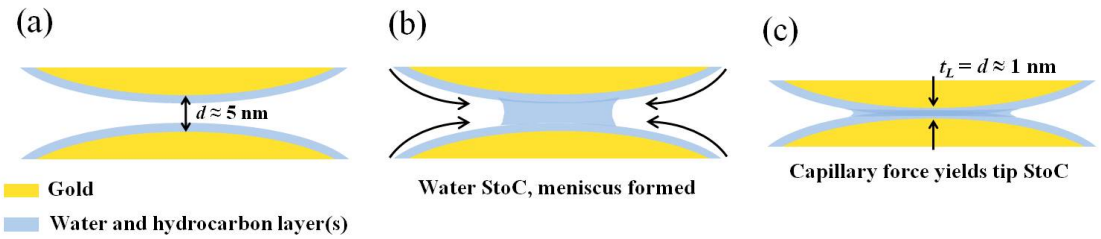

Figure 5.5: Schematic of tip-tip StoC process. (a) Tip apex NPs are separated at $d \approx 5$ nm. (b) At this point the attractive Van der Waals force cause the adsorbed water to become unstable and water-to-water StoC occurs forming a water meniscus. (c) The relatively strong capillary force causes the tip apex NPs to StoC while the remaining water and hydrocarbon molecular layers ($t_L \approx 1$ nm thickness) form an insulating barrier between the gold NP surfaces.

Additional evidence for the presence of water is given by the relatively large pull-off force (F_{PO}) typically required to fully break NP-NP (apex-apex) contact $F_{PO} \gtrapprox 70$ nN. This is commonly found in AFM studies in ambient conditions as the capillary force can dominate the contact adhesion strength [163]. This effect remains present when the tip apex NPs are under laser illumination thus indicating laser heating does not remove the adsorbed water layers or meniscus.

The Joule heating (caused by the absorption of laser light) in the vicinity of the NP tip apices is roughly estimated to result in a local temperature $T \sim 100\,^{\circ}\text{C}$ at the surface layer [117, 118, 166]. As the molecules are adsorbed (or close) on the Au surfaces it is expected significantly higher temperatures would be required to remove the water layers. This is consistent with the pull-off behaviour described above. Finally, it is noted here that the apex NPs are expected to have a cooling relaxation time $\tau_c \sim \mathcal{O}(\text{ns})$ [118]. Therefore the heating, and hence thermal expansion and contraction of the NGJ, is expected to

approximately follow the laser pulse train (20 MHz repetition rate), which has a mark-space ratio of 1/50. This will therefore have only a small effect on the average separation of the apex NP's over the spectrometer ($\tau_{int} = 3$ ms) and electronic DC amplification ($\tau_{int} = 35$ ms) integration periods.

The fact that StoC does not coincide with CC is also common in AFM and STM experiments performed under ambient conditions, as naturally-adsorbed surface layers ($t_L \approx 1$ nm - 2 nm thickness [167]), i.e. water and hydrocarbons, on the tip apices can provide electrical insulation [167–169]. The applied force required to push through the insulating layer is consistent with other conductive AFM studies [167, 169]. For simplicity the effect of the surface layer is not currently incorporated into the QCM. It is expected that such a surface layer will produce a confinement dependent red-shift in the resonance wavelength of the LSPP modes [170], and increase the quantum transport mediated conductivity [96, 171, 172].

5.4 Results

Each PZ scan investigates three interaction regimes: capacitive near-field coupling (50 nm $> d >$ 1 nm), non-local quantum regimes (1 nm $> d >$ 0 nm), and physical contact with conductive coupling ($d \leq 0$ nm). Crucially, this setup enables the resolution of the gradual transition between each regime dynamically. The measured DF scattering spectra shown in Fig. (5.6), within the capacitive regime ($d \sim 40$ nm), show a single LSPP scattering peak centred near $\lambda_0 \approx 765$ nm (mode A). This LSPP resonance is attributed to a hybridised version of one of the more 'NP apex localised' LSPPs described in Sec. (5.2.1). As d is reduced, this peak red-shifts and strengthens due to increasing near-field interactions between the LSPPs on each NP. As the cavity shrinks below 20 nm, a second LSPP scattering peak emerges at shorter wavelengths (mode B, $\lambda_0 \approx 560$ nm) and quickly increases in intensity.

Modes A and B smoothly red-shift, as described in Sec. (2.3.4), until an estimated separation $d \approx 5$ nm, whereupon attractive inter-tip forces overwhelm the AFM-cantilever restoring force and snap the tips into close proximity [163]. However no current flow is detectable because this StoC point does not coincide with CC and the metal surfaces remain separated. StoC reduces d to ~ 1 nm, significantly increasing the plasmonic interaction and dramatically changing the

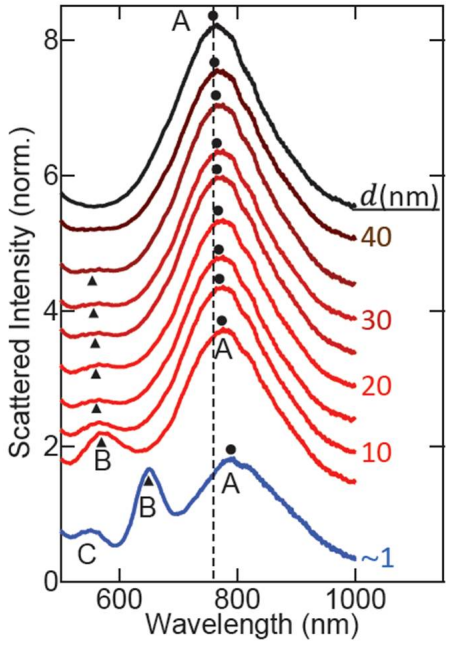

Figure 5.6: Measured DF scattering spectra (vertically offset for clarity) from the NP dimer at different separations d. The LSPP resonances are labelled A-C.

LSPP scattering resonances (blue curve, Fig. (5.6)). This increased coupling further red-shifts modes A and B and reveals a new higher-order resonance (mode C) resonant at $\lambda_0 \approx 550$ nm. After StoC, increased PZ displacement applies an additional compressive force (approximately 0.1 nN nm^{-1} of PZ displacement) pushing the NPs into closer proximity. In this particular experimental run, after 11.4 nN of externally applied force, current flow is detected through the tips, indicating metal-to-metal surface contact. Numerical QCM calculations confirm that the coupled LSPP modes observed are tightly confined in the NGJ and these modes are described in detail in Sec. (5.5).

As demonstrated in Fig. (5.7), simultaneously monitoring the optical and electrical properties during approach reveals unprecedented detail about LSPP evolution through the sub-nanometre regime. The experimentally measured scattering response displayed in Fig. (5.7a) shows that as the applied force increases and d is thus reduced, all three modes red-shift and modes A and B weaken while mode C intensifies. It is possible that the experimentally found linewidths of modes A and B decrease in concert with this reduced scattering strength while the broadening of mode C is due to increased scattering loss. These spectral changes are well-reproduced by the QCM simulations that include quantum tunnelling, shown in Fig. (5.7b).

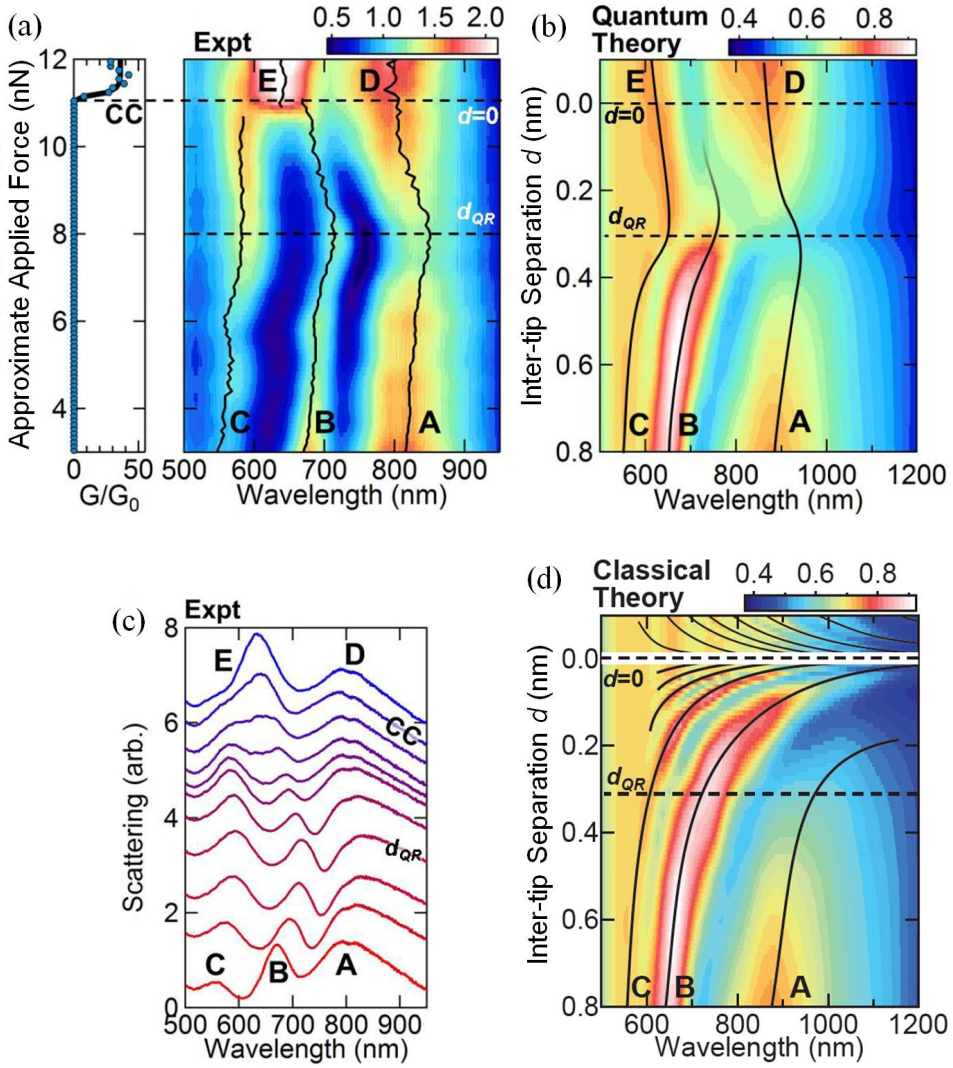

Figure 5.7: Optical detection of onset of quantum tunnelling in NP dimer with sub-nanometre separation. (a) Simultaneously measured electrical conductance and DF optical back-scattering as the force applied to the inter-NP cavity (after StoC) increases. Conductive contact indicates $d = 0$, with onset of the QR at d_{QR}. (b) Theoretical total scattering intensity from the model NP functionalised tip-tip system incorporating quantum mechanical tunnelling via the QCM [173]. The threshold (at d_{QR}) indicates where quantum-tunnelling-induced charge screening overcomes the near-field capacitive interaction between LSPPs. (c) Selected experimental spectra from the last 1 nm to contact in (a), shown vertically shifted for clarity. (d) Theoretical scattering intensity as in (b) but using a purely classical formalism. Solid **black** lines mark scattering peaks in (a), (b) and (d).

Inter-tip distance calibration is performed by identifying the characteristic red-shift to blue-shift LSPP mode behaviour at d_{QR} in the theoretical simulation

with the same characteristic d_{QR} transition point in the experimental data. Additionally, the spectral shifts in plasmonic modes at StoC found in simulation were matched to experiment, and the CC point was used to set $d = 0$. This quantum regime-based optical distance calibration ('plasmon ruler') using the QCM simulation is equivalent to a traditional distance calibration using electronic tunnelling current measurements and STM simulations. A method for approximately determining distance scales is thus obtained, which agrees with previous AFM studies showing StoC separations $d \sim \mathcal{O}(1\text{ nm})$.

For $d \gtrapprox 0.4$ nm, the LSPP interactions are approximately consistent with the classical NP dimer picture (Fig. (5.7d)) presented in Sec. (2.3.4). The classical LSPP interactions account for the rapidly increasing red-shifts as d decreases and the observed transfer of oscillator strength from modes A and B to mode C. While these higher-order coupled LSPP modes have been predicted theoretically [89, 90], they are now clearly revealed dynamically on approach.

Beyond 8 nN however, a new regime deviating strongly from the classical predictions is seen, with A and B now shifting back to shorter wavelengths instead of red-shifting asymptotically. This crossover is clearly seen in the QCM simulations at $d \approx 0.31$ nm. The quantum and classical predictions diverge at this crossover point (d_{QR}) because the plasmon interactions enter the quantum regime when d is sufficiently small to support a critical electron tunnelling rate between the surfaces. While electron confinement within each NP is minimally affected, the quantum tunnelling here dramatically modifies the correlations between electronic fluxes and ideally demands a more sophisticated treatment based on solving the time-dependent Schrödinger equation [153]. The net result is that QT charge transfer screens the LSPP surface charge, decreasing the enhanced fields and reducing plasmonic coupling. For $d < d_{QR}$, QT increases exponentially and quickly dominates, reducing the capacitative coupling, and resulting in Charge Transfer Plasmon Polariton (CTPP) modes that blue-shift as $d \to 0$.

It is expected that a combination of plasmon-assisted (plasmon enhanced photo-assisted) and plasmon-induced tunnelling transport mechanisms describe the LSPP coupling to electron tunnelling. Plasmon-assisted tunnelling is taken into account in the QCM, however plasmon-induced tunnelling is not considered as the contribution of hot electrons with $\Omega > \Omega_F$ to σ_0^{QT} is neglected. In both transport mechanisms, an optically induced (LSPP enhanced) oscillat-

ing ($\sim$ 100 THz) potential drives the optical frequency QT. Future investigations could apply a larger V_{DC} and hence further validate this hypothesis by direct measurement of a rectified DC photocurrent. It is also noted here that molecules within the NGJ could also enhance electron transport at specific frequencies unrelated the geometrically defined LSPP resonances.

After conductive contact ($d = 0$) when the conductance first jumps above G_0 before further increasing, two LSPP scattering peaks are observed, modes D (800 nm) and E (640 nm). Tracking modes A, B, and C through the QR as $d \to 0$ shows the gradual nature of this contact transition, in marked contrast to the singular transition predicted classically where a dense continuum of modes builds up in the touching limit, as shown in Fig. (2.13) [89,90]. At d_{QR} mode A weakens dramatically, before a new peak appears which blue-shifts and intensifies towards CC. While mode B weakens at d_{QR}, mode C strengthens as predicted by the QCM. In both theory and experiment, modes B and C are replaced by mode E on contact. Spectra and conductance change minimally for increasing contact force after CC, indicating a stable final contact. As described in general in Sec. (2.3.4), mode E is characterised by surface charge highly confined around the periphery of the contacted surfaces while the QCM simulations approximate the contact geometry as two smooth gold surfaces. The experimental contact geometry is unlikely to satisfy this assumption and the contact will be determined by the asperities of the rough gold coatings. The largest discrepancy is indeed at the CC point, where the uncertainty in the asperity-mediated contact geometry is greatest (with less effect at d_{QR}). Experiments on a variety of NP functionalised AFM tips show repeatable crossover behaviour at $d \approx d_{QR}$, with a typical example shown in Fig. (5.8). This crossover behaviour thus forms an optical fingerprint of the new tunnelling plasmonics regime.

In addition to the quantum-based simulations provided by the QCM, the experimental geometry was also modelled using an entirely classical framework, as shown in Fig. (5.7d). These results show that as $d \to 0$, the LSPP modes (A, B and C) continue to red-shift and higher-order modes continue to appear in the scattering spectrum. These observations are completely consistent with the classical picture of plasmonic interactions where, in the limit of tangentially touching spheres, a broadband mode continuum develops [174]. Several modes are also observed after contact (where $d < 0$) that blue-shift as the tip surfaces overlap further, similar to the results for overlapping spheres shown

in Sec. (2.3.4). Contrasting the classical simulations with the QCM results (Fig. (5.7b)) highlights the remarkable effect of QT on plasmonic interactions. Crucially, only by incorporating QT effects via the QCM can the experimental results be reproduced allowing the clear identification of where the plasmonic interaction crosses-over into the quantum regime.

For comparison, Fig. (5.8) presents the correlated electrical and optical characterisation of the NP functionalised tip-tip system from another representative experiment (using a different pair of NP functionalised AFM tips). These results were obtained under similar conditions as those described in Sec. (5.3), except the applied DC potential $V_{DC} = 0.5$ mV was 10 times greater. As described above, immediately at StoC (zero externally applied force) three modes (A, B, and C) are observed, each corresponding to a LSPP resonance of the NP functionalised tip-tip system. Less externally applied force is required to push through the insulating layer, likely due to the specifics of the atomic-scale geometry and the 100 times greater electrostatic force created by the larger applied potential, thus effectively reducing the resolution of the scan.

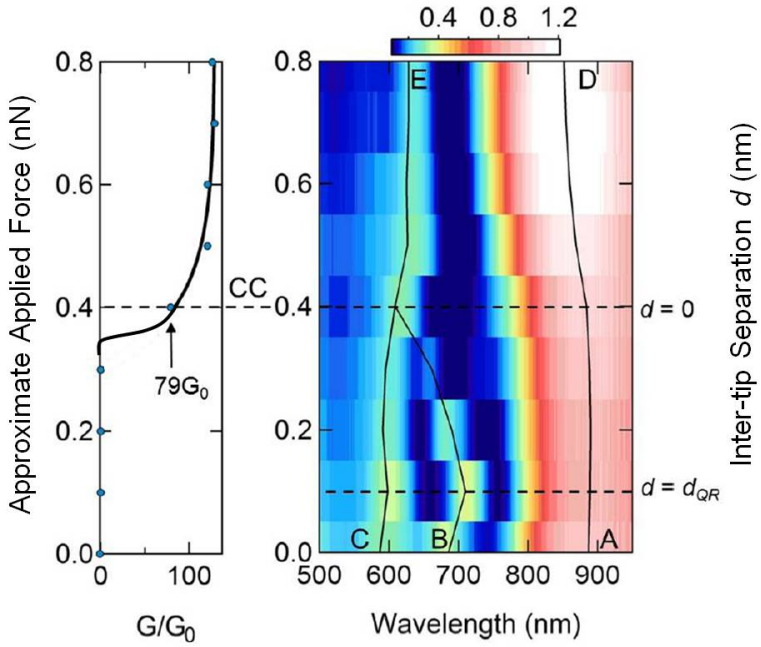

Figure 5.8: Simultaneously measured DC conductance and DF scattering versus the force applied to the inter-NP cavity.

Prior to CC, a crossover at $d = d_{QR}$ is observed where the LSPP modes stop red-shifting and begin blue-shifting. This crossover point is the optical signature

of QT modifying plasmonic coupling and corresponds to the threshold point where QT charge transfer counterbalances the near-field capacitive interactions between the metal surfaces. An evolution into only two modes after contact (D and E) is observed, as in all experiments. It should be noted that the relative strength of mode E is significantly less than that shown in Fig. (5.7a). This is likely because around CC the strengths of the LSPP modes are highly dependent on the precise experimental conditions, e.g. specifics of the contact geometry and molecular species present. Nonetheless, the spectral positions remain rather systematically robust. The DF scattering spectra and the NGJ conductance are observed to stabilise after CC, indicating the formation of a stable nanojunction after contact. Other experimental runs give similar results to those described here. It is important to note that this consistency also confirms the robustness of the NP dimer alignment technique.

To understand LSPP evolution through the QR, the cavity field-distribution is calculated within the QCM accounting for quantum effects, and is shown in Fig. (5.9). This allows a model to be constructed of tunnelling plasmonics (Fig. 5.9a). For $d > d_{QR}$ (I), spectra are dominated by the near-field interaction of the cavity-localised surface charges and LSPPs couple according to classical and hydrodynamic models. Once $d \sim d_{QR}$ the system enters the QR (II) and QT opens a conductance channel between the surfaces, modifying the LSPP charge distribution, screening the electric field, and reducing the interaction strength.

The tunnelling (which is strongly concentrated across the thinnest barrier region, due to the exponential dependence on separation) pinches off the field distribution in the centre of the nanogap, thus separating the single field lobe into two lobes in the contact crevices on either side of the neck (Fig. 5.9b). Although the light impinges from above, the field in the upper side crevice is weaker due to the asymmetry introduced by retardation. As d is reduced further (III) these QT CTPP modes, concentrated around the contact crevices, blue-shift as their apex becomes blunter. Around d_{QR} the mode strengths become weakest because the tunnelling increases sufficiently to screen the charges across the nanogap, but cannot provide sufficient current to drive the charge-transfer modes into the crevices. Hence at this point the total separated charge localised to the contact region decreases, reducing the optical cross-section.

The onset of quantum tunnelling fundamentally limits optical field confinement in plasmonic nanocavities, e.g. between NP dimers with sub-nanometre

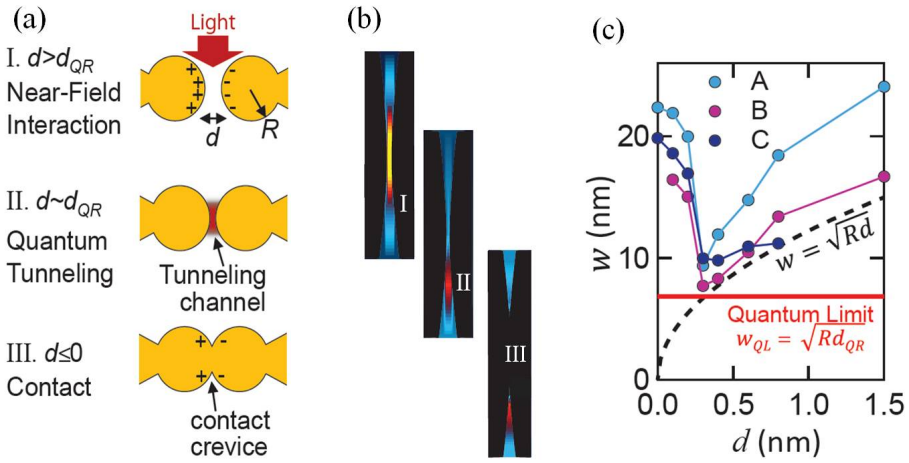

Figure 5.9: Evolution of the LSPP modes through the QR and the quantum limit of plasmonic confinement. (a) Plasmonic interactions within the three regimes accessed in experiment. (b) Near-field distributions for modes B $\rightarrow$ E from the QCM theory in each regime [173]. Images are of a 40 nm by 5 nm region, with the same intensity scale. (c) The lateral confinement width w of each mode, extracted from the simulated near-field distribution (FWHM of intensity maximum), as the cavity width d is reduced. The dashed line marks the classical approximation $w = \sqrt{Rd}$. The onset of quantum tunnelling effects at $d = d_{QR} = 0.31$ nm sets a quantum limit (w_{QL}) on LSPP mode confinement in sub-nanometre plasmonic cavities.

separation. The plasmonic surface charge between two spherical surfaces is confined laterally to $w \approx \sqrt{Rd}$ [89], as confirmed by the simulations shown in Fig. (5.9b). However, QT limits w to $w \geq w_{QL} = \sqrt{Rd_{QR}}$. Further reducing d rapidly increases w, as the surfaces are quantum-mechanically blurred at this atomic-scale. The tunnelling plasmonics regime thus represents the quantum limit of compression of light which is plasmonically-squeezed into a nanogap, as verified in our experiments and QCM calculations. The quantum-limited mode volume is approximated as $V_{\text{min}} = \frac{1}{4}\pi R\, d_{QR}^2$ and estimated to be $V_{\text{min}} \approx 1.7 \times 10^{-8}\lambda_0^3$ from the experiments at λ_0 = 850 nm (mode A at d_{QR}). Here it is assumed the physical volume is approximately equal to the mode volume found from Purcell analysis as the vast majority of the energy stored in the electric near-field is contained within the nanogap rather than the Au NPs [175]. As this limit for plasmonics is six orders of magnitude smaller than the tightest field confinement observed in photonic crystal cavities [176], it still offers unprecedented opportunities for directly visualising atomic-scale and molecular processes with eV-scale photon energies.

5.5 Analysis

In this section a toy model developed to enable an intuitive explanation of the quantum tunnelling mediated LSPP behaviour is first presented, followed by a more in-depth analysis of the character of the LSPP modes A, B and C.

5.5.1 Tunnelling Plasmonics Regime

With the onset of QT charge transfer, the LSPP charge distributions are modified by the conductive coupling. To provide an intuitive, physical description of LSPP interactions transitioning into the QT regime, a simple and crude model of QT and the effect it has on plasmonic charge localisation was developed. The approach follows that in [98], where the plasmonic properties of NP dimers linked by a conductive nanojunction were examined in a purely classical formalism. However, here the model is extended to the case where the nanojunction conductivity is determined by the QT properties of a nanogap.

The LSPP surface charge Q_{SP} is given by

$$Q_{SP} = \varepsilon_0 E_{SP} A_{SP} \tag{5.5}$$

where E_{SP} is the LSPP-enhanced local field, A_{SP} is the surface area of the LSPP, and a vacuum environment is assumed. When the surfaces are close enough to allow QT across the nanogap, a charge Q_{QT} is transferred between the surfaces over a half optical cycle ($\tau_{1/2} = \lambda_0/2c$) given by

$$Q_{QT} = \sigma_0^{QT}(d)\, E_{QT} A_{QT} \lambda_0 / 2c \tag{5.6}$$

where $\sigma_0^{QT}(d)$ is the DC conductivity of the QT junction, E_{QT} is the electric field driving the QT, and A_{QT} is the QT nanojunction area. Herein it is assumed that the electron tunnelling time is short compared to the optical half-cycle. The QT channel transfers this charge across the nanogap, thereby neutralising a fraction X of the LSPP charge

$$X = \frac{Q_{QT}}{Q_{SP}} = \sigma_0^{QT}(d)\, \frac{\lambda_0}{2\varepsilon_0 c} \tag{5.7}$$

where it is assumed that $A_{SP} = A_{QT}$ and $E_{SP} = E_{QT}$ (a good approximation

given R is large). In the low-voltage domain ($eV_{opt} \ll (\Omega_F \wedge \varphi_{WF})$), the DC tunnelling conductivity of a planar metal-insulator-metal junction is calculated as

$$\sigma_0^{QT}(d) = \left(\frac{4\pi m_e^* e^2}{h^3}\right) d \int_0^{\Omega_F} T^{QT}(\Omega, d)\, d\Omega \tag{5.8}$$

Accurate determination of the realistic tunnelling probability $T^{QT}(\Omega, d)$ and associated $\sigma_0^{QT}(d)$ requires the full theoretical approaches previously mentioned. However, in the simplest case of a 1D rectangular energy barrier (no image potential) of height φ_{WF} the solution to Eqn. (5.8) is analytic (WKB approximation) [177], and therefore Eqn. (5.8) simplifies to

$$\sigma_0^{QT}(d) = \frac{3q^{QT}e^2}{4\pi h} \exp\left(-2q^{QT}d\right) \tag{5.9}$$

where $q^{QT} = \sqrt{2m_e^*\varphi_{WF}}/\hbar$ is the semi-classical electron tunnelling wavenumber. In Fig. (5.10a), the QT conductivity calculated for this simple model is compared against that predicted by the appropriate DFT calculations used in the QCM (using the Au work function as barrier height ($\varphi_{WF} = 4.8$ eV)).

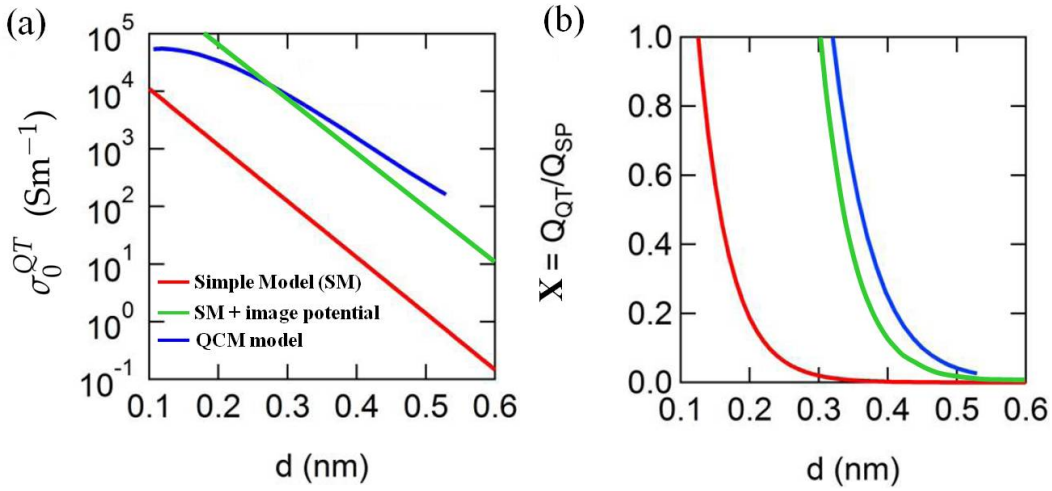

Figure 5.10: (a) DC conductivity σ_0^{QT} of a NGJ of width d. The tunnelling probability is determined using a rectangular barrier (simple model, red), simple model with image potential correction (**green**) and DFT simulations (QCM model, blue). (b) Fraction X of LSPP charge (Q_{SP}) transferred by quantum tunnelling (Q_{QT}) at different barrier widths [173].

At $d = 0.31$ nm, the quantum crossover point d_{QR} defined in Sec. (5.4), the simple model predicts $\sigma_0^{QT} = 98.6$ Sm^{-1} which is much smaller than the 7.4×10^3 Sm^{-1} calculated under the QCM model. This discrepancy is unsurprising given the simplicity of the rectangular barrier model used to derive Eqn. (5.9). A more complex expression for σ_0^{QT} that includes the reduction of the height and width of the potential barrier due to the image potential is also considered (Fig. (5.10)) [177][3]. When the effect of the image potential is recognised the agreement is improved dramatically with $\sigma_0^{QT} = 5.3 \times 10^3$ Sm^{-1} at $d = 0.31$ nm.

Using Eqn. (5.7) and the calculated $\sigma_0^{QT}(d)$ from the simple, improved and QCM models, the fraction X of the LSPP charge transported per half-cycle (Fig. (5.10b) is calculated. These results were obtained for $\lambda_0 = 850$ nm which is near the LSPP resonance wavelengths observed in theory and experiment. At $d = 0.36$ nm, the full theory predicts that half ($X = 0.5$) the LSPP charge is transferred across the nanogap, near the $d_{QR} = 0.31$ nm crossover point obtained by the full numerical simulation (Fig. (5.7b)). An intuitive explanation for the QR red-shift to blue-shift crossover is therefore found as the critical point where sufficient charge is transported between the NPs to modify the LSPP charge distribution.

Combining Eqn. (5.7) and Eqn. (5.9), setting $X = 0.5$, and noting that the fine structure constant $\alpha = e^2/2\varepsilon_0 hc \approx 1/137$ gives

$$d'_{QR} = \frac{1}{2q^{QT}} \ln\left[\frac{3q^{QT}\lambda_0\alpha}{2\pi}\right] = \frac{1}{2q^{QT}} \ln\left[\frac{3q^{QT}\alpha c}{\omega}\right] \tag{5.10}$$

Evaluated for $q^{QT} = 1.1$ Å^{-1} ($\varphi_{WF} = 4.8$ eV) and $\lambda_0 = 850$ nm, Eqn. (5.10) gives $d'_{QR} = 0.16$ nm. Full QCM calculations show that already at $d_{QR} = 0.31$ nm sufficient screening develops via the quantum transport to overcome the increasing charge buildup, consistent with the estimate for d'_{QR} above that is based on a reduced tunnelling conductivity. The expression for σ_0^{QT} that includes image potential effects can be evaluated graphically and yields a value of $d'_{QR} = 0.35$ nm in good agreement with d_{QR} estimated from the QCM. Therefore properly including the coherent quantum transport strongly enhances the tunnelling rate, increases the distance at which tunnelling plasmonics takes over, and hence dic-

[3]The expression for the image potential used by Simmons in [177] is a factor of two too large and was corrected accordingly.

tates the emergence of QT mediated CTPPs. Thus it is shown that this simple charge transfer time-scale model provides a reasonable estimate of the onset of the QR in LSPP interactions. The logarithmically increasing dependence of d'_{QR} with λ_0 shown in Eqn. (5.10) is unphysical, however the expression is approximately valid. A more detailed analysis is provided in Appendix (A).

5.5.2 Understanding the Plasmonic Modes

An improved understanding of the measured LSPP modes is gained by considering the simulated near-field distributions in the QCM. First, over the whole NP at the tip apices (shown schematically in Fig. (5.11a) and Fig. (5.11b)), before examining the field distribution in the inter-NP nanocavity itself. The calculated z-component of electric near-field (magnitude $|\widetilde{E}_z|$ and phase φ_z) for modes A, B, and C at a separation $d = 0.6$ nm are shown in Figs. (5.11c-5.11h), corresponding to the geometry in Fig. (5.11b). Note that a logarithmic colour-scale for $|\widetilde{E}_z|$ is used to help visualise the weaker fields away from the nanocavity. Only the z-component of the field is considered as it is much stronger than the x- and y-components and more important for the plasmonic interactions in this geometry since it is parallel to the NP dimer (tip-tip) axis.

Nanocavity localisation is observed for each LSPP mode although the field enhancement associated with modes B and C is greater than that for mode A. The maximum field enhancement (normalised to the incident field) in the nanocavity for modes A, B, and C is approximately 300, 550, and 350, respectively. It is indeed found that mode A is relatively weakly localised to the nanocavity and is spread out over more of the extended neck-NP structure, whereas modes B and C are nanocavity resonances with tightly confined surface charge.

While the LSPP modes of simple individual NP homo-dimers are well known, those for dimers with constituent NPs on the end of long conductively connected tips remain poorly understood. In contrast to an isolated NP dimer, it is found that LSPP modes with a certain symmetry in electric field magnitude over the whole tip-NP system can have a different local symmetry in field magnitude within the nanogap volume. This is the case for modes A, B and C. The phase distributions in Fig. (5.11) show that the field varies more rapidly around the NP for modes B and C than for mode A, indicating that modes B and C are

higher-frequency LSPP resonances of the whole system. However the modes cannot be labelled hybridised dipole, quadrupole etc. by just considering their nature in the nanocavity. The distinction between the field symmetry has to be qualified whether in the nanocavity or of the entire NP-tip structure.

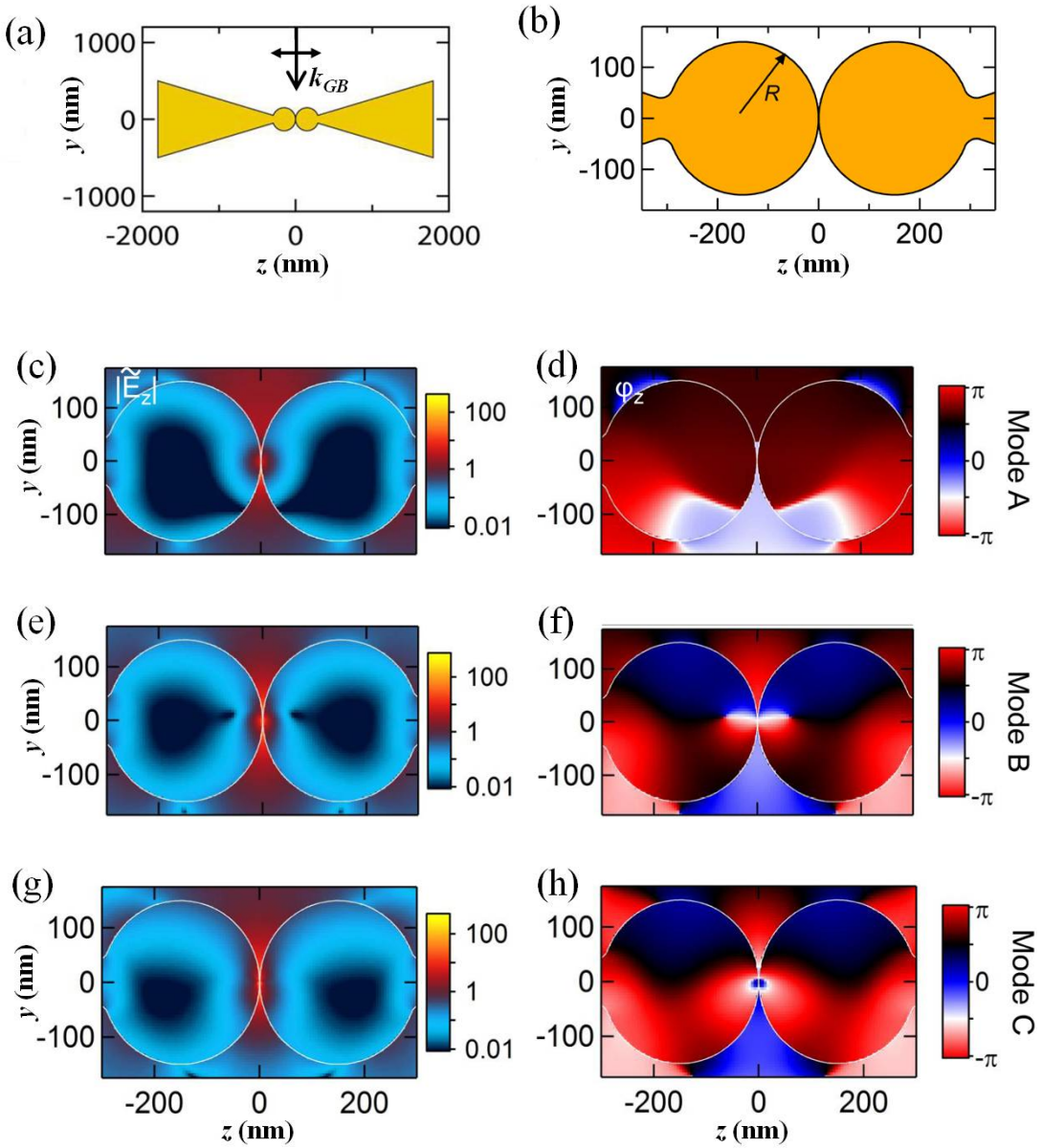

Figure 5.11: Near-field magnitude and phase in the vicinity of the AFM tips apex NPs [173]. Schematic showing (a) the simulated dual tip-NP geometry and (b) the geometry at the NP apices (with neck emphasised). (c,e,g) The QCM-calculated near-field magnitude ($|\tilde{E}_z|$) of the NP dimer shown in (b) at a separation $d = 0.6$ nm for modes A, B, and C. (d,f,h) Associated phase (φ_z).

Within the nanogap region, defined in Fig. (5.12a), the phase varies smoothly through the NP-NP nanocavity for modes A and B, suggesting local hybridised dipolar-like field distributions. This can be seen more clearly in the zoomed in field distributions of Fig. (5.12).

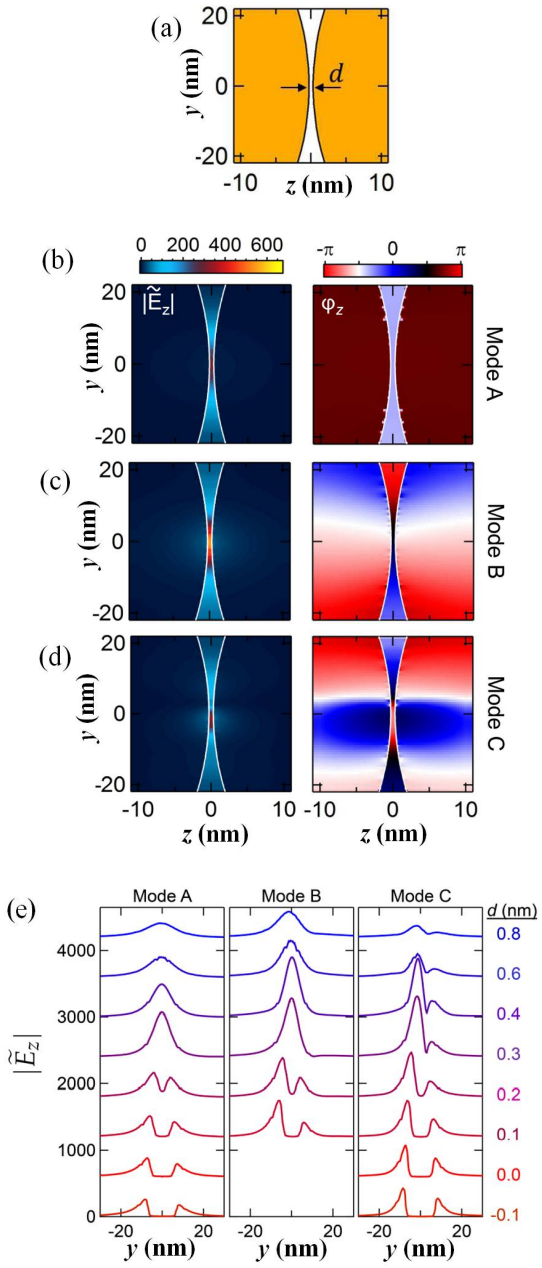

Figure 5.12: (a) Nanogap geometry. The NP dimer nanocavity-localised near-field distributions (magnitude $|\widetilde{E}_z|$ and phase φ_z) for modes (b) A, (c) B, and (d) C at a separation $d = 0.6$ nm [173]. The white line demarcates the NP surface. (e) The near-field magnitude of modes A, B, and C along a line midway between the NP surfaces for different separations, at $x = z = 0$.

The π phase jump in the nanocavity observed for mode C indicates it is a higher-order nanocavity resonance consistent with a hybridised quadrupolar charge distribution in the nanogap arising from the rapid charge oscillation characteristic of higher-order resonances created via plasmon hybridisation [74, 89].

To compare the localisation of the three LSPP modes in the nanogap, the electric field confinement factor γ_C is calculated and is given by

$$\gamma_C = \frac{\int_{\text{cavity}} \left|\widetilde{E}\right|^2 dy\, dz}{\int \left|\widetilde{E}\right|^2 dy\, dz} \tag{5.11}$$

where the nanocavity domain is defined by a $(\Delta y,\, \Delta z) = (40\text{ nm},\, 20\text{ nm})$ area centred at $(y,\, z) = (0,\, 0)$ and the denominator integral spans the entire simulation region. At a separation of $d = 0.4$ nm, this yields confinement factors of 0.57, 0.78, and 0.79 for modes A, B, and C, respectively, showing that the field intensity distribution associated with modes B and C is more concentrated within the nanocavity than the mode A field intensity.

The differences in nanocavity confinement and peak field enhancements indicate that the LSPP charge associated with mode A is less-localised to the cavity and extends over more of the neck-NP structure in comparison to modes B and C. For these reasons, as the AFM tips (NPs) approach, the experimentally measured red-shift of mode A is significantly less than that of modes B and C, as shown in Fig. (5.6). This also partially explains why the quantitative agreement between experiment and the QCM for the wavelength and linewidth of mode A is not as close as for modes B and C. The relatively extended nature of mode A increases the susceptibility of the mode to the geometry of the extended neck (and possibly AFM tip structure). These geometrical aspects are particularly challenging to exactly reproduce in the theoretical treatment, and thus a greater discrepancy between experiment and theory is to be expected.

The electric near-field along a line midway between the NP surfaces as the nanocavity width is reduced is shown in Fig. (5.12e). For $d > 0.3$ nm, modes A and B show a single field maximum at the point on the NP dimer axis ($y = 0$) while mode C, being higher-order, exhibits a rapid field oscillation. At $d = 0.2$ nm, the QT charge transfer has increased sufficiently to suppress the field near

the QT channel at $y = 0$, indicating the emergence of QT charge-transfer modes before contact. When the NPs eventually touch ($d = 0$ nm), the field is completely excluded from the centre point and localised to the anti-wedge regions in the crevices around the contact. Overlapping the NP surfaces produces contact modes similar to those seen for classical overlapping NP dimers (Sec. (2.3.4)), although QT blurs the apex of the anti-wedge regions in contrast to the infinitely sharp geometries considered in such classical simulations [75, 89, 170].

Finally, it is difficult to determine discrepancies between experiment and the theoretical QCM that allude to other non-local effects that are not fully taken into account, e.g. non-local screening phenomena. It is important to consider the main sources of such possible discrepancies in more detail, as listed below

- Non-local screening and confinement effects not taken fully into account in the QCM (outside the tunnelling volume) that are expected to blue-shift (reduce the magnitude of the red-shift of the LSPP modes before d_{QR}) and slightly broaden the LSPP modes.

- The molecular layer(s) present in the NGJ are not considered in the QCM and are likely to modify σ_0^{QT} and red-shift the LSPP modes. Such layer(s) could account for the discrepancy in strength of LSPP modes B and C found experimentally compared to those obtained from the QCM.

- Idealised geometry used in the QCM, most notably the simplifications of the smooth 50 nm Au coating, neck region and tip length can all modify the wavelength and linewidth of the LSPP modes.

- Different dielectric properties of the thin-film Au tip coating compared to those used in the QCM could strongly modify the linewidth of the LSPP modes. This could be the primary reason for the increased linewidth of all LSPP modes predicted by the QCM compared to experiment.

- Assumed 1D (smooth interface surfaces) linear (low-voltage domain) tunnelling. It is quite possible the large field enhancements at the NGJ and relatively intense laser illumination drive the system into a non-linear photoemission regime [178]. Additionally, plasmon-induced transport is not considered, and is likely to increase σ_0^{QT} yet further.

- Illumination and collection conditions, e.g. light scattering from the base of the tip modelled in the QCM would not be collected in experiment as all light scattering from outside the NP apex region is spatially filtered.

All of these points will be addressed in future theoretical work, and the influence such approximations have on the predictions will be critical to understand. It is interesting to note that certain *relative* effects not predicted by the QCM are observed in the experimental data, e.g. the reduced magnitude of LSPP mode red-shift before d_{QR} and the significantly increased linewidth of mode E compared to modes B and C (Fig. (5.7a)). The reduced magnitude of red-shift has been predicted by recent full hydrodynamic simulations and found experimentally [179], while the linewidth discrepancy is predicted by *ab initio* TDDFT calculations [153]. Both studies include the additional non-local screening effects not treated in the QCM and therefore might suggest that these particular discrepancies could be due to non-local surface charge smearing. However, these remaining non-local effects are clearly not the dominant physical processes determining the LSPP mode behaviour in the deep sub-nanometre NGJ regime.

5.5.3 Coherent Plasmon-Exciton Coupling

Evidence of the extremely small mode volumes accessed (Sec. (5.4)) may indeed have already been measured experimentally. As introduced in Sec. (2.3.3), under certain conditions the hybridisation of an active emitting molecular transition and a LSPP mode is possible. When the hybridisation is sufficiently strong the coherent coupling forms a mixed-state of a plasmon and molecular exciton, a plasmon enhanced exciton-polariton. In this case it is possible that the active species are hydrocarbon molecules adsorbed on the Au NP surfaces due to, e.g. operating in ambient conditions, SEM contamination or packaging contamination.

Achieving strong plasmon-exciton coupling depends on the enhancement of the Local Density Of photonic States (LDOS) at the positions of the molecules, the oscillator strength of the emitting molecular transition, the spectral overlap of the relevant LSPP mode and molecular transition, and the number of molecules present [180–182]. Assuming the molecules are aligned parallel with the NP dimer axis an estimate of the maximum LDOS enhancement (γ_{LDOS}) within the NGJ is found from the Purcell factor (F_p) associated with LSPP modes

$$\gamma_{LDOS} \approx F_p = \frac{3Q^{\ell}_{LSPP}}{4\pi^2 V}\left(\frac{\lambda_0}{n_{air}}\right)^3 \tag{5.12}$$

For LSPP mode B at $V = V_{\min}$ this yields a value of $\gamma_{LDOS} \approx 5 \times 10^7$ that is generally 10^3-10^4 times greater than the values currently experimentally realised [175, 176, 183, 184]. This extreme enhancement of the LDOS can be attributed to the quantum-limited mode volume achieved, the relatively high value of $Q^{\ell}_{LSPP} \approx 15$ for LSPP mode B, and the low refractive index of the NGJ air medium.[4] Following from Fermi's golden rule, the spontaneous radiative decay rate of a quantum emitter is proportional to the number of photonic states the local environment offers for the decay. Thus the radiative decay rate associated with the molecules in the NGJ is strongly enhanced.

For plasmonic cavities the Purcell factor can only be considered as an approximate guideline for the true LDOS value. More rigorous calculations that include absorption show that Purcell analysis generally significantly underestimates the LDOS in plasmonic NGJs [175]. For plasmonic (lossy) NGJs the *sum* of the radiative (η^r_m) and non-radiative (η^{nr}_m) decay rates is proportional to the LDOS, $(\eta^r_m + \eta^{nr}_m) \propto$ LDOS, rather than the $\eta^r_m \propto$ LDOS relation found when assuming the cavity is loss-less. The molecular species expected to be present in the NGJ are likely to have relatively low free-space quantum efficiency, e.g. $\eta^r_0/(\eta^r_0 + \eta^{nr}_0) \sim 10^{-2}$ where η^r_0 and η^{nr}_0 are the free-space radiative and non-radiative decay rates associated with the emitting molecular transition. It is therefore expected that non-radiative decay is dominant. However, in the large closely-spaced NP dimer systems used here, the scattering is very strong and dominates absorption. It is therefore expected that η^r_m will be strongly enhanced compared to η^{nr}_m as the NP dimer does not provide relatively many additional, fast, non-radiative routes for decay. In the following simple model it is therefore assumed that the contribution to the plasmon-molecule coupling from the enhanced non-radiative decay (quenching) is negligible compared to the contribution from the enhanced radiative decay.

Additionally, the large electric-field in the NGJ ($E \sim 10^9$ Vm^{-1}) maximises (up to saturation) the absolute number of excitation (and therefore emission) events. It should also be noted that this plasmonic dimer approach also removes

[4] Note the LDOS value stated would be reduced by approximately a factor of two if the NGJ medium was taken to be water.

some of the difficulty in placing the quantum emitters at the precise position of maximum electric field enhancement (maximum LDOS) and strength (maximum absolute number of interaction events). In this case the cavity (NGJ) is formed around the quantum emitters rather than having to precisely place the quantum emitters in the cavity, e.g. at a field anti-node in a planar microcavity.

A simplified classical coupled harmonic oscillator model can be used to approximately describe the light-exciton coupling [185]. Under the assumptions that the excitonic molecular absorption transition energy (E_m^A) and emission transition energy (E_m^E) are approximately equal and resonant with the LSPP mode (zero de-tuning), i.e. $E_m = E_{LSPP}^{\ell} \approx E_m^A \approx E_m^E$, the two conditions required for strong coupling in a plasmonic nanocavity are [181, 185]

$$g > \frac{\left|\Gamma_{LSPP}^{\ell} - \Gamma_m\right|}{4} \tag{5.13}$$

$$\Omega_R > \frac{\left(\eta_{LSPP}^{\ell} + \eta_m\right)}{2} \tag{5.14}$$

where g is the 'zero linewidth' coupling energy between the molecular transitions and the LSPP mode, Γ_m is the total homogeneous plus inhomogeneous linewidth of the emitting molecular transition, η_{LSPP}^{ℓ} and η_m are the total decay rates of the LSPP mode and emitting molecular transition[5] respectively, and Ω_R is the Rabi-oscillation frequency.

The first condition (Eqn. (5.13)) is generally satisfied when g is large and the molecular transitions are 'impedance' matched with the LSPP mode, i.e. equal in linewidth.[6] The second condition (Eqn. (5.14)) shows that strong coupling begins to become evident when the light-exciton energy transfer rate (Ω_R) is on the order of, or greater than, the individual total decay rates associated with the emitting molecular transition and the LSPP mode. Under this condition, a periodic exchange of energy at frequency Ω_R (vacuum Rabi-oscillations[7]) can

[5] Note the total decay rate η_m includes contributions from additional homogeneous broadening (due to the large number of non-radiative decay routes), and inhomogeneous broadening, and thus is significantly greater than $(\eta_m^r + \eta_m^{nr})$.

[6] This condition is not satisfied for quantum dots at room temperature in high-Q cavity systems. Room temperature strong coupling in high-Q systems can be achieved using relatively large numbers of organic molecules with large oscillator strengths, such as J-aggregates [186].

[7] Multi-photon effects are negligible due to low cavity Q-factor (short cavity photon lifetime).

occur between the coupled plasmon-exciton modes before the excitation decays. Under the assumption that Eqn. (5.13) is satisfied, the magnitude of the Rabi-splitting energy ($\hbar\Omega_R$) is found to be [185]

$$\hbar\Omega_R = 2\left(g^2 - \frac{\left(\Gamma^{\ell}_{LSPP} - \Gamma_m\right)^2}{16}\right)^{1/2} \tag{5.15}$$

Furthermore, neglecting non-radiative decay effects, an analytical expression for g is found to be [181]

$$g^2 \approx \frac{1}{2}\hbar^2\eta^r_0\eta^{\ell}_{LSPP}\gamma_{LDOS}N_m \tag{5.16}$$

Now making the valid assumption that $\Gamma_m \sim \Gamma^{\ell}_{LSPP}$ at room temperature enables an approximate expression for the Rabi-splitting energy to be determined by substituting Eqn. (5.16) into Eqn. (5.15)

$$\hbar\Omega_R \approx \left(2\hbar\Gamma^{\ell}_{LSPP}\eta^r_0\gamma_{LDOS}N_m\right)^{1/2} \tag{5.17}$$

where N_m is the number of molecules present in the NGJ. Note that η^r_0 is proportional to the oscillator strength of the emitting molecular transition. Substituting Eqn. (5.17) into Eqn. (5.14) yields the condition for the onset of measurable strong plasmon-exciton coupling

$$\eta^r_0 \gtrapprox \frac{\left(\Gamma^{\ell}_{LSPP} + \Gamma_m\right)^2}{32\hbar\Gamma^{\ell}_{LSPP}\gamma_{LDOS}N_m} = \frac{\left(\eta^{\ell}_{LSPP} + \eta_m\right)^2}{16\eta^{\ell}_{LSPP}\gamma_{LDOS}N_m} = \frac{\eta_{SC}}{N_m} \tag{5.18}$$

where η_{SC} is the 'strong coupling' decay rate (defined for brevity).

The total decay rate associated with the plasmonic nanocavity is typically $\eta^{\ell}_{LSPP} = \Gamma^{\ell}_{LSPP}/2h \approx 1 \times 10^{13}$ s^{-1}. A standard dye-molecule has $\eta^r_0 \sim 0.25 \times 10^9$ s^{-1} and $\eta_m = 6 \times 10^{12}$ s^{-1} [181], and hence, for LSPP mode B, $(\eta^r_0/\eta_{SC})N_m \sim (10^3)N_m$. Using this analysis for systems where strong coupling to single quantum dots has been observed yields $(\eta^r_0/\eta_{SC}) \sim 10$ for a typical microcavity system [182] and $(\eta^r_0/\eta_{SC}) \sim 100$ for a typical photonic crystal nanocavity system [184]. Both experiments are performed at cryogenic temperatures to keep the total linewidth of the quantum dot's transitions low compared to that of the

high-Q cavity mode linewidth. This implies Eqn. (5.13) is satisfied, and Eqn. (5.18) is valid to good approximation. Therefore, as expected, the condition for the onset of strong coupling is satisfied in both cases. For the present NP dimer system this basic model therefore demonstrates the condition for strong coupling could be satisfied by at least three orders of magnitude. The extreme enhancement of the LDOS and relatively large LSPP mode linewidth relax the general requirement for quantum emitters with strong, narrow absorption and emission transitions. Analysis shows that even for molecular transitions with $\Gamma_m \sim 0.5$ eV ($\Delta\lambda_0 \sim 200$ nm at $\lambda_0 = 670$ nm) strong coupling could be possible, i.e. Eqn. (5.13) and Eqn. (5.14) are satisfied. Therefore, even for the weak, broad absorption and emission transitions expected for the molecules situated in the present NGJ, measurement of mixed plasmon-exciton modes may be feasible.

Unexplained Experimental Results

The molecules present in the NGJ are expected to have significantly weaker active transition oscillator strengths compared to standard dye molecules or quantum dots, however spectral signatures of strong coupling such as mixed LSPP-exciton mode-splitting or anti-crossing may still be measurable [181]. Anomalous mode-splitting is indeed observed in the same experimental runs shown in Fig. (5.7a) and Fig. (5.8). The measured scattering spectra taken just after StoC, i.e. the region below 3 nN of applied force not shown in Fig. (5.7a), are shown in Fig. (5.13).

At $d \sim 1$ nm mode B splits into two distinct peaks before converging back to a single peak as d is reduced further. At $d \sim 1$ nm, $\frac{\eta_m^r}{\eta_{SC}} \sim 50N_m$ for mode B. This shows strong coupling might be possible, even for molecules with broad transitions and relatively low oscillator strength. It is proposed that initially, as d decreases, the available LDOS in the vicinity of the molecules increases (and molecular alignments possibly change) and thus the mixed mode-splitting becomes greater. It is suggested that the disappearance of the the mixed mode-splitting could be due to the molecules re-orientating, photobleaching, or being progressively 'pushed' out of the NGJ as d is reduced to the atomic-scale.

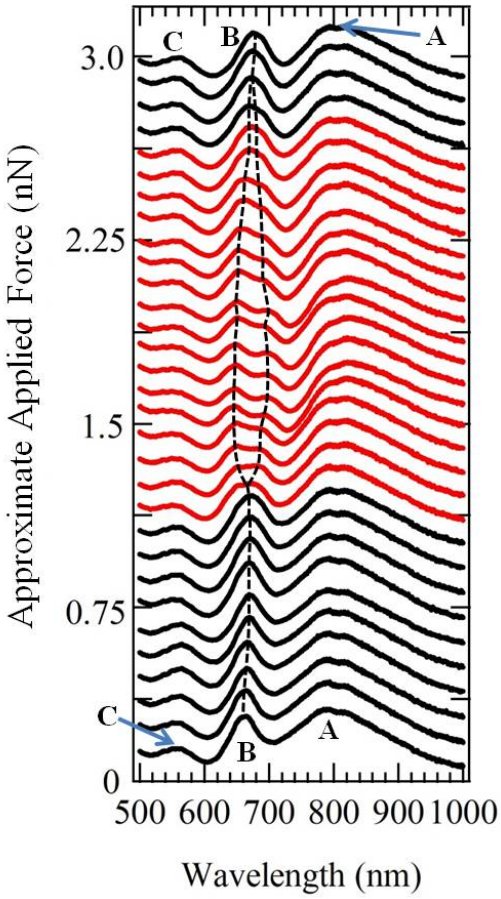

Figure 5.13: Evolution of LSPP modes with increasing applied compressive force (reducing d) after StoC. Dashed **black** lines guide the eye. Mode B has clearly split into two distinct peaks (possibly two mixed plasmon-exciton modes (red spectra)) at around 1.9 nN of applied force ($d \sim 1$ nm).

To fully verify that the strong coupling regime has been reached would require tuning of either the molecular transition (exciton) energy or the LSPP mode energy in order to observe anti-crossing behaviour of the mixed plasmon-exciton modes. However, at around zero de-tuning, the two peaks in the scattering spectra are expected to be approximately similar in shape and cross-section, as both correspond to equally mixed plasmon-exciton modes [181,182,187]. Fortuitously, the mode-splitting shown in Fig. (5.13) shows two approximately similar peaks around 1.7 nN of applied force (20% difference in height). Therefore, from the peak-splitting, approximate values for the Rabi-splitting energy and molecular exciton emission energy can be extracted, and are found to be $\hbar\Omega_R \approx 150$ meV and $E_m \approx 1.8$ eV respectively. It is expected the true value for

Ω_R will be slightly less than that determined here, however reasonable conclusions can still be made.

Using the experimentally found value of Ω_R and assuming the limiting case of very broad absorption and emission molecular transition linewidths $\Gamma_m \approx 0.5$ eV, i.e. $Q_m \approx 3.5$ (linewidth approximately an order of magnitude greater than that of a typical J-aggregate), yields $g \approx 125$ meV (calculated from Eqn. (5.15)) and (just) satisfies the strong coupling conditions. The free-space spontaneous radiative decay time of the molecules in the NGJ can now be estimated from g (Eqn. (5.16))

$$\tau_0^r \approx \frac{\hbar^2 \eta_{LSPP}^{\ell} \gamma_{LDOS} N_m}{2g^2} \tag{5.19}$$

Evaluating Eqn. (5.19) yields $\tau_0^r \sim$(5 ns $\times N_m$). If the NJG contains only one active molecule then $\tau_0^r \sim 5$ ns, however if the NGJ is full with active molecules of similar size to water then $\tau_0^r \sim 10$ μs. These radiative decay times determine the approximate range of oscillator strength (f_m) that could be associated with the active molecules within the NGJ. If one molecule is present $f_m \approx 4$ and if the NGJ is full $f_m \sim 2 \times 10^{-3}$ ($N_m \approx 4000$). Typical quantum emitters have oscillator strengths ranging from $f_m \sim 0.5$ for weakly emitting organic molecules to $f_m \sim 50 - 100$ for large inorganic quantum dots. Therefore it is possible extremely weak transitions are measurable due to the strong coupling with the nanocavity LSPP mode.

It is interesting to note the same effect is possibly briefly observed in Fig. (5.8) around 0.3 nN of applied force. The associated scattering spectra are shown in Fig. (5.14). Analysis of the data shows that the mixed mode-splitting is approximately 40% greater in magnitude, and centred slightly to the right ($\lambda_0 = 690$ nm), of that shown in Fig. (5.13). This could indicate the same molecular species is present in both experimental runs, even though a different pair of NP functionalised AFM tips were used. In this case the increased mixed mode-splitting of the disimilar peaks observed could be primarily due to the different energy of LSPP mode B (different de-tuning) and the reduced NP separation (modified LDOS). As the peak-splitting occurs within the quantum regime, analysis of the results is further complicated by the strong tuning (blue-shifting) of LSPP mode B. Therefore, an approximate value for the Rabi-splitting energy cannot be extracted from these low resolution measurements. Finally, perhaps due to the weak coupling between the LSPP mode and molec-

ular excitons at around 0.2 nN of applied force, it is noted that the lineshape of LSPP mode B abruptly changes just before mode-splitting occurs.

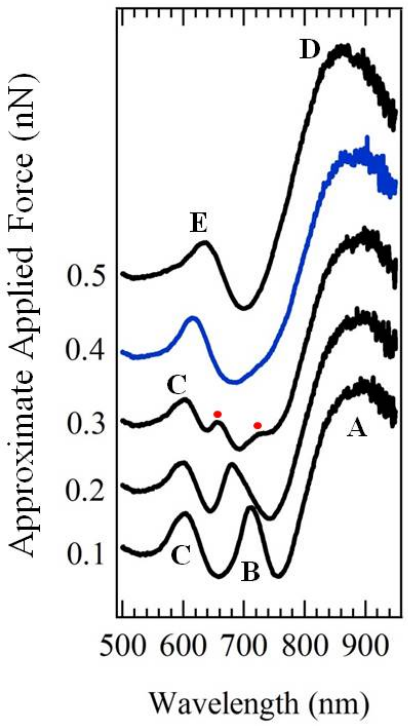

Figure 5.14: Evolution of LSPP modes with increasing applied compressive force (reducing d) after StoC. The blue spectrum marks CC while the red dots show the possible splitting of a mixed plasmon-exciton mode at approximately 0.3 nN of applied force ($d \approx 0.3$ nm).

These interesting results invite further controlled experimentation to confirm the strong coupling hypothesis. For example, the entire tips could be coated in high damage threshold organic dye molecules with excitonic transitions at energies and linewidths matched to the LSPP modes. If the mode-splitting observed is indeed a manifestation of strong plasmon-exciton coupling, this would be the first experimental evidence for such coupling within a plasmonic NP dimer nanocavity containing a small number of molecules. Finally, it is noted here that although the author believes plasmon-exciton coupling is the most likely explanation of the observed results, LSPP mode splitting phenomena could also possibly result from asymmetries in the NP geometry and composition (heterodimer), enabling both bright and dark LSPP mode excitation and anti-crossing phenomena [74]. Additionally, the double quantum well po-

tential formed due to the presence of molecules in the NGJ would permit symmetric and anti-symmetric plasmon wavefunction solutions of different energy and hence could also provide a possible explanation. Both these explanations are however considered unlikely, as the heterodimer hypothesis predicts splitting of LSPP mode C, while the non-degenerate wavefunction hypothesis (at the least) requires very narrow barrier widths that are not present immediately after StoC.

5.6 Conclusions

Contrasting the classical simulations with the experimental and QCM results (Fig. (5.7)), clearly shows the dramatic effect of non-local quantum tunnelling on plasmonic interactions. Only by incorporating non-local QT effects via the QCM can the experimental results begin to be properly accounted for, thus enabling the clear identification of where the plasmonic interaction crosses-over to the quantum regime. Other effects, such as non-local screening outside the tunnelling region, cannot attribute for the measured LSPP response, and therefore it is found that QT dominates the plasmonic interactions in nanocavities formed by NP dimers with ångström scale inter-NP separation.

These experimental and theoretical investigations of plasmonic interactions in sub-nanometre metal inter-NP cavities demonstrate that quantum mechanics is highly important at approximately the 0.3 nm scale where non-local tunnelling plasmonics controls the optical response. The findings finally experimentally resolve the unphysical nature of the long-standing classical predictions for the plasmonic response for nearly-touching NPs. The results also imply that QT establishes a quantum limit for plasmonic field enhancement and confinement. Additionally, it is possible measurements in the sub-nanometre regime show the first experimental evidence of strong plasmon-exciton coupling in plasmonic NGJs within NP dimer systems. Understanding both of these aspects of plasmonic phenomena is crucial for describing light-metal interactions down to the atomic-scale. It is also expected stabilising single-atom contacts or wires will give direct plasmonic access to the quantum transport regime around $1G_0$ [146].

The present work opens up exciting new prospects that aim to direct and control the chemistry of single molecules within nanogaps (e.g. for

enhanced photocatalysis), exploit single-molecule plasmon-assisted transport across nanogaps (e.g. for single molecule electronics), enable extreme non-linear interactions (e.g. attosecond pulse generation), access photoelectrochemistry on the sub-zeptoliter scale and possibly admit the study of plasmon-exciton (plexciton) quasiparticles.

Chapter 6

Summary and Outlook

In the preceding chapters the theoretical background, experimental apparatus and techniques, and new experimental results revealing the interaction of light with metallic nanosystems on the sub-nanometre scale have been presented and analysed. Here a brief summary of the work carried out for this thesis is provided, followed by suggested avenues for new or continued investigation.

In Chapter (2) a light-weight overview of the theoretical framework describing plasmonic interactions propagating on flat planar interfaces was first presented to introduce the mixed-state of light and metal described by SPPs. From this foundation, it was described how the control of SPPs via localisation on isolated sub-wavelength scale NPs is a powerful phenomena that contributed to the resurrection of metal optics as the now ubiquitous field of plasmonics. This led onto a more detailed theoretical review of coupled LSPPs in NP dimer systems and the objectives of the current work were made clear.

As two nanosystems move into single nanometre separation their plasmonic (and hence optical) response is dominated by the electromagnetic coupling across the NGJ created. A huge number of future (and current) applications will rely on the this tunable, non-linear optical response, and the associated nano-localised, extreme field and LDOS enhancements obtained. The fascinating sub-nanometre regime is almost unexplored by plasmonics orientated experiments and only now is becoming accessible to viable theoretical treatments. The absolute necessity to investigate and understand this truly nanoscale regime where spatially non-local effects, predominantly quantum tunnelling, control the plasmonic interactions has been the driving force behind the experimental and theoretical investigations in this thesis.

The experimental apparatus realised to access and interrogate the challenging sub-nanometre domain between two almost-touching NPs is described in Chapter (3). The sub-nanometre NGJ was created by the appropriate axial tip-to-tip placement of two conducting AFM probes with NP functionalised apices. The description of the overall setup is divided into three sections specifying the mechanical, electronic and optical components. All three of these systems were required to work in concert to enable high-quality simultaneous optical and electronic measurement of the LSPP mediated scattering response of a dynamically controlled, atomically separated, NP dimer system.

The detail behind the dynamic AFM tip-to-tip (NP dimer) alignment strategy used to enter the sub-nanometre regime was presented in Chapter (4). A novel non-linear EFM technique was implemented by placing an AC potential across the AFM tips, and measuring the harmonic frequencies generated by the non-linear electromechanical response of the tip-tip system using lock-in detection. The tips (NPs) are brought into nanometre-precise 3D alignment by adjusting the tip (NP) positions to maximise signal harmonics, thus creating an effective NP dimer system.

Finally, in Chapter (5) the experimental facilities constructed, and techniques developed, are combined to simultaneously perform low-background supercontinuum confocal laser DF nano-spectroscopy and DC conductance measurements on NP dimer systems with sub-nanometre separation. By simultaneously capturing both the electrical and optical scattering properties of a NP dimer, with controllable sub-nanometre separation, the first evidence for the quantum regime of optically driven tunnelling plasmonics has been observed in exquisite detail. The experimental results are found to be in good agreement with a very recently developed QCM where non-local quantum tunnelling effects are taken into account for large-scale ($>$ 3 nm dimension) plasmonic systems. These experimental and theoretical investigations of plasmonic interactions in metallic NP dimer nanocavities demonstrate that quantum mechanics plays a critical role at the 0.3 nm scale where non-local tunnelling plasmonics determines the optical response. The findings also strongly imply that quantum tunnelling establishes a limit for plasmonic field localisation and enhancement in nanogaps. The exceptionally large LDOS within the NGJ created may also enable strong coupling of light to molecular excitons thus creating mixed plasmon-exciton (plexciton-polariton) states. Understanding these aspects of plasmonic response

is crucial for describing light-matter interactions down to the atomic-scale, and is hence highly relevant to a huge variety of existing, and future, research paths and plasmonic technologies.

The experimental system that has been developed, and the results reported in this thesis, suggest many interesting opportunities for further investigation. For example, the work presented here opens up exciting new prospects including:

- The possibility to direct and control the chemistry of single molecules within nanogaps, e.g. for enhanced photocatalysis.
- The exploitation of single-molecule plasmon-assisted transport across nanogaps, e.g. for single molecule (optical frequency) electronics.
- Access to photoelectrochemistry on the sub-zeptoliter scale.
- The plasmonic control of non-linear electron tunnelling processes by light.
- Study of optical frequency tunnelling and non-linear optical frequency rectification phenomena.
- Investigations of the quantum-limit of electric-field mediated enhancement in SERS and optimised sensing geometries.
- The capability to dynamically investigate NP dimer systems bridged by 1D atomic chains formed on the make or break of NP contact. Such discrete steps in nanojunction conductance could lead to associated discrete plasmonic switching phenomena.
- Extreme classical non-linear phenomena, e.g. high-harmonic generation.
- Ultra-high LDOS enhancement and strong plasmon-exciton coupling within NP dimer systems.

In general, the experimental apparatus and techniques described in this work may be used for initial experimental investigations relating to fundamental research and applications that rely on, or are optimised by, nanostructures with sub-nanometre features. The results and interpretations presented in this thesis are expected to be of interest to the general plasmonics research community and beyond.

Appendix A

Charge Transfer Model

The anomalous dependence of Eqn. (5.10) on λ_0 can be explained by a more rigorous treatment of the physical system by including the dielectric properties of the fictitious quantum tunnelling medium and the Au NPs. These physical properties are included by considering the displacement field. Following Gauss's law, integrating over a Gaussian pillbox containing one of the AFM tip apex NP surfaces (assumed flat, as $a \gg d$) and assuming that the electric field created due to the localisation of free surface charges is significantly larger than the incident field gives

$$\oint_A \widetilde{\mathbf{D}} \cdot d\mathbf{A} = \widetilde{Q}_{SP} \Rightarrow \varepsilon_0 \left(\widetilde{\varepsilon}^{QT} E_{SP} + \widetilde{\varepsilon}_{Au} E_{Au} \right) = \frac{\widetilde{Q}_{SP}}{A_{SP}} \tag{A.1}$$

where E_{SP} is the LSPP enhanced electric field in the nanojunction, E_{Au} is the electric field within the metal surface, Q_{SP} is the amount LSPP free surface charge, A_{SP} is the surface area over which the LSPP charge is situated. Finally $\widetilde{\varepsilon}_{Au}$ is the dielectric function of Au, and $\widetilde{\varepsilon}^{QT}$ is the dielectric function of the fictitious tunnelling medium in the nanojunction, given by

$$\widetilde{\varepsilon}^{QT} = 1 - \frac{\omega_p^2}{\omega \left(\omega + i\gamma^{QT}(d) \right)} \tag{A.2}$$

where $\gamma^{QT}(d)$ is the quantum tunnelling damping parameter with typical values shown in [153] and ω_p is the plasma frequency of Au. Similarly the dielectric

function of Au is given by

$$\widetilde{\varepsilon}_{Au} = 1 - \frac{\omega_p^2}{\omega\left(\omega + i\gamma_{Au}\right)} \tag{A.3}$$

Now re-arranging Eqn. (A.1) for the magnitude of $\widetilde{Q}_{SP}$ gives

$$Q_{SP}(\omega, d) = \varepsilon_0 A_{SP} \left| \left(\widetilde{\varepsilon}^{QT}(\omega, d) E_{SP} + \widetilde{\varepsilon}_{Au}(\omega) E_{Au} \right) \right| \tag{A.4}$$

The magnitude of electric current through the tunnelling nanojunction I_{NJ} is found by

$$I_{NJ}(\omega, d) = \sigma_{QT}(\omega, d) A_{QT} E_{QT} \tag{A.5}$$

where A_{QT} is the surface area of the nanojunction, E_{QT} is the electric field magnitude driving the tunnelling current flow and σ_{QT} is the magnitude of the effective tunnelling conductivity given by

$$\sigma_{QT}(\omega, d) = \frac{\gamma^{QT} \sigma_0^{QT}}{\left(\omega^2 + (\gamma^{QT})^2\right)^{1/2}} \tag{A.6}$$

where $\sigma_0^{QT}(d) = \varepsilon_0 \omega_p^2 / \gamma^{QT}(d)$ (due to the assumption $T(\Omega, d)$ adiabatically follows the field, hence a DC description of tunnelling can be used). Using Eqn. (A.5) the amount of Q_{QT} transferred across the nanojunction over half an optical-cycle $\tau_{1/2} = \lambda_0 / 2c$ is

$$Q_{QT}(\omega, d) = \sigma_{QT}(\omega, d) A_{QT} E_{QT} \left(\frac{\lambda_0}{2c} \right) = \sigma_{QT}(\omega, d) A_{QT} E_{QT} \left(\frac{\pi}{\omega} \right) \tag{A.7}$$

Hence a general expression for X is found

$$X = \frac{Q_{QT}(\omega, d)}{Q_{SP}(\omega, d)} = \frac{\sigma_{QT}(\omega, d) A_{QT} E_{QT} \left(\frac{\lambda_0}{2c} \right)}{\oint_A \widetilde{\mathbf{D}}(\omega, d) \cdot d\mathbf{A}} \tag{A.8}$$

Under the typical conditions described in Eqn. (A.1), the expression for X reduces to

$$X \approx \frac{\sigma_{QT}(\omega, d) A_{QT} E_{QT} \left(\frac{\lambda_0}{2c}\right)}{\varepsilon_0 A_{SP} \left|(\widetilde{\varepsilon}^{QT}(\omega, d) E_{SP} + \widetilde{\varepsilon}_{Au}(\omega) E_{Au})\right|} \tag{A.9}$$

Now, under the general assumptions $d \gtrapprox 2$Å, i.e. $\gamma^{QT} > \omega_p \gg \gamma_{Au}$, and that ω is relatively low, i.e. ω around typical LSPP resonance frequencies so that $E_{SP} \gg E_{Au}$, Eqn. (A.9) further reduces to

$$X \approx \frac{\sigma_0^{QT}(d) A_{QT} E_{QT} \left(\frac{\lambda_0}{2c}\right)}{\varepsilon_0 A_{SP} E_{SP}} \tag{A.10}$$

as $\sigma_{QT}(\omega, d) \approx \sigma_0^{QT}(d)$ and $\widetilde{\varepsilon}^{QT} \approx 1$. Making the assumptions as in the main text that $A_{SP} = A_{QT}$ and $E_{SP} = E_{QT}$, finally gives Eqn. (5.7)

$$X \approx \sigma_0^{QT}(d) \left(\frac{\lambda_0}{2\varepsilon_0 c}\right) \tag{A.11}$$

Therefore the λ_0 dependence of Eqn. (5.7) and hence that of Eqn. (5.10) is approximately valid in the combined separation and frequency regime assumed.

The following contains more detail on how taking into account the displacement field modifies the unphysical limiting behaviour (in ω) of the charge-transfer time-scale model in [98] to give physically plausible results. The condition for the onset of the blue-shift is given by [98]

$$\tau = \frac{Q_{SP}}{I_{NJ}} \leq \frac{\pi}{2\omega} \tag{A.12}$$

where τ is the necessary time required for the charge transport and the furthest RHS term is found due to the simple time-scale argument in [98]. Using Eqns. (A.4) and (A.5) in Eqn. (A.12) gives

$$\frac{\varepsilon_0 A_{SP} \left|\left(\widetilde{\varepsilon}_{QT}(\omega) E_{SP} + \widetilde{\varepsilon}_{Au}(\omega) E_{Au}\right)\right|}{\sigma_{QT}(\omega) A_{QT} E_{QT}} \leq \frac{\pi}{2\omega} \tag{A.13}$$

The limiting behaviour can be understood as follows. In the case where only the electric field (not displacement field) is considered (nanojunction is considered as a vacuum with no tunnelling, as in the main text) the necessary time required for the charge transport (i.e. for the onset of the blue-shift) is given by Eqn. (A.12)

$$\begin{aligned} \tau = \frac{\pi}{2\omega} &\rightarrow \infty \text{ as } \omega \rightarrow 0 \\ &\rightarrow 0 \text{ as } \omega \rightarrow \infty \end{aligned} \tag{A.14}$$

However when the frequency dependent properties of the fictitious tunnelling junction and Au NPs are taken into account the expression for τ is modified considerably. Under the general assumptions $d > 2$Å, i.e. $\gamma^{QT} > \omega_p \gg \gamma_{Au}$, and $E_{SP} = E_{QT}$, the low and high frequency behaviour of the time allowed for charge transfer τ is determined.

For small ω the field inside the Au NPs is negligible compared to that outside, $E_{SP} \gg E_{Au}$. Additionally $\sigma_{QT} \approx \sigma_0^{QT}$. Under these conditions Eqn. (A.13) reduces to (under the assumption $E_{SP} = E_{QT}$)

$$\frac{\varepsilon_0 A_{SP}\left(\varepsilon_{QT}(\omega)\right)}{\sigma_0^{QT} A_{QT}} \leq \frac{\pi}{2\omega} \tag{A.15}$$

An expression for the time allowed for charge transport is found by re-arranging Eqn. (A.15). As $\omega \rightarrow 0$ we now have

$$\tau = \frac{\pi\varepsilon_0}{2\sigma_0^{QT}} = \left(\frac{\pi\varepsilon_0}{2}\right)\rho_0^{QT} \tag{A.16}$$

therefore in the DC limit the upper bound for the time allowed for the charge transfer process is not dependent on ω but is proportional to the effective quantum DC tunnelling resistivity ρ_0^{QT} of the nanojunction. The greater ρ_0^{QT} the greater the amount of time required to transfer the necessary charge. Likewise, as ρ_0^{QT} decreases, the required amount of time decreases.

For large ω ($\omega \gg \gamma^{QT}$) it is assumed that $E_{SP} \approx E_{Au} \approx E_{inc}$ (where E_{inc} is the incident field) as the electrons in the Au NPs do not screen the incident field as effectively because $\omega > \omega_p$. Therefore the amount of charge localisation at the nanojunction is relatively small. Therefore (via Eqn. (A.1)) Eqn (A.13) is

modified to (under the assumption $E_{SP} = E_{QT}$)

$$\frac{\varepsilon_0 A_{SP} \left| \left(\widetilde{\varepsilon}_{QT}(\omega) - \widetilde{\varepsilon}_{Au}(\omega) \right) \right|}{\sigma_{QT}(\omega) A_{QT}} \leq \frac{\pi}{2\omega} \tag{A.17}$$

In this case, from Eqn. (A.17), the time allowed for charge transport is

$$\tau \to \infty \ \text{ as } \ \omega \to \infty \tag{A.18}$$

Therefore the upper bound for the time allowed is no longer zero but is infinity. This can be understood because as $\omega \to \infty$, $Q_{SP} \to 0$ rapidly compared to the decreasing time of an optical cycle. Here $Q_{SP} \to 0$ because as $\omega \gg \omega_p$ the electrons can no longer respond to the incident field and hence no surface charge density is induced. Therefore the amount of charge to be transported is effectively zero and thus the charge transport can take place over any period of time. The time-scale model is thus *not applicable* for $\omega \gg \omega_p$.

The general condition for the onset of the blue-shift in terms of σ_{QT} is

$$\sigma_{QT}(\omega) \geq \frac{2\omega}{\pi A_{QT} E_{QT}} \left| \left(\oint_A \widetilde{\mathbf{D}} \cdot d\mathbf{A} \right) \right| \tag{A.19}$$

It should be noted the RHS is (for $d \gtrapprox 2$Å) a biquartic function of σ_0^{QT} and a high-order polynomial function of ω. An explicit expression for the necessary value of σ_0^{QT} as a function of ω could hence be obtained if required. The value for σ_0^{QT} can be compared against that found from analytical Quantum Mechanical (QM) theory [177] at different d to find the distance required for the onset of the blue-shift.

In the typical tunnelling regime (3Å$\leq d \leq$ 6Å, i.e. $E_{QT} \gg E_{Au}$ and $\gamma^{QT} > \omega_p > \omega \gg \gamma_{Au}$) at optical frequencies. In this case Eqn. (A.19) simplifies significantly and reduces to

$$\sigma_0^{QT} \gtrapprox \frac{2\varepsilon_0 \omega A_{SP}}{\pi A_{QT}} \tag{A.20}$$

In terms of current density J_0^{QT} we have

$$J_0^{QT} \gtrapprox \frac{2\varepsilon_0 \omega A_{SP} E_{SP}}{\pi A_{QT}} \tag{A.21}$$

In the regime of interest 2.5Å$\leq d <$ 6Å Eqn. (A.21) can hence be used to equate to the tunnelling current density found from analytical QM theory [177] to determine a value for d_{QR}. For separations 1Å$\leq d <$ 2.5Å the condition $\gamma^{QT} > \omega_p > \omega \gg \gamma_{Au}$ no longer holds. Under this situation the full Eqn. (A.19) needs to be used appropriately. In the 2Å$\leq d <$ 3Å regime it is found that the limit for J_0^{QT} decreases with increasing ω rather than increasing with increasing ω.

Appendix B

List of Symbols and Abbreviations

Symbols

α	Fine structure constant.
α^{ℓ}	Polarisibilty of ℓ^{th} localised surface plasmon mode of spherical nanoparticle.
β_i^z	Total z-component of non-linear damping coefficient of tip system i.
β_{0i}^z	z-component of fundamental damping coefficient of tip system i.
β_{TT}^z	z-component of air squeez viscous damping coefficient of tip system i.
χ_e	Effective electric susceptibility.
δ	Height of parabolic tip apex.
δ_{Au}	Skin-depth of gold.
δ_e	Penetration depth of induced surface charge.
δ_d	Penetration depth of surface plasmon polariton electric field into dielectric.
δ_m	Penetration depth of surface plasmon polariton electric field into metal.
ε_0	Permittivity of free-space.
ε_1	Real part of complex scalar dielectric function.
ε_2	Imaginary part of complex scalar dielectric function.
ε_{air}	Scalar relative permittivity of air.
$\widetilde{\varepsilon}_{Au}$	Complex scalar relative permittivity of gold.
ε_{bk}	Scalar background contribution to dielectric function.

ε_d	Scalar relative permittivity of a dielectric.
$\widetilde{\varepsilon}_m$	Complex scalar dielectric function of a metal.
$\widetilde{\varepsilon}^{QT}$	Complex scalar dielectric function of fictitious tunnelling medium.
$\widetilde{\varepsilon}_r$	Relative complex scalar permittivity.
$\widetilde{\varepsilon}_r^L$	Relative complex scalar permittivity for longitudinal excitations.
$\widetilde{\varepsilon}_r^T$	Relative complex scalar permittivity for transverse excitations.
η	Normalised refractive index.
η_0^r	Spontaneous radiative decay rate of molecule in free-space.
η_0^{nr}	Spontaneous non-radiative decay rate of molecule in free-space.
η_{SC}	Total decay rate limit for strong coupling.
η_m	Total decay rate of molecule.
η_m^r	Spontaneous radiative decay rate of molecule.
η_m^{nr}	Spontaneous non-radiative decay rate of molecule.
η_{LSPP}^{ℓ}	Plasmonic cavity total decay rate.
γ	Phenomenological electron collision frequency.
γ_C	Electric-field confinement factor.
γ_I	Phenomenological electron collision frequency for the I^{th} oscillator.
γ_{LDOS}	Local density of optical states enhancement factor.
γ^{QT}	Quantum tunnelling damping parameter.
Γ_{LSPP}^{ℓ}	Localised surface plasmon polariton ℓ^{th} mode energy linewidth.
Γ_m	Total linewidth of molecular exciton resonance.
κ	Extinction coefficient.
λ	Wavelength of light in dielectric medium.
λ_0	Wavelength of light in free-space.
λ_{spp}	Wavelength of surface plasmon polariton.
λ_{lspp}	Wavelength of localised surface plasmon polariton.
μ_0	Permeability of free-space.
μ_a	Coefficient of viscosity of air.
$\widetilde{\mu}_r$	Complex scalar relative permeability.
ω	Angular frequency.
ω_{0i}	Resonance frequency tip system i.
ω_{0I}	Resonance frequency of I^{th} oscillator.
ω_{np}^{ℓ}	Localised surface plasmon resonance frequency of ℓ^{th} mode.
ω_p	Bulk plasma frequency.
ω_P	Pump frequency.

ω_{sp}	Surface plasmon frequency.
ω_S	Signal frequency.
Ω	Electron energy.
Ω_F	Fermi energy.
Ω_R	Rabi-frequency.
ϕ	Spherical azimuthal coordinate/diameter.
Φ	Electrostatic potential.
$\varphi^{3\omega_S}$	Phase of signal at $3\omega_S$ with respect to the driving potential.
φ_{HD}	Phase of harmonic distortion signal at $3\omega_S$ with respect to the driving potential.
φ_i	Phase of tip i oscillation with respect to the driving potential.
φ_{WF}	Work-function.
φ_z	Phase of z-component of electric near-field.
π	Pi (3.14159...).
ψ	Phase of the superposition of the signal and harmonic distortion with respect to the driving potential.
ψ_ℓ	Ricatti-Bessel function of order ℓ.
ρ_{Au}	Mass density of gold.
ρ_{ext}	External charge density.
ρ_{int}	Internal charge density.
$\widetilde{\sigma}$	Complex scalar conductivity.
σ_0	Zero-frequency scalar conductivity.
σ^{QT}	Scalar quantum tunnelling conductivity.
σ_0^{QT}	Zero-frequency scalar quantum tunnelling conductivity.
σ_1	Real part of complex scalar conductivity.
σ_2	Imaginary part of complex scalar conductivity.
$\widetilde{\sigma}_m$	Complex scalar conductivity function of a metal.
σ_s	Squeeze number.
τ	Phenomenological electron relaxation time.
$\tau_{1/2}$	Period of half an optical cycle.
τ_{int}	Integration time.
τ_c	Cooling relaxation time.
τ_{LSPP}^{ℓ}	Localised surface plasmon polariton ℓ^{th} mode lifetime.
τ_0^r	Radiative decay time of molecule in free-space.
τ_P	Laser pulse-width.

τ_{TC}	Lock-in amplifier measurement time constant.
θ	Spherical polar coordinate.
θ_1, θ_2	Define range of illumination angles.
θ_c	Maximum collection angle.
θ_i	Angle of incidence of electromagnetic wave.
θ_{tip}	Tip (full) cone-angle.
Θ	Difference between signal and harmonic distortion phase.
v	Effective refractive index weighting factor.
ξ_ℓ	Ricatti-Bessel function of order ℓ.
$\wedge$	Logical conjunction (AND).
a	Nanoparticle radius.
a_0	Inter-atomic distance.
$\widetilde{a}_\ell$	Mie scattering coefficient.
A	Effective cross-sectional area of a nanojunction.
$d\mathbf{A}$	Infinitesimal area element vector.
A_C	Cap area of collection cylinder.
A_d	Field amplitude coefficient in dielectric.
A_F	Parallel plate area determined by experimental fit.
A_ℓ^m	Spherical polar expansion coefficient.
A_L	Laser illumination area.
A_{LI}	Lock-in amplifier gain.
A_m	Field amplitude coefficient in metal.
A_{ov}	Area of cantilever overlap.
A_{QT}	Effective quantum tunnelling nanojunction area.
A_{SP}	Surface area of localised surface plasmon polariton charge.
A_T	Transimpedance amplifier gain.
$\mathbf{B}$	Magnetic flux density field vector.
$\widetilde{b}_\ell$	Mie scattering coefficient.
B_ℓ^m	Spherical polar expansion coefficient.
c	Speed of light *in vacuo*.
c_{Au}	Specific heat capacity of gold.
C	Total tip system capacitance.
C_0	Infinite parallel plate capacitance coefficient.
C_0^m	Amplitude of capacitance modulation.

C_{abs}^{qs}	Quasi-static absorption cross-section.
C_{bk}	Constant background capacitance.
C_A	Capacitance associated with tip apices.
C_C	Capacitance associated with tip cones.
C_{ext}	Mie extinction cross-section.
C_{ext}^{qs}	Quasi-static extinction cross-section.
C_F	Additional fringe capacitance.
$\widetilde{c}_i$	Complex Fourier coefficient of current at frequency $i\omega_S$.
C_L	Capacitance associated with cantilevers.
C_{NP}	Nanoparticle heat capacity.
C_s	Stray capacitance.
C_{sca}	Mie scattering cross-section.
C_{sca}^{BEMAX}	Scattering cross-section calculated by BEMAX.
C_{sca}^{qs}	Quasi-static scattering cross-section.
d	Nanosystem separation.
$\mathbf{D}$	Electric displacement field vector.
d_0	Separation in z when inter-nanoparticle force is zero.
$d_0^{x,y}$	Separation in x,y,z when inter-nanoparticle force is zero.
d_{QR}	Quantum cross-over separation.
D_L	Laser beam diameter
D_{OC}	Diameter of the refracting core of the objective.
d_{QR}	Quantum regime crossover distance.
d'_{QR}	Simple model estimate of quantum regime crossover distance.
D_S	Diameter of dark-field beam-stop.
e	Electron charge.
$\mathbf{E}$	Electric field vector.
$\mathbf{E_0}$	Electric field amplitude vector.
E_e	Electron energy.
E_{LSPP}^{ℓ}	Localised surface plasmon polariton ℓ^{th} mode resonant energy.
E_m^A	Resonance energy of absorbing molecular transition.
E_m^E	Resonance energy of emitting molecular transition.
E_{QT}	Electric field driving quantum tunnelling.
E_{SP}	Localised surface plasmon polariton enhanced electric field.
E_T	Thermal excitation energy.
E_x, E_y, E_z	Electric field component amplitudes.

f	Frequency.
F	Electrostatic force.
f_{0i}	Resonance frequency of cantilever.
f_{0i}^{e}	Effective resonance frequency of cantilever.
f_A	Empirical correction factor.
F_A^z	z-component of driving electrostatic force associated with tip apex.
F_{bk}^z	z-component of driving electrostatic force associated the background capacitance.
F_C^z	z-component of driving electrostatic force associated with tip cone.
F_{EL}^z	z-component of driving electrostatic force.
F_F^z	z-component of driving electrostatic force associated the cantilever fringe capacitance.
F_{flu}	Laser fluence.
F_L^z	z-component of driving electrostatic force associated with cantilever.
f_m	Oscillator strength.
F_p	Purcell factor.
F_{PO}	Pull-off force.
f_S	Frequency used for alignment scans.
F_{TT}^z	z-component of Lennard-Jones force.
F_{VdW}^z	z-component of Van der Waals force.
f_z	z-component correction factor.
G	Distance off tip-tip axis.
G_0	Quantum conductance of one dimensional ballistic channel.
G_{DC}	Zero-frequency conductance.
g_x	x position of tip 2 in alignment grid.
g_y	y position of tip 2 in alignment grid.
G_x	Alignment grid length in x.
G_y	Alignment grid length in y.
h	Planck's constant/Cone height.
$\hbar$	Dirac constant.
H	Hamaker constant.
$\mathbf{H}$	Magnetic field vector.
$\widetilde{h}_\ell^{(1)}$	Spherical Hankel function of the 1^{st} kind of order ℓ.
H_x, H_y, H_z	Magnetic field component amplitudes.

i	Imaginary unit.
I	Current.
I_0	Average optical intensity.
I^{AC}	Alternating current signal.
I_0^{AC}	Alternating current signal amplitude.
$\widetilde{I}^{\omega_S}$	Complex component of current signal at ω_S.
$\widetilde{I}^{3\omega_S}$	Complex component of current signal at $3\omega_S$.
$\widetilde{I}_C^{3\omega_S}$	Corrected complex component of current signal at $3\omega_S$.
I_c	Conduction current.
$\widetilde{\mathbf{I}}_\mathbf{d}$	Displacement current vector.
I_{DC}	Zero frequency (DC) current.
$\widetilde{I}_{HD}$	Complex component of harmonic distortion background. current signal at $3\omega_S$.
$\Im[...]$	Imaginary part.
j_ℓ	Spherical Bessel function of order ℓ.
$\mathbf{J_{ext}}$	External current density.
k	Wavenumber of light in dielectric medium.
k_x,k_y,k_z	Wavevector components of light in dielectric medium.
k_0	Free-space wavenumber of light.
k_{0i}^z	z-component of fundamental cantilever spring constant of tip system i.
k_i^z	Total z-component of cantilever spring constant of tip system i.
k_B	Boltzmann constant.
$\widetilde{\mathbf{k}}_\mathbf{E}$	Evanescent light complex wavevector in dielectric medium.
k_{ei}^z	z-component of effective cantilever spring 'constant' of tip system i.
$k_{ei}^{z\prime}$	z-component of time-averaged effective cantilever spring 'constant' of tip system i.
$\mathbf{k_{GB}}$	Wavevector of incident Gaussian beam.
$\widetilde{k}_{lspp}$	Tangential component of complex wavenumber.
$k_{\|\|}$	In-plane wavevector component of light in dielectric medium.
$\widetilde{k}_{spp}$	x-component of complex surface plasmon polariton wavevector.
k_{TT}^z	z-component of air squeeze elastic damping cantilever spring constant.

$\widetilde{k}_{zd}$	z-component of complex surface plasmon polariton wavevector in dielectric.
$\widetilde{k}_{zm}$	z-component of complex surface plasmon polariton wavevector in metal.
l	Side length of parallel plate.
ℓ	Orbital angular momentum number.
l_{arc}	Length of circular arc.
L_C	Length of collection cylinder.
L_{spp}	Surface plasmon polariton propagation length.
m	Azimuthal number.
$\mathbf{M}$	Magnetisation field vector.
m_i	Effective mass of oscillating tip system i.
m_e^*	Effective optical mass of electron.
m_I^*	Effective optical mass of an electron contributing to the I^{th} oscillator.
n	Real part of complex scalar refractive index.
$\widetilde{n}$	Complex scalar refractive index.
N	Number of discrete points.
n_{air}	Refractive index of air.
n_e	Conduction electron density.
N_e	Absolute number of conduction electrons.
n_d	Refractive index of a dielectric medium.
n_d^e	Effective refractive index of a dielectric medium.
n_{glass}	Refractive index of microscope slide.
n_I	Electron density contributing to the I^{th} oscillator.
N_m	Absolute number of molecules.
$\mathbf{P}$	Total internal polarisation field vector.
P_0	Average optical power.
P_a	Ambient air pressure.
P_ℓ^m	Associated Legendre polynomial.
$\widetilde{\mathbf{q}}$	Complex wavevector of light within an absorbing medium.
$\widetilde{q}$	Complex wavenumber of light within an absorbing medium.
$\widetilde{\mathbf{q}}_\mathbf{0}$	Complex wavevector of light at the bulk plasma frequency.
q^{QT}	Wavenumber of a tunnelling electron.
Q	Charge.

Q_{0i}	Quality factor of tip system i.
Q_{LSPP}^{ℓ}	Localised surface plasmon polariton ℓ^{th} mode quality factor.
Q_{QT}	Quantum tunnelling charge.
Q_{SP}	Localised surface plasmon polariton surface charge.
$\mathbf{r}$	Position vector.
R	Tip apex radius.
$\bar{R}$	Reduced tip apex radius.
$\widetilde{\mathbf{r}}_{\mathbf{0}}$	Complex amplitude vector of electron oscillation.
R_C	Collection cylinder cap radius.
R_{cl}	Current limiting resistance.
$\widetilde{\mathbf{r}}_{\mathbf{e}}$	Complex electron position vector.
$\Re[...]$	Real part.
t	Time.
t_L	Thickness of insulating water and hydrocarbon layer(s).
T	Absolute temperature.
T^{ω_S}	Period of signal at ω_S.
$T^{3\omega_S}$	Period of signal at $3\omega_S$.
T^{QT}	Electron tunnelling probability.
U	Electrostatic potential energy.
V	Mode volume.
V_0	Alternating potential amplitude.
$V_0^{3\omega_S}$	Amplitude of harmonic distortion voltage signal at $3\omega_S$.
$\widetilde{V}_L^{3\omega_S}$	Complex voltage signal at $3\omega_S$ measured by lock-in amplifier.
V_{AC}	Alternating potential signal after amplification.
V_0^{AC}	Alternating potential signal amplitude.
V_{DC}	Amplitude of stationary potential.
v_g	Group velocity.
$V_{\min}$	Quantum limited plasmon mode volume.
V_{np}	Nanoparticle volume.
V_{off}	Zero-frequency offset potential.
V_{opt}	Optically induced potential.
v_p	Phase velocity.
V_0^T	Alternating potential amplitude across atomic force tips.
w	Lateral localised surface plasmon polariton confinement width.

w_{QL}	Quantum limit of mode confinement.
x, y, z	Global lab frame co-ordinates.
X	Fraction of neutralised charge.
$\hat{\mathbf{z}}$	Unit vector in the z-direction.
z_{mi}	Amplitude of oscillation of tip i.
z_i^{off}	Additional offset in position of tip i.
Z_c	Load impedance associated with total tip system capacitance.
Z_s	Load impedance associated with stray capacitance of the system.

Abbreviations

1D, 2D, 3D	One, two, three-dimensions.
AC	Alternating current.
AFM	Atomic force microscopy.
APP	Amici prism pair.
BEM	Boundary element method.
BEMAX	Boundary element method for axially symmetric systems.
BF	Bright-field.
BP	Bulk plasmon.
BPF	Band pass filter.
BS	Beamsplitter.
CAD	Computer aided design.
CC	Conductive contact.
CCD	Charge coupled device.
CDCP	Chromatic dispersion compensation plate.
CI	Collection iris.
CP	Confocally-aligned pinhole.
CTPP	Charge transfer plasmon polariton.
DC	Direct current.
DDA	Discrete dipole approximation.
DF	Dark-field.
DFT	Density Functional Theory.
DSO	Digital storage oscilloscope.
EBD	Electron-beam deposition.
EBL	Electron-beam lithography.
EFM	Electrostatic force microscopy.
EMF	Electromotive force.
FDTD	Finite difference time domain.
FWHM	Full-width half-maximum.
GLMT	Generalised Lorentz Mie Theory.
GPIB	General purpose interface bus.
HD	Harmonic distortion.
LDOS	Local density of photonic states.
LP	Linear polariser.
LSP	Localised surface plasmon.

LSPP	Localised surface plasmon polariton.
MCBJ	Mechanically controllable break-junction.
NA	Numerical aperture.
ND	Neutral density.
NGJ	Nanogap or nanojunction.
NP	Nanoparticle.
ODE	Ordinary differential equation.
p-	Parallel.
PCF	Photonic crystal fibre.
PZ	Piezoelectric.
QCM	Quantum corrected model.
QR	Quantum regime.
QT	Quantum tunnelling.
RC	RC time constant.
RHS	Right hand side.
RPP	Radiative plasmon polariton.
s-	*Senkrecht* (German: perpendicular).
SC	Semiconductor.
SEM	Scanning electron microscope.
SERS	Surface enhanced Raman scattering.
SG	Signal ground.
SMU	Source measure unit.
SN	Signal to Noise ratio.
SP	Surface plasmon.
SPDT	Single-pole double-throw.
SPP	Surface plasmon polariton.
SSTM	Static scanning tunnelling microscopy.
STM	Scanning tunnelling microscopy.
StoC	Snap-to-contact.
TDDFT	Time-dependent density functional theory.
TE	Transverse electric.
TM	Transverse magnetic.
TTL	Transistor transistor logic.
VA	Voltage amplifier.
WKB	Wentzel, Kramers, Brilluoin.

Bibliography

[1] C. Girard and E. Dujardin, "Assembly of functional molecular nanostructures on surfaces," *Journal of Optics A: Pure and Applied Optics*, vol. 8, pp. 73–86, 2006.

[2] E. Gomar-Nada, J. Puigmartí-Luis, and D. B. Amabilino, "Near-field optical properties of top-down and bottom-up nanostructures," *Chemical Society Reviews*, vol. 37, pp. 490–504, 2008.

[3] Z. L. Wang, B. D. Miller, Y. Liu, and Z. Zhang, *Handbook of Nanophase and Nanostructured Materials: Materials Systems and Applications*. New York, US: Kluwer Academic/Plenum Publishers, 2002.

[4] J. A. Schuller, E. S. Barnard, W. Cai, Y. C. Jun, J. S. White, and M. L. Brongersma, "Plasmonics for extreme light concentration and manipulation," *Nature Materials*, vol. 9, pp. 193–204, 2010.

[5] M. Westphalen, U. Kreibig, J. Rostalski, H. Lüth, and D. Meissner, "Metal cluster enhanced organic solar cells," *Solar Energy Materials and Solar Cells*, vol. 61, pp. 97–105, 2000.

[6] P. K. Jain, X. Huang, I. H. El-Sayed, and M. A. El-Sayed, "Review of Some Interesting Surface Plasmon Resonance-enhanced Properies of Noble Metal Nanoparticles and Their Applications to Biosystems," *Plasmonics*, vol. 2, pp. 107–118, 2007.

[7] K. Kneipp., H. Kneipp, I. Itzkan, R. R. Dasari, and M. S. Feld, "Surface-enhanced Raman scattering and biophysics," *Journal of Physics: Condensed Matter*, vol. 14, pp. R597–R624, 2002.

[8] I. I. Smolyaninov, A. V. Sayats, A. Gungor, and C. C. Davis, "Single-photon tunneling via localised surface plasmons," *Physical Review Letters*, vol. 88, no. 18, p. 187402, 2002.

[9] R. Bardhan, S. Lal, A. Joshi, and N. J. Halas, "Theranostic nanoshells: from probe design to imaging and treatment of cancer," *Accounts of Chemical Research*, vol. 44, pp. 936–946, 2011.

[10] H. A. Atwater and A. Polman, "Plasmonics for improved photovoltaic devices," *Nature Materials*, vol. 9, pp. 205–213, 2010.

[11] Y. B. Zheng, B. Kiraly, P. S. Weiss, and T. J. Huang, "Molecular plasmonics for biology and nanomedicine," *Future Medicine: Nanomedicine*, vol. 7, no. 5, pp. 751–770, 2012.

[12] K. F. MacDonald and N. I. Zheludev, "Active plasmonics: current status," *Laser and Photonics Reviews*, vol. 4, no. 4, pp. 562–567, 2010.

[13] Y. Fu and X. Zhou, "Plasmonic lenses: a review," *Plasmonics*, vol. 5, pp. 287–310, 2010.

[14] S. Maier, *Plasmonics: Fundamentals and applications*. New Jersey, US: Springer, 2007.

[15] P. Drude, "Zur Elektronentheorie der Metalle," *Annals of Physics*, vol. 1, pp. 566–613, 1900.

[16] D. Bohm and D. Pines, "A collective description of electron interactions: III. Coulomb interactions in a degenerate electron gas," *Physical Review*, vol. 92, p. 609, 1953.

[17] D. Pines, "Glancing angle deposition: Fabrication, properties, and applications of micro- and nanostructured thin films," *Physical Review*, vol. 92, no. 5, p. 626, 1953.

[18] R. W. Wood, "XLII. On a remarkable case of uneven distribution of light in a diffraction grating spectrum," *Philosophical Magazine*, vol. 4, p. 396, 1902.

[19] G. Mie, "Beitrage zur Optik truber Medien, speaiell kolloidaler Metallosungen," *Annalen der Physik*, vol. 25, p. 377, 1908.

[20] J. Zenneck, "Über die Fortpflanzung ebener elektromagnetischer Wellen längs einer ebenen Leiterfläche und ihre Beziehung zur drahtlosen Telegraphie," *Annalen der Physik*, vol. 23, p. 846, 1907.

[21] L. Rayleigh, "Inorganic chiral optical materials," *Proceedings of the Royal Society (London)*, vol. A79, p. 399, 1908.

[22] U. Fano, "The Theory of Anomolous Diffraction gratings and of quasi-stationary waves on Metallic surfaces (Sommerfield's waves)," *Journal of the Optical Society of America*, vol. 31, pp. 213–222, 1941.

[23] R. H. Ritchie, "Plasma losses by fast electrons in thin films," *Physical Review*, vol. 106, pp. 874–881, 1957.

[24] C. J. Powell and J. B. Swan, "Origin of the characteristic electron energy losses in aluminum," *Physical Review*, vol. 115, p. 869, 1959.

[25] E. A. Stern and R. A. Ferrell, "Surface plasma oscillations of a degenerate electron gas," *Physical Review*, vol. 120, p. 130, 1960.

[26] R. H. Ritchie, E. T. Arakawa, J. J. Cowen, and R. N. Hamm, "Surface Plasmon resonant effect in Grating Diffraction," *Physical Review Letters*, vol. 21, no. 22, pp. 1530–1533, 1968.

[27] E. Kretschmann and H. Raether, "Radiative Decay of non-radiative Surface Plasmons excited by Light," *Zeitschrift für Naturforschung*, vol. 23A, pp. 2135–2136, 1968.

[28] T. Turbader, "Complete absorption of light by thin metal films," *Proceedings of the Physical Society (London)*, vol. 73, pp. 40–44, 1959.

[29] A. Otto, "Excitation of nonradiative surface plasma waves in silver by the method of frustrated total reflection," *Zeitschrift für Physik*, vol. 216, p. 398, 1968.

[30] S. L. Cunningham, A. A. Maradudin, and R. F. Wallis, "Effect of a charge layer on the surface plasmon polariton dispersion curve," *Physical Review B*, vol. 10, p. 3342, 1974.

[31] U. Kreibig and P. Zacharias, "Surface plasmon resonances in small spherical silver and gold particles," *Zeitschrift für Physik*, vol. 231, p. 128, 1970.

[32] M. P. Marder, *Condensed Matter Physics*. New Jersey, US: J. Wiley and Sons, 2^{nd} ed., 2011.

[33] V. G. Veselago, "The electrodynamics of substances with simultaneously negative values of ε and μ," *Soviet Physics Uspekhi*, vol. 10, no. 4, pp. 509–514, 1968.

[34] S. A. Ramakrishna, "Physics of negative refractive index materials," *Reports on Progress in Physics*, vol. 68, pp. 449–521, 2005.

[35] F. J. G. de Abajo, "Non-local effects in the plasmons of strongly interacting nanoparticles, dimers, and waveguides," *Journal of Physical Chemistry C*, vol. 112, pp. 17983–17987, 2008.

[36] J. A. Scholl, A. L. Koh, and J. A. Dionne, "Quantum plasmon resonances of individual metallic nanoparticles," *Nature*, vol. 483, pp. 421–427, 2012.

[37] J. Zuloaga, E. Prodan, and P. Nordlander, "Quantum plasmonics: optical properties and tunability of metallic nanorods," *American Chemical Society Nano*, vol. 4, no. 9, pp. 5269–5276, 2010.

[38] U. Kreibig and M. Vollmer, *Optical Properties of Metal Clusters*. Berlin, GER: Springer-Verlag, 1995.

[39] E. Palik and G. Ghosh, *Handbook of Optical Constants of Solids II*. New York, US: Academic Press, 1991.

[40] C. Sönnichsen, *Plasmons in Metal Nanostructures*. PhD thesis, Ludwig-Maximilians-University of Munich, Munich, GER, 2001.

[41] A. Vial, "Improved Analytical fit of Gold Dispersion: Application to the modelling of extinction spectra with a finite-difference-time-domain method," *Physical Review B*, vol. 71, p. 085416, 2005.

[42] S. Link and M. A. El-Sayed, "Shape and size dependence of radiative, non-radiative and photothermal properties of gold nanocrsytals," *International Reviews in Physical Chemistry*, vol. 19, no. 3, pp. 409–453, 2000.

[43] C. Kittel, *Introduction to Solid State Physics*. New York, US: J. Wiley and Sons, 8^{th} ed., 2005.

[44] R. Fuchs and K. L. Kliewer, "Surface plasmon in a semi-infinite free-electron gas," *Physical Review B*, vol. 3, no. 7, pp. 2270–2278, 1971.

[45] W. L. Barnes, A. Dereux, and T. W. Ebbesen, "Surface plasmon subwavelenght optics," *Nature*, vol. 424, pp. 824–830, 2003.

[46] M. Faraday, "The Bakerian lecture: experimental relations of gold (and other metals) to light," *Philosophical Transactions*, vol. 147, p. 145, 1835.

[47] D. L. Jeanmaire and R. P. V. Duyne, "Assembly of functional molecular nanostructures on surfaces," *Journal of Electroanalytical Chemistry*, vol. 84, p. 1, 1977.

[48] K. L. Wustholz, A. Henry, J. M. McMahon, R. G. Freeman, N. Valley, M. E. Piotti, M. J. Natan, G. C. Schatz, and R. P. V. Duyne, "Structure-activity relationships in gold nanoparticle dimers and trimers for surface-enhanced Raman spectroscopy," *Journal of the American Chemical Society*, vol. 132, no. 31, pp. 10903–10910, 2010.

[49] D. K. Lim, K. S. Jeon, H. M. Kim, J. M. Nam, and Y. D. Suh, "Nanogap-engineerable Raman-active nanodumbbells for single-molecule detection," *Nature Materials*, vol. 9, pp. 60–67, 2010.

[50] E. Ozbay, "Plasmonics: merging photonics and electronics at nanoscale dimensions," *Science*, vol. 311, no. 5758, pp. 189–193, 2006.

[51] C. Burda, X. Chen, R. Narayanan, and M. A. El-Sayed, "Chemistry and Properties of Nanocrystals of Different Shapes," *Chemical Reviews*, vol. 105, pp. 1025–1102, 2005.

[52] Y. Sun and Y. Xia, "Shape-controlled synthesis of gold and silver Nanoparticles," *Science*, vol. 298, no. 5601, pp. 2176–2179, 2002.

[53] J. C. Love, B. D. Gates, D. B. Wolfe, K. E. Paul, and G. M. Whitesides, "Fabrication and wetting properties of metallic half-shells with submicron diameters," *Nano Letters*, vol. 2, no. 8, pp. 891–894, 2002.

[54] J. Aizpurua, P. Hanarp, S. D. Sutherland, M. Kall, G. W. Bryant, and F. J. G. de Abajo, "Optical Properties of Gold Nanorings," *Physical Review Letters*, vol. 90, no. 5, pp. 704–709, 2003.

[55] B. Nikoobakht and M. A. El-Sayed, "Preparation and growth mechanism of gold nanorods (NRs) using seed-mediated growth method," *Chemistry of Materials*, vol. 15, no. 10, pp. 1957–1962, 2003.

[56] A. Sánchez-Iglesias, I. Pastoriza-Santos, J. Pérez-Juste, B. Rodríguez-González, F. J. G. de Abajo, and L. M. Liz-Marzán, "Synthesis and optical properties of gold nanodecahedra with size control," *Advances in Materials*, vol. 18, pp. 2529–2534, 2006.

[57] P. S. Kumar, I. Pastoriza-Santos, B. Rodríguez-González, F. J. G. de Abajo, and L. M. Liz-Marzán, "High-yield synthesis and optical response of gold nanostars," *Nanotechnology*, vol. 19, no. 1, p. 015606, 2007.

[58] Y. G. Sun and Y. N. Xia, "Gold and silver nanoparticles: A class of chromophores with colors tunable in the ranges from 400 nm to 750 nm," *Analyst*, vol. 128, no. 6, pp. 686–691, 2003.

[59] M. L. Stockman, "Nanofocusing of optical energy in tapered plasmonic waveguides," *Physical Review Letters*, vol. 93, no. 13, p. 137404, 2004.

[60] F. J. G. de Abajo, "Optical excitations in electron microscopy," *Reviews of Modern Physics*, vol. 82, no. 1, pp. 209–275, 2010.

[61] E. C. le Ru and P. G. Etchegoin, *Principles of Surface-Enhanced Raman Spectroscopy: and Related Plasmonic Effects*. Amsterdam, NL: Elsevier, 2008.

[62] M. Born and E. Wolf, *Principles of Optics*. Cambridge, UK: Cambridge University Press, 7^{th} ed., 1999.

[63] E. S. Kooij, W. Ahmed, H. J. W. Zandvliet, and B. Poelsema, "Localized plasmons in noble metal nanospheroids," *Journal of Physical Chemistry C*, vol. 115, no. 21, pp. 10321–10332, 2011.

[64] C. F. Bohren and D. R. Huffman, *Absorption and Scattering of Light by small Particles*. New York, US: J. Wiley and Sons, 1^{st} ed., 1983.

[65] J. M. Pitarke, V. M. Silkin, E. V. Chulkov, and P. M. Echenique, "Theory of surface plasmons and surface-plasmon polaritons," *Reports on Progress in Physics*, vol. 70, pp. 1–187, 2007.

[66] E. Prodan, P. Nordlander, and N. J. Halas, "Electronic structure and optical properties of gold nanoshells," *Nano Letters*, vol. 3, no. 10, pp. 1411–1415, 2003.

[67] J. D. Jackson, *Classical Electrodynamics*. New York, US: J. Wiley and Sons, 3^{rd} ed., 1999.

[68] M. W. Knight, J. Fan, F. Capasso, and N. J. Halas, "Influence of excitation and collection geometry on the dark field spectra of individual plasmonic nanostructures," *Optics Express*, vol. 18, no. 3, pp. 2579–2587, 2010.

[69] N. M. Morjarad, V. Sandoghdar, and M. Agio, "Plasmon spectra of nanospheres under a tightly focused beam," *Journal of the Optical Society of America B*, vol. 25, no. 4, pp. 651–658, 2008.

[70] G. Gouesbet and G. Gréhan, *Generalized Lorenz-Mie Theories*. Berlin, GER: Springer, 2011.

[71] F. J. G. de Abajo and A. Howie, "Relativistic electron energy loss and electron-induced photon emission in inhomogeneous dielectrics," *Physical Review Letters*, vol. 80, pp. 5180–5183, 1998.

[72] B. T. Draine and P. J. Flatau, "Discrete-dipole approximation for scattering calculations," *Journal of the Optical Society of America*, vol. 11, no. 4, pp. 1491–1499, 1994.

[73] C. Oubre and P. Nordlander, "Optical properties of metallodielectric nanostructures calculated using the finite difference time domain method," *Journal of Physics and Chemistry B*, vol. 108, no. 46, pp. 17740–17747, 2004.

[74] P. Nordlander, C. Oubre, E. Prodan, K. Li, and M. I. Stockman, "Plasmon hybridization in nanoparticle dimers," *Nano Letters*, vol. 4, no. 5, pp. 899–903, 2004.

[75] D. Y. Lei, A. Aubry, Y. Luo, S. A. Maier, and J. B. Pendry, "Plasmonic interaction between overlapping nanowires," *American Chemical Society Nano*, vol. 5, no. 1, pp. 597–607, 2011.

[76] A. I. Fernández-Domínguez, A. Wierner, F. J. García-Vidal, S. A. Maier, and J. B. Pendry, "Transformation-optics description of nonlocal effects in plasmonic nanostructures," *Physical Review Letters*, vol. 108, p. 106802, 2012.

[77] J. F. G. de Abajo and A. Howie, "Retarded field calculation of electron energy loss in inhomogeneous dielectrics," *Physical Review B*, vol. 65, p. 115418, 2002.

[78] J. Gersten and A. Nitzan, "Electromagnetic theory of enhanced Raman scattering by molecules adsorbed on rough surfaces," *Journal of Chemical Physics*, vol. 73, no. 7, pp. 3023–3038, 1980.

[79] J. M. McMahon, S. K. Gray, and G. C. Schatz, "Optical properties of nanowire dimers with a spatially nonlocal dielectric function," *Nano Letters*, vol. 10, p. 3473, 2010.

[80] C. David and F. J. G. de Abajo, "Spatial non-locality in the optical response of metal nanoparticles," *The Journal of Physical Chemistry C*, vol. 115, pp. 19470–19547, 2011.

[81] C. M. Aikens, S. Li, and G. C. Schatz, "From discrete electronic states to plasmons: TDDFT optical absorption properties of Ag_n (n=10, 20, 35, 56, 84, 120) tetrahedral clusters," *Nano Letters*, vol. 112, no. 30, pp. 11272–11279, 2010.

[82] J. Zuloaga, E. Prodan, and P. Nordlander, "Quantum description of the plasmon resonances of a nanoparticle dimer," *Nano Letters*, vol. 9, no. 2, pp. 887–891, 2009.

[83] L. Vitali, S. D. Borisova, G. G. Rusina, E. V. Chulkov, and K. Kern, "Inelastic electron tunnelling microscopy: A route to the identification of tip-apex structure," *Physical Review B*, vol. 81, p. 153409, 2010.

[84] E. Townsend and G. W. Bryant, "Plasmonic properties of metallic nanoparticles: the effects of size quantization," *Nano Letters*, vol. 12, no. 1, pp. 429–434, 2012.

[85] O. L. Muskens, V. Giannini, J. A. Sánchez-Gil, and J. G. Rivas, "Strong enhancement of the radiative decay rate of emitters by single plasmonic nanoantennas," *Nano Letters*, vol. 7, no. 9, pp. 2871–2875, 2007.

[86] A. Manjavacas, F. J. G. de Abajo, and P. Nordlander, "Quantum plexcitonics: strongly interacting plasmons and excitons," *Nano Letters*, vol. 11, pp. 2318–2323, 2011.

[87] X. Wu, S. K. Gray, and M. Pelton, "Quantum-dot-induced transparency in a nanoscale plasmonic resonator," *Optics Express*, vol. 18, no. 23, p. 23633, 2010.

[88] N. J. Halas, S. Lal, W. Chang, S. Link, and P. Nordlander, "Plasmons in strongly coupled metallic nanostructures," *Chemical Reviews*, vol. 111, pp. 3913–3961, 2011.

[89] I. Romero, J. Aizpurua, G. W. Bryant, and F. J. G. de Abajo, "Plasmons in nearly touching metallic nanoparticles: singular response in the limit of touching dimers," *Optics Express*, vol. 14, no. 21, pp. 9988–9999, 2006.

[90] A. Aubry, D. Y. Lei, S. A. Maier, and J. B. Pendry, "Interaction between plasmonic nanoparticles revisted with transformation optics," *Physical Review Letters*, vol. 105, p. 233901, 2010.

[91] A. Aubry, D. Y. Lei, S. A. Maier, and J. B. Pendry, "Conformal transformation applied to plasmonics beyond the quasistatic limit," *Physical Review B*, vol. 82, p. 205109, 2010.

[92] H. Xu, E. J. Bjerneld, M. Käll, and L. Börjesson, "Spectroscopy of single hemoglobin molecules by surface enhanced Raman scattering," *Physical Review Letters*, vol. 83, p. 4357, 1999.

[93] J. Berthelot, A. Bouhelier, C. J. Huang, J. Margueritat, G. C. des Francs, E. Finot, J. Weeber, A. Dereux, S. Kostcheev, H. I. el Ahrach, A. Baudrion, J. Plain, R. Bachelot, P. Royer, and G. P. Wiederrecht, "Tuning of an optical dimer nanoantenna by electrically controlling its load impedance," *Nano Letters*, vol. 9, no. 11, pp. 3914–3921, 2009.

[94] R. F. Oulton, V. J. Sorger, T. Zentgraf, R. Ma, C. Gladden, L. Dai, G. Bartal, and X. Zhang, "Plasmon lasers at deep sub-wavelength scale," *Nature*, vol. 461, pp. 629–632, 2009.

[95] S. Kim, J. Jin, Y. Kim, I. Park, Y. Kim, and S. Kim, "High harmonic generation by resonant plasmon field enhancement," *Nature*, vol. 453, pp. 757–760, 2008.

[96] P. Song, P. Nordlander, and S. Gao, "Quantum mechanical study of the coupling of plasmon excitations to atomic-scale electron transport," *The Journal of Chemical Physics*, vol. 131, p. 074071, 2011.

[97] L. V. Brown, H. Sobhani, J. B. Lassiter, P. Nordlander, and N. J. Halas, "Heterodimers: Plasmonic properties of mismatched nanoparticle pairs," *American Chemical Society Nano*, vol. 4, no. 2, pp. 819–832, 2010.

[98] O. Pére-González, N. Zabala, A. G. Borisov, N. J. Halas, P. Nordlander, and J. Aizpurua, "Optical spectroscopy of conductive junctions in plasmonic cavities," *Nano Letters*, vol. 10, no. 8, pp. 3090–3095, 2010.

[99] T. Li, W. Hu, and D. Zhu, "Nanogap electrodes," *Advanced Materials*, vol. 22, pp. 286–300, 2010.

[100] S. K. Ghosh and T. Pal, "Interparticle coupling effect on the surface plasmon resonance of gold nanoparticles: From theory to applications," *Chemical Reviews*, vol. 107, p. 4797, 2007.

[101] L. Yang, H. Wang, B. Yan, and B. M. Reinhard, "Calibration of silver plasmon rulers in the 1-25 nm separation range: Experimental indications of distinct plasmon coupling regimes," *The Journal of Physical Chemistry C*, vol. 114, no. 2, pp. 4901–4908, 2010.

[102] S. Marhaba, G. Bachelier, C. Bonnet, M. Broyer, E. Cottancin, N. Grillet, J. Lermé, J. Vialle, and M. Pellarin, "Surface plasmon resonance of single gold nanodimers near the conductive contact limit," *The Journal of Physical Chemistry C*, vol. 113, no. 11, pp. 4349–4356, 2009.

[103] S. S. Aćimović, M. P. Kreuzer, M. U. González, and R. Quidant, "Plasmon near-field coupling in metal dimers as a step toward single-molecule sensing," *American Chemical Society Nano*, vol. 3, p. 1231, 2009.

[104] J. Merlein, M. Kahl, A. Zuschlag, A. Sell, A. Halm, J. Boneberg, P. Leiderer, A. Leitenstorfer, and R. Bratschitsch, "Nanomechanical control of an optical antenna," *Nature Photonics*, vol. 2, pp. 230–233, 2008.

[105] J. Kern, S. Grossmann, N. V. Tarakina, T. Häckel, M. Emmerling, M. Kamp, J. Huang, P. Biagioni, J. C. Prangsma, and B. Hecht, "Atomic-scale confinement of resonant optical fields," *Nano Letters*, vol. DOI: 10.1021/nl302315g, 2012.

[106] H. Duan, A. I. Fernández-Domínguez, M. Bosman, S. A. Maier, and J. K. W. Yang, "Nanoplasmonics: classical down to the nanometer scale," *Nano Letters*, vol. 12, no. 3, pp. 1683–1689, 2012.

[107] D. R. Ward, N. J. Halas, J. W. Ciszek, J. M. Tour, Y. Wu, P. Nordlander, and D. Natelson, "Simultaneous measurements of electronic conduction and Raman response in molecular junctions," *Nano Letters*, vol. 8, no. 3, pp. 919–924, 2008.

[108] J. Tian, B. Liu, X. Li, Z. Yang, B. Ren, S. Wu, N. Tao, and Z. Tian, "Study of molecular junctions with a combined surface-enhanced Raman and mechincally controllable break junction method," *Journal of the American Chemical Society*, vol. 128, no. 46, pp. 14748–14749, 2006.

[109] J. Chen, W. Yang, K. Dick, K. Deppert, H. Q. Xu, L. Samuelson, and H. Xu, "Tip-enhanced Raman scattering of *p*-thiocresol molecules on individual gold nanoparticles," *Applied Physics Letters*, vol. 92, p. 093110, 2008.

[110] A. Taguchi, N. Hayazawa, Y. Saito, H. Ishitobi, A. Tarun, and S. Kawata, "Controlling the plasmon resonance wavelength in metal-coated probe using refractive index modification," *Optics Express*, vol. 17, no. 8, pp. 6509–6518, 2009.

[111] Y. H. Kahng, J. Choi, K. Jeong, B. C. Park, D. H. Kim, J. Lyou, H. Lee, T. Lee, and S. J. Ahn, "Fabrication of ball shaped atomic force microscopy tips by ion-beam-induced deposition of platinum on multiwall carbon nanotubes," *Ultramicroscopy*, vol. 110, pp. 82–88, 2009.

[112] Y. Gan, "Invited review article: A review of techniques for attaching micro- and nanoparticles to a probe's tip for surface force and near-field optical measurements," *Review of Scientific Intruments*, vol. 78, p. 081101, 2007.

[113] Y. Zou, P. Steinverzel, T. Yang, and K. B. Crozier, "Surface plasmon resonances of optical antenna atomic force microscope tips," *Applied Physics Letters*, vol. 94, p. 171107, 2009.

[114] B. Yeo, J. Stadler, T. Schmid, R. Zenobi, and W. Zhang, "Tip-enhanced Raman spectroscopy - It's status, challenges and future directions," *Chemical Physics Letters*, vol. 472, pp. 1–13, 2009.

[115] R. Dorn, S. Quabis, and G. Leuchs, "Sharper focus for a radially polarized light beam," *Physical Review Letters*, vol. 110, no. 23, p. 233901, 2003.

[116] J. M. Dudley and J. R. Taylor, "Ten years of nonlinear optics in photonics crystal fibre," *Nature Photonics*, vol. 3, pp. 85–90, 2009.

[117] G. Baffou and H. Rigneault, "Femtosecond-pulsed optical heating of gold nanoparticles," *Physical Review B*, vol. 84, p. 035415, 2011.

[118] G. Baffou, R. Quidant, and F. J. G. de Abajo, "Nanoscale control of optical heating in complex plasmonic systems," *American Chemical Society Nano*, vol. 4, no. 2, pp. 709–716, 2010.

[119] G. Schmid and B. Corain, "Nanoparticulated gold: synthesis, structures, electronics, and reactivities," *European Journal of Inorganic Chemistry*, vol. 2003, no. 17, pp. 3081–3098, 2003.

[120] R. Dorn, S. Quabis, and G. Leuchs, "The focus of light-linear polarization breaks the rotational symmetry of the focal spot," *Journal of Modern Optics*, vol. 50, no. 12, pp. 1917–1926, 2003.

[121] M. Gondran and A. Gondran, "Energy flow lines and the spot of Poisson-Arago," *American Journal of Physics*, vol. 78, no. 6, pp. 598–602, 2010.

[122] A. Curry, G. Nusz, A. Chilkoti, and A. Wax, "Substrate effect on refractive index dependence of plasmon resonance for individual silver nanoparticles observed using darkfield micro-spectroscopy," *Optics Express*, vol. 13, no. 7, pp. 2668–2677, 2010.

[123] C. Sönnichsen, T. Franzl, T. Wilk, G. von Plessen, and J. Feldmann, "Plasmon resonances in large noble-metal clusters," *New Journal of Physics*, vol. 4, pp. 93.1–93.8, 2002.

[124] C. A. Clifford and M. P. Seah, "Improved methods and uncertainty analysis in the calibration of the spring constant of an atomic force microscope cantilever using static experimental methods," *Measurement Science and Technology*, vol. 20, pp. 125501–125512, 2009.

[125] J. F. Rhoads, S. W. Shaw, and K. L. Turner, "Nonlinear dynamics and its applications in micro- and nanoresonators," *Journal of Dynamic Systems, Measurement, and Control*, vol. 132, p. 034001, 2010.

[126] T. Ouisse, M. Stark, F. Rodrigues-Martins, B. Bercu, S. Huant, and J. Chevrier, "Theory of electric force microscopy in the parametric amplification regime," *Physical Review B*, vol. 71, p. 205404, 2005.

[127] B. R. Gray, *Design of RF and Microwave Parametric Amplifiers and Power Upconverters*. PhD thesis, Georgia Institute of Technology, Georgia, USA, 2012.

[128] N. C. Bruce, A. García-Valenzuela, and D. Kouznetsov, "The lateral resolution limit for imaging periodic conducting surfaces in capacitive microscopy," *Journal of Physics D: Applied Physics*, vol. 33, no. 22, p. 2890, 2000.

[129] W. H. Press, S. A. Teukolsky, W. T. Vetterling, and B. P. Flannery, *Numerical Recipes in C++*. New York, US: Cambridge University Press, 2^{nd} ed., 1992.

[130] M. Bao and H. Yang, "Squeeze film air damping in MEMS," *Sensors and Actuators A: Physical*, vol. 136, no. 1, pp. 3–27, 2007.

[131] J. Colchero, A. Gill, and A. M. Baró, "Resolution enhancement and improved data interpretation in electrostatic force microscopy," *Physical Review B*, vol. 64, p. 245403, 2001.

[132] J. Toset, I. Casuso, J. Samitier, and G. Gomila, "Deflection-voltage curve modelling in atomic force microscopy and its use in DC electrostatic manipulation of gold nanoparticles," *Nanotechnology*, vol. 18, p. 015503, 2007.

[133] D. Sarid, J. P. Hunt, R. K. Workman, X. Yao, and C. A. Peterson, "The role of adhesion in tapping-mode atomic force microscopy," *Applied Physics A*, vol. 66, pp. S283–S286, 1998.

[134] C. Argento and R. H. French, "Parametric tip model and force-distance relation for Hamaker constant determination from atomic force microscopy," *Journal of Applied Physics*, vol. 80, no. 11, pp. 6081–6090, 1996.

[135] G. V. P. Kumar, "Plasmonic nano-architectures for surface enhanced Raman scattering: a review," *Journal of Nanophotonics*, vol. 6, p. 064503, 2012.

[136] P. J. Schuck, D. P. Fromm, A. Sundaramurthy, G. S. Kino, and W. E. Moerner, "Improving the mismatch between light and nanoscale objects with gold bowtie nanoantennas," *Physical Review Letters*, vol. 94, p. 017402, 2005.

[137] E. Cubukcu, E. A. Kort, K. B. Crozier, and F. Capasso, "Plasmonic laser antenna," *Applied Physics Letters*, vol. 89, p. 093120, 2006.

[138] A. G. Curto, G. Volpe, T. H. Taminiau, M. P. Kreuzer, R. Quidant, and N. F. van Hulst, "Unidirectional emission of a quantum dot coupled to a nanoantenna," *Science*, vol. 329, pp. 930–933, 2010.

[139] M. L. Juan, M. Righini, and R. Quidant, "Plasmon nano-optical tweezers," *Nature Photonics*, vol. 5, pp. 349–356, 2011.

[140] M. Schnell, A. García-Etxarri, A. J. Huber, K. Crozier, J. Aizpurua, and R. Hillenbrand, "Controlling the near-field oscillations of loaded plasmonic nanoantennas," *Nature Photonics*, vol. 3, pp. 287–291, 2009.

[141] L. Novotny and N. van Hulst, "Antennas for light," *Nature Photonics*, vol. 5, pp. 89–90, 2011.

[142] A. V. Bragas, S. M. Landi, and O. E. Martíez, "Laser field enhancement at the scanning tunneling microscope junction measured by optical rectification," *Applied Physics Letters*, vol. 72, no. 17, pp. 2075–2077, 1998.

[143] J. K. Viljas and J. C. Cuevas, "Role of electronic structure in photoassisted transport through atomic-sized contacts," *Physical Review B*, vol. 75, p. 075406, 2007.

[144] D. R. Ward, F. Hüser, F. Pauly, J. C. Cuevas, and D. Natelson, "Optical rectification and field enhancement in a plasmonic nanogap," *Nature Nanotechnology*, vol. 5, pp. 732–736, 2010.

[145] C. Ye, M. Li, J. Luo, L. Chen, Z. Tang, J. Pei, L. Jiang, Y. Song, and D. Zhu, "Photo-induced amplification of readout contrast in nanoscale data storage," *Journal of Materials Chemistry*, vol. 22, pp. 4299–4305, 2012.

[146] N. Ittah, G. Noy, I. Yutsis, and Y. Selzer, "Measurement of electronic transport through $1G_0$ gold contacts under laser irradiation," *Nano Letters*, vol. 9, no. 4, pp. 1615–1620, 2009.

[147] J. Mitra, L. Feng, M. G. Boyle, and P. Dawson, "Electromagnetic interaction between a metallic nanoparticle and surface in tunnelling proximity

- modelling and experiment," *Journal of Physics D: Applied Physics*, vol. 42, p. 215101, 2009.

[148] P. Bharadwaj, A. Bouhelier, and L. Novotny, "Electrical Excitation of Surface Plasmons," *Physical Review Letters*, vol. 106, p. 226802, 2011.

[149] C. Chen, C. A. Bobisch, and W. Ho, "Visualization of Fermi's golden rule through imaging of light emission from atomic silver chains," *Science*, vol. 325, no. 5943, pp. 981–985, 2009.

[150] N. L. Schneider, G. Schull, and R. Berndt, "Optical probe of quantum shot-noise reduction at a single-atom contact," *Physical Review Letters*, vol. 105, p. 026601, 2010.

[151] W. Zhang, X. Cui, and O. J. F. Martin, "Local field enhancement of an infinite conical metal tip illuminated by a focused beam," *Journal of Raman Spectroscopy*, vol. 40, pp. 1338–1342, 2009.

[152] F. Huang and J. J. Baumberg, "Actively tuned plasmons on elastomerically driven Au nanoparticle dimers," *Nano Letters*, vol. 10, no. 5, pp. 1787–1792, 2010.

[153] R. Esteban, A. G. Borisov, P. Nordlander, and J. Aizpurua, "Bridging quantum and classical plasmonics with a quantum-corrected model," *Nature Communications*, vol. 3, p. 825, 2012.

[154] P. B. Johnson and R. W. Christy, "Optical constants of the noble metals," *Physical Review B*, vol. 6, no. 12, pp. 4370–4379, 1998.

[155] J. M. Pitarke, F. Flores, and P. M. Echenique, "Tunneling spectroscopy: surface geometry and interface potential effects," *Surface Science*, vol. 234, pp. 1–16, 1990.

[156] E. Chulkov, V. Silkin, and P. M. Echenique, "Image potential states on metal surfaces: binding energies and wave functions," *Surface Science*, vol. 437, pp. 330–352, 1999.

[157] B. Hetényi, F. D. Angelis, P. Giannozzi, and R. Car, "Reconstruction of frozen-core all-electron orbitals from pseudo-orbitals," *Journal of Chemical Physics*, vol. 115, no. 13, p. 5791, 2001.

[158] L. Novotny and B. Hecht, *Principles of Nano Optics*. Cambridge, UK: Cambridge University Press, 2006.

[159] K. J. Savage, M. M. Hawkeye, B. F. Soares, and J. J. Baumberg, "From microns to kissing contact: dynamic positioning of two nano-systems," *Applied Physics Letters*, vol. 99, p. 053110, 2011.

[160] P. Johansson, "Light emission from a scanning tunneling microscope: fully retarded calculation," *Physical Review B*, vol. 58, no. 16, pp. 10823–10834, 1998.

[161] J. Aizpurua, S. P. Apell, and R. Berndt, "Role of tip shape in light emission from the scanning tunneling microscope," *Physical Review B*, vol. 62, no. 3, pp. 2065–2073, 2000.

[162] N. Agraït, A. L. Yeyati, and J. M. van Ruitenbeek, "Quantum properties of atomic-sized conductors," *Physics Reports*, vol. 377, pp. 81–279, 2003.

[163] B. Cappella and G. Dietler, "Force distance curves by atomic force microscopy," *Surface Science Reports*, vol. 34, no. 1–3, pp. 1–104, 1999.

[164] V. Barcons, A. Verdaguer, J. Font, M. Chiesa, and S. Santos, "Nanoscale capillary interactions in dynamic atomic force microscopy," *The Journal of Physical Chemistry C*, vol. 116, pp. 7757–7766, 2012.

[165] X. N. Xie, H. J. Chung, D. M. Tong, C. H. Sow, and A. T. S. Wee, "Field-induced meniscus dynamics and its impact on the nanoscale tip-surface interface," *Journal of Applied Physics*, vol. 102, p. 084313, 2007.

[166] A. Downes, D. Salter, and A. Elfick, "Heating effects in tip-enhanced optical microscopy," *Optics Express*, vol. 14, no. 12, pp. 5216–5222, 2006.

[167] H. J. Mamin, E. Ganz, D. W. Abraham, R. E. Thomson, and J. Clarke, "Contamination-mediated deformation of graphite by the scanning tunneling microscope," *Physical Review B*, vol. 34, pp. 9015–9018, 1986.

[168] J. W. Tringe, T. A. Uhlman, A. C. Oliver, and J. E. Houston, "A single asperity study of au/au electrical contacts," *Journal of Applied Physics*, vol. 93, pp. 4661–4669, 2003.

[169] S. C. Meepagala, F. Real, and C. B. Reyes, "Tip-sample interaction forces in scanning tunnelling microscopy: effects of contaminants," *Journal of Vacuum Science and Technology B*, vol. 9, no. 2, pp. 1340–1342, 1991.

[170] J. B. Lassiter, J. Aizpurua, L. I. Hernandez, D. W. Brandl, I. Romero, S. Lal, J. H. Hafner, P. Nordlander, and N. J. Halas, "Close encounters between two nanoshells," *Nano Letters*, vol. 8, no. 4, pp. 1212–1218, 2008.

[171] N. J. Tao, C. Z. Li, and H. X. He, "Scanning tunneling microscopy applications in electrochemistry-beyound imaging," *Journal of Electroanalytical Chemistry*, vol. 492, pp. 81–93, 2000.

[172] Y. F. Wang, J. Kröger, R. Berndt, H. Vázquez, M. Brandbyge, and M. Paulsson, "Atomic-scale control of electron transport through single molecules," *Physical Review Letters*, vol. 104, p. 176802, 2010.

[173] K. J. Savage, M. M. Hawkeye, R. Esteban, A. G. Borisov, J. Aizpurua, and J. J. Baumberg, "Revealing the quantum regime in tunnelling plasmonics," *Nature*, vol. 491, no. 7425, pp. 574–577, 2012.

[174] A. I. Fernández-Domínguez, S. A. Maier, and J. B. Pendry, "Collection and concentration of light by touching spheres: a transformation optics approach," *Physical Review Letters*, vol. 105, p. 266807, 2010.

[175] A. F. Koenderink, "On the use of Purcell factors for plasmon antennas," *Optics Letters*, vol. 35, no. 24, pp. 4208–4210, 2010.

[176] J. Gao, J. F. McMillan, M. Wu, J. Zheng, S. Assefa, and C. W. Wong, "Demonstration of an air-slot mode-gap confined photonic crystal slab nanocavity with ultrasmall mode volumes," *Applied Physics Letters*, vol. 96, p. 051123, 2010.

[177] J. G. Simmons, "Generalized formula for the electric tunnel effect between similar electrodes separated by a thin insulating film," *Journal of Applied Physics*, vol. 34, no. 6, pp. 1793–1803, 1963.

[178] D. C. Marinica, A. K. Kazansky, P. Nordlander, J. Aizpurua, and A. G. Borisov, "Quantum plasmonics: nonlinear effects in the field enhancement of a plasmonic nanoparticle dimer," *Nano Letters*, vol. 12, pp. 1333–1339, 2012.

[179] C. Cirací, R. T. Hill, J. J. Mock, Y. Urzhumov, A. I. Fernández-Domingínguez, S. A. Maier, J. B. Pendry, A. Chilkoti, and D. R. Smith, "Probing the ultimate limits of plasmonic enhancement," *Science*, vol. 337, pp. 1072–1074, 2012.

[180] C. V. Vlack, P. T. Kristensen, and S. Hughes, "Spontaneous emission spectra and quantum light-matter interactions from a strongly coupled quantum dot metal-nanoparticle system," *Physical Review B*, vol. 85, p. 075303, 2012.

[181] S. Savasta, R. Saija, A. Ridolfo, O. D. Stefano, P. Denti, and F. Borghese, "Nanopolaritonics: vacuum Rabi splitting with a single quantum dot in the center of a dimer nanoantenna," *American Chemical Society Nano*, vol. 4, no. 11, pp. 6369–6376, 2010.

[182] J. P. Reithmaier, G. Sek, A. Löffler, C. Hofmann, S. Kuhn, S. Reitzenstein, L. V. Keldysh, V. D. Kulakovskii, T. L. Reinecke, and A. Forchel, "Strong coupling in a single quantum dot-semiconductor microcavity system," *Nature*, vol. 432, pp. 936–946, 2004.

[183] E. J. R. Vesseur, F. J. G. de Abajo, and A. Polman, "Broadband Purcell enhancement in plasmonic ring cavities," *Physical Review B*, vol. 82, p. 165419, 2010.

[184] T. Yoshie, A. Scherer, J. Hendrickson, G. Khitrova, H. M. Gibbs, G. Rupper, C. Ell, O. B. Shchekin, and D. G. Deppe, "Vacuum Rabi splitting with a single quantum dot in a photonic crystal nanocavity," *Nature*, vol. 432, pp. 200–203, 2004.

[185] J. R. Tischler, M. S. Bradley, Q. Zhang, T. Atay, A. Nurmikko, and V. Bulović, "Solid state cavity QED: strong coupling in organic thin films," *Organic Electronics*, vol. 8, pp. 94–113, 2007.

[186] D. G. Lidzey, D. D. C. Bradley, T. Virgili, A. Armitage, and M. S. Skolnick, "Room temperature polariton emission from strongly coupled organic semiconductor microcavities," *Physical Review Letters*, vol. 82, no. 16, pp. 3316–3319, 1999.

[187] N. T. Fofang, T. Park, O. Neumann, N. A. Mirin, P. Nordlander, and N. J. Halas, "Plexcitonic nanoparticles: plasmon-exciton coupling in nanoshell J-aggregate complexes," *Nano Letters*, vol. 8, pp. 3481–3487, 2008.